

**Effect of hot electrons on the
hydrodynamic of shocks and implosions
for shock ignition**

Jocelain Trela

June 2019

Table of contents

1	Introduction	1
1.1	Fusion reactions	2
1.1.1	Energy of a fusion reaction	2
1.1.2	Fusion reaction rate	3
1.1.3	Thermonuclear ignition	5
1.2	Key parameters in Inertial Confinement Fusion	7
1.2.1	ICF confinement time	7
1.2.2	Fuel depletion	9
1.2.3	Burn efficiency	9
1.2.4	ICF reactor	10
1.2.5	Central hot spot ignition conditions	13
1.3	Classical approaches to ICF	16
1.3.1	Indirect drive	17
1.3.2	Direct drive	17
1.3.3	Shell implosion in direct drive	17
1.4	Shock ignition scheme	23
1.4.1	Principle of shock ignition	24
1.4.2	Hydrodynamic studies for shock ignition target design	25
1.4.3	Hot electron generation in shock ignition implosion	29
1.5	Thesis outline	31
2	Laser matter interaction	33
2.1	Ablative drive	33
2.1.1	Critical density	33
2.1.2	Collisional absorption	34
2.1.3	Stationary laser-driven ablation	36
2.2	Collective effects in plasmas	39
2.2.1	Ion acoustic waves	40

2.2.2	Electron plasma waves	40
2.2.3	Linear wave damping	41
2.2.4	Non-linear wave damping	43
2.3	Anomalous absorption of laser light	44
2.3.1	Resonant absorption	45
2.3.2	Parametric decay	48
2.3.3	Stimulated Brillouin scattering	49
2.3.4	Filamentation	51
2.3.5	Stimulated Raman scattering	52
2.3.6	Two-plasmon decay	55
2.4	Conclusion	57
3	Hydrodynamic and shock waves	59
3.1	Linear hydrodynamic in planar geometry	59
3.1.1	Conservation laws	59
3.1.2	Perturbation theory of fluid motion	60
3.1.3	Sound waves	62
3.1.4	Compression wave created by a piston	63
3.1.5	Rarefaction waves	63
3.1.6	Compression waves	65
3.2	Shocks	66
3.2.1	Conservation laws	66
3.2.2	Hugoniot curves	68
3.2.3	Set of accessible states and reshock	71
3.3	Interaction of a shock with a discontinuity	74
3.3.1	Shock at contact discontinuity	74
3.3.2	Shock collision	76
3.3.3	Shock coalescence	78
3.4	Conclusion	79
4	Hydrodynamic of shock ignition in the absence of hot electrons	81
4.1	Shock ignition theory in planar geometry	81
4.1.1	Classical scheme in planar geometry	82
4.1.2	Shock ignition techniques	86
4.2	Toward realistic shock ignition scheme	95
4.2.1	Most robust shock ignition technique	96
4.2.2	Shock pressure amplification in realistic spherical implosion	98

4.3	Experimental study of implosion at relatively low spike intensity	101
4.3.1	Experimental setup	101
4.3.2	Self Emission Shadowgraphy	103
4.3.3	LILAC simulations	104
4.3.4	Effect of the spike launching time on the implosions performance .	108
4.4	Conclusion	111
5	Effect of hot electron in planar geometry	113
5.1	Description of hot electron in CHIC	114
5.2	Experimental study of shock propagation at high intensity on PALS	120
5.2.1	Experimental set-up and diagnostics	121
5.2.2	Characterization of shock breakout mistiming due to planar geometry simulations	125
5.2.3	CHIC simulations	128
5.2.4	Conclusion	139
5.3	Radiography of a shock perturbed by hot electrons on OmegaEP	140
5.3.1	CHIC simulations for the target and radiography design	140
5.3.2	Experimental set-up and preliminary radiography results	148
5.3.3	Post-processor radiographic for planar CHIC simulation	153
5.3.4	Conclusion	156
5.4	Design of shock ignition relevant experiment in planar geometry on LMJ .	157
5.5	Conclusion	168
6	Effect of hot electron in spherical geometry	171
6.1	Experimental set-up	172
6.2	Hot electron measurement by high-energy differential-filtering photon spec- troscopy	174
6.3	Hot electron measurement with HXRD	176
6.4	LILAC simulations	180
6.5	Effect of the hot electron preheat on the performance of implosions	184
6.6	Conclusion	187
7	Conclusions	189
	References	195

Chapter 1

Introduction

The production of energy and its environmental impact is a worldwide concern. Currently, the fossil fuels (coal, natural gas, petroleum and other liquids) are the first source of energy. But the limitation in available stock for these resources, as well as their dramatic environmental impact (greenhouse effect), clearly showed that alternative sources of energy have to be developed. These are the renewable and nuclear energies. Renewable energies seem to be an ideal alternative and their use has strongly increased in last decades. Yet some issues arise when one considers the possibility that they fully replace the production of energy by burning fossil fuels. In particular, the space available for hydro-electric plants, solar plants or wind turbines is limited and does not always match the areas where the energetic demand is strongest. On the other hand, the production of energy from nuclear power plants is independent from these geographic concerns, but many other issues arise from its use: limitation in fuel stocks, management of the radioactive wastes, risk of accidents with dramatic ecological impact...

These three issues are directly inherent to the way current nuclear power plants produce energy: the fission of a heavy nucleus into lighter ones. Yet, another exothermic type of nuclear reaction exists: the fusion of light nuclei into a heavier one. This type of reaction is the way by which stars generate energy and it has been used in a uncontrolled way on earth in nuclear weaponry. Controlled fusion has never been achieved on Earth but a hypothetical controlled-fusion power plant would have many advantages compared to the existing ways of producing energy. The light atoms used as fuel are naturally very abundant and well spread around the Earth. The products of fusion reactions are not radioactive and only some elements from the power plant would be activated with life-time of around 100 years [1] (which is much more manageable than the 240 000 years of current nuclear wastes). Also, the conditions that allow fusion reactions to occur are so difficult to maintain that any incident

would result in the shut-off of the power plant, without any risk of chain reactions leading to major accidents.

These arguments make fusion a very promising source of energy which, despite the complexity of the realization of a fusion power plant, justifies the large efforts made worldwide in order to explore this solution.

1.1 Fusion reactions

1.1.1 Energy of a fusion reaction

A fusion reaction consists in two light nuclei X_1 and X_2 merging into a heavier one X_3 , with the emission of light particle X_4 . This reaction is noted



In such reaction, the numbers of protons and of neutrons are conserved but not the mass. According to Einstein's mass-energy equivalence theorem, if the mass of the final products is smaller than the mass of the initial particles, then the reaction releases an energy

$$Q = \left(\sum_f m_f - \sum_i m_i \right) c^2, \quad (1.2)$$

where m is the mass, the subscripts i and f denote the initial and final nuclei, respectively, and c is the speed of light. This variation of mass is due to difference in binding energies in the nuclei involved in the reaction. A nucleus composed of Z protons and $(A - Z)$ neutrons has a mass

$$m = Zm_p + (A - Z)m_n - \Delta m, \quad (1.3)$$

where m_p and m_n are the masses of the proton and of the neutron, respectively. The missing mass Δm is equivalent to the binding energy

$$B = \Delta m c^2. \quad (1.4)$$

This positive energy allows nuclei to be stable despite the repulsive force between the positively charged protons. Figure 1.1 shows the binding energy per nucleon (protons and neutrons of a nucleus) as a function of mass number. The most stable nuclei, with the highest binding energies, are around $A = 56$. For the light elements, this curve is very steep, with a peak for ${}^4\text{He}$. The fusion reaction of these nuclei, especially if it results in the production of

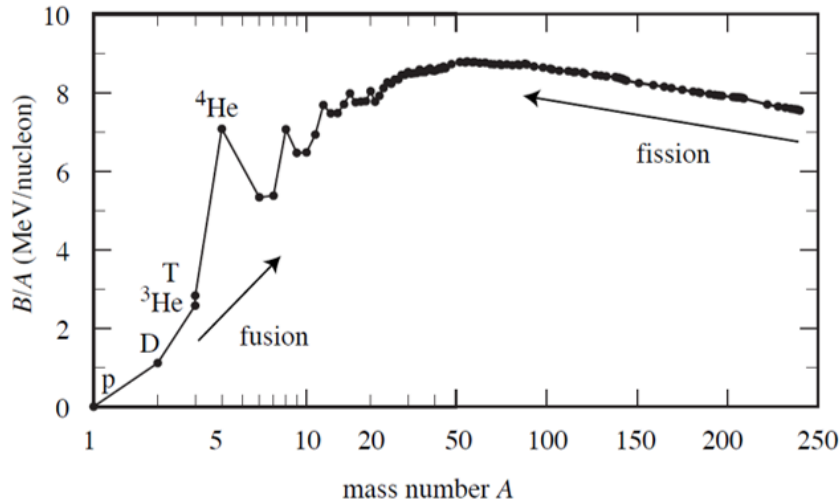


Fig. 1.1 Binding energy per nucleon versus mass number A , for the most stable isotopes. For $A = 3$, the unstable tritium is included in view of its importance for controlled fusion. Notice that the mass number scale is logarithmic in the range 1–50 and linear in the range 50–250 [2].

a α particle (${}^4\text{He}$ nucleus), releases a lot of energy per nucleon, and therefore per unit mass. On the other side of the curve maximum, there are heavy nuclei which can release energy though fission. But the slope of the curve for heavy nuclei is less steep than for light nuclei, showing that fission releases less energy per unit mass than fusion.

As an example, the fusion of the nuclei of deuterium, formed by a proton and a neutron, and of tritium, formed by a proton and two neutrons, is



where n denote the neutron. This reaction releases 17.6 MeV. Due to the conservation of momentum, this energy is distributed between the particles inversely proportional to their mass. Since the α particle is four times more massive than the neutron, the kinetic energy is 3.5 MeV for the α particle and 14.1 MeV for the neutron. This implies that if 1 mg of DT fuel were fully burned, its 10^{20} reactions would release around 340 MJ (equivalent to the explosion of 80 kg of TNT).

1.1.2 Fusion reaction rate

There is a large variety of possible fusion reactions and an important step toward fusion as an energy source is to identify those that are the most suitable to be realized on Earth. The energy released by the reaction is actually not the most relevant parameter since many reactions

release more than a MeV. A more critical parameter is the probability of the reaction to occur. In order to fuse, the two positively charged nuclei must come into contact, overcoming the repulsive Coulomb force. Considering classical physics only, the energy of the particles must be higher than the height of the Coulomb barrier, which is of the order of 1 MeV for deuteron. However, quantum mechanics allows for tunneling of particles with energies smaller than the barrier height, making the fusion reactions possible at energies as low as few tens keV. The probability of tunneling though the Coulomb barrier increases with the energy of the particles such that, in the absence of resonance, the fusion of particles with higher velocities is more likely.

Considering a volume V which contains a mixture of two species of nuclei, the number of fusion reactions ΔN occurring between in a time interval Δt is

$$\Delta N = n_1 n_2 \sigma(v) v V \Delta t, \quad (1.6)$$

where n_1 and n_2 are the particle densities of the two species of nuclei, and $\sigma(v)$ is the cross section of the fusion reaction between these two, which depends of the relative velocity $v = |v_1 - v_2|$ of the particles. In the conditions for fusion, the fuel is usually a plasma in thermal equilibrium and the velocity of the particles of a species is characterized by a Maxwellian distribution

$$f_j(v_j) = \left(\frac{m_j}{2\pi k_B T} \right)^{3/2} \exp \left(-\frac{m_j v_j^2}{2k_B T} \right), \quad (1.7)$$

where the subscript $j = 1, 2$ corresponds to the species of nuclei, T the plasma temperature and k_B the Boltzmann constant. The product $\sigma(v)v$ can then be averaged over this distribution

$$\langle \sigma v \rangle = \int \int \sigma(v) v f_1(v_1) f_2(v_2) dv_1 dv_2. \quad (1.8)$$

This double integral over the particle velocities v_1 and v_2 can be expressed as the product of simple integrals over the relative velocity v and the velocity of the center of mass v_c

$$\langle \sigma v \rangle = \int f_c(v_c) dv_c \times \int \sigma(v) v f_r(v) dv, \quad (1.9)$$

where $f_c(v_c)$ is a Maxwellian distribution of particles of mass $m_1 + m_2$ and velocity $v_c = (m_1 v_1 + m_2 v_2) / (m_1 + m_2)$ and $f_r(v)$ is a Maxwellian distribution of particle of mass $m_r = m_1 m_2 / (m_1 + m_2)$ and velocity v . By definition of the normalized Maxwellian distribution, the first integral is equal to 1. By writing the volume element in velocity space as $dv = 4\pi v^2 dv$, the reaction cross section can be express as an integral over the velocity v only

$$\langle \sigma v \rangle = 4\pi \int_0^{\infty} v^3 \sigma(v) f_r(v) dv. \quad (1.10)$$

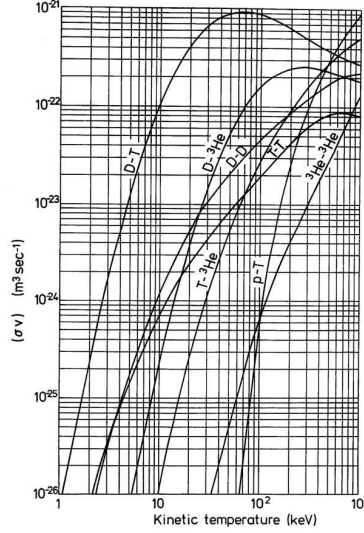


Fig. 1.2 Maxwell averaged fusion reaction rate as a function of plasma temperature for the reactions relevant to controlled fusion energy [<http://www.kayelaby.npl.co.uk>].

Unlike σ , which depends on the relative velocity of the particles, the reaction rate $\langle \sigma v \rangle$ depends on the temperature of the fuel. The reaction rate as a function of temperature for several fusion reactions is presented in Figure 1.2. For temperatures below 500 keV, the DT fusion reaction rate is the highest. In the laboratory, even a temperature of 10 keV is very difficult to achieve. As a comparison, the temperature in the center of the sun, where the fusion reactions naturally occur, is around 1.3 keV. Due to this limitation, the fusion of hydrogen isotopes (DT) is the most promising for the production of energy.

1.1.3 Thermonuclear ignition

Considering a volume of DT fuel, the thermonuclear ignition is achieved when the energy released by fusion reactions in this volume exceed the energy losses. This corresponds to a self-heating state of the plasma, where no external source of energy is needed in order to maintain it in a burning state. For an equimolar DT plasma such that the ion density is $n_D = n_T = n/2$, the volumetric power released by the fusion reactions is

$$W_{fus} = \frac{1}{4} n^2 \langle \sigma v \rangle \epsilon_{DT}, \quad (1.11)$$

where $\langle \sigma v \rangle$ is the fusion reaction rate for the DT reaction described in the previous section and $\epsilon_{DT} = 17.6$ MeV is the energy released by one fusion reaction. 80% of this energy is

carried by neutrons. Because they are neutral particles, they interact weakly with the plasma and will most probably escape it. The remaining 20% of the released energy is carried by alpha particles, which have a much shorter penetration depth. Assuming that the plasma has a stopping power large enough, these particles will deposit their energy in the plasma, thereby heating it with a power

$$W_\alpha = \frac{1}{5}W_{fus}. \quad (1.12)$$

The main mechanism by which a fusion plasma loses its energy is by the emission of Bremsstrahlung radiation. Electron-ion collisions generate high energy radiation for which the plasma is transparent. The volumetric power loss is

$$W_{brem} = A_b Z n_e n_i T^{1/2} = 5.34 \times 10^{-17} Z n_e n_i T^{1/2} \text{W/cm}^3, \quad (1.13)$$

where n_e and n_i are the electron and ion densities in cm^{-3} , respectively, Z the charge state of the plasma and T the temperature in keV. For a DT plasma ($Z = 1$), $n_e = n_i = n$ and both W_α and P_b depend only on n^2 and T . Figure 1.3 presents these powers normalized to n^2 . For a temperature above 4.3 keV, W_α is larger than W_{brem} and the plasma is in a self-heating condition. This temperature is therefore the minimum requirement in order to achieve ignition. Taking in consideration additional energy loss mechanisms increases this minimum temperature.

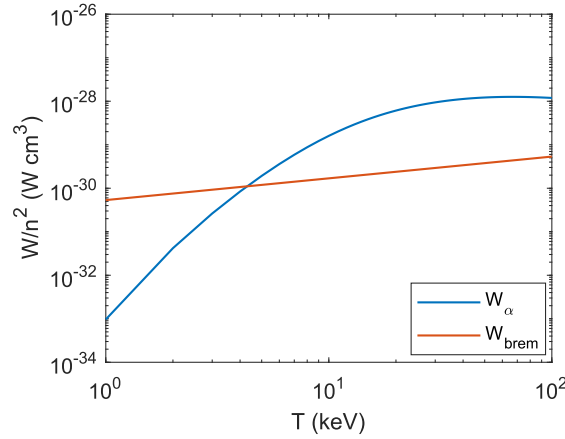


Fig. 1.3 Power deposited by α particles (heating) and Bremsstrahlung power (loss) as a function of the plasma temperature. The powers have been normalized by the square of the plasma particle density n . The two curves cross at $T = 4.3$ keV.

1.2 Key parameters in Inertial Confinement Fusion

Once the conditions of self-heating are reached, the plasma needs to be confined in order to stay in these conditions. At temperature of a few keV, the plasma will melt any material it comes in contact with. For example, the Tungsten is the chemical element with the highest melting point at 0.3 eV. Additionally, direct contact with cold material would rapidly cool down the plasma, stopping the fusion reactions. A way to confine the plasma without any contact is to use magnetic fields. The plasma is composed of charged particles that, in presence of a magnetic field, will have a circular motion around the field lines. This is the principle of magnetic confinement fusion (MCF). Another possibility is to use the plasma own inertia as a means of confinement. In this case the plasma is confinement for very short times. This is the principle of the inertial confinement fusion (ICF).

E

1.2.1 ICF confinement time

Even though ICF does not use external means of confinement of the fusion plasma, one can express a characteristic time during which the fuel burns.

Let's consider a homogeneous sphere of DT fuel in fusion conditions, without any mean of confinement. A rarefaction wave will start on the surface of the plasma and propagate inward at the sound velocity $c_s = \sqrt{(Z+1)k_B T / m_i}$, where $m_i = 2.5m_p$ is the average ion mass of DT. The position of the front of this wave as a function of time t is

$$R(t) = R_f - c_s t, \quad (1.14)$$

where R_f is the initial radius of the fuel sphere. The decompressed fuel quickly cools down, therefore only the fusion reactions in the unperturbed volume have to be considered. The rate of these reactions is

$$\frac{dN}{dt} = n_D n_T \langle \sigma v \rangle V(t), \quad (1.15)$$

where $V(t) = \frac{4\pi}{3} R(t)^3$ is the volume of the unperturbed fuel. Integrating this expression from the initial time $t = 0$ to the final time $t = R_f / c_s$, at which the rarefaction wave reaches the center of the plasma, gives the number of fusion reactions

$$N_f = n_D n_T \langle \sigma v \rangle \frac{4\pi}{3} \int_0^{R_f/c_s} R(t)^3 dt = n_D n_T \langle \sigma v \rangle V_f \frac{R_f}{4c_s}, \quad (1.16)$$

where $V_f = \frac{4\pi}{3}R_f^3$ is the initial volume of the fuel. If the plasma was confined for the time t_c , during which the fusion reactions occurred in the full sphere (with constant volume V_f), the number of reactions would be

$$N = n_D n_T \langle \sigma v \rangle V_f t_c. \quad (1.17)$$

The comparison of equations 1.16 and 1.17 allows to define the confinement time for inertial confinement as

$$t_c = \frac{R_f}{4c_s}. \quad (1.18)$$

The confinement time is four times smaller than the time the rarefaction wave takes to reach the center of the target. This is due to the spherical geometry. At later times, when the rarefaction wave is closer to the center, the volume of unperturbed plasma is very small and the number of fusion reactions is almost negligible in comparison to the initial time. Due to the high plasma temperature this time is very short. At 20 keV, the sound velocity is $c_s = 1200 \text{ km/s} = 1200 \mu\text{m/ns}$. For a sphere of plasma with 200 μm radius, the confinement time is 20 ps. This is very short in comparison to MCF, where the plasma can be confined hundreds of seconds.

During the confinement time, the net power output of the plasma corresponds to the power transported by the neutrons $W_{neutron} = W_{fus} - W_\alpha$. In a balanced self-heating plasma $W_\alpha = W_{brem}$, so that the energy released during the confinement is $(W_{fus} - W_{brem})t_c$. Since an energy $3nk_B T$ has been necessary to heat the plasma to the temperature T , the condition in order to have net energy gain writes

$$(W_{fus} - W_{brem})t_c - 3nk_B T > 0. \quad (1.19)$$

This expression can be rewritten as

$$n t_c > 3 k_B T \left(\frac{W_{fus}}{n^2} - \frac{W_{brem}}{n^2} \right)^{-1}. \quad (1.20)$$

Since W_{fus} and W_{brem} are proportional to n^2 , the left hand part of this equation depends on temperature alone (for a given fusion reaction). This expression corresponds to the Lawson criterion [3]. For DT fusion reactions and a temperature of 5 keV, this condition writes $n t_c > 10^{15} \text{ s.cm}^{-3}$. With an ICF confinement time of 10 ps, a density of 10^{26} cm^{-3} is therefore necessary to have an energy gain. This density is around 1000 times larger than typical solid densities, which shows that ICF requires a compression of the fusion fuel. On the other hand, with confinement time of 100 s, MCF requires a density of only 10^{13} cm^{-3} .

1.2.2 Fuel depletion

In the previous calculation of the number of fusion reactions (1.16), the number of deuterium and tritium ions has been considered constant. This corresponds to the assumption that the number of fusion reactions is small, hence fuel depletion can be neglected. However, fuel depletion must be taken in account in order to provide a better estimation of the number of fusion reactions.

For an equimolar mixture of DT, $n_D = n_T = n_i/2$, and the evolution of the deuterium (or tritium) population is

$$\frac{dn_D}{dt} = \frac{dn_T}{dt} = -n_D n_T \langle \sigma v \rangle. \quad (1.21)$$

The solution of this equation is

$$n_D(t) = \frac{n_{D0}}{1 + n_{D0} \langle \sigma v \rangle t}, \quad (1.22)$$

where n_{D0} is the number of deuterium ions at $t = 0$. Assuming that the fusion reactions occur only during the confinement time t_c , the number of fusion reactions is

$$N_f = [n_{D0} - n_D(t_c)] V_f = \frac{n_{D0}^2 \langle \sigma v \rangle t_c}{1 + n_{D0} \langle \sigma v \rangle t_c} V_f. \quad (1.23)$$

As expected, the comparison of this expression with equation 1.17 shows that fuel depletion reduces the number of fusion reactions.

1.2.3 Burn efficiency

The burn efficiency is the ratio between the number of fusion reactions that occurred during the confinement time and the total number of possible fusion reactions $N_{tot} = n_{D0} V_f$. From equation 1.23, it can be expressed as

$$\Phi_B = \frac{N_f}{N_{tot}} = \frac{n_{D0} \langle \sigma v \rangle t_c}{1 + n_{D0} \langle \sigma v \rangle t_c}, \quad (1.24)$$

Replacing t_c by its expression and n_{D0} by $\rho_f / (2m_i)$, where ρ_f is the fuel mass density, equation 1.24 can be expressed as

$$\Phi_B = \frac{\rho_f R_f}{H_B + \rho_f R_f}, \quad (1.25)$$

where $H_B = 8m_i c_s / \langle \sigma v \rangle$ is called the burn parameter. Figure 1.4, left, presents the burn parameter for DT fusion as a function of temperature. While temperatures in the range 5 to

10 keV are enough to ignite the fuel, the energy released by the fusion reactions quickly rises its temperature to the range 20 to 70 keV. In this range, the value of H_B is almost constant, staying between 7 and 9 g/cm². The burn efficiency as a function of the areal density for $H_B = 8$ g/cm² is presented in Figure 1.4, right. To obtain 30% of burn efficiency, an areal density of ~ 3 g/cm² is required. This value is a key parameter for ICF.

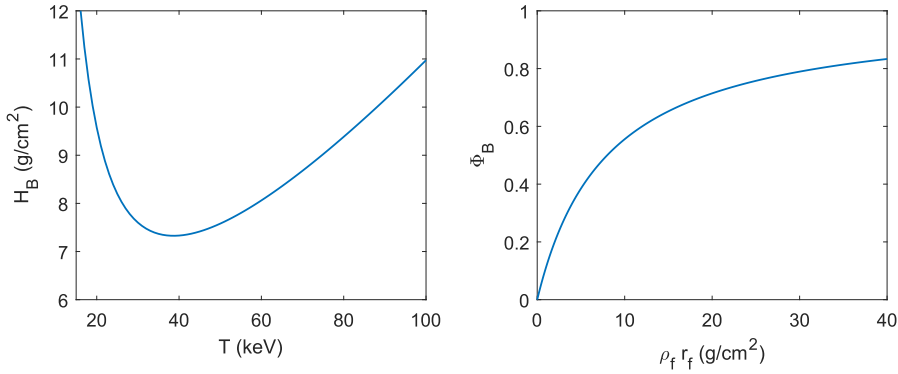


Fig. 1.4 Burn parameter as a function of plasma temperature (left) and burn fraction as a function of the fuel areal density for $H_B = 8$ (right). The minimum of the burn parameter curve is $H_B = 7.2$ g/cm² for $T = 40$ keV.

1.2.4 ICF reactor

In order to efficiently produce energy from fusion reactions, an ICF reactor has to meet some physical requirements for the fuel such as a temperature larger than 5 keV and an areal density around 3 g/cm². At the same time, it is constrained by technological requirements and limitations.

Gain requirement

During fusion, the target is brought in conditions for fusion using a driver with an energy E_d and then it releases a certain amount a fusion energy E_f . The ratio of these two energies defines the target gain $G = E_f/E_d$. It is a key parameter that characterizes the efficiency of the fusion process. The requirement for the gain can be evaluated from the energy balance of a hypothetical ICF reactor such as presented in Figure 1.5.

In order to limit the potential damages to the structure of the reactor, it seems unrealistic to have a fusion energy exceeding $E_f = 400$ MJ. This energy, carried by neutrons and x-rays is then converted in the fusion chamber walls into thermal energy, which is then converted into electrical energy by a standard thermal cycle with maximal efficiency $\eta_{th} = 40\%$ [4].

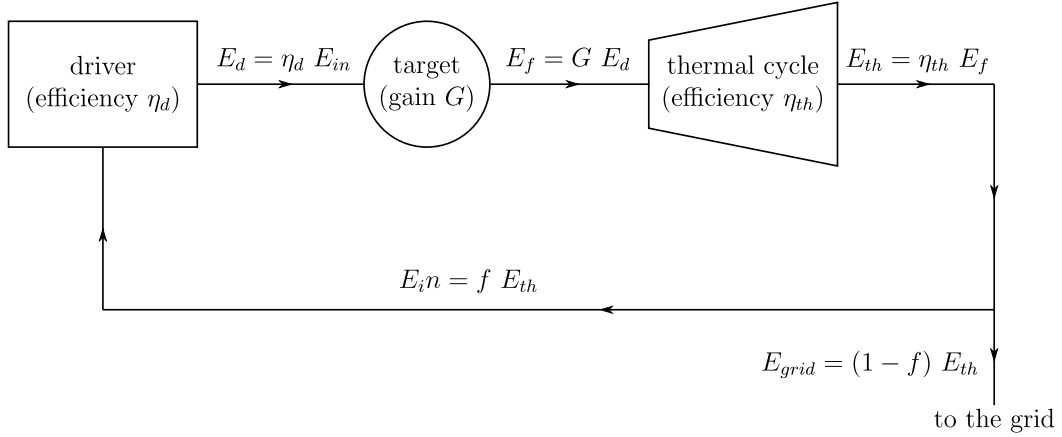


Fig. 1.5 Energy balance for an ICF reactor [2].

A fraction f of the electrical energy is reused in the facility to power the driver with an efficiency $\eta_d \simeq 10\%$. From this loop, the energy balance of the reactor can be written as

$$f \eta_{th} \eta_d G = 1 \quad (1.26)$$

The electrical energy not used to power the facility is sent to the grid as net electrical energy $E_{grid} = (1 - f) \eta_{th} E_f$. Considering an explosion repetition rate ν_{rep} , the net power out of the plant is

$$P_{grid} = \left(\eta_{th} - \frac{1}{\eta_d G} \right) E_f \nu_{rep} \quad (1.27)$$

In order to be attractive for industries, such power plant has to produce around 1 GW of net electrical power. Applying the parameter described in this section assuming $\eta_d = 10\%$ and $\nu_{rep} = 10$ Hz, the required gain is $G > 70$. Generally, a target gain between 30 and 100 is aimed in ICF.

Few terms have been neglected in this calculation. Tritium is an unstable isotope decaying to ${}^3\text{He}$ with a half life of 12.3 years and which does not exist in nature. Therefore, it has to be produced within the DT fuel cycle. The use of lithium in the wall of the chamber allows to produce it though the reaction ${}^6\text{Li} + n \rightarrow \alpha + T$. This exothermic reaction produces 4.8 MeV and therefore contributes to the power production of the reactor. The total energy released by the DT and Li-n reaction is

$$E_{DT} + E_{Li-n} = E_{DT} \left(1 + \frac{\epsilon_{Li-n}}{\epsilon_{DT}} \right) = 1.28 E_{DT}. \quad (1.28)$$

The Li-n reaction could increase the power output of the reactor by $\sim 25\%$ [5]. On the other side, the auxiliary system of the plant uses part of the produced electrical power.

Compression requirement

As seen before, the fusion energy released in an explosion has to be limited to ~ 400 MJ. Considering a burn efficiency of 30%, the mass of DT that can be used is limited to ~ 4 mg. A sphere of cryogenic DT of 4 mg, with a density $\rho_{DT} = 0.25$ g/cm³, has a radius of $R_f = 1.6$ mm and an areal density $\rho_f R_f = 0.039$ g/cm². It is a hundred time lower than the 3 g/cm² required for a 30% burn efficiency. Therefore the fuel needs to be spherically compressed.

The mass of a sphere of DT is

$$M_f = \frac{4\pi}{3} R_f^3 \rho_f = \frac{4\pi (R_f \rho_f)^3}{3 \rho_f^2}. \quad (1.29)$$

To have 4 mg of DT with an areal density of 3 g/cm², the density has to be ~ 170 g/cm³. This corresponds to a compression factor $\rho_f / \rho_{DT} = 670$. Reaching such a high compression is one of the most challenging goal of ICF.

Fuel energy balance

An homogeneous compression and heating of an ICF target in order to reach the conditions for ignition is not possible due to the amount of energy it would required. Indeed, the target needs to be compressed by a factor ~ 1000 and heated to temperature ~ 10 keV. The most energy efficient configuration is to have the driver first compressing the fuel with the energy E_{comp} , and then heating the compressed fuel with the energy E_{heat} .

During the compression, the fuel is kept as cold as possible in order to minimize the energy required to compress it. In these conditions, its pressure is mostly the Fermi pressure due to electron degeneracy

$$P_F = \frac{(2\pi^2)^{2/3} \hbar^2}{5m_e(2.5m_p)^{5/3}} \rho^{5/3} = A_F \rho^{5/3}, \quad (1.30)$$

where $A_F = 2.16$ if P_F is in Mbar and ρ in g/cm³. Hence, the energy required to compress a volume V_0 at the density ρ_{DT} to a volume V_f at the density ρ_f is

$$E_{comp} = \int_{V_f}^{V_0} P dV = \alpha M_f \int_{\rho_f}^{\rho_0} \frac{P_F}{\rho^2} d\rho, \quad (1.31)$$

where the target adiabat parameter α have been introduced to take in account the real target pressure $P = \alpha P_F$, which results from the target heating during the compression. This heating is rather small, such that α typical values are in the range 1 to 3. Due to the high

compression, the initial density contribution in the integral calculation can be neglected and the compression energy is

$$E_{comp} \simeq \frac{3}{2} \alpha M_f A_F \rho_f^{2/3}. \quad (1.32)$$

Taking $\alpha = 1$, $M_f = 4$ mg and $\rho_f = 170$ g/cm³, the energy required for the compression is $E_{comp} = 43$ kJ.

Then, to heat the whole target to the temperature T_h , the energy E_{heat} is necessary. As the fuel is heated, it quickly reaches a state where it can be described as an ideal gas so that E_{heat} is given by

$$E_{heat} = \frac{3}{2} (n_e + n_i) k_B T_h V_f = \frac{3}{2.5 m_p} M_f k_B T_h. \quad (1.33)$$

With $M_f = 4$ mg and $T_h = 10$ keV, the energy for heating is 4.6 MJ. It is much higher than the energy used for compression. It is actually too large to meet the gain requirement $G > 70$. The conversion of the energy of the driver into the fuel internal energy is a process with a low efficiency around 10%. Neglecting the energy required for the compression, the driver energy has to be around 46 MJ, leading to a gain of 8.7 (the expected fusion energy for this example is 400 MJ). It is therefore unrealistic to heat the whole target in order to efficiently produce energy.

A solution is to heat only a small portion of the fuel. In this hot spot, if the conditions for ignition are met, the fusion reactions will heat the cold part of the fuel by the propagation of a thermonuclear burn wave. Different configurations have been considered for the formation of this hot spot, either on the side of the fuel in the case of fast ignition scheme, or at its center for the classical scheme and shock ignition scheme.

1.2.5 Central hot spot ignition conditions

In the central hot spot configuration, the fuel is compressed to the required areal density of 3 g/cm² while been kept cold. In its center, a small volume is heated in order to match the conditions for ignition. These conditions can be determined from the power balance in the hot spot, in a similar way as in section 1.1.3. Because the hot spot is in contact with the cold fuel, additional loss mechanisms have to be taken in account. The hot spot energy balance is

$$\frac{dE_h}{dt} = P_\alpha - P_{brem} - P_{cond} - P_{mech} \quad (1.34)$$

where P_α is the power deposited by the α particles, P_{brem} is the power radiated by bremsstrahlung radiation, P_{cond} is the power loss by thermal conduction and P_{mech} is the contribution due to the mechanical work.

Considering a hot spot of radius R_h , temperature T_h and density ρ_h , P_{brem} and P_α are given by the equations 1.12 and 1.13

$$P_{brem} = A_b n^2 T_h^{1/2} V_h = \frac{4\pi A_b}{3m_i^2} \rho_h^2 R_h^3 T_h^{1/2}, \quad (1.35)$$

$$P_\alpha = \frac{1}{20} n^2 \langle \sigma v \rangle \varepsilon_{DT} V_h f_\alpha = \frac{\pi \varepsilon_{DT}}{15m_i^2} \rho_h^2 R_h^3 \langle \sigma v \rangle f_\alpha, \quad (1.36)$$

where $V_h = \frac{4\pi}{3} R_h^3$ is the volume of the hot spot and f_α is the fraction of the α particle energy deposited in the hot spot. At a temperature of 10 keV, the penetration depth of alpha particles is $\rho l_\alpha = 0.25 \text{ g/cm}^2$. This is ten times smaller than the fuel areal density at maximum compression so that the α particles will be unable escape the fuel. More importantly, a significant part of the α particles energy has to be deposited in the hot spot in order to compensate its energy losses. Therefore, the hot spot cannot be arbitrary small. If the hot spot areal density $\rho_h R_h$ is equal to ρl_α , 70% of the α particle energy is deposited in the hot spot.

The power loss by thermal conduction is

$$P_{cond} = -\chi_e \nabla T_e S_h, \quad (1.37)$$

where $\chi_e = \chi_0 T^{5/2}$ is the plasma thermal conductivity, ∇T_e is the temperature gradient at the surface of the hot spot and $S_h = 4\pi R_h^2$ is the surface of the hot spot. The value of $\chi_0 = 3 \times 10^{12} \text{ W/cm}^{-1} \text{ keV}^{-7/2}$ comes by considering the Spitzer model for electron conduction. ∇T_e can be approximated by evaluating the hot spot temperature and density profiles. By considering only the α heating and the conduction loss, and assuming a constant pressure in the hot spot, the temperature gradient is

$$\nabla T_e = \frac{4}{7} \frac{T_h}{R_h}. \quad (1.38)$$

The conduction loss then writes

$$P_{cond} = \frac{4}{7} \chi_0 \frac{T_h^{7/2}}{R_h} S_h = \frac{16\pi}{7} \chi_0 R_h T_h^{7/2}. \quad (1.39)$$

The loss by mechanical forces is

$$P_{mech} = P_h \frac{dV_h}{dt} = P_h S_h u, \quad (1.40)$$

where P_h is the hot spot pressure and $u = dR_h/dt$ is the velocity of the hot spot surface. The plasma in the hot spot can be described using the ideal gas law such that $p_h = \Gamma_B \rho_h T_h$, where $\Gamma_B = 7.75 \times 10^{14}$ erg/(g keV) is the DT gas constant.

The velocity u depends of the pressures in the hot spot P_h and in the cold fuel P_{fuel} . A simple expression for u can be found by in the two limiting cases: $P_h = P_{fuel}$ and $P_h \gg P_{fuel}$. The first case corresponds to an isobaric condition, where the difference in temperature between the hot spot and the cold fuel is compensated by a jump in density ($\rho_h \ll \rho_{fuel}$) resulting in $u = 0$. The other case assumes that the density in the hot spot and in the cold fuel are comparable (isochoric condition) so that the high temperature in the hot spot results into a high pressure jump. In this case, a shock wave is launched in the cold fuel and the velocity of the interface is the velocity of the material behind the shock. For an ideal gas this velocity writes

$$u = \left(\frac{3P_h}{4\rho_{fuel}} \right)^{1/2} = \left(\frac{3}{4} \Gamma_B T_h \frac{\rho_h}{\rho_{fuel}} \right)^{1/2} \quad (1.41)$$

In the limit $P_h \gg P_{fuel}$ the mechanic loss is

$$P_{mech} = 2\sqrt{3}\pi\Gamma_B^{3/2} \rho_h R_h^2 T_h^{3/2} \sqrt{\rho_h/\rho_{fuel}}. \quad (1.42)$$

The condition for hot spot self heating is $dE_h/dt > 0$. Inserting the equations 1.35, 1.36, 1.39 and 1.42 into 1.34 and divided each term by R_h , the condition writes

$$\left(\frac{\pi\varepsilon_{DT}}{15m_i^2} \langle \sigma v \rangle f_\alpha - \frac{4\pi A_b}{3m_i^2} T_h^{1/2} \right) (\rho_h R_h)^2 - 2\sqrt{3}\pi\Gamma_B^{3/2} \rho_h R_h T_h^{3/2} \sqrt{\rho_h/\rho_{fuel}} - \frac{16\pi}{7} \chi_0 T_h^{7/2} > 0 \quad (1.43)$$

This expression is a function of $\rho_h R_h$, T_h and ρ_h/ρ_{fuel} only. Figure 1.6 presents the regions where this condition is met for two specific cases: the isobaric condition $P_h = P_{fuel}$ ($\rho_h \ll \rho_{fuel}$) and the isochoric condition $\rho_h = \rho_{fuel}$. Both show a similar trend where ignition is not possible below the temperature at which the Bremsstrahlung loss dominates the α heating (1.1.3). At higher temperature, the increasing conduction loss leads to a higher $\rho_h R_h$ requirement. The isobaric case shows lower requirements due to the absence of mechanical loss and it is the most studied configuration for the production of energy through fusion. In this case, for a temperature of 10 keV, the hot spot areal density has to be larger than 0.23 g/cm² in order to ignite.

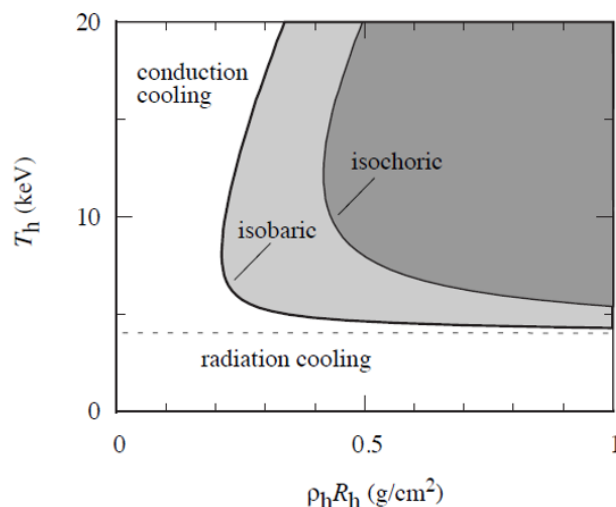


Fig. 1.6 Self heating condition for a DT hot spot in the $(\rho_h R_h, T_h)$ plan, for the isobaric ($P_h = P_{fuel}$) and isochoric ($\rho_h = \rho_{fuel}$) conditions.

1.3 Classical approaches to ICF

The main scheme considered to reach ignition is by the implosion of a cryogenic DT shell filled with DT gas. At the end of the implosion, a hot spot is formed in the gas, leading to a nuclear deflagration wave that propagates outward through the imploded shell. The driver for such implosions has to be able to deliver megajoules of energy in few nanoseconds, with a precise temporal shape. Lasers are ideal tools for this purpose. Using lasers, the implosion is driven either by direct illumination with the laser beams (direct drive) or after conversion of the laser light into x-ray radiation inside a cavity (indirect drive). Figure 1.7 presents these two approaches.

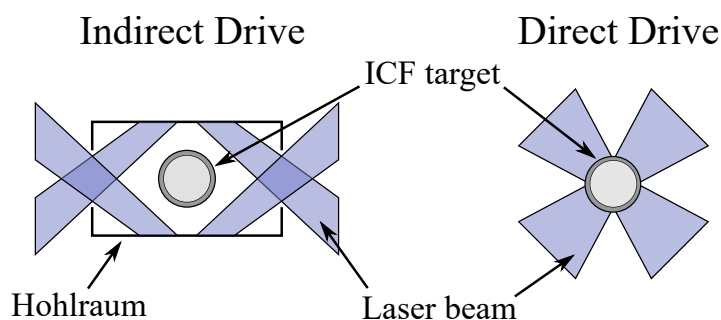


Fig. 1.7 Schematic of indirect drive(left) and direct drive (right) for inertial confinement fusion. In indirect drive the laser light is converted in X-rays by the hohlraum. In direct drive the laser light directly illuminates the ICF target.

1.3.1 Indirect drive

In the indirect drive configuration, the laser beams are absorbed at the inner surface of a high-Z cavity (usually gold) called "hohlraum" and converted in X-rays. These X-rays are close to black body equilibrium, leading to a very uniform symmetry of irradiation. This way, the non-uniformities of irradiation from the laser spots are smoothed and the implosion is closer to an ideal one-dimensional case. This configuration of irradiation have been chosen for the two actual megajoule class lasers: the National Ignition Facility (NIF, USA) and the Laser MegaJoule (LMJ, France). There are multiple drawbacks for this scheme: a significant part of the energy is lost due to X-ray conversion, the hohlraum inner walls expand during the implosion and they may block the laser propagation inside the hohlraum, the Cross Beam Energy Transfer at the hohlraum windows can perturb the irradiation symmetry, the indirect drive targets are complex and costly...

1.3.2 Direct drive

The direct drive is a much simpler configuration where laser light directly illuminates the target. This way, most of the issues encountered with indirect drive are not present, yet the implosion is very sensitive to the non-uniformities of irradiation. These non-uniformities imprint perturbations at the target surface, which are amplified during the implosion due to hydrodynamic instabilities such as Rayleigh-Taylor, Richtmeyer-Meshkov and Kelvin-Helmholtz instabilities. These perturbations are very detrimental to the implosion. They can cool down the hot spot, preventing the ignition, or even break the target during the implosion. Currently, there is no megajoule laser facility designed for the direct drive and only reduced scale implosion can be realized on intermediate laser facilities like the Omega Laser System (USA). While these installations do not have enough energy to reach ignition, they allow, through hydrodynamic scaling, to design efficient direct drive implosions that could be realized on future laser facility. In this thesis work, the discussion is restricted to this last approach.

1.3.3 Shell implosion in direct drive

In direct drive, the target surface is directly illuminated by the laser light creating a plasma that expands outward at high velocity. This process is called the ablation. By conservation of momentum, a high ablation pressure is applied at the surface of the target. The laser driver acts as a leaking piston with a pressure P_{abla} related to the absorbed intensity I_{abs} by $P_{abla} \propto I_{abs}^{2/3} \lambda_L^{-2/3}$, where λ_L is the laser wavelength.

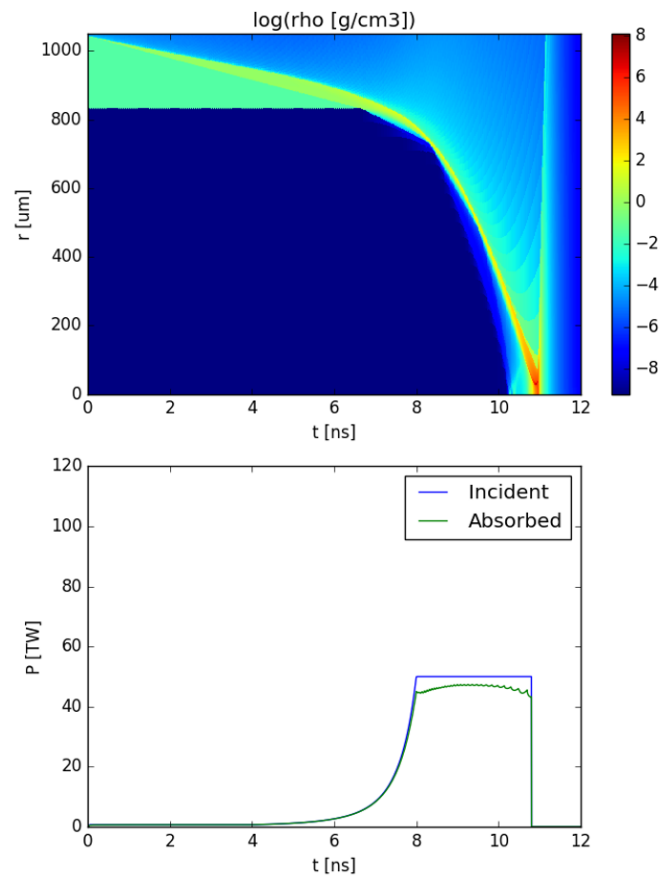


Fig. 1.8 One-dimensional spherical-geometry CHIC simulation of an implosion in the classical scheme (in direct drive). Top: Density map as a function of time and radius (in logarithmic scale). Bottom: Incident and absorbed laser power as a function of time. The target is a $1044 \mu\text{m}$ outer radius, $211 \mu\text{m}$ thick, cryogenic DT shell (at the density 0.25 g/cm^3 filled with gas DT (at the density 0.1 mg/cm^3).

The shell implosion, hot spot formation and target burn are dynamic processes too complex to be described with a simple analytic model. Radiation hydrodynamic simulations are then used in order to model the implosions. Figure 1.8 presents the results from a simulation realized using the code CHIC in one-dimensional spherical geometry. The laser power law corresponds to a pressure law that implodes the target in a five steps process:

- Low Intensity, adiabat shaping: Even at very low intensity, the pressure applied at the surface of the target is very large compared to its Fermi pressure. Therefore, the low intensity foot send a shock wave that propagates through the cold target, increasing its entropy. This increase in entropy is an important parameter for the implosion and it is usually described using the so-called adiabat $\alpha \propto P_{abla}/\rho^{5/3}$ where ρ is the density behind the shock wave.
- Intensity rising, adiabatic compression: While the intensity is rising, compression waves are sent though the target so that they all coalesce and breakout from the shell at the same time. Because the intensity rises slowly, the compression waves propagates at sound velocity and do not increase any further the shell entropy. At the moment of shock breakout, the whole target is put in motion and the implosion starts. It is also that moment that the target have the largest aspect ratio, the so called in flight aspect ratio $IFAR = R_0/\Delta$, where R_0 is the initial inner radius of the shell and Δ its thickness at shock breakout. Because the shell has been compressed, its thickness Δ has decreased.
- Maximum intensity, shell acceleration: The constant applied pressure accelerates and maintains the shell at the maximal implosion velocity u_{imp} . During this phase, the shell has approximately a constant density and the convergence effect increases its thickness. At the same time, the implosion of the shell compresses the gas, increasing its pressure.
- End of pulse, shell deceleration: When the gas pressure become comparable to the shell pressure (which corresponds to the ablation pressure increased by convergence effect), the shell starts to decelerate. At this time, it is inefficient to irradiate the target any more and the illumination can be stopped. During this phase, the shell thickness is approximately constant and the convergence effect increases its density up to the required areal density. A part of the shell kinetic energy is converted into internal energy of the gas, creating a hot spot.
- Hot spot ignition, shell burn: If the hot spot reaches the conditions for ignition, its temperature quickly increases and a thermal ablation front forms at the inner surface

of the cold shell. This ablation front propagates outward through the shell, gradually increasing the hot spot mass and leading to the burn of the shell.

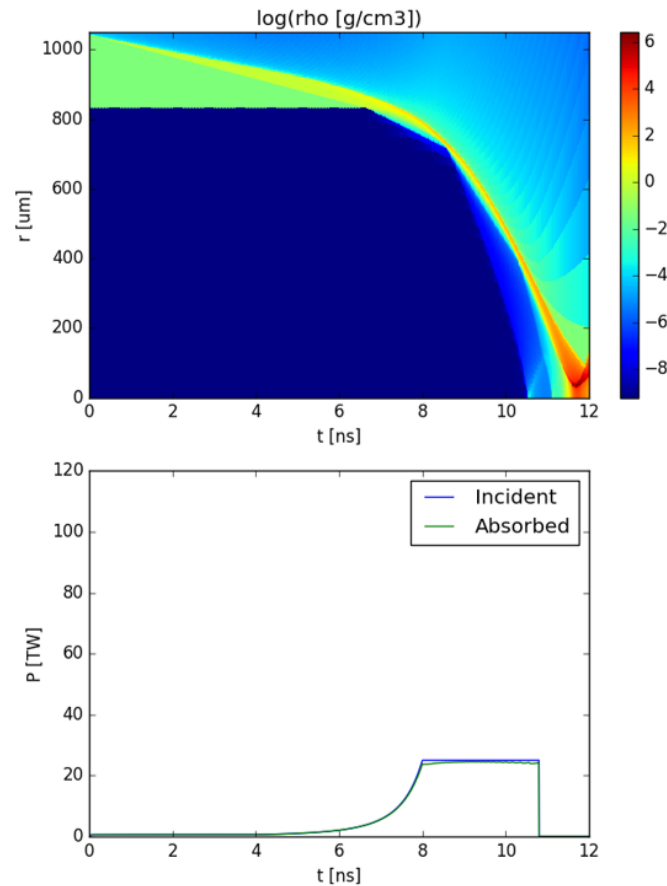


Fig. 1.9 One-dimensional spherical-geometry CHIC simulation of an implosion in the classical scheme (in direct drive). The implosion is driven at low velocity such that the target does not ignite. Top: Density map as a function of time and radius (in logarithmic scale). Bottom: Incident and absorbed laser power as a function of time. The target is a $1044 \mu\text{m}$ outer radius, $211 \mu\text{m}$ thick, cryogenic DT shell (at the density 0.25 g/cm^3 filled with gas DT (at the density 0.1 mg/cm^3)).

Since the hot spot internal energy comes mostly from the shell kinetic energy, the hot spot temperature condition for ignition leads to a condition on a minimum implosion velocity, called the ignition velocity (for a given target design and adiabat). Figure 1.9 presents the results of a simulation with similar parameters as for the simulation presented in Figure 1.8, but with a reduced maximum intensity and therefore not igniting. The maximum laser power has been reduced from 50 TW to 25 TW, leading to a reduction of the implosion velocity from 330 km/s to 290 km/s. Hence, the gain dropped from 100 to 0.17. High implosion

velocities are required in order to create a hot spot with sufficient temperature so that the target burns. Even though, higher implosion velocities lead to a reduction of the gain and to an increase of hydrodynamic instabilities.

Implosion efficiency

To be interesting for energy production, the target gain of an ICF implosion needs to be high (section 1.2.4). This is defined as the ratio of the energy released by the fusion reactions to the laser energy invested into the implosion. If the target ignites the fusion energy is

$$E_f = M_f \Phi_B \varepsilon_f / 2m_i, \quad (1.44)$$

where M_f is the fuel mass, Φ_B the burn fraction, ε_f the energy release per fusion reaction and m_i the average ion mass.

The laser energy is related to the shell kinetic energy $E_k = \eta_{hydro} E_L$, where η_{hydro} is the hydrodynamic efficient, which also depends on the implosion velocity. Considering a rocket model, the implosion velocity can be expressed as

$$\frac{u_{imp}}{u_{ex}} = -\ln\left(\frac{M_1}{M_0}\right) \quad (1.45)$$

where u_{ex} is the velocity of the expanding plasma. M_0 and M_1 are the initial mass of the shell and the mass at the end of the acceleration phase, respectively. In this model, the hydrodynamic efficiency can be written as

$$\eta_{hydro} = \frac{M_1/M_0 [\ln(M_1/M_0)]^2}{1 - M_1/M_0}. \quad (1.46)$$

Figure 1.10 presents the hydrodynamic efficiency as a function of the ratio u_{imp}/u_{ex} . For an irradiation intensity of 10^{15} W/cm² and a wavelength of $0.35 \mu\text{m}$, the plasma expansion velocity is around 430 km/s, which is larger than the implosion velocity in most of the ICF designs. For $u_{imp} < u_{ex}$, the curve from Figure 1.10 can be approximated by $\eta \propto u_{imp}^{0.75}$. The gain then writes

$$G = \frac{E_f}{E_L} = \frac{\eta_{hydro} \Phi_B \varepsilon_f}{m_i u_{imp}^2} \propto u_{imp}^{-1.25}. \quad (1.47)$$

This relation can be interpreted in two ways. Since the fusion energy is independent from the implosion velocity, if a target burns, any additional energy invested in the shell kinetic energy is a waste and leads to a decrease of the gain. On the other hand, at a given laser energy, reducing the implosion velocity means having a larger mass and therefore, if

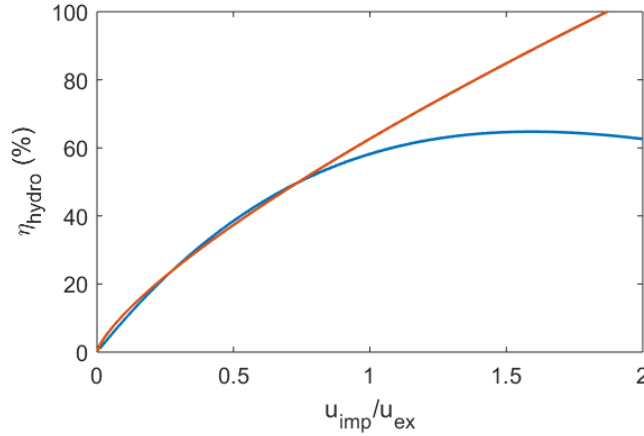


Fig. 1.10 Hydrodynamic efficiency as a function of implosion velocity calculated with a rocket effect model (blue) and its fit $\eta_{hydro} \propto (u_{imp}/u_{ex})^{0.75}$ (red).

the target burn, a larger fusion energy. One of the main goal for direct drive ICF is to reach ignition with the lowest implosion velocity possible in order to achieve higher gain.

Hydrodynamic stability

Hydrodynamic instabilities are another main concern for ICF. In particular, Rayleigh-Taylor instability (RTI), increases the amplitude of the perturbations at a interface between two fluids when the density and pressure gradients between these fluids have opposite signs, in other words, when a light fluid pushes a denser fluid. During the implosion, this happens at the shell outer surface during its acceleration and at its inner surface during the deceleration phase. At the outer surface, the initial perturbation h_0 is amplified exponentially by the RTI

$$h(t) = h_0 \exp(\sqrt{A_t k g t}) = h_0 \exp\left(\sqrt{A_t k \Delta \frac{g t^2}{\Delta}}\right), \quad (1.48)$$

where $A_t = (\rho_2 - \rho_1)/(\rho_2 + \rho_1)$ is the Atwood number, with ρ_1 and ρ_2 the densities of the fluids on each side of the outer surface, k the perturbation wave number and g the acceleration of the surface. During the acceleration phase, the target approximately shrinks by a factor of two. Hence the traveled distance during this phase is $R_0/2 = g t^2/2$. The fraction in 1.48 then become $R_0/\Delta = IFAR$. Neglecting the ablated mass, the shell kinetic energy is equal to the work done on it

$$\frac{1}{2} M u_{imp}^2 \sim 2\pi p_{abla} R_0^3. \quad (1.49)$$

With the accelerated mass $M \sim 4\pi \rho_{sb} R_0^2 \Delta$, this equation writes

$$IFAR = \frac{R_0}{\Delta} \propto \frac{u_{imp}^2}{c_s^2}, \quad (1.50)$$

where $c_s^2 = p_{abla} / \rho_{sb}$ is the shell sound velocity during the acceleration phase. Equation 1.48 then writes

$$h_{outer} \propto \exp(u_{imp} \sqrt{k\Delta}) \quad (1.51)$$

At the end of the acceleration phase, the amplitude of the perturbation has grown exponentially with the implosion velocity. It also depends on the ratio between the shell thickness and the wavenumber of the perturbation mode. Inside the shell, the amplitude of this perturbation decays exponentially in space. At the inner surface, the perturbation is

$$h_{inner} = h_{outer} \exp(-k\Delta) \quad (1.52)$$

For $k\Delta \gg 1$, the outer surface perturbation does not reach the inner surface, $h_{inner} = 0$. For $k\Delta \ll 1$, the perturbation at the inner surface follows the outer surface perturbation, $h_{inner} = h_{outer}$. While this scenario leads to a large deformation of the hot spot, it is not the most critical. Indeed, if $k\Delta \sim 1$, the perturbation at the inner surface is small, while the outer surface perturbation has an amplitude comparable to the shell thickness, making it likely to break.

During the deceleration phase, the RTI growth is similar but the shell is less likely to break since it is thicker. Yet, the RTI largely increases the surface of contact between the hot spot and the cold shell. This leads to a larger energy loss through electronic conduction, cooling the hot spot down and preventing ignition.

1.4 Shock ignition scheme

An implosion at lower velocity is more stable and has a higher potential gain. Yet, if the velocity is lower than the ignition velocity, the hot spot does not reach the temperature needed for ignition. In this case, the hot spot temperature has to be raised with an additional source of energy. This idea of separating the target compression from hot spot heating led to alternative schemes for ICF, such as the shock ignition scheme.

1.4.1 Principle of shock ignition

The idea of using a converging shock wave in order to ignite a precompressed ICF target has been first proposed by Shcherbakov in 1983 [6]. In this design, the target is initially a 1 mm radius liquid sphere of DT at the density 0.1 g/cm^3 . This target is first compressed to a relatively high density of 40 g/cm^3 and moderate temperature of 100 eV using a laser pulse of moderate intensity. Then a strong converging shock with a velocity of $\simeq 150 \text{ km/s}$ is sent into the target so that when it bounces on itself at the center, it creates a non isobaric hot spot which meets the requirements for ignition. In this design, the ignition shock is driven for $\sim 0.37 \text{ ns}$ (time for ignition to occur) so that the mechanical energy invested is 30 kJ. Assuming a hydrodynamic efficiency of 10%, the laser spike require a power of 860 TW, which is above the current laser capability. In order to be considered for ICF, the shock ignition scheme has to propose a design with lower requirements on the total laser energy and on the spike power, while keeping a high gain.

In 2007, Betti *et al.* [7] proposed a novel scheme for shock ignition based on the implosion of cryogenic DT shell. In this scheme, a cryogenic DT shell is imploded similarly to the classical scheme but with a lower implosion velocity. This results in the formation of a hot spot with a temperature slightly below the ignition threshold (about 2-3 keV, similarly to the simulation presented in Figure 1.9). Then, at the end of the acceleration phase, a strong converging shock is created in the shell using an intense laser spike. This shock is amplified through convergence effects and through its collision with the rebound shock close to the inner shell surface. When it enters the hot spot, it increases the temperature enough to reach ignition. In their article, Betti *et al* presented the example of a massive target reaching ignition with 290 kJ of invested energy. The target is a $240 \mu\text{m}$ thick cryogenic shell of $726 \mu\text{m}$ outer shell radius coated with $103 \mu\text{m}$ of wetted foam (plastic ablator saturated with DT ice). The driving laser pulse is composed of an assembly pulse ($\sim 100 \text{ TW}$, 243 kJ) and an intense power spike ($\sim 500 \text{ TW}$, 47 kJ). While this spike power is much higher than the assembly pulse, its short duration makes it less costly in energy. This implosion must be compared to an implosion without ignition shock but with equivalent hydrodynamic stability, meaning the same implosion velocity ($u_{imp} \simeq 225 \text{ km/s}$), mean adiabat ($\langle \alpha \rangle \simeq 2$) and irradiation intensity. In their article, Hermann et al [8] show that such implosion required a larger target of 1.5 mm outer diameter and 1.2 MJ in order to ignite. Therefore, this shock ignition scheme could allow to achieve ignition with four time less energy than the classical scheme. Also, the laser power required for the spike is $\sim 500 \text{ TW}$, which is the maximum output of NIF [9]. This shock ignition scheme could therefore be tested on megajoule laser facilities if they were in direct drive configuration.

Following this article, a proof of principle experiment have been realized at the Omega Laser System [10] by Theobald *et al.* [11]. Due to the limited power available on this facility (~ 20 TW), it was not possible to realize full size shock ignition implosions. Therefore, the assembly power has been reduced to ~ 7 TW, which allows to send a late shock wave with a fast rise to ~ 18 TW. The targets were surrogate $40\ \mu\text{m}$ thick CH shell with an outer radius of $430\ \mu\text{m}$ and filled with D_2 with pressure ranging from 4 to 45 bar. Since these targets are far from ignition, their gain is negligible and the neutron yield (total number of D-D fusion reaction) is used as a figure of merit. The highest neutron yield obtained during this experiment is $\sim 8 \times 10^9$ neutrons for a total invested energy of 18.6 kJ. As a comparison, an implosion with similar target dimensions and laser pulse, but without spike, yielded $\sim 1.8 \times 10^9$ neutrons for a slightly larger invested energy of 19.4 kJ. Therefore, the spike-shock-generated implosion has produced ~ 4.4 times more neutrons compared the implosion without spike (with same laser energy). These encouraging results led the ICF scientific community to investigate the shock ignition scheme using various target designs and pulse shapes.

1.4.2 Hydrodynamic studies for shock ignition target design

In 2009, Ribeyre *et al.* [12] investigated the possibility of realizing shock ignition with the HiPER baseline capsule. At the difference of the target considered by Betti, the HiPER target is a thick all-DT cryogenic shell initially designed for the fast ignition scheme [13]. The shell is $211\ \mu\text{m}$ thick with a outer radius of $1044\ \mu\text{m}$. It is imploded at a low adiabat ~ 1 and at a rather low implosion velocity of ~ 290 km/s (driven by a maximum absorbed power of 25 TW). This implosion is very close to the one presented in Figure 1.9, and does not ignite either. Using one dimensional simulations with the code CHIC, the authors investigated the effect of the spike absorbed power and spike launching time on the thermonuclear gain. The results of these simulations are presented in Figure 1.11. It appears that for a power lower than 50 TW, the target does not ignite. Then for power over 80 TW, the thermonuclear yield depends weakly on the spike power and the main control parameter is the spike launching time. Figure 1.12 presents the results of a CHIC simulation for the same target and laser parameters as Figure 1.9 but with a intensity spike of 100 TW. The target thermonuclear yield is 20 MJ, as expected from Figure 1.11. It correspond to a gain 180.

Shock ignition of HiPER-like targets have been further studied in [14] using analytic description, with the support of 1D and 2D simulations. They show that the minimum spike power required for shock ignition depends strongly on the implosion velocity. At high implosion velocity, the target self ignites and no spike is required (it is the classical ICF scheme) while for low implosion velocity, the required spike power sharply rises to

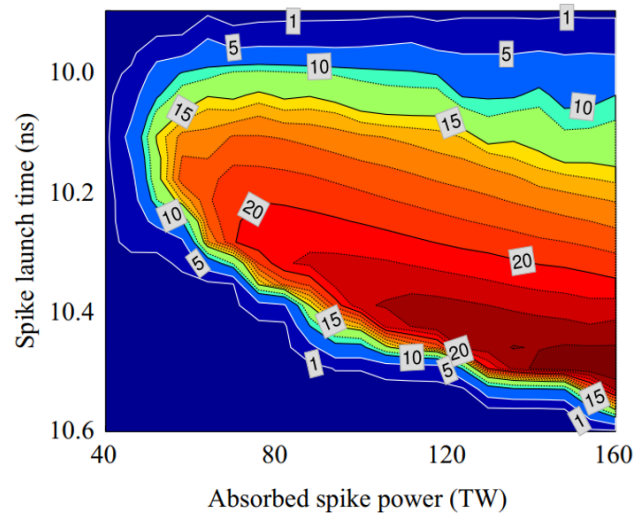


Fig. 1.11 Isocontours of the HiPER target thermonuclear yield (MJ) as a function of the spike absorbed power and launching time [12].

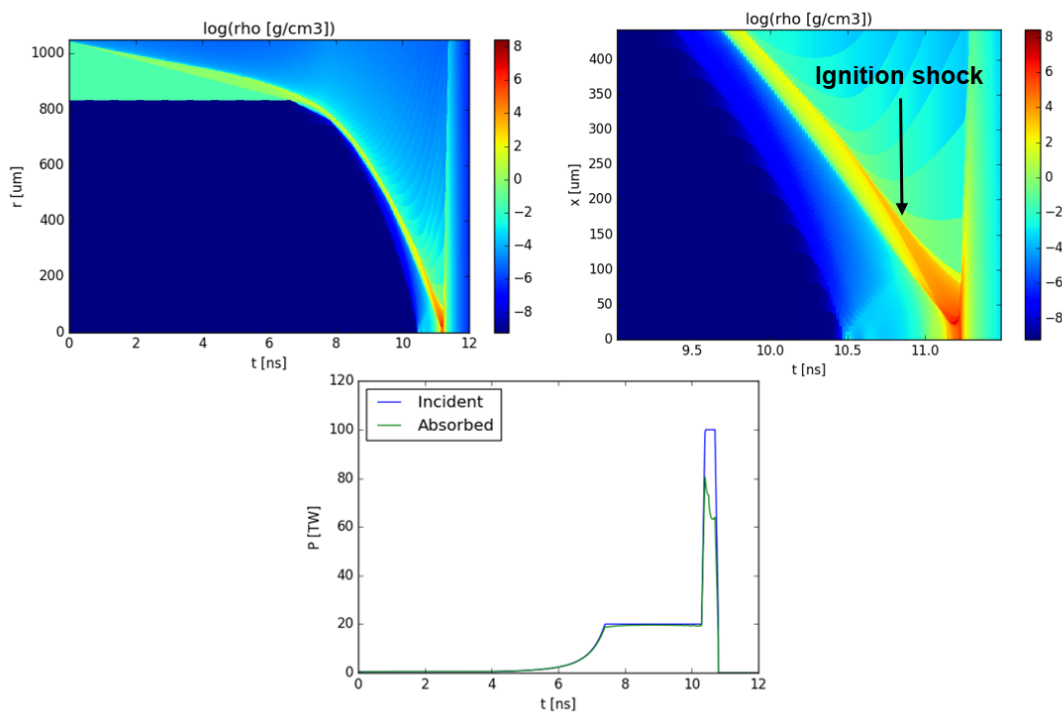


Fig. 1.12 One dimensional CHIC simulation of a shock ignition like implosion. Top: Density map as a function of time and radius (in logarithmic scale). Bottom: Incident and absorbed laser power as a function of time. The target is a 1044 μ m outer radius, 211 μ m thick, cryogenic DT shell (at the density 0.25 g/cm³ filled with gas DT (at the density 0.1 mg/cm³).

unreasonable values. This leads to consider implosion velocities in the range of 240-290 km/s for the shock ignition. In [15], the authors use a Guderley self similar solution of converging shock propagation [16] in order to describe the propagation of the ignition shock in the hot spot. The pressure and density profiles obtained with their model, both before and after the ignition shock collapse, are in reasonable agreement with full numerical simulations [17]. From this model, they calculate an analytic criterion for shock ignition. Figure 1.13 presents this criterion, which is a function of the hot spot areal density $\rho_0 r_0$ and the ignition shock velocity as it enters the hot spot u_0 . It appears that the minimum requirements for ignition are $\rho_0 r_0 \simeq 0.015 \text{ g/cm}^2$ and $u_0 \simeq 750 \text{ km/s}$. The shock pressure corresponding to this velocity is $\sim 17 \text{ Gbar}$. The pressure of the shock sent by the laser spike at the outer surface of the shell is amplified by convergence effects and through its collision with the main diverging shock, allowing it to potentially reach such pressure. These two amplification mechanisms have been described in [17]. The convergence effects are modeled with a Guderley self-similar description of the ignition shock propagation in the shell and the shock collision is modeled using the Rankine-Hugoniot equations. These models are in agreement with numerical simulations within 10% and show that an ablation pressure of $\sim 300 \text{ Mbar}$ is sufficient to reach $\sim 17 \text{ Gbar}$. A more precise description of the ignition and main shock propagation in [18] and [19] confirmed these results while leading to a correction of more than 20% on the ignition criterion (as presented in Figure 1.13) due to the finite Mach number of the ignition shock in the hot spot.

The robustness of shock ignited targets has been studied in [20]. Using 1D simulations, the authors confirmed that the gain is relatively independent from the spike energy as long as the critical spike power is reached, allowing ignition. However, increasing the spike power can be beneficial since it broadens the spike launching time window. Also, the implosion performances are shown to tolerate variations of few percents in mass and/or energy and power. Using 2D simulations, they also investigated the effects of irradiation non-uniformity and target offset. The shock ignition scheme appears to mitigate the hydrodynamic instabilities during the deceleration phase while being very sensitive to target position offset.

Since the shock ignition of an HiPER target is less requiring in energy than the classic scheme, it allows to consider the implosion of up-scaled targets. Families of homothetic HiPER targets have been investigated in [21]. Figure 1.14 presents the laser energy and spike power requirements for the ignition of such targets with scaling factor of 1, 1.2 and 2 (corresponding to outer radius of 1044, 1250 and 2088 μm). The scale-2 target (red square) can ignite on NIF (or LMJ) where the maximum available energy is 1.5 MJ with a maximum spike power of 500 TW. However, these implosions are close to the maximum capability of

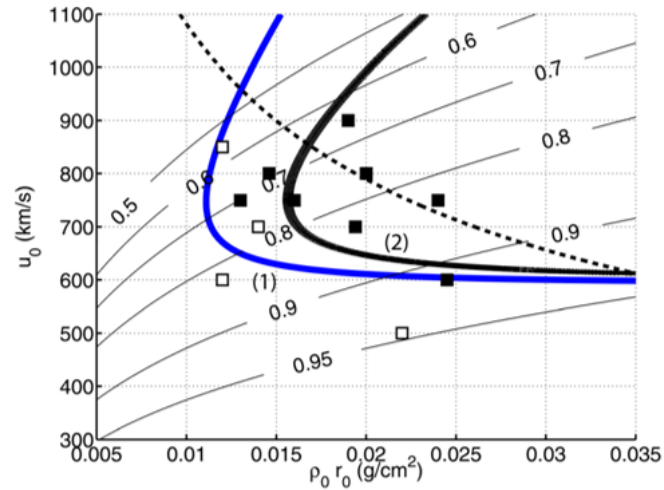


Fig. 1.13 Ignition criterion as a function of the hot spot areal density $\rho_0 r_0$ and the initial velocity u_0 of the ignition shock when it enters the hot spot. Blue solid curve for total deposition of α -particle energy in the hot spot and black for α fraction from scaling law. The dashed line as the ignition criterion from Sherbakov[6]. Square symbols are the results of full numerical simulation: black are ignited target and white non-ignited ones [15].

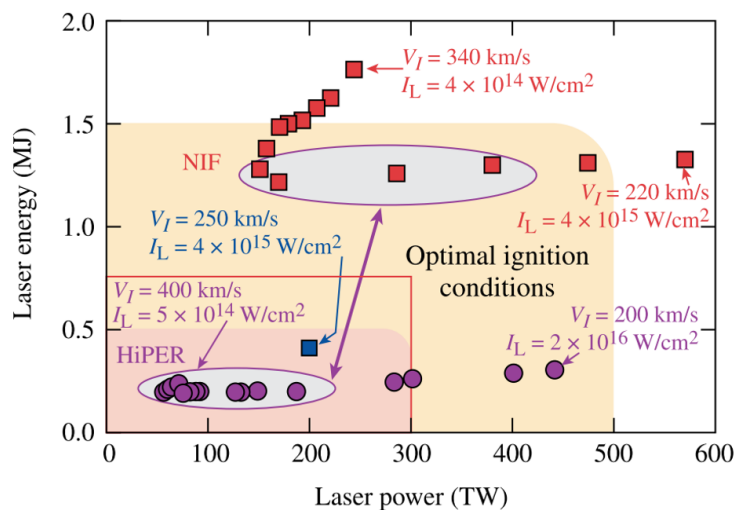


Fig. 1.14 Laser power and energy requirement for ignition of HiPER targets with scaling factor of 1 (circles), 1.2 (blue square) and 2 (red squares) [21].

the facility and a smaller scale of 1.2 (blue square) is considered to be more realistic since it is within the NIF safety domain (red line).

In parallel to these studies on the implosion of the HiPER full-DT target, the implosion of targets as described by Betti [7], up-scaled to NIF energy, have been investigated. In 2009 Perkins *et al.* [22] have studied such homothetic family of targets using 1D simulations. For a given target size, the spike power, energy and timing have been scanned in order to determine the highest gain. The gains calculated in this way range from 53 to 164 for an invested energy of 0.17 to 1.59 MJ, respectively. While NIF is supposed to be able to deliver 1.6 MJ, its safety operation consider a total laser energy of 750 kJ, which would corresponds to a gain of ~ 105 .

This work has been completed by Anderson *et al.* [23]. This later design aims to be potentially used on NIF since it takes all the known constraints of this facility into account. The target is a 161 μm DT shell of 1044 μm outer radius and coated with 31 μm plastic ablator. Because NIF is designed for indirect drive, the beams have to be repointed in order to optimize the homogeneity of irradiation. This geometry of irradiation is called polar direct drive[24]. In addition, the 192 beams of NIF are separated in two groups of 98 beams. The first one is the assembly pulse, used to compress the target, with a main compression power of 130 TW (the actual single beam power varies depending of the angle of incidence of the beam on the target due to the polar direct drive configuration). At 8.95 ns, the power of this pulse is increased to 215 TW and the other 98 other NIF beams are turned on with the same power, resulting in a spike power of 430 TW. The total delivered energy is 750 kJ. Two dimensional simulations, with this design have predicted a gain above 50 with good robustness to uniformity of irradiation.

1.4.3 Hot electron generation in shock ignition implosion

The hydrodynamic studies presented in the previous section show that the shock ignition is a promising scheme for ICF. However, a major problem has not been studied in details in those, *i.e.*, the generation of supra thermal electrons during the spike and their energy deposition in the imploding target. Indeed, in order to generate a ignition shock with a pressure high enough so that it triggers the ignition of the target, an intensity on target of several 10^{15} W/cm² is required. At these intensities, collective effects in the plasma can lead to anomalous absorption of the laser into a population of electrons with energies much higher than the energy of the thermal electrons in the corona [25]. These hot electrons do not deposit their energy locally (in the plasma corona) or at the surface of the solid target. Instead, they penetrate in the shell and deposit their energy over a certain range which depends on hot electron temperature and the density of the shell.

Hot electrons have actually been a subject of concern from the early stage of ICF studies. In 1983, McCall [26] presented results of classical ICF implosions realized with laser systems operating at the wavelengths λ of 1 μm (Nd:glass) or 10 μm (CO_2). In both case, it appeared that the experiments were dominated by hot electron effects. In particular, preheat from in-depth penetration of the hot electrons has been shown to reduce the achieved compressed fuel densities. However, the effects of hot electrons have been smaller for the experiment with $\lambda = 1 \mu\text{m}$. This is due to a reduction of the interaction parameters $I\lambda^2$, where I is the laser intensity. Indeed, a large amount of hot electrons is expected for value of $I\lambda^2$ above $\sim 6 \times 10^{13} \text{ W}\cdot\mu\text{m}/\text{cm}^2$ [27]. For a given laser wavelength, this defines a threshold intensity above which hot electrons have to be considered. For $\lambda = 10 \mu\text{m}$ this intensity is $6 \times 10^{11} \text{ W}/\text{cm}^2$ and for $\lambda = 1 \mu\text{m}$ it is $6 \times 10^{13} \text{ W}/\text{cm}^2$. In both cases, the typical intensity used in classical scheme for ICF, which is of several $10^{14} \text{ W}/\text{cm}^2$, is above the threshold. This observation led to the current design for ICF, which uses a shorter wavelength of $\lambda = 0.351 \mu\text{m}$ (third harmonic of Nd:Glass). In this case, the threshold intensity is $\sim 5 \times 10^{14}$ so that the effect of hot electrons is negligible. For shock ignition, this threshold is exceeded during the spike and the hot electrons have to be taken into account. But at the difference of the classical scheme, in shock ignition, the hot electrons are generated at a late time (when the spike is launched). Due to the on going implosion of the shell, its areal density has increased at this time. If the increase is large enough, the hot electrons might be stopped in the outer part of the shell, preventing them from preheating the whole target. Moreover, they could be beneficial to the implosion by increasing the ignition shock pressure [28, 23].

A precise description of the hot electron source parameters in shock ignition regime is therefore necessary. This has been studied both experimentally and with the help of particle in cell simulations. These results have been used in order to implement the description of hot electrons in hydrodynamic codes used for the simulation of ICF implosions. Before using these codes for the design of more realistic shock ignition implosions, they have to be validated by comparison with experiments. In 2015, Nora *et al* [29] used the code LILAC with a suprathreshold electron-transport package [30] in order to interpret an experiment realized on the Omega Laser System. In this experiment, a solid sphere of CH doped with Titanium has been imploded with a shock ignition like pulse. The on-target intensity was up to $\sim 6 \times 10^{15} \text{ W}/\text{cm}^2$. The simulations took in consideration hot electron sources with temperature ranging from 50 to 100 keV and carrying up to 8% of the total incident laser energy. The main experimental observable was the intense X-ray emission due to the collapse of the shock at the center of the sphere. The simulations with hot electrons successfully reproduced the time of this emission, which allowed to infer a peak ablation pressure of 300 Mbar and a main shock pressure exceeding $\sim 1 \text{ Gbar}$. In 2017, Cristoforetti *et al.* [31] used the code

CHIC with a novel self-consistent module for the description of hot electrons [32] in order to interpret an experiment at the Prague Asterix Laser System [33]. This experiment focused on the study of laser-plasma instabilities and their role in the generation of hot electrons. In this experiment, a multi-layer target (Parylene C - Titanium - Copper) was irradiated with a 300 ps long pulse at the wavelength $0.438 \mu\text{m}$. The resulting on-target intensity was $6 \times 10^{15} \text{ W/cm}^2$. The main observables in this experiment were the backscattered energy from laser plasma instabilities and the corona temperature. The simulations reproduced well the Stimulated Raman Scattering level and the plasma temperature.

The results from these experiments show that hot electrons are of importance for shock ignition relevant experiments, but also they show that hydrodynamic codes are able to qualitatively reproduce such experiments. Yet the number of experiments relevant to shock ignition and interpreted with simulations taking in account the hot electrons is relatively small. In order to use these codes for the design of shock ignition implosion, further validation with dedicated experiments is required.

1.5 Thesis outline

The work proposed in this thesis aimed to characterize the effects of hot electrons on the hydrodynamic of shocks and implosions in the context of shock ignition. Especially, experiments are being interpreted using hydrodynamic codes which include modules for the description of hot electron generation and transport. The secondary objective of this work is the validation of these codes, or their improvement in order to reproduce the experimental observables.

The manuscript is organized as followed:

Chapter 1 In this chapter, the basic concept that leads to the shock ignition approach for inertial confinement fusion are presented. The classical scheme for Inertial Confinement Fusion is introduced through the consideration of the physical and technological constraints. The limitations of this scheme are then discussed and the Shock Ignition scheme is presented as an alternative scheme which might allow to overcome some of these limitations. A state of the art of shock ignition is then realized, emphasizing the effects of hot electrons in shock ignition implosions.

Chapter 2 In shock ignition, direct laser irradiation is used in order to drive the implosion of the target. In this chapter, the mechanisms of laser-plasma interaction in the regime of intensities of shock ignition are presented. At low intensity, collisional absorption results in an ablation pressure which creates a shock wave. At higher

intensity, collective effects in the plasma lead to additional anomalous absorption mechanisms which can produce hot electrons. Shock waves and hot electrons are the two main consequences of the laser plasma interaction.

Chapter 3 Shocks are a key element of the shock ignition scheme. In this chapter, the basic hydrodynamic equations are derived in order to describe the different waves that can propagate in ICF targets: sound waves, rarefaction waves and shock waves. The description of the interaction of shocks with discontinuities is a major concern for shock ignition. Such interactions are analyzed by considering the set of accessible states of a fluid.

Chapter 4 Neglecting the effect of hot electrons in a first approximation, shock ignition implosions can be described through hydrodynamic alone. In this chapter, the hydrodynamic of shock ignition is studied in order to highlight the key features of the scheme. To do so, the solutions of shock interaction described in the Chapter 3 are used to simulate planar shock ignition. Then an experiment relevant to shock ignition is presented and interpreted with hydrodynamic simulations, highlighting these key elements.

Chapter 5 The hot electrons generated in shock ignition are expected to significantly perturb shock propagation. Planar experiments allow to characterize both the hot electron source parameters and their effects on the hydrodynamic with an easier access for diagnostics. In this chapter, results from experiments realized in planar geometry are presented. These results are interpreted with simulations taking hot electrons in consideration.

Chapter 6 Depending on the source parameters, hot electrons could be beneficial or detrimental to shock ignition implosions. In this chapter, results from experiment in spherical geometry and relevant to shock ignition are presented. Similarly to chapter 5, these results are interpreted with simulations taking hot electrons in consideration, in order to evaluate their effect on the performances of implosion.

Chapter 7 In this chapter, the results presented in this work are summarized and perspectives for future works are proposed.

Chapter 2

Laser matter interaction

In the direct drive approach to inertial confinement fusion, the shell of fusion fuel is illuminated by laser radiation. In the classical scheme, the laser intensity is moderate (10^{13} to a few 10^{14} W/cm²) and collisional absorption is the main mechanism of absorption of the laser energy into plasma temperature. For the higher intensities required for shock ignition (10^{15} to 10^{16} W/cm²), other mechanisms of absorption due to collective effects (coupling of the light wave with plasma waves) have to be taken in account.

In this chapter, the quasi-stationary ablation profile created by collisional absorption is first presented. Then the plasma waves and their damping mechanisms are presented. Finally, the main mechanisms of laser plasma interaction at intensities relevant to shock ignition are presented.

2.1 Ablative drive

2.1.1 Critical density

When a solid target is illuminated by an intense laser radiation, matter is first vaporized and ionized through multi-photon absorption, creating a plasma which expands in the vacuum toward the laser radiation. The laser then propagates in an increasing profile of electron density, where it has to satisfy the plasma dispersion relation for electromagnetic waves

$$k^2 c^2 = \omega^2 - \omega_p^2, \quad (2.1)$$

where k and ω are the wave number and frequency of the electromagnetic wave, respectively, c is the speed of light in vacuum and ω_p is the electronic plasma frequency. This frequency is characteristic of the oscillation of the electrons in the plasma, and depends on their density

$$\omega_p = \sqrt{\frac{n_e e^2}{\epsilon_0 m_e}}, \quad (2.2)$$

where n_e is the number electron density, e the elementary charge, ϵ_0 the permittivity of free space and m_e the electron mass. Along the propagation of the laser radiation in the plasma, the electron density increases and, following the dispersion relation, the wave number of the electromagnetic wave decreases. When it reaches $k = 0$, for $\omega = \omega_p$, the electromagnetic wave cannot propagate any further in the plasma (it is then reflected or absorbed). The electron density corresponding to this condition is called the critical density

$$n_c [\text{cm}^{-3}] = \frac{\epsilon_0 m_e \omega^2}{e^2} \simeq \frac{1.1 \times 10^{21}}{\lambda^2 [\mu\text{m}^2]}, \quad (2.3)$$

where λ is laser wavelength. For shorter wavelength, the critical density is higher, meaning that the laser radiation penetrates deeper in the plasma. The wavelength considered for direct drive ICF is $\lambda = 0.351 \mu\text{m}$, such that the critical density is $n_c \simeq 9 \times 10^{21} \text{ cm}^{-3}$. This density is much lower than the electron density of the solid target, which for the case of a fully ionized CH is $\simeq 3.4 \times 10^{23} \text{ cm}^{-3}$, verifying that the laser radiation does not propagate up to the solid target.

2.1.2 Collisional absorption

The electrons of the plasma oscillate in the electric field of the laser. This motion is coherent and after one optical period, the electrons are back to their original position and velocity, so that no energy has been transferred from the laser to the plasma. But, if during this coherent motion an electron collides with an ion, resulting in a change of its momentum, its motion is no longer coherent. The energy gained by this electron is then transferred to the plasma through electron-electron collisions, rising its temperature. A more detailed description of the electron-ion collision shows that the conservation of momentum imposes the absorption of a photon during the collision. This three body collision is called inverse Bremsstrahlung and it is the main mechanism of absorption of laser radiation at intensities relevant for the classical scheme for ICF (around 10^{14} W/cm^2).

The evolution of the intensity of the laser radiation along its propagation axis x can be expressed as

$$\frac{\partial I_L(x)}{\partial x} = -\kappa I_L, \quad (2.4)$$

where κ is the coefficient for collisional absorption given by

$$\kappa = \frac{\nu_{ei}}{c} \left(\frac{n_e}{n_c} \right)^2 \frac{1}{\sqrt{1 - n_e/n_c}}. \quad (2.5)$$

The electron-ion collision rate ν_{ei} is the characteristic frequency of this absorption and, within the Spitzer's model, is given by

$$\nu_{ei} = \frac{4\sqrt{2\pi}}{3} \frac{n_e Z e^4 \ln \Lambda_{ei}}{m_e^{1/3} T_e^{3/2}}, \quad (2.6)$$

where Z is the plasma charge state, Λ_{ei} the electron-ion Coulomb logarithm and T_e the plasma temperature in energy unit.

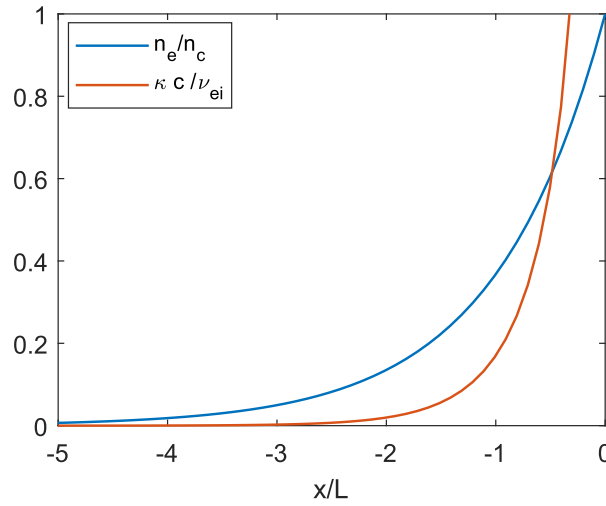


Fig. 2.1 Example of electron density profile and corresponding absorption coefficient. The absorption is getting important when n_e/n_c tends toward unity.

The absorption coefficient is strongly dependent on the electron density and it becomes very large when n_e tends toward n_c . This shows that, in the regime where the laser radiation is not fully absorbed before it reaches the critical density, most of the intensity is absorbed close to n_c . Even though κ diverges for $n_e = n_c$, its integral does not. Assuming an exponential profile for the under critical electron density $n_e/n_c = \exp(x/L)$, as presented in Figure 2.1, the fraction of the laser intensity absorbed on its way toward the critical density and on its way back (after reflection) is

$$A_L = 1 - \exp\left(-2 \int_{-\infty}^0 \kappa(x) dx\right). \quad (2.7)$$

Since most of the intensity is absorbed close to the critical density, the electron-ion collision frequency can be considered constant $v_{ei}^c = v_{ei}(n_e = n_c)$. The absorbed fraction can then be expressed as

$$A_L = 1 - \exp \left[-2 \frac{v_{ei}^c}{c} \int_{-\infty}^0 \exp \left(\frac{2x}{L} \right) \frac{1}{\sqrt{1 - \exp(x/L)}} dx \right], \quad (2.8)$$

$$A_L = 1 - \exp \left(-\frac{8}{3} \frac{v_{ei}^c}{c} L \right). \quad (2.9)$$

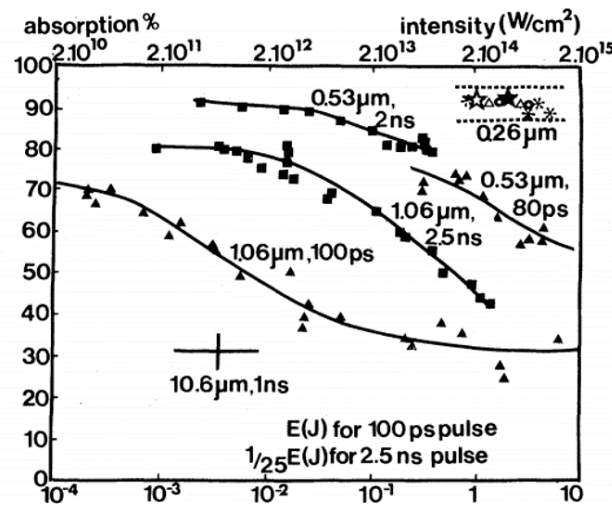


Fig. 2.2 The fraction of absorbed laser light vs incident flux for various experimental conditions [34].

Figure 2.2 [34] presents the fraction of absorbed laser light as a function of the laser intensity for several wavelengths and pulse durations. It shows that the absorbed fraction decreases when the laser intensity increases. This is due to the increase of electron temperature and the density gradient steepening. Another important results is the increase of absorbed fraction when the laser wavelength is reduced. Indeed, lasers with shorter wavelength penetrate to higher densities, leading to a more efficient absorption.

2.1.3 Stationary laser-driven ablation

Few hundreds of picoseconds after the beginning of the laser matter interaction, the plasma reaches a quasi-stationary state. Figure 2.3 presents the temperature and density profiles corresponding to this state, in which four zones can be identified:

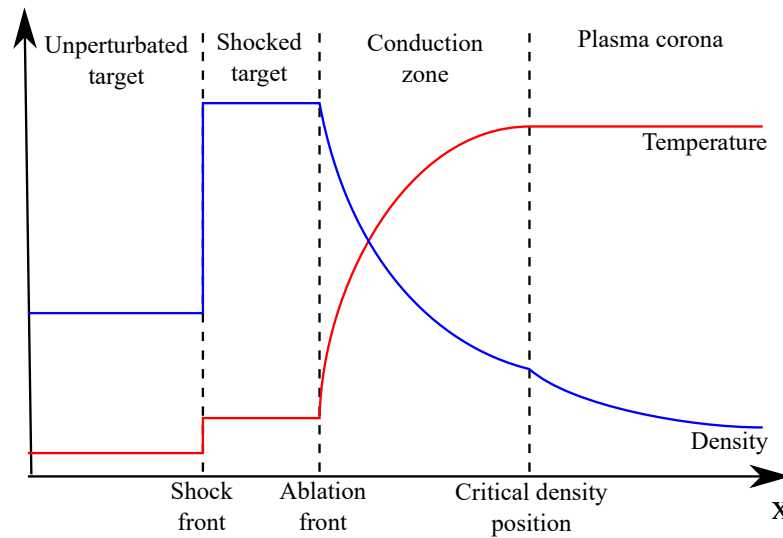


Fig. 2.3 Profiles of density (in blue) and temperature (in red) in stationary laser-driven ablation. Four zones are visible: the unperturbed target, the shocked target, the conduction zone and the plasma corona. These zones are separated by the shock front, the ablation front and the position of the critical density, respectively.

- The plasma corona: It corresponds to under-critical plasma. It is the only region in which the laser radiation propagates and therefore is absorbed. In this region the plasma has a low density and a high temperature. Due to its high electronic conduction, the plasma corona is approximately isotherm.
- The conduction zone: It corresponds to the over critical plasma. In this zone the thermal energy is transported from the hot corona to the colder dense part of the target, mostly though electronic conduction. In this region the density and temperature change a lot, but the pressure is rather constant.
- The shocked target: The pressure created by the ablation process leads to the creation of a shock wave that propagates in the solid target. The density, temperature and pressure in this region are higher than in the unperturbed target due to the non-isotropic compression induced by the shock wave.
- The unperturbed target: This is the zone not reached yet by the shock wave. Its density is the initial solid density of the target and its temperature is the ambient temperature.

The stationary ablation does not refer to a situation where all of these zones are at equilibrium. It only refers to the equilibrium of energy flux at the critical density, separating the corona from the conduction zone, which writes

$$I_{abs} = u\Delta E + Q, \quad (2.10)$$

where $I_{abs} = A_l I_L$ is the absorbed laser intensity, $u\Delta E$ the flux of energy per unit surface associated with the flux of mass passing through the critical density and Q the heat required in order to maintain the corona at a constant temperature, compensating its cooling down due to its expansion. Assuming that the laser energy is locally deposited at the critical density, the ablation process can be described by a Chapman-Jouguet deflagration [2]. In these conditions, the plasma corona at the critical density has a velocity u equal to its isothermal sound velocity $c_T = \sqrt{(P_{corona}/\rho_c)}$, where P_{corona} and ρ_c are the pressure and density of the corona at the critical density. Also, the pressure is discontinuous at the critical density so that the pressure in the conduction zone P_{cond} is twice the pressure in the plasma corona P_{corona} . Because the P_{cond} is equal to the ablation pressure P_a , it writes $P_a = P_{cond} = 2 P_{corona}$.

Under these conditions the equation 2.10 writes

$$I_{abs} = 4\rho_c c_T^3. \quad (2.11)$$

From this relation, the temperature at the critical density, the ablation pressure and the mass ablation rate can be expressed as functions of the laser parameters only. Indeed, the mass density is related to the electron number density and therefore to the laser wavelength by

$$\rho_c [\text{g/cm}^3] = \frac{A m_p}{Z} n_c \simeq \frac{A 1.8 \times 10^{-3}}{Z \lambda^2 [\mu\text{m}^2]}, \quad (2.12)$$

where A is the mass number of the ions, Z the charge state of the plasma and m_p is the proton mass. The definition of the isothermal sound velocity allows determining the temperature at the critical density

$$\frac{1+Z}{A m_p} T_c = c_T^2 = \left(\frac{I_{abs}}{4\rho_c} \right)^{2/3}. \quad (2.13)$$

The ablation pressure is twice the pressure of the corona at the critical density $P_a = 2 P_{corona}$:

$$P_a = 2 \rho_c c_T^2 = \left(\frac{\rho_c}{2} \right)^{1/3} I_L^{2/3}. \quad (2.14)$$

The mass ablation rate is the flux of mass passing through the ablation front. Since the conduction zone is stationary, the same mass flux goes through the critical density. Also, at the critical density, $u = c_T$ so that the mass ablation rate writes

$$\dot{m}_a = \rho_c c_T = \left(\frac{\rho_c}{2}\right)^{2/3} I_L^{1/3}. \quad (2.15)$$

In many design for ICF, the DT shell is coated with CH ablator in order to increase laser absorption. Using CH average mass number $A = 13/2$ and atomic number $Z = 7/2$, explicit expressions for these relations are obtained:

$$c_T = 4.16 \times 10^7 I_{14}^{1/3} \lambda_{\mu m}^{2/3} \text{ cm/s}, \quad (2.16)$$

$$T_c = 2.61 I_{14}^{2/3} \lambda_{\mu m}^{4/3} \text{ keV}, \quad (2.17)$$

$$P_a = 12 I_{14}^{2/3} \lambda_{\mu m}^{-2/3} \text{ Mbar}, \quad (2.18)$$

$$\dot{m}_a = 1.44 \times 10^5 I_{14}^{1/3} \lambda_{\mu m}^{-4/3} \text{ g}/(\text{cm}^2 \text{ s}), \quad (2.19)$$

where $\lambda_{\mu m}$ is the laser wavelength in μm and I_{14} the absorbed laser intensity in $10^{14} \text{ W}/\text{cm}^2$. For a given laser intensity, a shorter laser wavelengths leads to a higher ablation pressure. This scaling is one of the reasons for the megajoules lasers to operate at their third harmonic $\lambda = 0.351 \mu m$ (their fundamental being $1.05 \mu m$). At this wavelength, an absorbed intensity of $I_{abs} = 5 \times 10^{14} \text{ W}/\text{cm}^2$ leads to an ablation pressure $P_a = 70 \text{ Mbar}$ and a temperature for the plasma corona of $T_c = 1.89 \text{ keV}$. This is the typical intensity considered in the classical scheme for ICF. For the shock ignition scheme, higher intensities are considered in order to generate higher ablation pressure. As an example, an absorbed intensity of $5 \times 10^{15} \text{ W}/\text{cm}^2$ results in an ablation pressure of 327 Mbar and a corona temperature of 8.79 keV .

2.2 Collective effects in plasmas

A characteristic behavior of plasmas is their ability to sustain collective effects. In the simplest case, these collective effects are waves which correspond to fluctuations of the density with specific frequencies. The plasma is composed of electrons and ions, whose motion take place on two different time scales. The heavier ions have a motion slower than the electrons. As a results, in a plasma without large imposed magnetic field, there are two kinds of waves: the high frequency electron plasma waves and the low frequency ion acoustic waves.

2.2.1 Ion acoustic waves

Ion acoustic waves are low frequency oscillations of density, with frequency ω much smaller than the electron plasma frequency ω_{pe} . The phase velocity of these waves v_ϕ is in the range $v_{Te} \gg v_\phi \gg v_{Ti}$, where v_{Te} and v_{Ti} are the electron and ion thermal velocities, respectively. Therefore, the contribution of both ions and electrons have to be considered in order to determine their dispersion relation. However, the electrons having a mass much smaller than the ions, their inertia can be neglected. They simply follow the ions motion so that the ion acoustic wave is quasi-neutral. The dispersion relation of ion acoustic waves, relating the frequency ω to the wavenumber k , is

$$\omega^2 = k^2 c_s^2 + 3 k^2 v_{Ti}^2 \quad (2.20)$$

where $c_s = \sqrt{Z T_e / m_i}$ is the ion acoustic velocity and $v_{Ti} = \sqrt{T_i / m_i}$ is the ion thermal velocity. The term $3 k^2 v_{Ti}^2$ appears as a correction due to the ion temperature. This dispersion relation is linear, very similarly to a classical sound wave of velocity v_s . Since the phase and group velocities of the wave are identical, $\omega/k = \partial\omega/\partial k = v_s$, these waves propagate without much deformation. Finally, the condition of existence of ion acoustic waves $v_s \gg v_{Ti}$, can be rewritten as a condition on the ion and electron temperature $Z T_e \gg 3 T_i$. Therefore, ion acoustic waves can only exist in plasma where the electron temperature is much larger than the ion temperature.

2.2.2 Electron plasma waves

Electron plasma waves are high frequency oscillations of charge density and their frequency ω is close to ω_{pe} . Due to this high frequency feature, ions can be considered as a static neutralizing background, so that the charge density fluctuations are only due to the electrons motion. Using Poisson's law, it appears that the density fluctuation δn_e is associated with an electrostatic wave, meaning that the wave vector \vec{k} is in the same direction as the oscillating electric field \vec{E}

$$e \delta n_e = i \epsilon_0 \vec{k} \cdot \vec{E}, \quad (2.21)$$

The factor i in this expression denotes a $\pi/2$ shift between the maximum amplitudes of the density perturbation and the electric field.

The dispersion relation for these waves is

$$\omega^2 = \omega_{pe}^2 + 3k^2 v_{Te}^2 \quad (2.22)$$

where ω_{pe} is the plasma electron frequency given by (2.2) and $v_{Te} = \sqrt{T_e/m_e}$ is the electron thermal velocity. The frequency of these waves is essentially ω_{pe} , with a small thermal correction dependent on the wavenumber. Since electron plasma waves are high frequency oscillations, their phase velocity $v_\phi = \omega/k$ is very large. It can be of the order of light speed and therefore it verifies the condition $v_\phi \gg v_{Te}$. On the other hand, their group velocity $v_g = \partial\omega/\partial k = 3v_{Te}^2/v_\phi$ is very small compared to the electron thermal velocity. Therefore, these waves do not carry energy on large distances, they tend to accumulate it locally until they are damped.

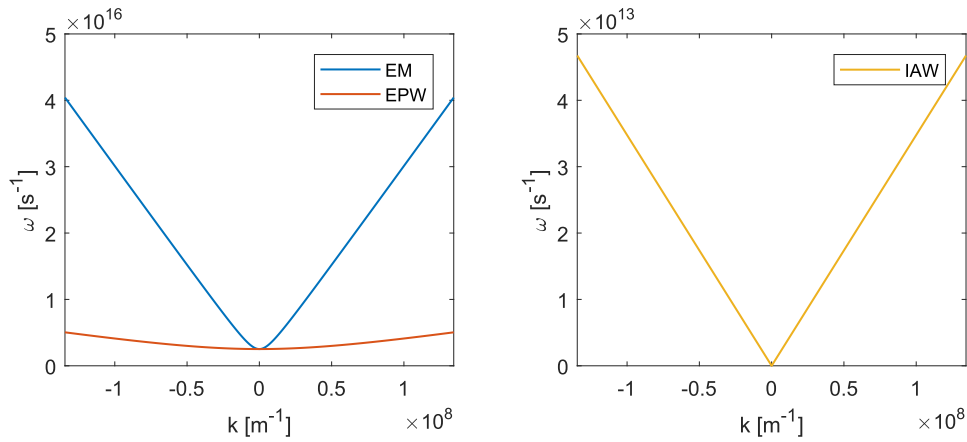


Fig. 2.4 Dispersion relation of electromagnetic waves (EM), electron plasma waves (EPW) and ion acoustic waves (IAW) in the range $\pm(2\lambda_D)^{-1}$. The plasma conditions are $n_e = 2 \times 10^{21} \text{ cm}^{-3}$, $T_e = 2 \text{ keV}$, $T_i = 0.4 \text{ keV}$, $A = 13/2$ and $Z = 7/2$, so that $\lambda_D = 7.4 \times 10^{-9} \text{ m}$.

Figure 2.4 presents the dispersion relations of transverse electromagnetic wave (EM), electron plasma wave (EPW) and ion acoustic wave (IAW) for parameters typical of an ICF plasma corona. The dispersion curves are displayed in the range $\pm(2\lambda_D)^{-1}$, where $\lambda_D = v_{Te}/\omega_{pe} = 7.4 \times 10^{-9} \text{ m}$ is the Debye length.

2.2.3 Linear wave damping

For both electron plasma waves and ion acoustic waves, the dispersion relations are actually derived from the expression $\varepsilon(\vec{k}, \omega) = 0$, where ε is the plasma permittivity. This permittivity is a complex quantity, so that the solution of the equation $\varepsilon(\vec{k}, \omega) = 0$ has a real and an imaginary part, $\omega(\vec{k}) = \omega' + i\omega''$. Equations (2.20) and (2.22) are only the real part ω' of this solution in two different limiting cases. The imaginary part ω'' describes the evolution of the amplitude of the wave. If ω'' is positive, the amplitude of the wave grows in time, which is impossible if the plasma is stable. On the other hand, if ω'' is negative, the amplitude of the wave decreases in time at a rate $\gamma = -\omega''$ called the damping rate. Two linear mechanisms

contribute to the damping of the electron plasma wave and ion acoustic wave. These are collisional damping and Landau damping.

Collisional damping is due to the electron-ion collisions. It is very similar to the mechanism of absorption of the laser light close to the critical density. Through collisions, the coherent motion of the electrons in the plasma wave is perturbed, leading to an isotropization of their distribution and a damping of the wave. The damping rate is $\gamma = \omega_{pe}^2 v_{ei} / \omega$, where v_{ei} is the electron-ion collision rate given by (2.6). For an electron plasma wave, $\omega = \omega_{pe}$ and therefore $\gamma = v_{ei}$. However, the plasma corona is rather collisionless due to its high temperature and low density, so that the collision damping rate is very small.

Landau damping is a collisionless mechanism. It results from the resonance of the wave with a part of the thermal distribution function of the particles in the plasma. Taking the example of an electron plasma wave, most of the electrons have velocities very different than the wave phase velocity ω/k . These particles simply oscillate in the electrostatic field without gain or loss of energy. On the other hand, some electrons have velocities close to the wave phase velocity. They experience a field which is approximately constant for a time long enough so that they can exchange energy with the wave. The electrons with velocities slightly lower than the wave phase velocity will gain energy, while the electrons with velocities slightly larger will lose energy. The net energy gain or loss for the wave then depends on the slope of the electron velocity distribution close to the resonance. If the distribution decreases with velocity, as it is the case for a Maxwellian distribution, the wave loses energy.

The Landau damping rate of an electron plasma wave is given by [25]

$$\frac{\gamma}{\omega} = \sqrt{\frac{\pi}{8}} \frac{v_{\phi}^3}{v_{Te}^3} \exp\left(-\frac{v_{\phi}^2}{2v_{Te}^2}\right), \quad (2.23)$$

where $v_{\phi} = \omega/k$ is the electron plasma wave velocity and $v_{Te} = \sqrt{T_e/m_e}$ is the electron thermal velocity. The damping rate has been normalized to the frequency of the wave. It appears that this damping is large for small values of v_{ϕ} , where many particles of the Maxwellian distribution are resonant. Since the plasma wave frequency is rather constant with $\omega = \omega_{pe}$, this corresponds to large wave number k . On the other hand for small values of v_{ϕ} , large values of k , the damping is negligible due to the small number of electrons that can resonantly interact with the wave. For values $k > 0.4\lambda_D$, the damping becomes large enough to prevent electron plasma wave from existing.

The Landau damping rate of an ion acoustic wave is very similar to the rate for the electron plasma wave

$$\frac{\gamma}{\omega} = \sqrt{\frac{\pi}{8}} \left[\frac{\omega_{pi}}{\omega_{pe}} + \frac{v_s^3}{v_{Te}^3} \exp\left(-\frac{v_s^2}{2v_{Te}^2}\right) \right]. \quad (2.24)$$

The first term ω_{pi}/ω_{pe} is due to the damping on the electrons while the other corresponds to the ions. Since the phase velocity of the ion acoustic wave is constant, $v_s = \sqrt{c_s^2 + 3v_{Ti}^2}$, the Landau damping depends only on the ratio of the electron to ion temperature $Z T_E/T_i$. The Figure 2.5 presents the Landau damping rate normalized to the wave frequency for electron plasma waves (EPW) and ion acoustic waves (IAW) for parameters typical of a ICF plasma corona (identical to the parameter used in Figure 2.4).

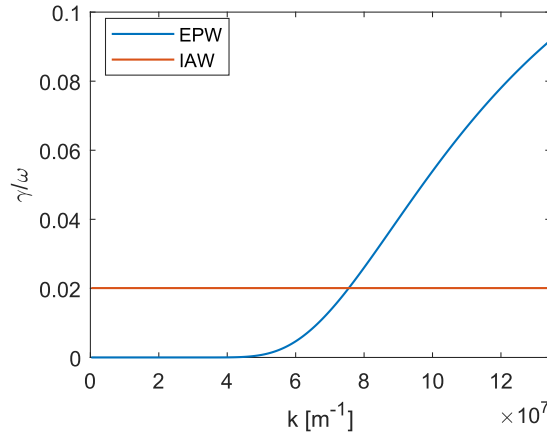


Fig. 2.5 Landau damping of electron plasma wave (EPW) and ion acoustic wave (IAW). The plasma conditions are $n_e = 2 \times 10^{21} \text{ cm}^{-3}$, $T_e = 2 \text{ keV}$, $T_i = 0.4 \text{ keV}$, $A = 13/2$ and $Z = 7/2$.

2.2.4 Non-linear wave damping

Under some conditions that will be described in the next section, an electron plasma wave of very large amplitude can be generated. In this case, non-linear mechanisms of damping of the plasma wave limit its growth. The two main non-linear mechanisms of electron plasma wave damping are wave-breaking and the collapse of electron plasma waves.

In the absence of ion motion, the only non-linear damping mechanism is wave-breaking. For an electron plasma wave of large enough amplitude, the quiver velocity of the electrons in the electric field, $eE/m_e\omega$, can become comparable to the phase velocity of the wave ω/k . In this situation numerous initially-cold electrons can resonantly interact with the wave in a similar way as for the Landau damping. The energy carried by the wave is then quickly transferred to these resonant electrons, resulting in the creation of a population of hot electrons. The velocity of the hot electrons is equal to the phase velocity of the wave,

such that they have an average energy $E_h = m_e c^2 (\gamma_\phi - 1)$, where γ_ϕ is the Lorentz factor associated to the wave phase velocity v_ϕ . Indeed, since this velocity can be of the order of magnitude of the speed of light, the relativistic correction has to be considered.

The characteristic time of wave-breaking is quasi-instantaneous, if the threshold amplitude of the wave is reached. Yet, the assumption that the ions are static requires that the wave growth rate is faster than the typical ion dynamic, which is given by the ion plasma frequency ω_{pi} . If this is not the case, the dynamic of ions has to be considered, leading to other mechanism of wave damping such as the collapse of the electron plasma wave.

The collapse is a non linear mechanism of damping resulting from the coupling of electron plasma waves with ion acoustic waves. Qualitatively, it corresponds to the formation of cavities where an electron plasma wave of large dimension get fragmented into waves of smaller dimension. This fragmentation leads to a transfer of the energy of the plasma wave with an initially small wavenumber (large wavelength) toward waves with larger wavenumber (small wavelength), where the Landau damping is important [35]. The energy of the wave is then damped into electrons, forming a hot electron tail distribution similarly to wave-breaking, but of lower characteristic energy. Indeed, the damped waves having higher wavenumbers, their phase velocities are smaller and therefore, the energy an electron can acquire is also smaller. On the other hand, the threshold amplitude required for the collapse to occur is smaller than wave-breaking. Hence, in first approximation, the collapse will happen before (at lower amplitude) than the wave-breaking, given that the growth rate of electron plasma waves is slower than the ion plasma frequency. The hot electrons characteristic energy is then lower than expected from wave-breaking.

2.3 Anomalous absorption of laser light

In order to generate a strong converging shock, the shock ignition scheme uses laser irradiation at intensities higher than in the classical scheme. At these intensities, the absorption of the laser radiation is no longer due to collisional absorption only and several other mechanisms of laser plasma interaction take place. These are summed up in Figure 2.6. Collective effects mostly lead to perturbations of the laser propagation and its anomalous absorption into plasma waves (in contrast to collisional absorption where the laser energy is absorbed into thermal electrons). The damping of these plasma waves can then lead to the acceleration of electrons to energies significantly higher than the plasma electron temperature, as described in the previous section.

A complete analytic description of these phenomena is complex due to their competitive interplays, the finite interaction length of the plasma corona, the plasma inhomogeneity,

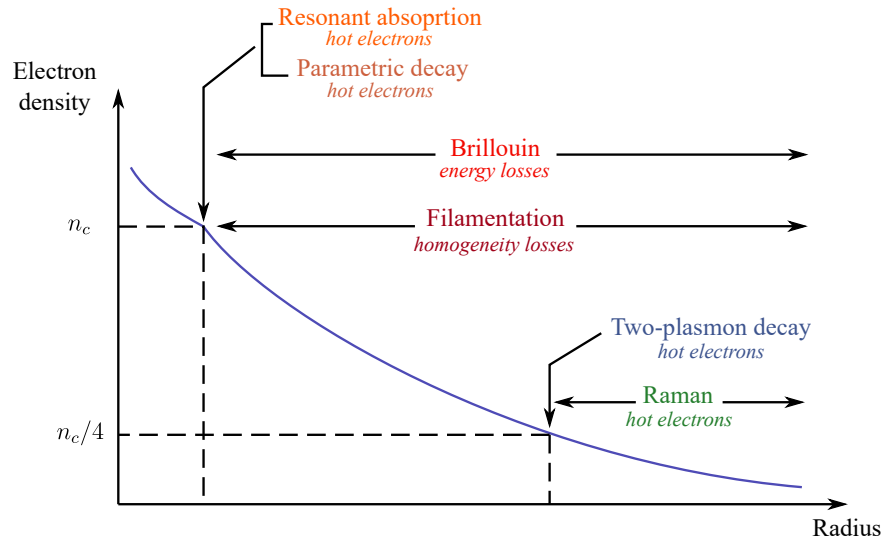


Fig. 2.6 Main mechanisms of interaction in the plasma corona.

geneties. . . Nonetheless, the description of these mechanisms allows to understand their domains of existence as well as their main characteristics. The comparison of theory with simulations and experimental data completes this description by providing phenomenological laws. These laws can then be used to predict, in first approximation, the laser absorption and potential hot electron production for given laser-plasma parameters.

2.3.1 Resonant absorption

Resonant absorption [36, 37] is a linear mechanism in which a part of the energy of the incident light is transferred to an electron plasma wave. This coupling requires the electric field of the light wave to oscillate in the direction of the density gradient. In the example described in section 2.1.2, where the plasma density gradient is in the direction of the laser propagation (and therefore normal to the electric field), this mechanism of absorption cannot occur. However, if the laser radiation has an oblique incidence and it is p-polarized (the electric field of the light wave lies in the plane of incidence), the electric field at the point of reflection is in the direction of the density gradient and resonant absorption can occur.

Considering a light wave propagating in vacuum in the (y, z) plan, its free space wave vector \vec{k}^{FS} has the two components $k_y^{FS} = k^{FS} \sin \theta$ along y and $k_z^{FS} = k^{FS} \cos \theta$ along z , where θ is the angle of the wave vector with respect to the z axis. If the wave now propagates toward a plasma with a density gradient along z , its wave vector has to satisfy the dispersion relation for electromagnetic waves. Since the density gradient is along z only, the projection of the wave vector on y is constant, $k_y = k_y^{FS}$, while its projection along z is given by

$$\left(\frac{\omega}{\cos\theta}\right)^2 = \omega_{pe}^2 + k_z^2 c^2. \quad (2.25)$$

The wave is reflected where $k_z = 0$. This corresponds to $\omega = \omega_{pe} \cos\theta$ or $n_e = n_c \cos^2\theta$. Therefore, a light wave with an angle of incidence is reflected at a density lower than the critical density. Also, since the absorption coefficient given by Eq. (2.5) quickly decreases when the density is lower than the critical density, the collisional absorption efficiency decreases when the angle of incidence increases.

At the point of reflection, the electric field is along z only and therefore, in the same direction as the density gradient. In this field, the electron oscillate with an amplitude z_{osc} . The variation of electron density is then

$$\delta n_e = n_e(z + z_{osc}) - n_e(z) \simeq z_{osc} \nabla n_e, \quad (2.26)$$

where $\nabla n_e = \partial n_e / \partial z$ is the density gradient of the plasma. At the critical density, the frequency of oscillation of this density fluctuation is the electron plasma frequency, $\omega = \omega_{pe}$ and an electron plasma wave can be resonantly excited.

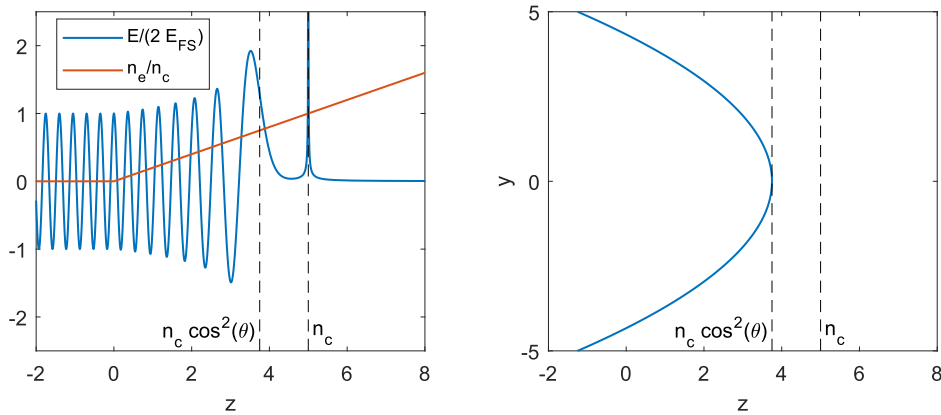


Fig. 2.7 Electric field of an obliquely incident p-polarized light wave incident on a linear density gradient with an angle $\theta = \pi/6$ (left). Trajectory of a ray of this light wave in the (y, z) plane (right). The ray is reflected at the density $n_c \cos^2(\theta)$ and shows resonant absorption at the critical density n_c .

Even if the electromagnetic wave is reflected at a density lower than the critical density, its electric field can excite a plasma wave at the critical density though tunneling. Figure 2.7 presents a scheme of resonant absorption for a light wave incident at $\theta = \pi/6$ on a linear density gradient. The light wave propagates in the plasma with a parabolic trajectory up to the density $n_e = n_c \cos^2(\theta)$. In the region $n_e = 0$, its electric field is described by a cosine and in the region $0 < n_e < n_c \cos^2(\theta)$, it is described by the Airy function. The Airy function

is the solution of the propagation equation for planar electromagnetic waves in a plasma with a linear density gradient. At the point of reflection of the wave, the electrical field is along z only and it has an exponentially decaying amplitude. At the critical density, the resonance of this evanescent field with the electron plasma wave leads to a peak of electrical field, where the laser light is absorbed.

The laser intensity absorbed through this process can be approximated by [25]

$$I_{abs} \simeq \frac{c}{8\pi} E_{FS}^2 \phi^2(\tau), \quad (2.27)$$

where E_{FS} is the amplitude of the electric field of the light wave in free space. $\phi(\tau) \simeq 2.3\tau \exp(-2\tau^3/E)$ is a function characteristic of the efficiency of the resonant absorption with $\tau = (\omega L/c)^{1/3} \sin \theta$. This function is presented in Figure 2.8. The limit $\tau \rightarrow 0$ corresponds to the case of normal incidence where the field driving the plasma wave vanishes. For large values of τ , the distance between $n_c \cos^2 \theta$ and n_c is too large to allow tunneling. An optimal angle of incidence is found for $\sin \theta \simeq 0.8(c/\omega L)^{1/3}$, where the resonant absorption efficiency is maximum.

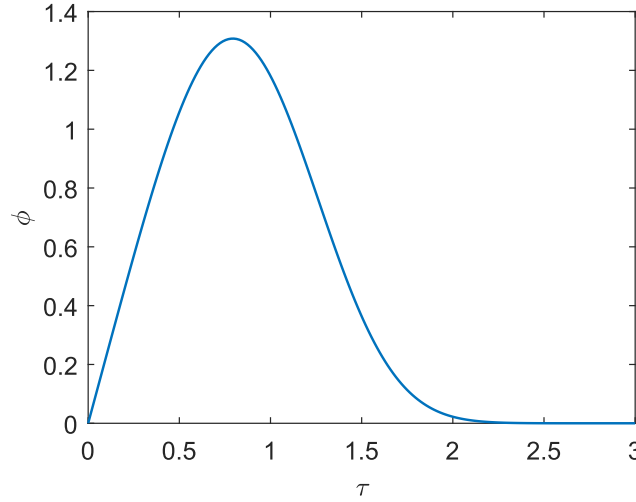


Fig. 2.8 Plot of the function $\phi(\tau)$, which characterizes the efficiency of resonant absorption.

The non-linear damping of the electron plasma wave generated by resonant absorption leads to the creation of a population of hot electrons. Numerous experiments [27, 38–40] and simulations [41–43] have highlighted the scaling between the laser interaction parameters, $I\lambda^2$, and the temperature of the hot electrons. In the regime $I\lambda^2 \in [10^{13}, 10^{15}]$, the temperature of the hot electron T_h can be approximated by [44]

$$T_h = 9.369 \times 10^{-10} (I\lambda^2)^{0.664} \text{ keV}. \quad (2.28)$$

In the regime $I\lambda^2 \in [10^{15}, 10^{17}]$ it is given by

$$T_h = 1.577 \times 10^{-3} (I\lambda^2)^{0.247} \text{ keV.} \quad (2.29)$$

where I is the laser intensity in W/cm^2 and λ the laser vacuum wavelength in μm . With parameters relevant to the shock ignition scheme, $I = 5 \times 10^{15} \text{ W/cm}^2$ and $\lambda = 0.351 \mu\text{m}$, $T_h \sim 9 \text{ keV}$. This hot electron temperature is actually very close to the plasma temperature during the laser spike ($\sim 8 \text{ keV}$) and the hot electrons are expected to deposit their energy locally or in the conduction zone, behaving very similarly to thermal electrons. From the hydrodynamic point of view, taking in account the resonant absorption is very similar to an increase of collisional absorption.

2.3.2 Parametric decay

The parametric decay instability [45] corresponds to the resonant coupling of the incident laser light with an ion acoustic wave and an electron plasma wave. It is a mechanism similar to resonant absorption, except that the spatial variation of density is due to ion acoustic wave and not to density gradient produced by the plasma expansion. The coupling of the three waves imposes matching relations for the wave-vectors \vec{k} and frequencies ω

$$\omega_0 = \omega_{iaw} + \omega_{epw}, \quad (2.30)$$

$$\vec{k}_0 = \vec{k}_{iaw} + \vec{k}_{epw}, \quad (2.31)$$

where the subscripts 0, *iaw* and *epw* refer to the incident laser wave, the ion acoustic wave and the electron plasma wave. Since the frequency of the ion acoustic wave is very small compared to the frequencies of the electron plasma wave and electromagnetic wave, equation (2.30) rewrites $\omega_0 \simeq \omega_{epw} \simeq \omega_{pe}$, where ω_{pe} is the electron plasma frequency. Therefore, parametric decay can only exist close to the critical density $n_e \simeq n_c$ where the frequency matching condition is met. Close to this density, the wave number of the electromagnetic wave become very small $\vec{k}_0 \rightarrow 0$, and the equation (2.31) writes $\vec{k}_{iaw} \simeq -\vec{k}_{epw}$.

In contrast to resonant absorption, this mechanism is unstable. The beating between the electric fields of the electromagnetic and electron plasma waves creates spatial fluctuations in the electric field intensity. Due to the ponderomotive force, this gradient of electric field acts as pressure on the ions which reinforce the initial density perturbation. The amplitude of the ion acoustic wave grows in time, which it turn increases the coupling between the

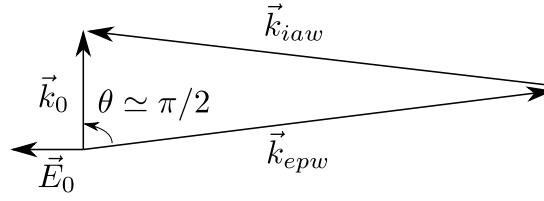


Fig. 2.9 Schematic of the parametric decay of an electromagnetic wave into an ion acoustic wave and a electron plasma wave.

electromagnetic wave and the electron plasma wave. The instability results from this feed-back loop.

The most unstable configuration for this instability is when the wave vectors \vec{k}_{iaw} and \vec{k}_{epw} lie in the plan (\vec{k}_0, \vec{E}_0) , with \vec{E}_0 the electric field of the incident electromagnetic wave. Also, the growth rate is maximum when the angle θ between \vec{k}_0 and \vec{k}_{epw} is close to $\pi/2$ as presented in Figure 2.9.

In principle, the non-linear damping of electron plasma waves generated by the parametric decay instability could lead to the production of hot electrons. Yet, the inhomogeneity of the plasma and the competition with the resonant absorption strongly limit the development of this instability. Simulations [46] showed that its effect on electron heating cannot be distinguished from the resonant absorption. Therefore the scaling laws for the hot electron temperature presented in the previous section can be considered to take in account the effect of this instability too.

2.3.3 Stimulated Brillouin scattering

The stimulated Brillouin scattering [47, 48] is a three waves parametric instability in which the incident laser light is coupled with an ion acoustic wave and a scattered electromagnetic wave. This coupling is unstable due to a feed-back loop similar to the parametric decay instability as presented in Figure 2.10. Given an initial ion acoustic wave characterized by a fluctuation of the density $\delta n/n$, the quiver motion of the electrons in the field of the incident laser radiation leads to a non-linear transverse current $J_{nl} \propto (\delta n/n)E_0$, where E_0 is the amplitude of the laser electric field. This current acts as a source term for a scattered wave of amplitude E_{sc} . The beating of this scattered wave with the incident one results in a low frequency variation of the electric field due to the term $E_0 E_{sc}^*$. If this beating is resonant with the ion acoustic wave, the ponderomotive force, pushing the electrons from the high intensity regions toward lower intensity ones, reinforces the density modulation $\delta n/n$.

To be resonant, the waves have to satisfy the matching conditions for their frequencies ω and wave numbers k

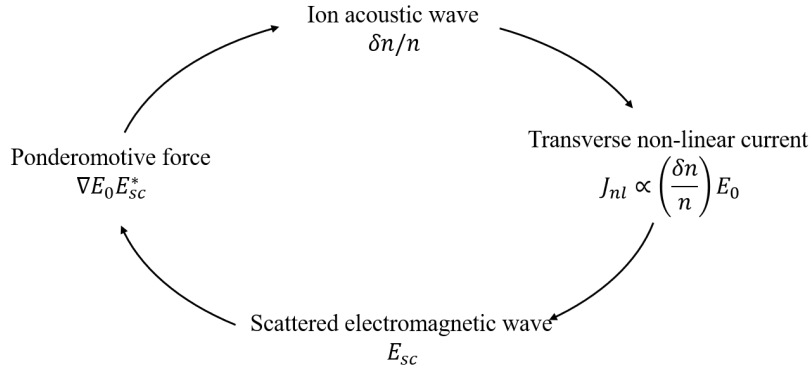


Fig. 2.10 Schematic of the feed back loop leading to stimulated Brillouin scattering instability.

$$\omega_0 = \omega_{sc} + \omega_{iaw}, \quad (2.32)$$

$$\vec{k}_0 = \vec{k}_{sc} + \vec{k}_{iaw}, \quad (2.33)$$

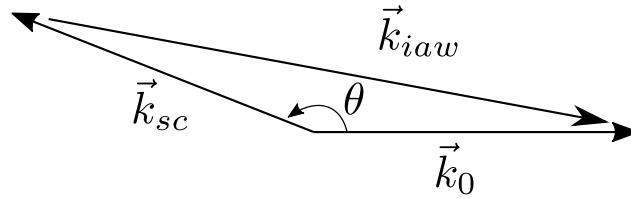


Fig. 2.11 Schematic of the wavenumber matching condition for stimulated Brillouin scattering.

where the subscripts 0, sc and iaw refer to the incident laser wave, the scatter electromagnetic wave and the ion acoustic wave, respectively. These waves also have to satisfy their own dispersion relations. Since the frequency of the ion acoustic wave is much smaller than the frequency of the incident electromagnetic wave, $\omega_{iaw} \ll \omega_0$, this instability can be excited in the entire plasma with density smaller than the critical density. It also implies that the scattered wave has a frequency close to that of the incident wave, $\omega_{sc} \simeq \omega_0$. Therefore, the wave vector matching condition rewrites $k_0 \simeq k_{sc}$ as shown in Figure 2.11.

The scattered wave can be emitted in any direction. However, the highest growth rate for this instability is obtained for backscattering, $\vec{k}_{sc} = -\vec{k}_0$ ($\theta = \pi$). Hence $k_{iaw} \simeq 2k_0$. It is also the most detrimental one since it leads to potential high reflectivity of the plasma corona, preventing an efficient absorption at the critical density. In this case, the growth rate writes [25]

$$\gamma = \frac{1}{2\sqrt{2}} \frac{k_0 v_{osc} \omega_{pi}}{\sqrt{\omega_0 k_0 c_s}}, \quad (2.34)$$

where $v_{osc} = eE/m_e\omega_0$ is the maximum velocity of the electrons in the field E , $\omega_{pi} = n_e Z^2 e^2 / \epsilon_0 m_i$ is the ion plasma frequency and $c_s = \sqrt{Z T_e / m_i}$ is the ion acoustic velocity.

In order to grow, the stimulated Brillouin scattering has to verify threshold conditions. These are due to the damping of the scattered and ion acoustic waves, the plasma inhomogeneities and the finite length where the instability can grow. In practice, this last condition is the most restrictive so that the threshold intensity is mostly determined by the gradient of density and expansion velocity in the plasma. Experimentally, the irradiation of solid targets with 1 ns pulses at a wavelength of $0.351 \mu\text{m}$ and intensity of $\simeq 10^{15} \text{ W/cm}^2$ has shown 5 to 10 % of laser energy reflected through stimulated Brillouin scattering [49].

2.3.4 Filamentation

The filamentation [50–53] instability corresponds to the pinching of the laser transverse profile due to the non-linearity in the refractive index of the plasma n_{nl} . Its principle is presented in Figure 2.12. The central area where the laser intensity is larger sees a higher refractive index than the wings, where the intensity is smaller. This transverse variation of refractive index acts similarly to a lens which reinforce the initial over-intensity.

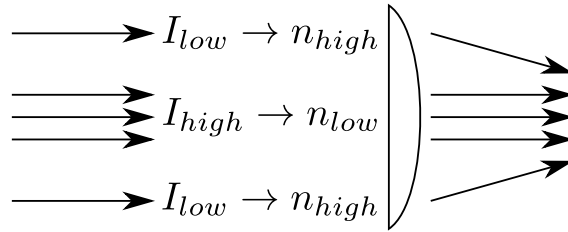


Fig. 2.12 Principle of filamentation. The transverse variation of intensity between I_{high} and I_{low} results in a transverse variation of refraction index n_{low} to n_{high} which act as a converging lens of the light.

In the corona, where the plasma is almost collisionless, the main mechanism of variation of the refractive index with intensity comes from the ponderomotive force. In the direction transverse to the beam, the gradient of intensity pushes the electrons from the high intensity region toward the region with lower intensity. Therefore the electron density is locally reduced. This reduction leads to a reduction of the electron plasma frequency ω_{pe} and an increase of the plasma refractive index $n_{nl} = \sqrt{1 - \omega_{pe}^2 / \omega_0^2}$. This mechanism is actually very similar to the stimulated Brillouin scattering, but in the case of filamentation, the ion acoustic wave are transverse to the beam direction of propagation. Figure 2.13 presents a schematic

of the matching condition for the wave vectors. Filamentation is a non-resonant four wave interaction.

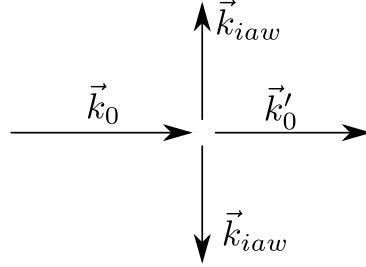


Fig. 2.13 Schematic of the wavenumber matching condition for ponderomotive filamentation. The incident laser radiation \vec{k}_0 is pinched into \vec{k}'_0 by its coupling with the two ion acoustic wave \vec{k}_{iaw} .

While filamentation does not produce any hot electrons by itself, it plays a major role in ICF implosion, by creating regions of higher intensity, and significantly degrading the symmetry of irradiation and therefore the symmetry of ablation pressure. The intensity in these regions can be over the threshold for parametric instabilities, even if the average intensity on target is below threshold. Indeed, the intensity threshold for ponderomotive filamentation is very low (with plasma parameter relevant to ICF, $I_{th} \simeq 5 \times 10^{13} \text{ W/cm}^2$ [54]) Also, the density gradients created by filamentation can be steeper than the average gradients in the plasma, which can lead to higher growth rate for parametric instabilities.

2.3.5 Stimulated Raman scattering

The stimulated Raman scattering [43, 47, 55] is a three waves parametric instability in which the energy of the incident laser radiation is transferred to a scattered electromagnetic wave and an electron plasma wave. This mechanism is very similar to stimulated Brillouin scattering. The only difference is that the ion acoustic wave is replaced by a electron plasma wave. The matching conditions then writes

$$\omega_0 = \omega_{sc} + \omega_{epw}, \quad (2.35)$$

$$\vec{k}_0 = \vec{k}_{sc} + \vec{k}_{epw}, \quad (2.36)$$

where the subscript epw refer to the electron plasma wave. This electron plasma wave has to satisfy its own dispersion relation $\omega_{epw}^2 \simeq \omega_{pe}^2 = n_e e^2 / m_e \epsilon_0$ for any value of its wave number \vec{k}_{epw} (neglecting thermal effects). Therefore, the scattered wave has a frequency

$\omega_{sc} \simeq \omega_0 - \omega_{pe}$. In order to be able to propagate in the plasma, the frequency of the scattered wave has to be larger than the electron plasma frequency $\omega_{sc} > \omega_{pe}$. Hence the instability can only exist if $\omega_0 > 2\omega_p$, which rewrites in term of densities as $n_e < n_c/4$. Stimulated Raman scattering can only occur at densities lower than the quarter critical density.

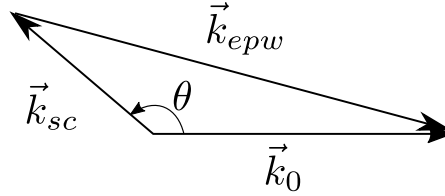


Fig. 2.14 Schematic of the wavenumber matching condition for stimulated Raman scattering.

Figure 2.14 presents the wave-vector matching condition for SRS. For given plasma density n_e and incident laser frequency ω_0 , the wave-vector conditions and wave dispersion relations allow to determine the wave-number of the electron plasma wave as a function of the angle between the incident and scattered waves, as presented in Figure 2.14. Depending of the angle θ , three directions of scattering can be distinguished: forward scattering for $\theta \simeq 0$, backward scattering for $\theta \simeq \pi$ and side scattering for $\theta \simeq \pi/2$. For the backward and side scattering, the growth rate of the electron plasma wave writes [25]

$$\frac{\gamma}{\omega_0} \simeq \frac{v_{osc}}{4c} \frac{k_{epw}}{k_0} \left(\frac{\omega_{pe}/\omega_0}{1 - \omega_{pe}/\omega_0} \right)^{1/2}, \quad (2.37)$$

where $v_{osc} = eE/m_e\omega_0$ is the quiver velocity of the electrons in the electric field E of the light wave. It appears that the growth rate is maximum for the largest value of k_{epw} , which corresponds to backscattering. Indeed, in the limit $n_e \ll n_c/4$, the wavenumber of the scattered light is $k_{sc} = k_0$ so that the wave number of the backscattered electron plasma wave is $k_{epw} = 2k_0$. On the other hand, the wavenumber of the sidescattered wave at $\theta = \pi/2$ is $k_{epw} = \sqrt{2}k_0$. Therefore, the largest growth rate is obtained for backscattering. The wavenumber of the backscattered wave is given by

$$\frac{k_{epw}}{k_0} = 1 + \left(1 - 2 \frac{\omega_{pe}}{\omega_0} \right)^{1/2}. \quad (2.38)$$

In the limit $n_e \ll n_c/4$, the growth rate writes in term of densities

$$\frac{\gamma}{\omega_0} \simeq \frac{v_{osc}}{2c} \left(\frac{n_e}{n_c} \right)^{1/4}. \quad (2.39)$$

In the limit $n_e \simeq n_c/4$, it writes

$$\frac{\gamma}{\omega_0} \simeq \frac{v_{osc}}{4c}. \quad (2.40)$$

The forward scattering is only significant at very low density, where $n_e \ll n_c/4$. Its growth rate is smaller than the backward scattering and, in this limit, it writes

$$\frac{\gamma}{\omega_0} \simeq \frac{v_{osc}}{2\sqrt{2}c} \frac{n_e}{n_c}. \quad (2.41)$$

Additionally, the condition of development of stimulated Raman scattering strongly depends on the damping of electron plasma waves. While the collisional damping remains low in the sub quarter critical plasma, this is not the case for Landau damping. Figure 2.15 presents the growth rate of backward stimulated Raman scattering (SRS) and stimulated Brillouin scattering (SBS) as a function of the plasma density in the range $n_c < n_c/4$. The collisional and Landau damping rate of the SRS are also represented. It shows that the Landau damping will suppress stimulated Raman scattering everywhere except at the vicinity of the quarter critical density. From the competitive interplay between SRS and SBS, the SBS should dominate everywhere with the exception of the quarter critical point [56].

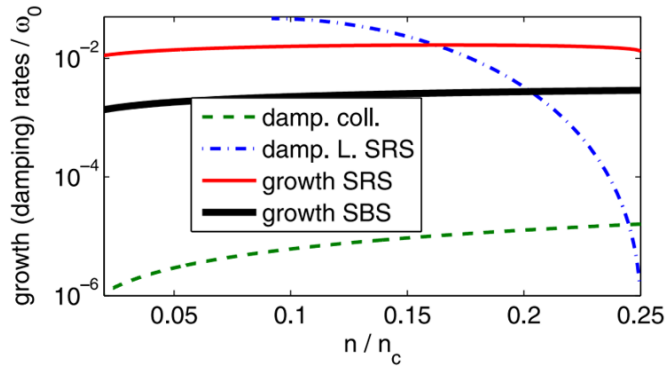


Fig. 2.15 Growth rate for Stimulated Brillouin scattering (SBS) and stimulated Raman scattering (SRS) normalized to the frequency of the incident laser wave ω_0 as a function of the plasma density normalized to the critical density n_c . The collisional damping rate (damp. coll.) and Landau damping (damp. L.) are also included [56].

The electron plasma wave, pumped by backward stimulated Raman scattering close to the quarter critical density, is damped through the non-linear mechanisms described in section 2.2.4. This damping leads to the generation of a population of hot electron emitted mostly in the direction of the plasma wave, and therefore, in the direction of the laser beam. The determination of the parameters of this distribution (its temperature, number of particles and cone of emittance) is very complex. Yet, empirical formulations based on simulations and experiments [29, 57–59] can be found. Using these formulations, the hot electron temperature

T_h and conversion efficiency η_h (the ratio of the energy carried by the hot electron over the incident laser energy) are

$$T_h = 34.3 + 1.5 T_e \text{ keV}, \quad (2.42)$$

$$\eta_h = 0.125 \left[1 - \exp \left(- (I/I_{th})^{1/3} - 1 \right) \right], \quad (2.43)$$

where T_e and I are the plasma electron temperature in keV and laser intensity in 10^{15} W/cm² at the quarter critical density, respectively. I_{th} is intensity threshold of the stimulated Raman scattering given by [60–62]

$$I_{th} = \frac{99.5}{L_n^{4/3} \lambda^{2/3}} \times 10^{15} \text{ W/cm}^2, \quad (2.44)$$

where $L_n = n_e / (\partial n_e / \partial x)$ is the density gradient length at the quarter critical density in μm and λ the vacuum wavelength of the incident laser light in μm . Typical value of these parameters in shock ignition implosions are $I = 5 \times 10^{15}$ W/cm², $\lambda = 0.351 \mu\text{m}$, $T_e = 2$ keV and $L_n = 50 \mu\text{m}$. With these parameters, the intensity threshold is $I_{th} \simeq 10^{15}$ W/cm² such that the hot electron temperature and conversion efficiency are $T_h \simeq 37$ keV and $\eta_h \simeq 12\%$.

2.3.6 Two-plasmon decay

Two-plasmon decay [62–65] is a three waves parametric instability in which the incident laser light decays into two plasma waves. The frequency ω and wave-vector \vec{k} matching conditions for this instability write

$$\omega_0 = \omega_1 + \omega_2, \quad (2.45)$$

$$\vec{k}_0 = \vec{k}_1 + \vec{k}_2, \quad (2.46)$$

where the subscripts 0, 1 and 2 refer to the incident laser wave and the two electron plasma waves, respectively. Since the dispersion relation of electron plasma waves gives $\omega_1 \simeq \omega_2 \simeq \omega_{pe}$, the equation (2.45) rewrites $\omega_0 \simeq 2 \omega_{pe}$. The two-plasmon decay instability can only grow where this condition is met, *i.e.* at the quarter critical density $n_e \simeq n_c/4$.

Because the dispersion relation of the electron plasma waves is very flat, a small variation in the plasma wave frequency can result in a large variation of its wavenumber. Therefore, the plasma wave amplified by this instability can have very large wavenumber. The growth rate of the two-plasmon decay instability writes

$$\gamma = \frac{\vec{k}_1 \cdot \vec{v}_{osc}}{4} \left| \frac{k_2^2 - k_1^2}{k_2 k_1} \right| \quad (2.47)$$

where \vec{v}_{osc} is the maximum velocity of the electrons in the field of the laser.

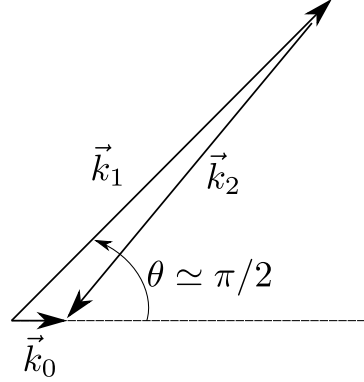


Fig. 2.16 Schematic of the wavenumber matching condition for two-plasmon decay in the limit of large wavenumber for the electron plasma waves.

Representing the wave vector of the largest plasma wave through its components parallel k_{\parallel} and perpendicular k_{\perp} to the incident light wave vector, the condition for the maximum growth rate can be found. First, it appears that the growth is maximized when the wave-vectors of the plasma waves lie in the plane $(\vec{k}_0, \vec{v}_{osc})$. In this plane, the instability growth rate is maximum where the condition $k_{\perp}^2 = k_{\parallel} (k_{\parallel} - k_0)$ is satisfied. The limit $k_{\perp} \rightarrow 0$ gives the shortest wave vector, $k_{\parallel} \simeq k_0$. In this case, the plasma wave is emitted in the direction of the laser. On the other hand, for very large wavenumbers $k_{\perp} \rightarrow \infty$, $k_{\parallel} \simeq k_{\perp}$, which corresponds to an emission with a $\pi/4$ angle with respect to the laser wave vector, as presented in Figure 2.16. Qualitatively the plasma waves excited by two-plasmon decay are expected to be emitted within a $\pm\pi/4$ aperture. Also, for large wave vector \vec{k}_1 , \vec{k}_0 becomes negligible so that $\vec{k}_2 = -\vec{k}_1$. Therefore, electron plasma waves are also generated backward, at $\pm 3\pi/4$ angles.

When the condition of maximum growth rate is satisfied, equation (2.47) rewrites

$$\frac{\gamma}{\omega_0} = \frac{v_{osc}}{4c}. \quad (2.48)$$

The maximum growth rate of the two-plasmon decay is identical to the one of stimulated Raman scattering at the quarter critical density.

Similarly to stimulated Raman scattering, the plasma waves excited by the two-plasmon decay instability are damped through non-linear mechanisms described in section 2.2.4. This damping leads to the production of hot electrons which are emitted in a $\pm\pi/4$ aperture,

which is much more divergent than the hot electrons from stimulated Raman scattering. Also, hot electrons are produced both forward and backward.

The overall picture of hot electron acceleration by two plasmon decay is very complex due to the effect of multibeam overlapping, pump depletion by stimulated Raman scattering, and other non-linear mechanisms. Again, empirical formula derived from simulations and experiments [66–68] are used in order to link the plasma and laser parameters to the hot electrons temperature T_h and conversion efficiency η_h

$$T_h = 15.5 + 17.7I/I_{th} \text{ keV}, \quad (2.49)$$

$$\eta_h = 0.026 \left[1 - \exp\left(-\sqrt{I/I_{th} - 1}\right) \right], \quad (2.50)$$

where I is the laser intensity in unit of 10^{15} W/cm^2 at the quarter critical density. I_{th} is intensity threshold of the two plasmon decay given by

$$I_{th} = 8.2 \frac{T_e}{L_n \lambda} \times 10^{15} \text{ W/cm}^2, \quad (2.51)$$

where T_e and $L_n = n_e / (\partial n_e / \partial x)$ are the electron temperature in keV and the density gradient length at the quarter critical density in μm , respectively. λ is the vacuum wavelength of the incident laser light in μm . With typical value of these parameters as presented in the previous section (relevant to shock ignition), the threshold intensity is $I_{th} \simeq 10^{15} \text{ W/cm}^2$ so that the hot electron temperature and conversion efficiency are $T_h \simeq 100 \text{ keV}$ and $\eta_h \simeq 2.2\%$. Only half of this amount of hot electrons are harmful for the implosion since the other half, in first approximation, is emitted backward.

2.4 Conclusion

In this chapter, a global description of the laser plasma interaction mechanisms in regime relevant for shock ignition has been given.

For short laser wavelength and moderate intensity, the main mechanism of absorption of laser light is collisional absorption (inverse Bremsstrahlung). This mechanism of absorption is mostly located at the critical density. It results in a quasi-stationary ablation profile characterized by four zones: the plasma corona, the conduction zone, the shock target and the unperturbed target. The scaling laws for the estimation of the ablation pressure, temperature at the critical density and ablated mass rate have been derived.

At shock ignition intensities, additional mechanisms have to be taken into account. They arise from collective effects which involve electron plasma waves and ion acoustic waves. The dispersion relations and damping mechanisms of these waves have been discussed. The non-linear damping of electron plasma wave is shown to potentially accelerate electrons, leading to the creation of a population of hot electrons.

A qualitative description of these coupling mechanisms of the laser light with plasma waves in the corona has been given. At the critical density, resonant absorption and parametric decay lead to the production of hot electrons with moderate temperatures, not harmful for implosions. At density lower than the critical density, stimulated Brillouin scattering and filamentation perturb the propagation of the laser. Stimulated Brillouin scattering may reflect a part of the laser energy and filamentation could lead to the apparition of local over-intensities. Finally, if laser intensity thresholds are reached, two-plasmon decay (at the quarter critical density) and the stimulated Raman scattering (below the quarter critical density) can produce hot electrons which can be detrimental to shock ignition implosions. Phenomenological laws for the temperature and conversion efficiency of these hot electrons have been given.

Chapter 3

Hydrodynamic and shock waves

Under the effect of the ablation pressure, a shock forms and propagates inside the target. This shock will interact with discontinuities, such as other shocks or contact discontinuities (interface between two materials), leading to the formation of new shocks, contact discontinuities or rarefaction waves. The description of shock propagation in spherical geometry is complex; however a good understanding of the shocks properties in planar geometry allows to understand most of the physical phenomena observed during an implosion.

In this chapter some notions of basic hydrodynamic, rarefaction wave properties and shock waves formation will be presented. Then the interaction of a shock with hydrodynamic discontinuities will be presented.

3.1 Linear hydrodynamic in planar geometry

3.1.1 Conservation laws

Let's consider a planar flow so that the fluid hydrodynamic variables are function of time t and space x only. The hydrodynamic variables of interest are the density ρ , the pressure p and the fluid velocity $u = dx/dt$. The flow is governed by the conservation law of mass, momentum and energy.

Mass conservation describes the fact that the variation of mass of a volume element results from the flow of mass into or out of this element,

$$\frac{\partial \rho}{\partial t} + \frac{\partial}{\partial x}(\rho u) = 0. \quad (3.1)$$

Momentum conservation expresses Newton's equation of motion. Neglecting volumetric forces (such as gravity) and for an ideal fluid, the force acting on a volume element is the pressure gradient so that the conservation law writes

$$\rho \frac{\partial u}{\partial t} + \rho u \frac{\partial u}{\partial x} = -\frac{\partial P}{\partial x}. \quad (3.2)$$

Energy conservation describes the fact that the variation in the total energy of a volume element results from the flux of energy through this element, the work of the pressure force and the energy supplied to the element from external source. Since the total energy per unit mass is the sum of the internal energy ε and the kinetic energy $u^2/2$, the energy conservation law takes the form

$$\frac{\partial}{\partial t} \left(\rho \varepsilon + \frac{\rho u^2}{2} \right) + \frac{\partial}{\partial x} \left[\rho u \left(\varepsilon + \frac{u^2}{2} \right) + Pu \right] = \rho Q, \quad (3.3)$$

where Q is the power generated per unit mass by external sources.

In the one dimensional case, the equations of conservation of mass, momentum and energy form a system of three equations for the four variables ρ , u , P and ε (assuming the external energy source Q is known). This system is actually closed since the thermodynamic properties of the fluid allow to express the internal energy as a function of pressure and density $\varepsilon = \varepsilon(\rho, P)$. For an ideal gas this equation of state is

$$\varepsilon = \frac{P}{(\gamma - 1)\rho}, \quad (3.4)$$

where γ is the isentropic exponent. For a monoatomic gas $\gamma = 5/3$.

In the case where the fluid cannot be described with the ideal gas equation of state, the internal energy is usually given as a function of density and temperature $\varepsilon = \varepsilon(\rho, T)$. Then the equation $P = P(\rho, T)$ must be added so that the system is closed.

3.1.2 Perturbation theory of fluid motion

The behaviour of small disturbances in the fluid hydrodynamic variables can be described using perturbation theory. In this case, the density writes $\rho = \rho_0 + \Delta\rho$, where ρ_0 is the average value of the density, independent of space and time, and $\Delta\rho$ is the perturbation (with $\Delta\rho \ll \rho_0$). The pressure and fluid velocity can be expressed in the same way: $P = P_0 + \Delta P$ and $u = u_0 + \Delta u$. For simplicity the fluid can be considered initially at rest, hence $u_0 = 0$ and $u = \Delta u$.

Using these expressions for the density and fluid velocity, and neglecting the second-order quantities, the mass conservation (3.1) writes

$$\frac{\partial \Delta \rho}{\partial t} + \rho_0 \frac{\partial u}{\partial x} = 0. \quad (3.5)$$

The motion of particles in a sound wave is isentropic, so that a small perturbation in pressure is related to a small change in density by the isentropic derivative $\Delta P / \Delta \rho = (\partial P / \partial \rho)_S$. The conservation of momentum (3.2) can then be expressed as

$$\rho_0 \frac{\partial u}{\partial t} = - \frac{\partial P}{\partial x} = - \left(\frac{\partial P}{\partial \rho} \right)_S \frac{\partial \Delta \rho}{\partial x}. \quad (3.6)$$

Differentiating 3.5 with respect to time and 3.6 with respect to space, the cross derivative $\partial^2 u / \partial t \partial x$ appears in both equations. Subtracting these equations so that the cross derivative simplifies, leads to the wave equation for density

$$\frac{\partial^2 \Delta \rho}{\partial t^2} = c^2 \frac{\partial^2 \Delta \rho}{\partial x^2}, \quad (3.7)$$

where $c = \sqrt{(\partial P / \partial \rho)_S}$ is the sound velocity. The pressure change $\Delta P = c^2 \Delta \rho$ and the fluid velocity change u also satisfy this wave equation. These equations have two families of solutions

$$\Delta \rho = \Delta \rho(x + ct), \quad \Delta P = \Delta P(x + ct), \quad u = u(x + ct), \quad (3.8)$$

and

$$\Delta \rho = \Delta \rho(x - ct), \quad \Delta P = \Delta P(x - ct), \quad u = u(x - ct). \quad (3.9)$$

The first and second solutions correspond to the propagation of the perturbation at sound velocity toward the positive and negative x , respectively. Noticing that $\partial(x \pm ct) / \partial x = \pm(1/c) \partial(x \pm ct) / \partial t$ allows to write the relationship between the fluid velocity change u , the density change $\Delta \rho$ and the pressure change ΔP

$$u = \pm \frac{c}{\rho_0} \Delta \rho = \pm \frac{\Delta P}{\rho_0 c}, \quad \Delta P = c^2 \Delta \rho = \pm \rho_0 c u. \quad (3.10)$$

The general solution to the wave equation for the density and fluid velocity is derived from the particular solution 3.8 and 3.9

$$\Delta \rho = \frac{\rho_0}{c} f_1(x - ct) + \frac{\rho_0}{c} f_2(x + ct), \quad (3.11)$$

$$u = f_1(x - ct) - f_2(x + ct), \quad (3.12)$$

where f_1 and f_2 are determined by the initial distribution of density and velocity

$$f_1 = \frac{1}{2} \left[\frac{c}{\rho_0} \Delta \rho(x, 0) + u(x, 0) \right], \quad (3.13)$$

$$f_2 = \frac{1}{2} \left[\frac{c}{\rho_0} \Delta \rho(x, 0) - u(x, 0) \right]. \quad (3.14)$$

3.1.3 Sound waves

As an example of such motion, Figure 3.1 (left) presents a typical sound wave. At t_0 , the fluid has an initial small perturbation of density and fluid velocity ($\Delta \rho \ll \rho_0$ and $u \ll c$). The amplitude of the perturbations are chosen such that $(c/\rho_0)\Delta \rho(x, 0) = u(x, 0)$, leading to $f_2 = 0$. In this case, only the term with f_1 contributes to the general solution of the wave propagation. This leads to the propagation of the perturbation towards the positive x at sound velocity c . At t_1 the profile of the perturbation is similar but it has moved by a distance $c(t_1 - t_0)$. A useful way to visualize this phenomenon is to represent the propagation of the front and rear end of the perturbations in the (x, t) plan (Figure 3.1, right). The area between the two parallel lines propagating at c correspond to the perturbed fluid.

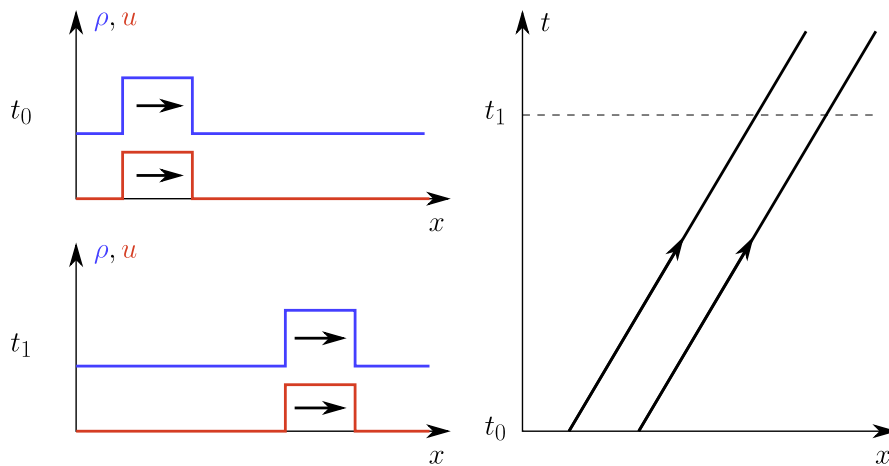


Fig. 3.1 Sound wave propagating toward the right direction ($f_2 = 0$).

Another example of sound wave propagation is presented in Figure 3.2. In this case, at t_0 , only the density is perturbed. Since $u(x, 0) = 0$, $f_1 = f_2$ and the general solution leads to the propagation of two sound waves of same amplitude, going in opposite direction. The perturbation at t_0 can be seen as the superposition of two sound waves that, for $t < t_0$, were propagating towards each other. The profiles of the density and fluid velocity perturbations do not change when they cross. In general, the crossing of sound waves do not change their profiles, as long as the overlapped amplitude of the perturbations stays small enough so that the perturbation theory is valid.

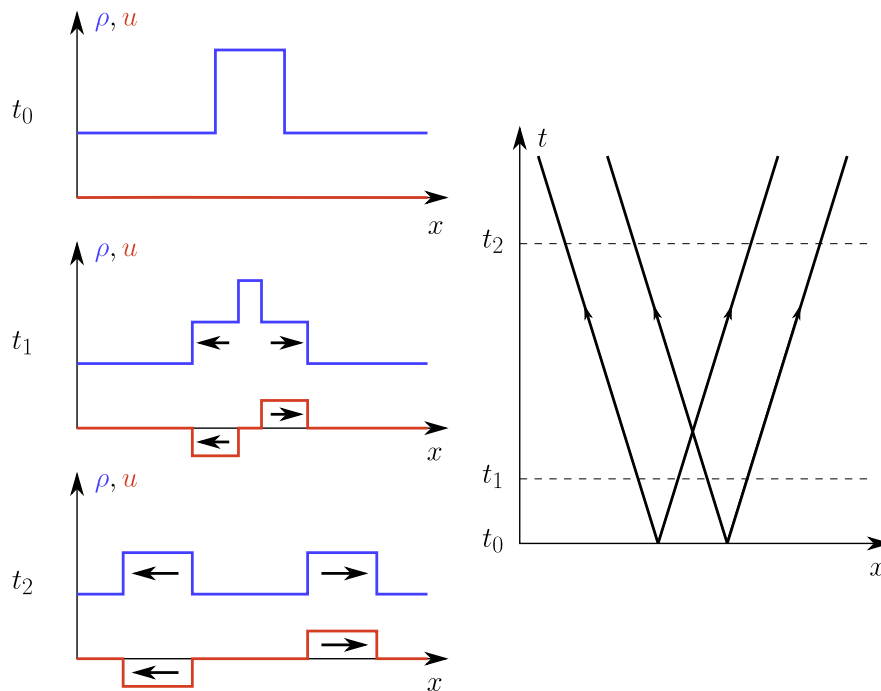


Fig. 3.2 Two sound waves propagating in opposite directions from an initial perturbation of density and pressure only (no initial fluid velocity, $f_1 = f_2$).

3.1.4 Compression wave created by a piston

The simplest way to generate a sound wave is by the work of a piston (Figure 3.3). The piston is a rigid wall that instantly starts moving at the velocity $u > 0$ at t_0 . The fluid in contact with it will move at the same velocity, and following 3.11, a perturbation of density and pressure will be created.

The front of this perturbation will propagate at sound velocity c inside the unperturbed fluid, compressing it ($\Delta\rho > 0$). If the piston moves at constant velocity, the interface between the piston and the fluid is in equilibrium so that no other perturbation is created. On the other hand, if the piston instantly stop moving at t_1 , the fluid velocity at the interface piston-fluid is fixed to $u = 0$. This leads to a new perturbation that will propagate in the perturbed fluid at the velocity $c - u \simeq c$. This results in the propagation of a sound wave of length $(t_1 - t_0)c$ similarly to Figure 3.1.

3.1.5 Rarefaction waves

Instead of moving forward, if the piston is moving backward, so that $u < 0$, a rarefaction wave is generated, meaning that the perturbed fluid has a density and a pressure lower than

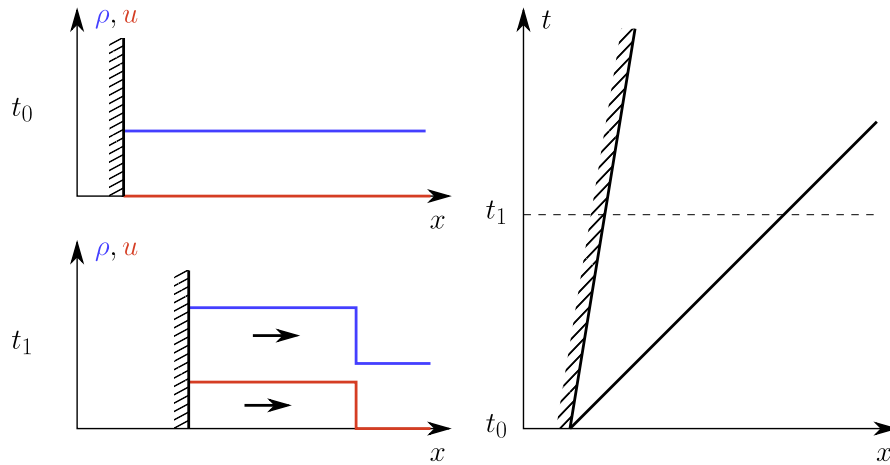


Fig. 3.3 Piston compression at low velocity.

the initial state ($\Delta\rho < 0$, $\Delta P < 0$). Like the compression wave, the front of this wave move inside the unperturbed fluid at the sound velocity c .

In the case where the piston velocity $|u|$ increases with time by a sequence of instantaneous accelerations, the variation of sound velocity with respect to the density (and pressure) has to be taken in consideration. Let's consider the fluid initially at the density ρ_0 , fluid velocity $u_0 = 0$, and with sound velocity c_0 . At t_0 , the piston is instantaneously accelerated to the velocity $u = -u_1$, with $u_1 \ll c_0$. A perturbed region is created between the front of the rarefaction wave, moving at c_0 , and the piston, moving at u_1 . In this region, the density is $\rho_1 = \rho_0 + \Delta\rho_1$ and the sound velocity is c_1 . At the time t_1 , the piston is again instantaneously accelerated to the velocity $u = -u_2$ with $u_2 > u_1$ and $u_2 \ll c_1$. A new rarefaction wave is created in the previously perturbed fluid with a front propagating at $c_1 - u_1$. In the linear theory, all fluid velocities are small compared to the sound velocity and the sound velocity is constant, independently of the fluid density or pressure. A more precise description of the sound velocity calculation shows that for any value of ρ and P , the equation of state verifies the relations

$$\left(\frac{\partial P}{\partial \rho}\right)_s > 0, \quad \left(\frac{\partial^2 P}{\partial \rho^2}\right)_s > 0. \quad (3.15)$$

These relations are true for ideal gases and for most of the materials, in the absence of phase transition. The first one corresponds to a condition of positive sound velocity $c > 0$. The second one shows that a decrease in density lead to a decrease in sound velocity $(\partial c^2 / \partial \rho)_s > 0$. Therefore, $c_1 < c_0$ and the distance between the two rarefaction wave fronts will increase along time ($(c_1 - u_1) < c_0$ since $u_1 > 0$). Considering only two wave fronts, this increase can be neglected, but if the piston is put in motion by a series of n instantaneous

accelerations, a fan of rarefaction waves is created as presented in Figure 3.4. The first rarefaction wave propagates at c_0 while the last one propagates at $c_{n-1} - u_{n-1} \simeq c_n - u_n$, where c_n is the sound velocity of the fluid behind the last rarefaction wave and u_n is the final velocity of the piston. This velocity does not have to be small compared to the initial sound velocity c_0 (it can even be larger than it).

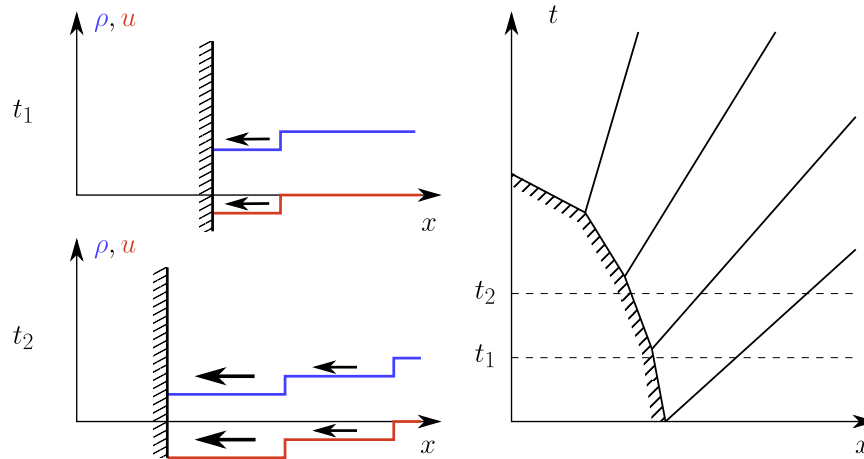


Fig. 3.4 Fan of rarefaction waves from a succession of small instant accelerations of a piston.

A specific solution to this example of sequence of rarefaction waves arises where the delay between the successive accelerations of the piston tends to zero. This corresponds to the instant acceleration of the piston to a velocity u_1 , not small compared to c_0 . In this case, all the rarefaction waves are issued from the initial position of the piston, creating the so called centered rarefaction wave (Figure 3.5). This wave is characterized by three lines: the head of the wave, its tail and the piston path. The head of the wave propagates in the unperturbed fluid at the sound velocity c_0 . Between the head and the tail, there is a transition region where the hydrodynamic variables decrease continuously. In the specific case of an ideal gas, the fluid velocity in the transition region has a linear profile. The tail of the wave propagates at the velocity $c_1 - u_1$, where c_1 is the sound velocity of the perturbed region between the tail and the piston.

3.1.6 Compression waves

Similarly to the rarefaction wave, the acceleration of the piston toward the positive x though a succession of instantaneous small accelerations can be considered. Each individual acceleration can be described using perturbation theory with a sound velocity function of the density. The first acceleration of the piston to the velocity u_1 will result in a sound wave with a front propagating in the unperturbed fluid at c_0 . Since $u_1 > 0$, the fluid behind the wave front is at

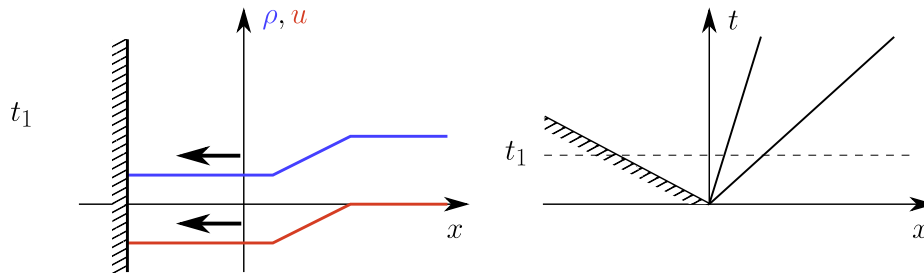


Fig. 3.5 Centered rarefaction wave.

the density $\rho_1 > \rho_0$, with the corresponding sound velocity $c_1 > c_0$. A second instantaneous acceleration of the piston to the velocity $u_2 > u_1$ will create a second sound wave, with its front propagating in the previously perturbed fluid at the velocity $c_1 + u_1 > c_0$. Since the velocity of the second wave front is higher than the first one, the distance separating them decreases with time and, at some point, the two waves will merge. This merging results in a new perturbation with amplitude ρ_2 propagating in the unperturbed fluid at the density ρ_0 . If the perturbation theory is still valid ($\rho_2 - \rho_0 \ll \rho_0$), this creates a sound wave with its front propagating at c_0 .

If the piston is then accelerated to higher velocity through many small accelerations, each sound wave created by the individual accelerations will catch up with the ones in front of it. After some time they will merge and result in a density jump not small compared to the initial density as represented in Figure 3.6. This corresponds to the formation of a shock, for which, the perturbation theory cannot be used. The acceleration of a piston to a high velocity, either continuously or through a succession of small accelerations, will always result in the formation of a shock inside the fluid. Moreover, the instantaneous acceleration of the piston to such velocity leads to the creation of a shock at the piston surface, showing the impossibility of the existence of centered compression wave.

3.2 Shocks

3.2.1 Conservation laws

A shock wave is a discontinuity of the hydrodynamic variables (density, pressure, fluid velocity ...) that propagates through a fluid. The differential conservation laws presented in section 3.1.1 consider a continuous variation of these variables and they cannot be used to describe such discontinuity. These conservation laws have to be rewritten in order to describe the shock dynamics.

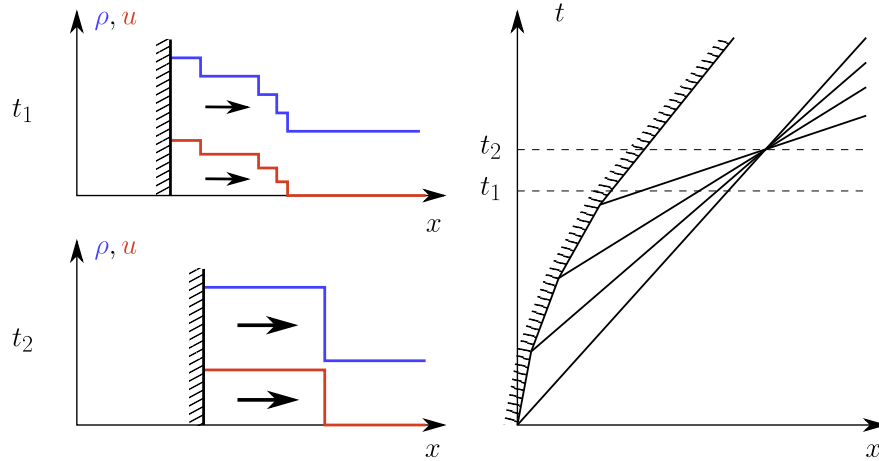


Fig. 3.6 Compression wave.

Let's consider a shock wave propagating at velocity D in an unperturbed fluid with the density ρ_0 , the pressure P_0 , the internal energy per unit mass ε_0 and the fluid velocity is u_0 . The hydrodynamic variables behind the shock front are ρ_1 , P_1 , ε_1 and u_1 . In the reference frame of shock front, the upstream velocity (in the unperturbed fluid) is $u_0 - D$ and the downstream velocity (in the shocked fluid) is $u_1 - D$. From the upstream fluid, the mass flow going in the shock front through a surface area S is $\dot{m}_0 = \rho_0(u_0 - D)S$. In the downstream fluid, the mass flow getting out of the shock front is $\dot{m}_1 = \rho_1(u_1 - D)S$. Due to the conservation of mass $\dot{m}_1 = \dot{m}_0$, which rewrite as

$$\rho_0(u_0 - D) = \rho_1(u_1 - D). \quad (3.16)$$

The momentums of the upstream and downstream mass flow are $\dot{m}_0(u_0 - D)$ and $\dot{m}_1(u_1 - D)$, respectively. According to Newton's law, this variation of momentum is due to the force acting on the fluid, which in this case in the pressure difference between the upstream and downstream fluid $S(P_1 - P_0)$. Separating the upstream quantity from the downstream one, the conservation of momentum writes

$$P_0 + \rho_0(u_0 - D)^2 = P_1 + \rho_1(u_1 - D)^2. \quad (3.17)$$

The total energy carried by the upstream mass flow is the sum of the kinetic energy $\dot{m}_0(u_0 - D)^2/2$ and the internal energy $\dot{m}_0\varepsilon_0$. Similarly, the downstream total energy flow is $\dot{m}_1(u_1 - D)^2/2 + \dot{m}_1\varepsilon_1$. This change in total energy is due to the difference in the work of pressure forces between the upstream and downstream fluids. This work per unit time is $-[P_1(u_1 - D)S - P_0(u_0 - D)S]$. Using 3.16, the conservation of energy writes

$$\frac{P_1}{\rho_1} + \frac{(u_1 - D)^2}{2} + \varepsilon_1 = \frac{P_0}{\rho_0} + \frac{(u_0 - D)^2}{2} + \varepsilon_0. \quad (3.18)$$

These equations of conservation of mass, momentum and energy through a shock front are called the Rankine-Hugoniot equations.

Using 3.16 and 3.17 into 3.18 allows to write

$$\varepsilon_1 - \varepsilon_0 = \frac{1}{2}(P_1 + P_0) \left(\frac{1}{\rho_0} - \frac{1}{\rho_1} \right). \quad (3.19)$$

This expression is especially useful since it does not include the fluid and shock velocities.

3.2.2 Hugoniot curves

For a fluid in a known hydrodynamic state, the Hugoniot curve is the set of all combinations of downstream variables, and shock velocity, that verify the Rankine-Hugoniot equations and the equation of state of the fluid. Indeed, with the upstream variables ρ_0 , P_0 , ε_0 and u_0 known, the three Rankine-Hugoniot equations and the fluid equation of state form a system of four equations for five unknown variables ρ_1 , P_1 , ε_1 , u_1 and D . Therefore, there is an infinite number of solutions for this system. But if one variable is fixed, all the others are determined.

In the case of an ideal gas, the equation of state is given by 3.4. The downstream variables and the shock velocity can then be expressed as a function of the upstream variables and one downstream variables alone, the pressure P_1 for example:

$$\frac{\rho_1}{\rho_0} = \frac{(\gamma + 1)P_1 + (\gamma - 1)P_0}{(\gamma - 1)P_1 + (\gamma + 1)P_0}, \quad (3.20)$$

$$\frac{\varepsilon_1}{\varepsilon_0} = \frac{P_1}{P_0} \times \frac{\rho_0}{\rho_1} = \frac{P_1}{P_0} \times \frac{(\gamma - 1)P_1 + (\gamma + 1)P_0}{(\gamma + 1)P_1 + (\gamma - 1)P_0}, \quad (3.21)$$

$$D = u_0 \pm \sqrt{\frac{(\gamma + 1)P_1 + (\gamma - 1)P_0}{2\rho_0}}, \quad (3.22)$$

$$u_1 = u_0 \pm \sqrt{\frac{2(P_1 - P_0)^2}{\rho_0[(\gamma + 1)P_1 + (\gamma - 1)P_0]}}. \quad (3.23)$$

The \pm sign in the expression of the shock velocity D and of the downstream fluid velocity u_1 depends if the shock propagates in the same direction as the upstream fluid velocity (case with the sign $+$) or in the opposite direction (in this case the sign is $-$). These Hugoniot

curves are presented in figure 3.7 for a fluid initially at the density $\rho_0 = 1 \text{ g/cm}^3$, pressure $P_0 = 1 \text{ bar}$, fluid velocity $u_0 = 0 \text{ m/s}$ and with a polytropic coefficient $\gamma = 5/3$.

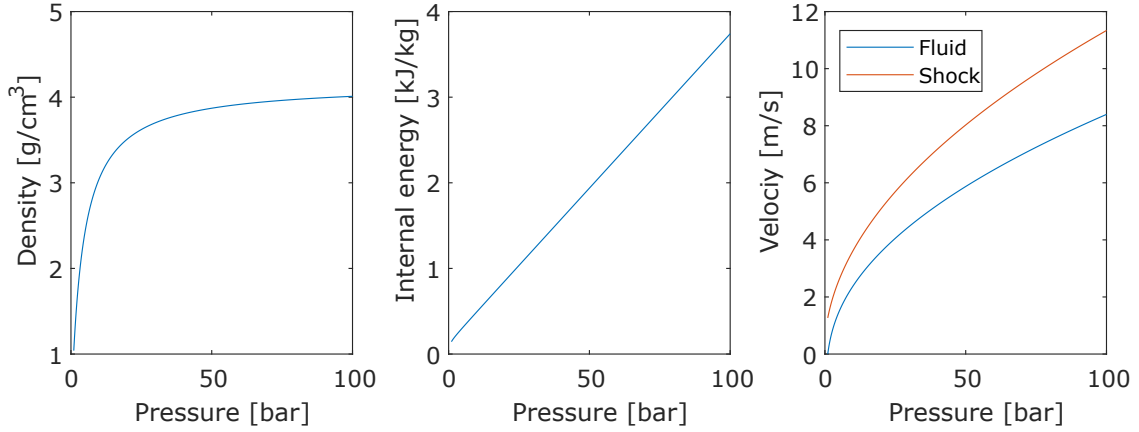


Fig. 3.7 Ideal gas Hugoniot curves ($\gamma = 5/3$), the fluid initial conditions are $\rho_0 = 1 \text{ g/cm}^3$, $P_0 = 1 \text{ bar}$ and $u_0 = 0 \text{ m/s}$.

These curves show that at low shock strength P_1/P_0 the shock efficiently compresses the fluid, resulting in a large increase of its density. At high shock strength, the density tends toward an asymptotic value and an increase in shock strength only results in an increase of the fluid internal energy. This asymptotic behaviour of the Hugoniot curve can be made explicit by considering the limit $P_1 \gg P_0$. In this case, and with $\gamma = 5/3$, equations 3.20, 3.21, 3.22 and 3.23 write as

$$\frac{\rho_1}{\rho_0} = \frac{\gamma+1}{\gamma-1} = 4, \quad (3.24)$$

$$\frac{\varepsilon_1}{\varepsilon_0} = \frac{\gamma-1}{\gamma+1} \times \frac{P_1}{P_0} = \frac{1}{4} \times \frac{P_1}{P_0}, \quad (3.25)$$

$$D = u_0 \pm \sqrt{\frac{(\gamma+1)P_1}{2\rho_0}} = u_0 \pm \sqrt{\frac{4}{3} \times \frac{P_1}{\rho_0}}, \quad (3.26)$$

$$u_1 = u_0 \pm \sqrt{\frac{2P_1}{(\gamma+1)\rho_0}} = u_0 \pm \sqrt{\frac{3}{4} \times \frac{P_1}{\rho_0}}. \quad (3.27)$$

Some properties of shock waves can be highlighted from these expressions. The comparison of the shock velocity in the reference frame of the upstream fluid $D - u_0$ with the sound velocity of the upstream fluid $c_{s0} = \sqrt{\gamma P_0/\rho_0}$ shows that a shock is always supersonic with respect to the fluid in which it propagates. Therefore, no sound wave can emerge from the

shock front and the shock will always catch up the sound waves co-propagating in upstream fluid. On the other hand, the comparison of the shock velocity in the frame of downstream fluid $D - u_1$ with its sound velocity $c_{s1} = \sqrt{\gamma P_1 / \rho_1}$ shows that the shock is always subsonic of the downstream fluid. Therefore, any sound wave co-propagating in the shocked fluid will catch up with the shock front. This is also true for the head of a rarefaction wave. Such case is presented in Figure 3.8. When the head of the rarefaction wave has reached the shock front, the density and fluid velocity profiles have a triangular shape. After that, the shock continues to propagate but its strength and velocity decrease along time. Such shock is called a blast wave.

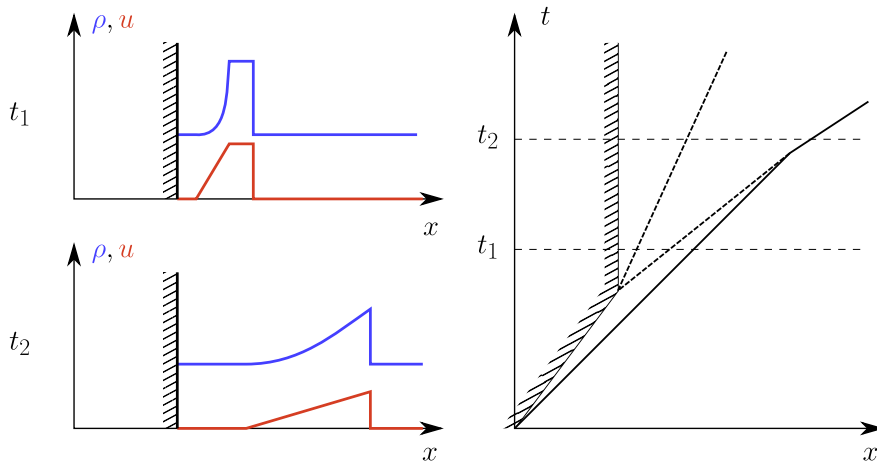


Fig. 3.8 Blast wave.

Another property of shocks is that they increase the fluid entropy. For an ideal gas with constant specific heat, the difference in entropy between the downstream fluid and the upstream fluid writes

$$S_1 - S_0 = c_v \ln \left(\frac{P_1}{\rho_1^\gamma} \times \frac{\rho_0^\gamma}{P_0} \right). \quad (3.28)$$

As seen before, for $P_1 \gg P_0$ the ratio ρ_1 / ρ_0 tends towards a constant value, and therefore the entropy difference tends toward $S_1 - S_0 \propto \ln(P_1 / P_0)$. This increase in the fluid entropy shows that shocks are an irreversible process.

The shocked fluid cannot come back to its initial state. This can be illustrated by considering the example of the blast wave. The fluid, initially at the density ρ_0 and the pressure P_0 , is shocked to a pressure $P_1 \gg P_0$. Then, a rarefaction wave decreases the pressure of the shocked fluid to $P_2 = P_0$. Since the rarefaction wave is isentropic, $P_2 / \rho_2^\gamma = P_1 / \rho_1^\gamma$. The density and internal energy of the fluid behind the rarefaction wave are

$$\frac{\rho_2}{\rho_0} = \left(\frac{P_0}{P_1}\right)^{1/\gamma} \left(\frac{\gamma+1}{\gamma-1}\right), \quad (3.29)$$

$$\frac{\varepsilon_2}{\varepsilon_0} = \left(\frac{P_1}{P_0}\right)^{1/\gamma} \left(\frac{\gamma-1}{\gamma+1}\right). \quad (3.30)$$

Even though the initial and final pressure are the same, the final density is lower than the initial one while the final internal energy is higher. The Figure 3.9 illustrates it. Initially the fluid is at the density $\rho_0 = 1.0 \text{ g/cm}^3$ and the pressure $P_0 = 1 \text{ Mbar}$. The corresponding internal energy, given by the ideal gas equation of state, is $\varepsilon_0 = 150 \text{ MJ/kg}$ ($\gamma = 5/3$). The fluid is compressed by a shock with a pressure $P_1 = 10 \text{ Mbar}$. The density and internal energy of the shocked fluid are given by the Hugoniot curve (in blue): $\rho_1 = 2.9 \text{ g/cm}^3$, $\varepsilon_1 = 510 \text{ MJ/kg}$. Then the fluid has an isentropic release due to the rarefaction wave (in red), bringing the pressure back to 1 Mbar. The final density and internal energy are: $\rho_2 = 0.7 \text{ g/cm}^3$, $\varepsilon_2 = 200 \text{ MJ/kg}$.

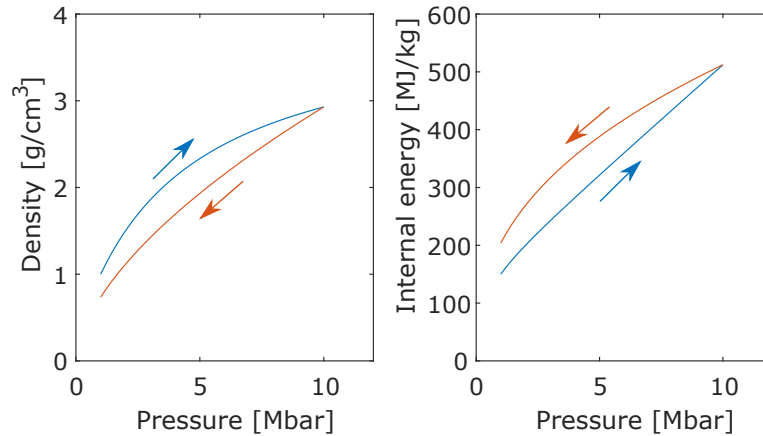


Fig. 3.9 Thermodynamic path of a fluid in the (P, ρ) and (P, ε) plans. First, the fluid is shock (Hugoniot curve in blue). Then it is released by a rarefaction wave back to its initial pressure (isentropic release in red).

3.2.3 Set of accessible states and reshock

As a general consideration, when the amplitudes of perturbations are too large to be described by sound waves, the only waves that can propagate in a fluid are either rarefaction waves or shock waves. Each of them has the possibility to either propagate forward (toward the positive x) or backward (toward the negative x). There is therefore, four types of waves that can propagate in a fluid.

For a fluid in a given hydrodynamic state, and for each type of wave, there is a set of combination of hydrodynamic variables that verifies the equations describing this wave. For the shocks, this set is the Hugoniot curve. The \pm sign in equations 3.22 and 3.23 correspond to the forward or backward wave.

For the rarefaction waves, this set is given by the isentropic states of the fluid. For an ideal gas, these states verify the condition $P/\rho^\gamma = \text{const}$. Similarly to the Hugoniot curve, the downstream density ρ_1 and internal energy ε_1 can be expressed as a function of the downstream pressure P_1 :

$$\frac{\rho_1}{\rho_0} = \left(\frac{P_1}{P_0} \right)^{\frac{1}{\gamma}} \quad (3.31)$$

$$\frac{\varepsilon_1}{\varepsilon_0} = \frac{P_1}{P_0} \times \frac{\rho_1}{\rho_0} = \left(\frac{P_1}{P_0} \right)^{1-\frac{1}{\gamma}} \quad (3.32)$$

A more complete description of the rarefaction wave [69] shows that within the isentropic flow of a rarefaction wave: $u \pm \frac{2}{\gamma-1}c = \text{const}$. The fluid velocity behind the wave then writes:

$$u_1 = u_0 \pm \frac{2}{\gamma-1}(c_1 - c_0) \quad (3.33)$$

with $c = \sqrt{\gamma P/\rho}$. Figure 3.10 presents these four curves in the (u, P) plan for a fluid initially at $\rho_0 = 1 \text{ g/cm}^3$, $P_0 = 10 \text{ Mbar}$, $u_0 = 10 \text{ km/s}$ and with $\gamma = 5/3$. After the propagation of a shock or a rarefaction wave, the final state of a fluid with these initial conditions will always be on one of these curves. From this new hydrodynamic state, four new curves describe the sets of accessible states though a shock or a rarefaction wave transformation.

As an example, the final state resulting from a succession of shocks is determined by considering a succession of hydrodynamic state and Hugoniot curves as presented in Figure 3.11. Initially the fluid is in the state represented by the blue dot ($\rho_0 = 1 \text{ g/cm}^3$, $P_0 = 2 \text{ Mbar}$), with the associated forward Hugoniot curve in blue. A shock with a pressure of 4 Mbar is driven in this fluid resulting in the hydrodynamic state represented by the red dot. The Hugoniot curve of this new state (in red) is less steep which allows to reach higher compression at lower pressure. A third and fourth shock at pressure of 8 and 16 Mbar, respectively, finally bring the fluid to its final state at a density of 3.38 g/cm^3 . Such succession of shocks allows to approach an isentropic compression (black dashed curve).

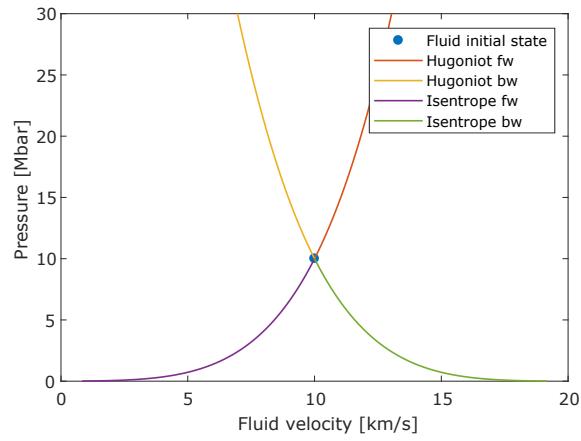


Fig. 3.10 Hugoniot and isentropic curves in the (u, P) plan, for the forward (fw) and backward (bw) waves and from a given hydrodynamic state: $\rho_0 = 1 \text{ g/cm}^3$, $P_0 = 10 \text{ Mbar}$, $u_0 = 10 \text{ km/s}$, $\gamma = 5/3$.

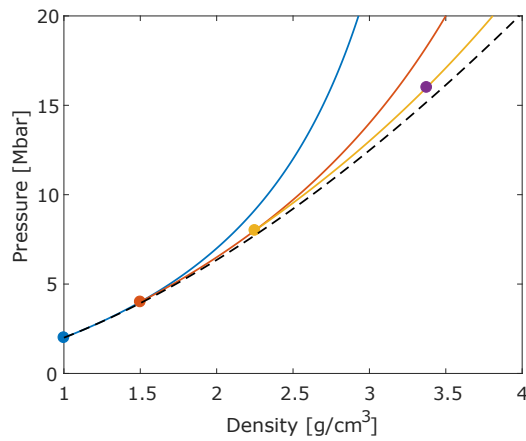


Fig. 3.11 Path in the (ρ, P) plan of a fluid initially at $\rho_0 = 1 \text{ g/cm}^3$, $P_0 = 2 \text{ Mbar}$, $u_0 = 0 \text{ km/s}$, $\gamma = 5/3$ and compressed by a succession of shock at 4, 8 and 16 Mbar. The black dashed curve correspond to an isentropic compression.

3.3 Interaction of a shock with a discontinuity

As seen in section 3.1.3, when sound waves cross each other, their hydrodynamic profiles do not change. This is not true for shocks and a more detailed description is needed in order to understand their behaviors when they cross discontinuities such as other shocks or contact discontinuities.

3.3.1 Shock at contact discontinuity

In a fluid described by an ideal gas equation of state, a contact discontinuity is a surface separating two zones of different density, temperature and internal energy. By definition, such surface is at mechanical equilibrium, meaning that there is continuity of pressure and fluid velocity across it.

When a shock reaches such discontinuity, it will result in two waves: a reflected wave propagating backward in the previously shocked fluid and a transmitted shock propagating forward in the second fluid. Depending of the density jump at the contact discontinuity, the reflected wave can be a shock or a rarefaction wave. Considering two fluids a and b , initially at the densities ρ_{a_0} and ρ_{b_0} , respectively, if $\rho_{a_0} < \rho_{b_0}$ the reflected wave is a shock and if $\rho_{a_0} > \rho_{b_0}$ the reflected wave is a rarefaction wave. This behaviours can be understood by taking in consideration the accessible states of both fluids and imposing the condition of existence of a contact discontinuity after the collision, where the pressure and fluid velocity are continuous.

Figure 3.12 presents the case where $\rho_{a_0} < \rho_{b_0}$. Initially the fluids a and b are in the state a_0 and b_0 where they have the same pressure and fluid velocity. The fluid a is then shocked to the state a_1 which is on the Hugoniot of the state a_0 (in blue). In order to find the states of the fluids resulting from the collision of the shock with the contact discontinuity, the accessible states of both fluids are considered (in yellow for the state a_1 and in red for the state b_0). The condition of existence of a contact discontinuity between the two fluids means that the resulting state in the (u, P) plan is the crossing point between the yellow and red curves, resulting in the states a_2 and b_1 . It is important to note that the equality of pressure and fluid velocity does not imply an equality of density and temperature between these two states. Also the fact that the two crossing curves are the Hugoniot ones means that the resulting waves are two shocks.

Figure 3.13 presents the other case, where $\rho_{a_0} > \rho_{b_0}$. While the Hugoniot and isentropic release curves of the states a_0 and a_1 are identical to the previous case, the Hugoniot curve of the state b_0 is less steep due to the lower density of the fluid. As the consequence, the Hugoniot curve of the state b_0 now crosses the isentropic release curve of the state a_1 (dashed

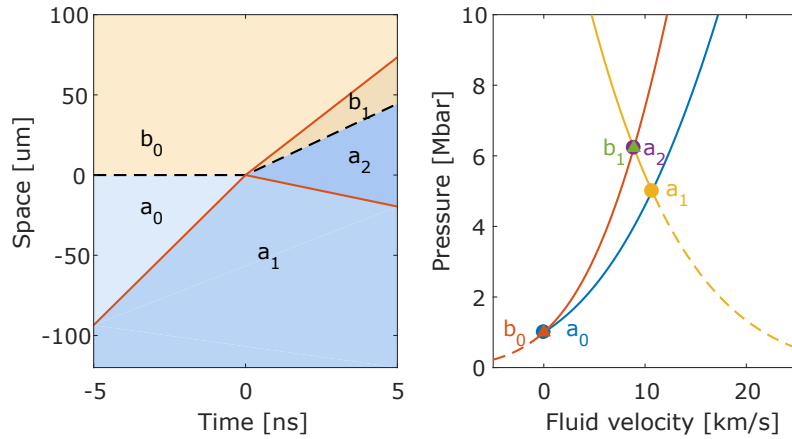


Fig. 3.12 Interaction of a shock discontinuity where $\rho_{a_0} < \rho_{b_0}$. On the left, a (t, x) diagram of the interaction, shocks are in red and contact discontinuity in black dashed. On the right, the representation of the Hugoniot (solid lines) and isentropic release (dashed lines) curves of the different states in the (u, P) plan.

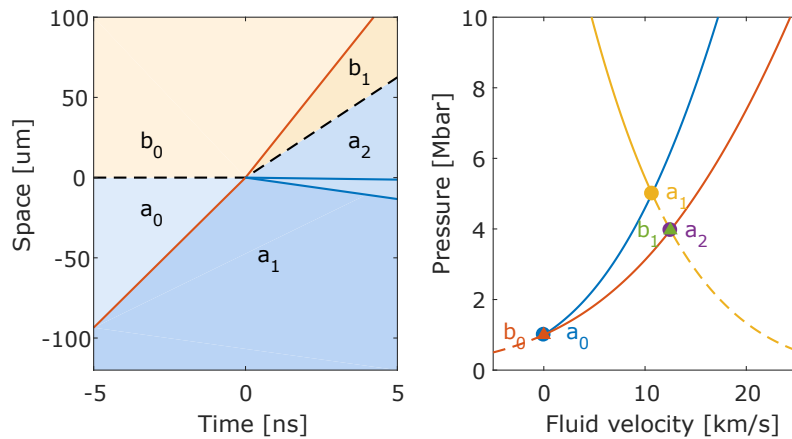


Fig. 3.13 Interaction of a shock discontinuity where $\rho_{a_0} > \rho_{b_0}$. On the left, a (t, x) diagram of the interaction, shocks are in red, head and tail of rarefaction wave in blue and contact discontinuity in black dashed. On the right, the representation of the Hugoniot (solid lines) and isentropic release (dashed lines) curves of the different states in the (u, P) plan.

yellow), meaning that the resulting waves are a shock wave in b_0 and a rarefaction wave in a_1 . As described in section 3.1.5, the rarefaction wave is characterized by two lines (Figure 3.13, left, in blue): the head of the wave is going at $u_{a_1} - c_{a_1}$ and the tail of the wave going at $u_{a_2} - c_{a_2}$, where u_i and c_i are the fluid velocity and sound velocity of the fluid in the state i , respectively.

A comparison between the initial and transmitted shocks from the example in Figure 3.12 and 3.13 shows that when the shock encounters a lower density fluid, its velocity increases while its pressure decreases. On the other hand, if the shock encounter a higher density fluid, its pressure increases and its velocity decreases. An analytic solution for the final pressure and transmitted shock velocity is difficult to obtain, but it can be shown that the shock pressure amplification P_{a_1}/P_{b_1} is a function only of the initial shock strength P_{a_1}/P_{a_0} and the density ratio of the contact discontinuity ρ_{b_0}/ρ_{a_0} . Figure 3.14 presents the results of the graphical solution of a shock at contact discontinuity as a function of these parameters. It appear that at low initial shock strength, the transmitted shock strength does not change much while the shock velocity changes a lot. On the other hand, at high initial shock strength, the change in shock velocity is less important but the shock strength is largely modified.

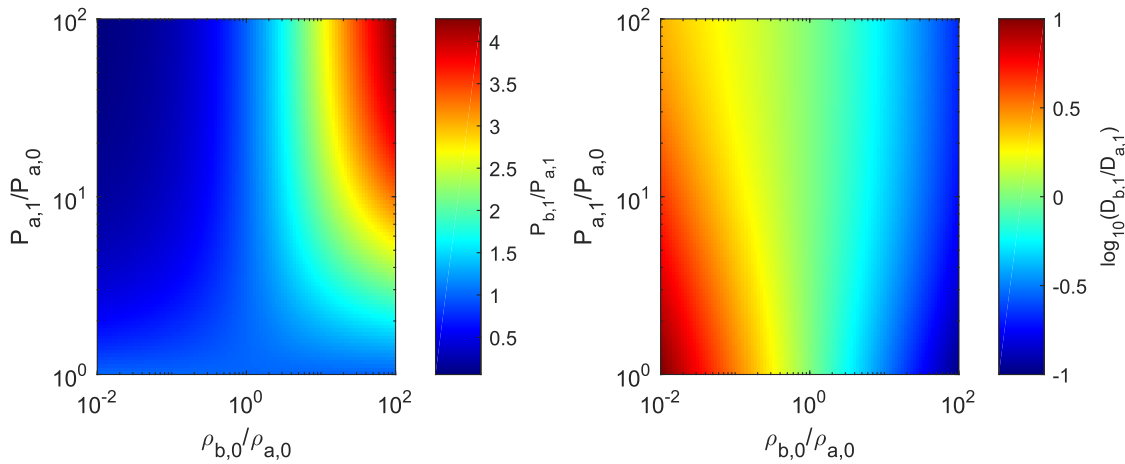


Fig. 3.14 Variation in pressure (left) and velocity (right) of a shock crossing a contact discontinuity for $\gamma = 5/3$.

3.3.2 Shock collision

The waves resulting from the collision between two counter-propagating shocks can be studied in a similar way as the interaction of a shock with a contact discontinuity. Figure 3.15 presents a example of such shock collision. In the fluid initially in the state a_0 , two shocks propagates toward each other. The states of the fluid behind the shocks are a_1 and a_2 ,

on the forward and backward Hugoniot curves of the state a_0 , respectively. In this example the collision is asymmetric since $P_{a_1} < P_{a_2}$. The fluid states resulting from the collision have to be on the Hugoniot or isentropic release curve of the states a_1 and a_2 , while sharing a contact discontinuity. This corresponds to the crossing point between the Hugoniot curves in the (u, P) plan. The resulting state are a_3 on the Hugoniot curve of a_1 (in red) and a_4 on the Hugoniot curve of a_2 (in yellow).

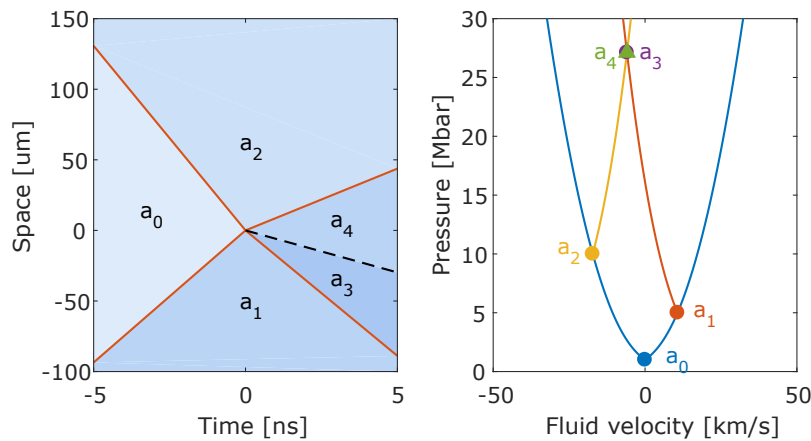


Fig. 3.15 Asymmetric shock collision. On the left, a (t, x) diagram of the collision, shocks are in red and contact discontinuity in black dashed. On the right, the representation of the Hugoniot curves of the different states in the (u, P) plan.

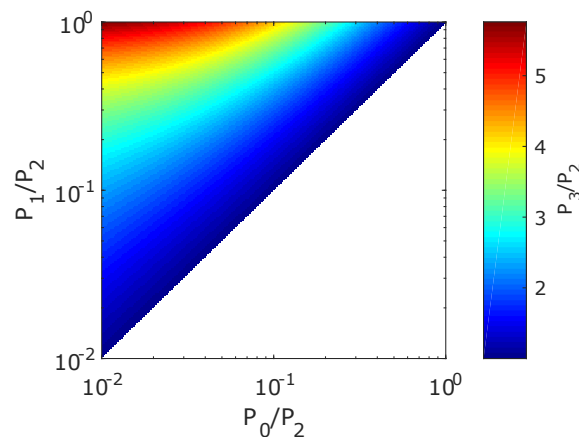


Fig. 3.16 Shock pressure amplification due to a shock collision for $\gamma = 5/3$.

Shock collisions are characterized by a large increase of the shock pressure. As for the interaction of a shock with a contact discontinuity, an analytic solution for the final pressure P_3 is difficult to obtain, but it can be shown that the shock pressure amplification

P_3/P_2 depends only of the ratio of the pressure of the two shocks P_1/P_2 and of the initial fluid pressure P_0/P_2 . Figure 3.15 presents the results of the graphical solution of shock collision as a function of these parameters where $P_2 > P_1 > P_0$. It appears that the closer the collision is to be symmetric (where $P_1/P_2 = 1$), the larger is the pressure amplification. Additionally, at P_1/P_2 constant, an increase of the initial fluid pressure P_0 decreases pressure amplification. This shows that, in order to generate high pressure through shock collisions, a symmetric collision in a fluid at low pressure is necessary. However, the maximum pressure amplification achievable through shock collision is $P_3/P_2 = 6$.

3.3.3 Shock coalescence

A shock coalescence corresponds to the case where a shock overtakes another one. It is similar to shock collision, but in the case where the shocks are co-propagating. A contact discontinuity, a transmitted shock wave and a reflected rarefaction wave result from this interaction.

Figure 3.17 presents an example of shock coalescence. The fluid is initially in the state a_0 . It is then shocked to the state a_1 , which is on the Hugoniot curve of the state a_0 (in blue). Then, the second shock brings the fluid in the state a_2 , which is on the Hugoniot curve of state a_1 (in red). After the shock coalescence, the transmitted and reflected waves propagate in the fluids with states a_0 and a_2 . Considering the condition of existence of a contact discontinuity, the crossing point between the accessible states of these fluids in the (u, P) plan gives the resulting waves. These are the states a_3 on the isentropic release curve of state a_2 and a_4 on the Hugoniot curve of state a_0 .

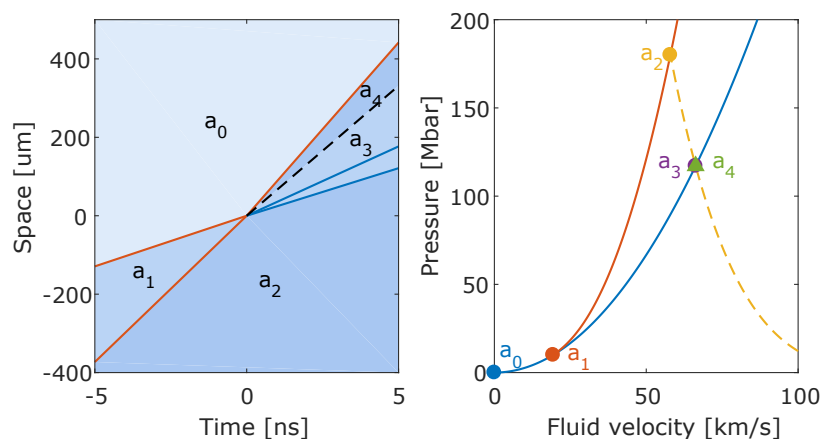


Fig. 3.17 Shock pressure amplification due to a shock collision for $\gamma = 5/3$.

The coalescence of shocks results in a decrease of the pressure of the shocked fluid. This can be very detrimental if the goal is to achieve high pressure through a succession of shocks as presented in Figure 3.11. Since a shock is always subsonic of the downstream fluid, a second shock following it will always end up overtaking the first one, leading to a decrease of the pressure. Similarly to the shock collision space (3.16), the Figure 3.18 presents the shock amplification P_3/P_2 as a function of the ratio of pressure of the shocks P_1/P_2 and the initial pressure of the fluid P_0/P_2 .

As expected, the amplification is always lower than unity, meaning that the coalescence leads to a decrease of the shock pressure. For a first shock pressure P_1 close to the second shock pressure ($P_1/P_2 \simeq 1$) or close to the initial pressure ($P_1/P_2 \simeq P_0/P_2$) the variation of pressure is small. Also, at constant pressure for both shocks, an increase in P_0 leads to a smaller decrease in final pressure. Finally, at a given initial and second shock pressure, P_0 and P_2 respectively, there is a pressure of the first shock P_1 for which the decrease in final pressure is the largest. Therefore, if the goal is to achieve a high pressure using two successive shocks, it is advisable to avoid this worst first shock pressure.

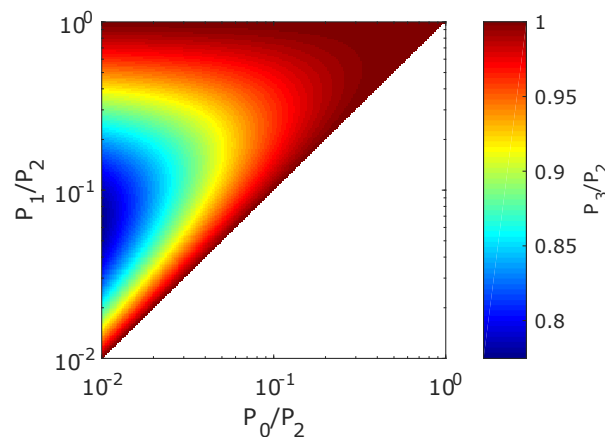


Fig. 3.18 Shock pressure amplification due to a shock coalescence for $\gamma = 5/3$.

3.4 Conclusion

In this chapter, continuous (sound waves, rarefaction waves) and discontinuous (shock waves) flow have been derived from the basic hydrodynamic equations.

Perturbation theory applied to the conservation of mass, momentum and internal energy allows to describe the propagation of small disturbance in a fluid. These perturbations of the flow are sound waves. The work of a piston with small positive or negative velocity (compared

to the fluid sound velocity) results in a compression or rarefaction wave, respectively. On the other hand, a large variation of piston velocity results in a centered rarefaction wave (if the velocity is negative) or a breakdown of the perturbation theory (if the velocity is positive).

In this last case, the wave has to be described as a discontinuity of the hydrodynamic variable. This is a shock wave. A fluid in a given hydrodynamic state has an associated Hugoniot curve, which is the set of its accessible states through the transformation induced by a shock wave. Taking in consideration the accessible states through a rarefaction wave (from the continuous theory) as well gives the set of all accessible states from a given hydrodynamic state, in the case of large amplitude transformation.

The interaction of a shock with another shock or a contact discontinuity can be solved by taking in consideration the curves of accessible states of the different fluids in contact. The intersection of their curves in the fluid velocity - pressure plan allows to fully determine the waves resulting from the interaction. In this way, the properties of shock collisions, shock coalescences or shock at contact discontinues can be understood.

Chapter 4

Hydrodynamic of shock ignition in the absence of hot electrons

At shock ignition intensities, parametric instabilities are expected to produce hot electrons. Those might be detrimental or beneficial to the implosion. However, they are assumed to have a perturbation effect, such that the main features of shock ignition are well described by hydrodynamic considerations only. A good understanding of the shock ignition hydrodynamic is required in order to be able to identify the positive or negative effect of hot electrons on implosions.

In this chapter, the method of solving of shock interaction with discontinuities presented in section 3.3 is coupled to a propagation code in order to simulate the classical and the shock ignition schemes. The shock ignition techniques described by Nora and Betti [70] though simulations are well reproduced with this code, allowing to highlight the key parameters for optimal shock ignition. To complete this description of the hydrodynamic of shock ignition, the robustness of the techniques is discussed and a most robust technique in planar geometry is proposed. Then the mechanism of amplification of the shock pressure in spherical geometry are discussed. Finally a shock ignition experiment realized on Omega Laser Facility is presented. In first approximation, the effect of hot electrons in this experiment can be neglected due to the rather low laser intensity.

4.1 Shock ignition theory in planar geometry

In the classical scheme for inertial fusion confinement, the shell is first accelerated to high implosion velocity. Then the shell kinetic energy is converted into gas internal energy during the deceleration phase. The beginning of the deceleration phase corresponds to the time at

which the main shock, sent in the shell at the beginning of the laser matter interaction has bounced on itself at the center of the gas and collides with the imploding shell. Yet, the description of the increase of the gas internal energy through PdV work does not allow to catch all the dynamic involved during the deceleration phase. A more complete description using shocks dynamic is required in order to understand the mechanism limiting the increase in gas pressure and how a ignition shock can overcome this limitation.

This work has been done by Nora and Betti [70] using one-dimensional hydrodynamic simulations with the code LILAC [30]. In their article, the authors considered a planar geometry, therefore neglecting the shock amplification due convergence. While this prevent from having a realistic scheme for shock ignition, it allows to have a good understanding of the physical phenomena involved.

In this section the model presented by Nora and Betti is used as a starting point for a semi-analytic description of the deceleration of a shell. The same target parameters are taken but the description of the implosion dynamic is realized using only Rankine-Hugoniot equations and graphical solving of shock interactions with other discontinuities. First are presented the mechanism of pressure increase in the gas and its limitation due to rarefaction waves. Then, different ignition shock launching times and amplitudes are considered, leading to different configurations of three discontinuities interaction. Finally the different techniques are compared between themselves and to a spherical geometry case.

4.1.1 Classical scheme in planar geometry

Maximum pressure achievable

The initial condition for the planar modeling of the implosion corresponds to the state of an imploding thick shell at the time when the main shock reaches the center of the gas. At that time, the whole target (shell and gas) has the same pressure and implosion velocity. The target parameters have been taken from a LILAC simulation of an Omega scale target. This leads to initial conditions as presented in Figure 4.1. The gas is a $150 \mu m$ thick slab with a density of 0.3 g/cm^3 and the shell is a $50 \mu m$ thick slab with a density of 15 g/cm^3 . Both regions are at a pressure of 50 Mbar and have a fluid velocity of -300 km/s (the velocity is negative since the target is imploding). The boundary condition at the shell outer surface is a constant pressure of 50 Mbar, such that the surface is at mechanical equilibrium. The boundary condition in $x = 0$ is a symmetry condition such that the fluid velocity is $u(x = 0) = 0$.

The Figure 4.2 presents the trajectories, at early time, of shocks and contact discontinuities in the (t, x) plan (left) and the corresponding graphical solving of the Hugoniot curves in the (u, P) plan (right). Initially, the gas is in the state g_0 and the shell in the state s_0 , with their

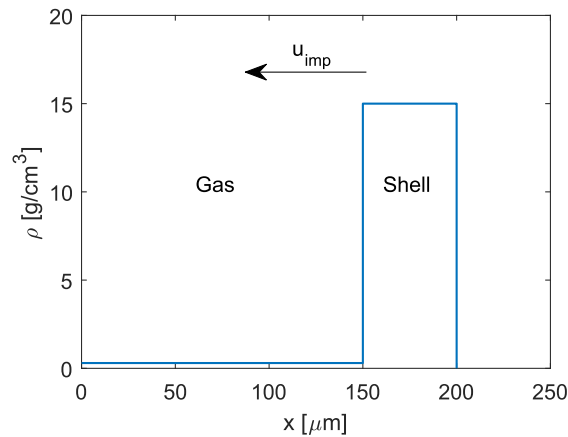


Fig. 4.1 Initial conditions of the planar implosion.

associated Hugoniot curves in blue and red, respectively. The boundary condition in $x = 0$ imposes a fluid velocity $u = 0$, which lead to the formation of a shock going outward. The state behind this shock is g_1 , on the Hugoniot curve of g_0 . This shock propagates through the gas and collides with the gas-shell contact discontinuity. The states resulting from this collision are given by the crossing point between the Hugoniot curves of the shell (in red) and shocked gas (in yellow). The transmitted shock bring the shell in the state s_1 , and the reflected shock bring the gas in the state g_2 .

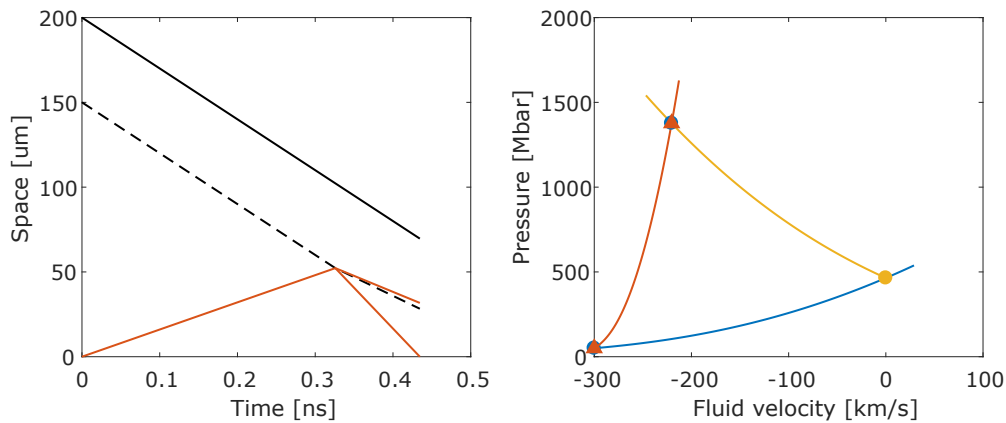


Fig. 4.2 Shock propagating back and forth in the gas at the beginning of the deceleration phase (left) and the corresponding graphical solving of Hugoniot curves in the (u, P) plan (right). The trajectories of shocks are in red, the shell-gas contact discontinuity is in dashed black and shell outer surface is in solid black.

If the dynamic of the transmitted shock is ignored, the situation of the target when the reflected shock reaches the position $x = 0$ is very similar to the initial condition. The pressure

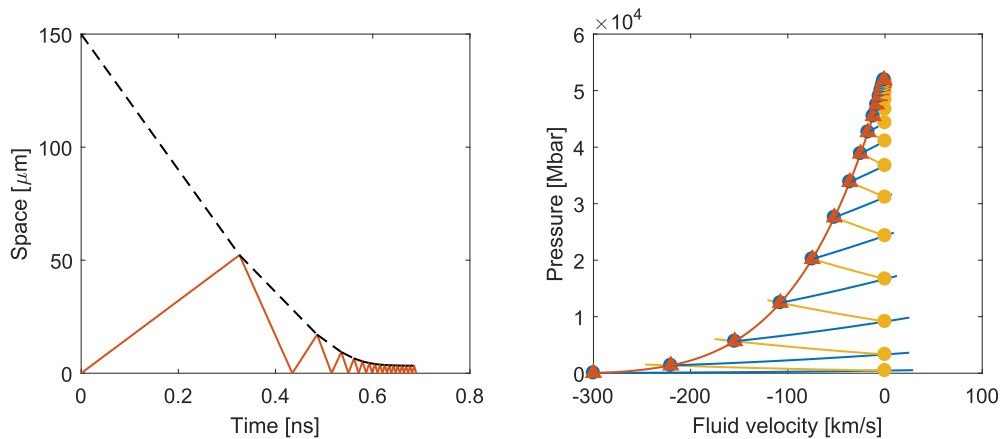


Fig. 4.3 Iterative solving of the shock bouncing back and forth in the gas, ignoring the dynamic of transmitted shock in shell (left) and the corresponding graphical solving of Hugoniot curves in the (u, P) plan (right). The trajectories of shocks are in red and the shell-gas contact discontinuity is in dashed black.

and fluid velocity are the same everywhere in the gas and at the shell contact discontinuity. The pressure has increase from 50 Mbar to 1350 Mbar and the fluid velocity decreased in absolute value from 300 km/s to 220 km/s. The shock going back and forth in the gas is the mechanism by which the shell kinetic energy is converted into gas internal energy (or pressure).

Still ignoring the dynamic of transmitted shocks in the shell, it is possible to calculate iteratively the trajectory of the shock propagating in the gas. The Figure 4.3 presents this trajectory (left) and the corresponding iterative solving of the Hugoniot curves (right). Every time the shock in the gas collides with the shell-gas contact discontinuity, the shell slows down while the gas pressure increases. The gas pressure then reaches a maximum value when the shell velocity reaches zero. With this example, this pressure is 52 Gbar.

Effect of rarefaction waves

In reality, the shocks transmitted into the shell cannot be neglected and their coalescence leads to the formation of rarefaction wave in the shell. A complete simulation of all the discontinuities propagation and interaction for this example have been realized. The rarefaction waves have been treated as sharp discontinuities for simplicity and contact discontinuities with density jump smaller than a percent have been neglected.

The Figure 4.4 presents the evolution of pressure at the center of the gas for the case with the rarefaction wave taken into consideration (in blue) and without them (in red). At early time the pressure increases are identical, but at 0.57 ns the pressure for the case with

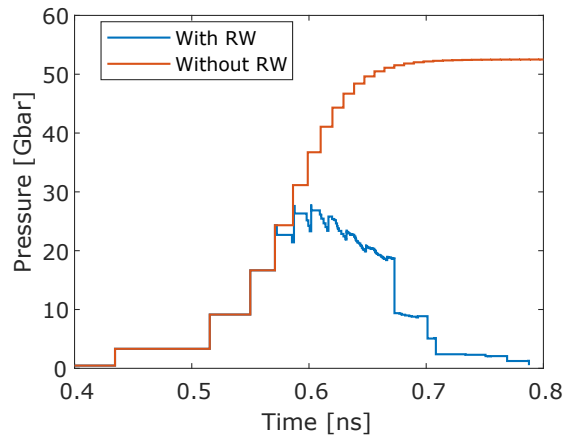


Fig. 4.4 Evolution of pressure at the center of the gas for the cases with rarefaction waves (in blue) and without (in red).

the rarefaction wave decreases from 24.3 Gbar to 22.7 Gbar. This decrease is due to a rarefaction wave originating from the coalescence of the two first transmitted shocks in the shell. Figure 4.5 presents the full simulation of the implosion with only these transmitted shocks represented (in red), as well as the rarefaction wave and contact discontinuity resulting from their coalescence. The rarefaction wave (in blue) propagates up the the gas center, decreasing its pressure to specific values. The coalescence of later transmitted shocks and their interaction with in-shell contact discontinuities lead to the creation of many rarefaction waves, which end up limiting the maximum pressure to 27.6 Gbar at the center of the gas.

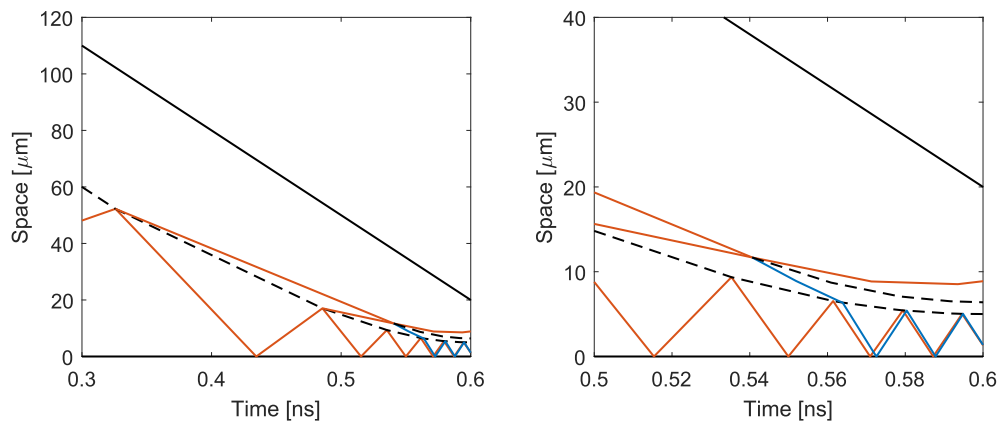


Fig. 4.5 Trajectories of discontinuities illustrating the effect of the type 1 rarefaction waves. Not all discontinuities have been represented. Shocks are in red, rarefaction waves in blue, contact discontinuities in dashed black and shell outer surface in solid black.

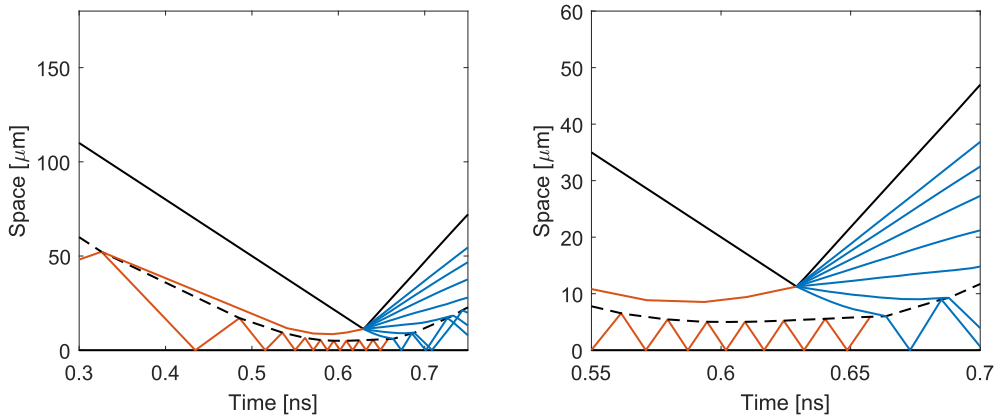


Fig. 4.6 Trajectories of discontinuities illustrating the effect of the type 2 rarefaction waves. Not all discontinuities have been represented. Shocks are in red, rarefaction waves in blue, contact discontinuities in dashed black and shell outer surface in solid black.

Later, at 0.67 ns, the pressure drops suddenly to very low value. This is due to the propagation of a rarefaction wave originating from the collision of the first transmitted shock with the shell outer surface. Figure 4.6 presents the full simulation of the implosion with only the first transmitted shock represented, as well as the rarefaction wave resulting from its collision with the shell outer surface (in solid black). Since this rarefaction wave has a very large amplitude, dropping the pressure from 18.2 Gbar to 50 Mbar, its has been modeled by a fan a rarefaction wave where the pressure drop by a factor two between each ones. As a consequence of the collision, the velocity of the shell outer surface instantly change from -300 km/s to 469 km/s, marking the beginning of the shell expansion.

These rarefaction waves can be referred as type I and II. The type I originates from the coalescence of shocks inside the shell. For thick target, such as the target considered for shock ignition, they are the ones limiting the maximum pressure achievable in the gas (as shown in this example). The type II rarefaction waves originate from the collision of a shock with the shell outer surface. They are the ones limiting the gas pressure in the case of thin target, as considered for the classical ICF scheme.

4.1.2 Shock ignition techniques

Considering a thick shock ignition target, the formation of type I rarefaction waves is the physical phenomenon limiting the pressure increase inside the gas. The main goal of the shock ignition scheme is to use a converging shock in order avoid their formation. Analytically, the strength and timing of this ignition shock can be chosen such that it results in specific configurations for the target implosion. In this section three of these configurations are

presented, all of them involving particular solutions of three discontinuities interaction in the (u, P) plan.

No-rarefaction technique

The no-rarefaction technique consists in sending the ignition shock such that it collides with the two first transmitted shocks at the moment they coalesce. If the strength of the ignition shock is well chosen, the collision results only in a diverging shock and a contact discontinuity. There is no rarefaction wave propagating inward.

Figure 4.7 presents the solving in the (u, P) plan of this three shock interaction for this example. The blue dot correspond to the initial state s_0 of the shell, at 50 Mbar and -300 km/s. The red dot corresponds to the state of the shell behind the first transmitted shock s_1 , on the forward Hugoniot curve of s_0 , and the yellow dot corresponds to the state of the shell behind the second transmitted shock s_2 , on the forward Hugoniot of s_1 . In the absence of ignition shock, the results of the coalescence of the two transmitted shocks will be a shock wave propagating outward in s_0 and a rarefaction wave propagating inward in s_2 . Now, an ignition shock is send inward by increasing the pressure of the top boundary condition. The state of the shell behind this shock is s_3 (purple dot in Figure 4.7), on the backward Hugoniot of s_0 . The results of the collision of the three shocks will be two waves, one propagating inward in s_2 and the other one propagating outward in s_3 . Yet, in the case of the no-rarefaction technique, the crossing point of the accessible states in the (u, P) plan for s_2 and s_3 matches the state s_2 . Therefore, after the collision of the shocks, no wave will be propagating in s_2 and the collision only results in a shock propagating outward, putting the shell in the state s_4 on the forward Hugoniot of s_3 .

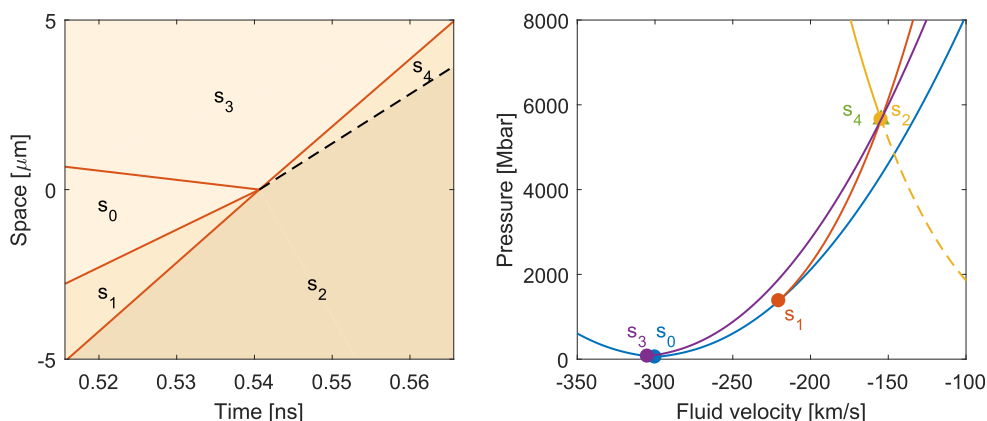


Fig. 4.7 Graphic solving of the no-rarefaction technique in the (u, P) plan (right) and corresponding shock trajectories in a fluid initially at rest (left).

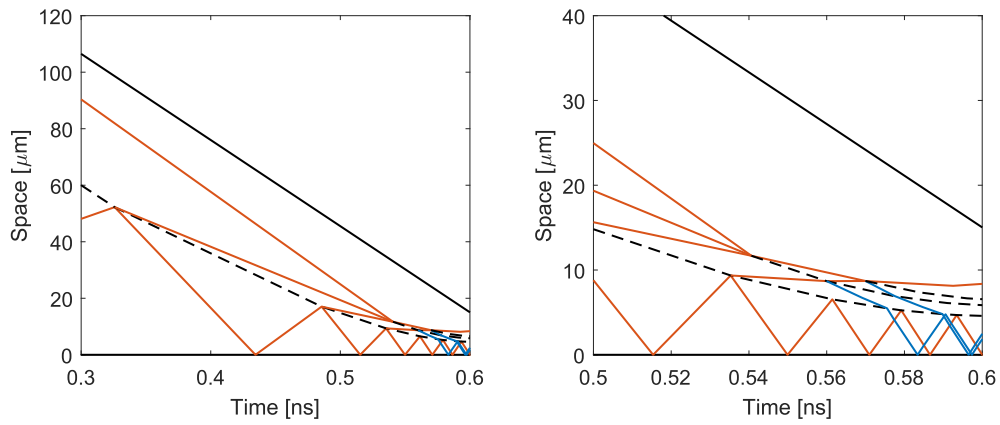


Fig. 4.8 Trajectories of discontinuities illustrating the no-rarefaction technique. Shocks are in red, rarefaction waves in blue, contact discontinuities in dashed black and shell outer surface in solid black.

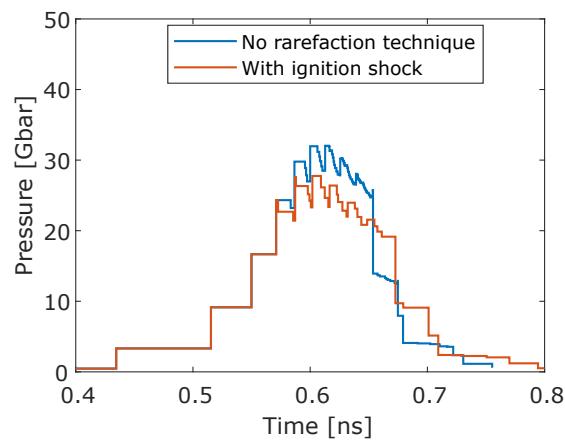


Fig. 4.9 Evolution of the pressure at the center of the gas for the no-rarefaction technique and without ignition shock.

Figure 4.8 presents the trajectories of discontinuities from a simulation of the no-rarefaction technique. The ignition shock is created at the outer surface of the shell at -0.43 ns with a pressure of 69.6 Mbar. As described before, the three waves collision results only into a contact discontinuity and a diverging shock. As a consequence, the rarefaction waves (coming from the interaction of the third transmitted shock with the contact discontinuity and the diverging shock in the shell) reach the center of the gas at later time compared to the case without ignition shock. Figure 4.9 presents the evolution of the pressure at the center of the gas for the no-rarefaction technique (NRT) and in absence of ignition shock (noSI). As expected, with the no-rarefaction technique, the first decrease in pressure due to the rarefaction wave originating from the shock coalescence is not present. This allows the pressure to reach 32.0 Gbar at the center of the gas, instead of 27.6 Gbar without ignition shock. This increase is small and it could be interesting to create a sequence a ignition shocks of increasing pressure in order to cancel the later rarefaction waves. Yet, these shocks would have to go though other discontinuities before reaching the collision of interest, which makes the calculation of their pressure and launching time more difficult.

No-transmission technique

The no-transmission technique consists in sending the ignition shock such that it collides with the first diverging shock at the moment it reaches the gas-shell contact discontinuity. If the strength of the ignition shock is well chosen, the collision results only in a converging shock and no transmitted shock propagating in the shell.

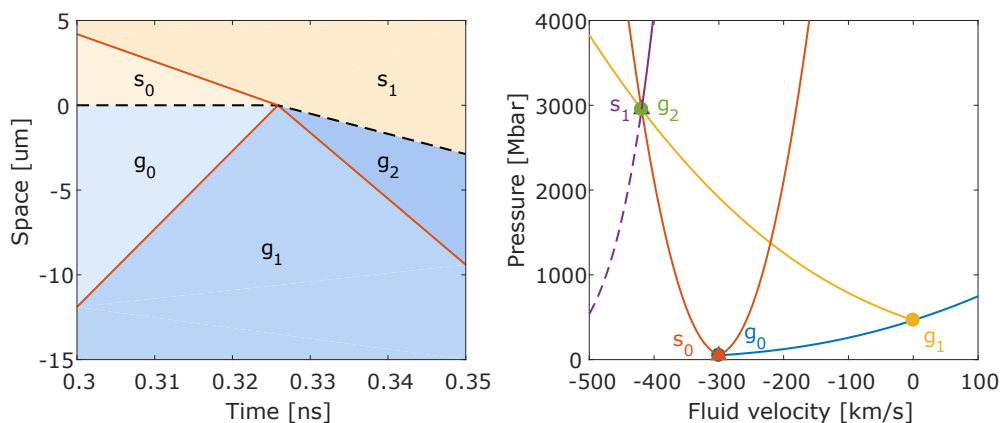


Fig. 4.10 Graphic solving of the no-transmission technique in the (u, P) plan (right) and corresponding shock trajectories in a fluid initially at rest (left).

Figure 4.10 presents the shocks and contact discontinuities trajectories for the no-transmission technique in the frame of the contact discontinuity moving at -300 km/s (left)

and the corresponding solving of the Hugoniot curves in the (u, P) plan (right). Initially the shell is in the state s_0 and the gas in the state g_0 . The main shock, propagating in the gas, put it in the state g_1 where $u = 0$ (due to the symmetry condition in $x = 0$). The ignition shock puts the shell in the state s_1 , on the backward Hugoniot of s_0 . The resulting states from the three waves interaction are given by the intersection between the accessible states of g_1 (in yellow) and s_1 (in purple). In the case of the no-transmission technique, the state s_1 is on the Hugoniot curve of g_1 so that no wave propagates in s_1 . The results of the collision is only a converging shock propagating in g_1 .

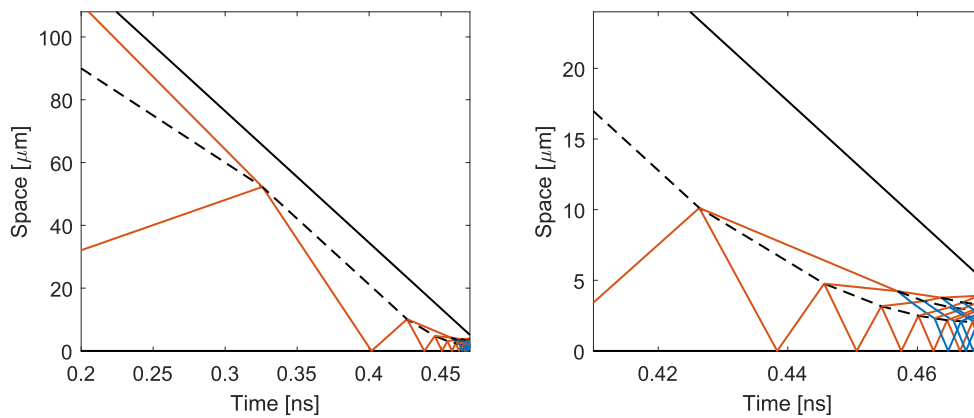


Fig. 4.11 Trajectories of discontinuities illustrating the no-transmission technique. Shocks are in red, rarefaction waves in blue, contact discontinuities in dashed black and shell outer surface in solid black.

Figure 4.11 presents the trajectories of discontinuities from the full simulation of the no-transmission technique. The ignition shock is sent from the shell outer surface at 0.02 ns with a pressure of 2.95 Gbar. As expected, no shock propagates after the three discontinuity collision. When the main shock reaches the center of the gas, the pressure is 2.95 Gbar and the fluid velocity is -420 km/s everywhere in the target. This situation is very similar to the initial condition but with higher parameters. This allows to reach significantly higher pressure compared to the case without ignition shock. Figure 4.12 presents the evolution of the pressure at the center of the gas for the no-transmission technique and for the case without ignition shock. Because the implosion velocity is higher, the implosion is faster and reaches a maximum pressure of 171 Gbar.

Re-shock technique

Similarly to the no-rarefaction technique, the re-shock technique aims at having the ignition shock collides with the two first transmitted shocks when they coalesce. But instead of a

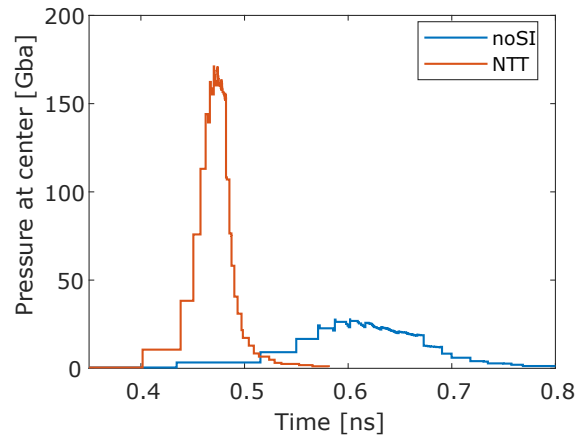


Fig. 4.12 Evolution of the pressure at the center of the gas for the no-rarefaction technique and without ignition shock.

shock of moderate pressure, a strong shock with a pressure equivalent to the pressure of the second transmitted wave is sent in the shell. This results into a quasi-symmetric collision with an important pressure amplification.

The Figure 4.13 presents the shocks and contact discontinuity for the re-shock technique in the frame of the unperturbed shell moving at -300 km/s (left) and the corresponding solving of the Hugoniot curves in the (u, P) plan (right). The states s_0 , s_1 and s_2 correspond to the unperturbed shell, and the states behind the first and second transmitted shocks, respectively. These states are identical to ones from the no-rarefaction technique. But for the re-shock technique, the pressure of the ignition shock, putting the shell in the state s_3 on the backward Hugoniot of s_0 , has the same pressure as the state s_2 . The resulting states from this collision are given by the intersection of the Hugoniot curve of the states s_3 and s_2 . While this collision can appear symmetric due to the identical pressure, the density of the states s_2 and s_3 are different. As a consequence, the pressure amplification of the shocks though the collision reach 6.55 (jumping from 5.66 Gbar to 37.0 Gbar), which is higher than the maximum achievable from a classic symmetric collision as described in 3.3.2.

Figure 4.14 presents the trajectories of the discontinuities from the full simulation of the re-shock technique. The pressure of the ignition shock after its collision with the transmitted shocks is very large. When it reaches the interface shell-gas, it accelerates it significantly, and then it bounces in the the gas back and forth similarly to the main shock. It appear that the diverging shock from the three shocks collision quickly reaches the shell outer surface, leading to the formation of type II rarefaction wave (fan of rarefaction wave in blue) much earlier that for the other techniques, or for the case without ignition shock. Figure 4.15 presents the evolution of the pressure at the center of the gas for the case of the re-shock

technique and for the case without ignition shock. The pressure quickly increases to values much higher than for the other techniques (up to 254 Gbar). Then, due to the early formation of the type II rarefaction waves, it quickly drop to low values. This means that when the gas reaches high pressure, a significant part of the shell has start to expand outward, therefore reducing the confinement time and the implosion performance. Considering thicker target for this scheme could lead to an implosion where only the type I rarefaction waves limit the maximum pressure. This could lead to a higher maximal pressure with an areal density, at the time of the pressure peak, also higher.

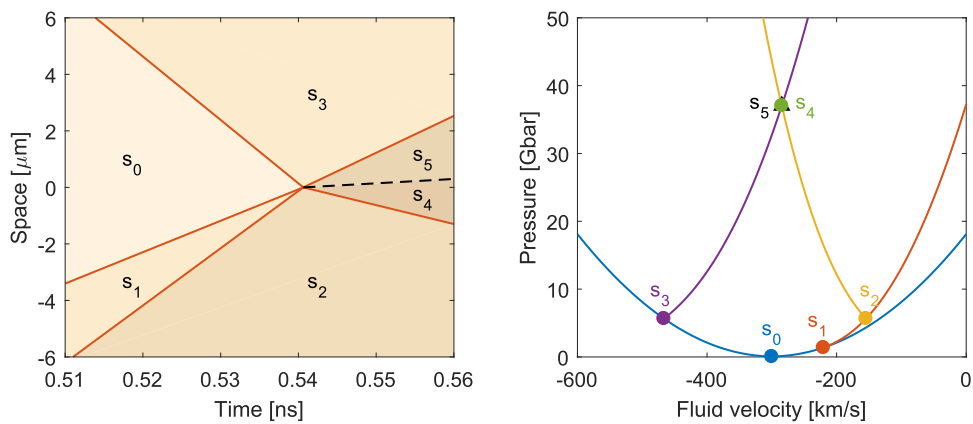


Fig. 4.13 Graphic solving of the re-shock technique in the (u, P) plan (right) and corresponding shock trajectories in a fluid initially at rest (left).

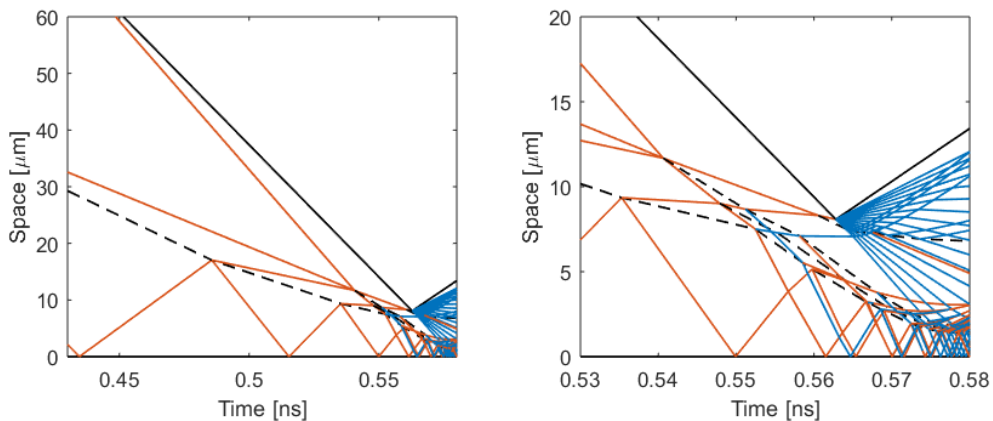


Fig. 4.14 Trajectories of discontinuities illustrating the re-shock technique. Shocks are in red, rarefaction waves in blue, contact discontinuities in dashed black and shell outer surface in solid black.

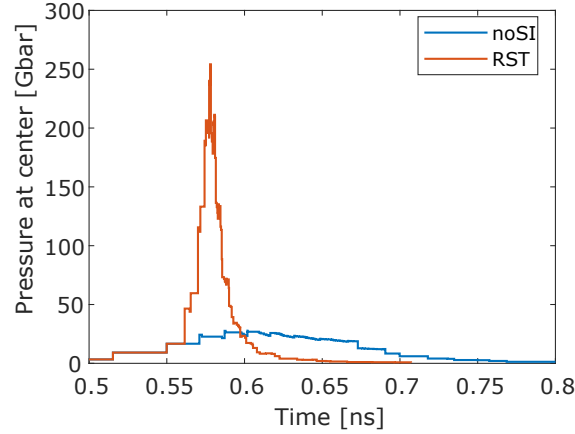


Fig. 4.15 Evolution of the pressure at the center of the gas for the re-shock technique and without ignition shock.

Energy equivalent implosion

In the examples described before, the energy invested in the implosion is not constant from a technique to another. Increasing the pressure of the boundary condition, in order to send a shock in the shell, increases the invested energy. The total invested energy in the implosion is the sum of the kinetic energy of the target at the initial time E_c and the piston energy due to the pressure work at the boundary condition E_{ps} .

The kinetic energy (expressed by unit area due to the planar geometry) is given by

$$E_c = (\rho_s d_s + \rho_g d_g) u_0^2, \quad (4.1)$$

where $\rho_{s,g}$ and $d_{s,g}$ are the density and thickness of the shell, gas, respectively. u_0 is the initial implosion velocity of the target. For the case without ignition shock, the work of the pressure force is constant between the initial time and the beginning of the target expansion, when the main shock reaches the shell outer surface, leading to the formation of type II rarefaction waves. This time corresponds to the end of the laser pulse, and of the pressure work, since any additional energy invested at later time is useless to the implosion. The piston energy for the case without ignition shock is therefore

$$E_{ps}^{noSI} = P_0 u_0 t_f, \quad (4.2)$$

where P_0 is the pressure at the boundary condition and t_f the time when the target expansion starts. For an implosion at 300 km/s, as described on the previous section, $t_f = 629$ ps, $E_c = 35.8$ kJ/mm² and $E_{ps}^{noSI} = 0.94$ kJ/mm², such that the total invested energy is $E_{tot} = E_c + E_{ps}^{noSI} = 36.7$ kJ/mm². For a higher implosion velocity of $u_0 = 414$ km/s, the

target kinetic energy increases to $E_c = 68.1 \text{ kJ/mm}^2$. On the other hand, the piston energy stays constant since the increase in work pressure (due to the increase in u_0) is compensated by a shorter implosion time $t_f = 450 \text{ ps}$.

Considering the no-transmission and re-shock techniques, as described in the previous section (with an initial implosion velocity of 300 km/s), the launching times of the ignition shock t_{si} are 17 ps and 424 ps, respectively. For these case where $t_{si} > 0$, the piston energy is given by

$$E_{ps}^{t_{si}>0} = P_0 u_0 t_{si} + P_{si} u_{si} (t_f - t_{si}), \quad (4.3)$$

where P_{si} and u_{si} are the pressure and the fluid velocity of the shell behind the ignition shock. The total energy invested for the no-transmission and the re-shock technique are therefore 92.0 kJ/mm^2 and 73.0 kJ/mm^2 . On the other hand, for the no-rarefaction technique, the launching time of the ignition shock is -527 ps , so that $t_{si} < 0$. The contribution to the piston energy due to pressure work at negative time is given by the difference between the pressure work behind the ignition shock $P_{si} u_{si}$ and the initial pressure work $P_0 u_0$. Therefore the piston energy for the case $t_{si} < 0$ is given by

$$E_{ps}^{t_{si}<0} = -(P_{si} u_{si} - P_0 u_0) + P_{si} u_{si} t_f = P_{si} u_{si} (t_f - t_{si}) - P_0 u_0 t_{si}. \quad (4.4)$$

With an implosion velocity of 300 km/s, the total invested energy for the no-rarefaction technique is 38.6 kJ/mm^2 .

In order to design energy equivalent implosions for the different shock ignition techniques, the initial implosion velocity has to be reduced. The reference case, without ignition shock, is the implosion at 414 km/s, so that the total invested energy is 69.0 kJ/mm^2 . The energy equivalent implosion for the no-rarefaction, no-transmission and re-shock techniques have implosion velocities of 403 km/s, 261 km/s and 293 km/s, respectively. Even though the re-shock technique requires a higher pressure than the no-transmission technique, its piston energy is lower due to a shorter pulse duration. This allows the energy equivalent simulation of the re-shock technique to have a higher implosion velocity than the no-transmission.

Figure 4.16 presents the evolution of the pressure at the center of the gas from the simulations of these different implosions. The maximum pressure achieved for the simulation without ignition shock (noSI, in blue) is 53 Gbar. The no-rarefaction technique (NRT, red) is only slightly better, with a maximum pressure of 61 Gbar, that being a 15% increase compared to the reference simulation. The no-transmission technique (NTT, in yellow) is much more efficient with a maximum pressure of 125 Gbar, which is 2.35 times the pressure of the reference case. Finally, the most efficient technique is the re-shock technique (RST,

in purple) with a maximum pressure of 240 Gbar, 4.45 times the pressure obtained without ignition shock.

Considering the planar geometry implosion of a thick shell, the re-shock technique is the most efficient distribution of the energy in order achieve high pressure in the gas.

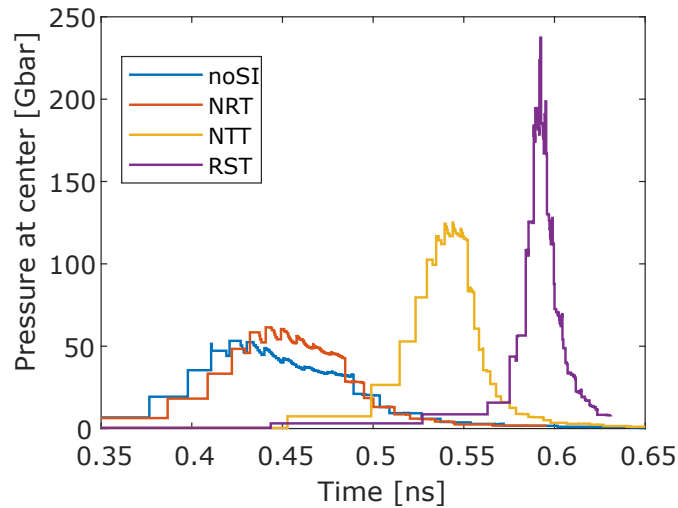


Fig. 4.16 Evolution of the pressure at the center of the gas without shock ignition pulse (noSI) and for the no-rarefaction (NRT), no-transmission (NTT) and re-shock (RST) techniques. All implosions are energy equivalent.

4.2 Toward realistic shock ignition scheme

From the planar shock ignition theory described in the previous section toward realistic shock ignition implosion, two major concerns have to be considered. These are the robustness of the technique compared to experimental uncertainty and the effect of spherical geometry on the ignition shock propagation.

The techniques described in the previous section require a precision in the ignition shock timing and pressure that cannot be achieved experimentally. Also, the real hydrodynamic profile of a target during its implosion is not perfectly known. Therefore, none of the techniques presented in the previous section can be applied for the design of realistic shock ignition implosions. The experimental uncertainty would result in a mistiming of the three discontinuities collision. Yet, these techniques show the main features of the shock ignition, from which a robust shock ignition scheme can be designed.

Additionally, the results presented in the previous section considered planar geometry only. Since shocks and rarefaction waves have a constant velocity in planar geometry, it

makes the description of their propagation trivial. In reality, shock ignition implosion are in converging spherical geometry. In this geometry, the velocity of a shock wave is not constant along its propagation and the fluid behind it is not any more homogeneous. The spherical geometry results in a much more complex description of the ignition shock and implosion dynamic. The main consequence of the spherical geometry on the ignition shock propagation is its amplification as it go through the shell.

4.2.1 Most robust shock ignition technique

Experimentally, the ignition shock is sent in the target using a laser intensity spike. The launching time of this spike has a typical uncertainty around ± 50 ps. Also, an instantaneous rising of the intensity is not possible and a shock ignition spike has a rising time around ~ 100 ps. Hence, the exact spike launching time cannot be determined and a uncertainty of $\sim \pm 100$ ps have to be considered on its timing. At the laser intensities required to send a strong shock in the shell, collective effects from the plasma can lead to anomalous absorption as described in the previous chapter. These effect are not well described in current hydrodynamic codes. This results in an uncertainty on the absorbed laser intensity during the spike, and therefore on the ignition shock pressure. The uncertainty on the target hydrodynamic profile before the ignition shock also have to be considered. Especially, the timing and pressure of the main diverging shock propagating in shell cannot be precisely known due to uncertainties on the intensity during the acceleration phase, as well as 2D effects.

A robust shock ignition technique can be deduced from the techniques described in the previous section. Especially, the no-transmission technique and the re-shock technique set two limiting cases of ignition shock timing. For the no-transmission technique, if the ignition shock is too early, it enters the gas before the main diverging shock as reached the gas-shell interface. In this case, the ignition shock acts as a late increase of the shell implosion velocity. This situation can actually be beneficial since this late increase of implosion velocity leads to better performances while limiting the hydrodynamic instability of the implosion. However, since the ignition shock pressure is limited by experimental constrains, the absence of shock collision in the shell leads to a relatively small pressure of the ignition shock when it enters the gas and therefore lower implosion performance. For the re-shock technique, if the ignition shock is too late, the transmitted diverging shocks in the shell have time to coalesce, creating type I rarefaction wave that will decrease the gas pressure.

Considering these two limit cases, the safest choice is the mean time between the time when the main shock collides for the first time with the gas shell interface (creating the first transmitted shock) and the time when the two first transmitted shocks coalesce. In such case, the ideal pressure for the ignition shock is the pressure behind the first transmitted shock

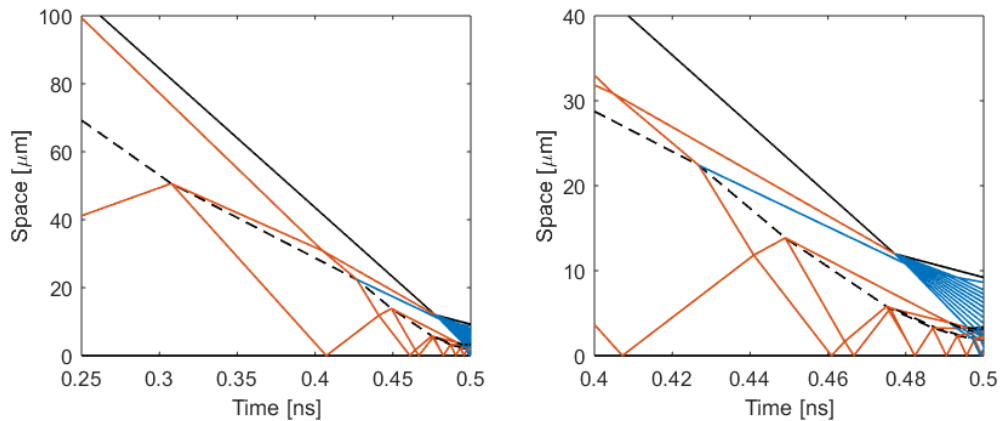


Fig. 4.17 Trajectories of discontinuities illustrating the most robust technique. Shocks are in red, rarefaction waves in blue, contact discontinuities in dashed black and shell outer surface in solid black.

so that their collision is symmetric, leading to an optimal pressure amplification. Figure 4.17 presents the trajectories of the discontinuities from a simulation of such implosion. In order to be equivalent in energy, as described in the previous section, the target implosion velocity is -327 km/s. The launching time of the ignition shock is 84 ps with a pressure of 1.64 Gbar. The collision of the ignition shock with the transmitted shock results in two shocks, a converging one and a diverging one. When the converging one reaches the shell-gas interface it increases the pressure of the gas by bouncing in it back and forth. It also creates a rarefaction wave which is not detrimental to the implosion since it is a diverging one. The diverging shock from the ignition shock collision quickly reaches the shell outer surface, leading to the creation of type II rarefaction waves. These decompress the shell, limiting the rising of pressure. Like for the re-shock technique, thicker target could allow to reach higher maximal pressure.

Figure 4.18 presents the evolution of the pressure at the center of the gas from this simulation. The maximum pressure achieved is 153 Gbar. It is intermediate between the no-transmission and the re-shock techniques. This maximum is very stable over a wide variation of the pressure and launching time of the ignition shock. A variation of ± 100 ps in the shock launching time and of $\pm 20\%$ in its pressure leads only to a maximum decrease of 1.2% in the maximum pressure normalized to the invested energy (increasing or decreasing the shock pressure lead to non energy equivalent implosions, a normalization is then necessary in order to compare the implosions). For comparison, the same variation applied to the other techniques leads to a maximum drop of the pressure by 48% for the no-transmission and 34% for the re-shock. Additionally to its stability to uncertainties on the ignition shock timing and pressure, the technique required a significantly lower shock pressure compared to the

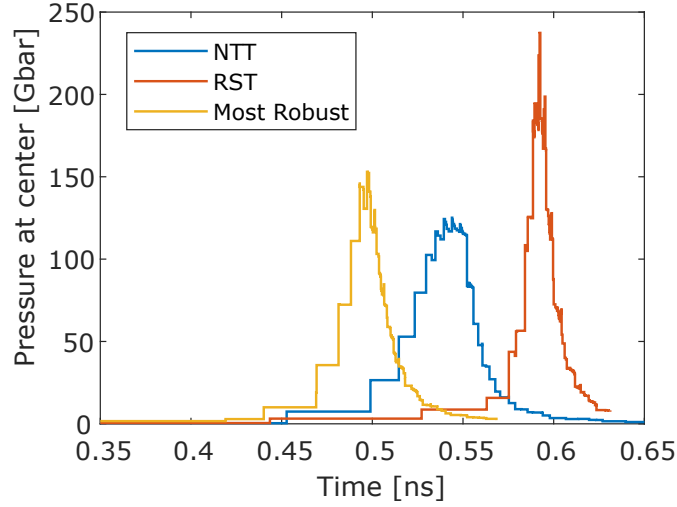


Fig. 4.18 Evolution of the pressure at the center of the gas for the no-transmission, re-shock and most robust techniques.

re-shock or no-transmission techniques. The ignition shock pressure for this robust technique is 1.64 Gbar where the no-transmission and re-shock techniques require 2.55 Gbar and 5.6 Gbar, respectively. The robust technique is therefore more likely to be achieved considering the experimental limitations on strong shock generation.

4.2.2 Shock pressure amplification in realistic spherical implosion

Theoretical description of the ignition shock propagation in the gas of an imploded HiPER target have shown that in order to ignite, the ignition shock needs to have a pressure of 20 Gbar when it enters the gas[19]. This pressure is far above the achievable ablation pressure. Fortunately, during its propagating from the ablation front (the shell outer surface) to the inner shell surface, the ignition shock pressure is amplified by various mechanisms. The overall shock amplification [19] writes $\chi = p_{sf}/p_{si} = \chi_{coll}\chi_{imp}\chi_{shell}$, where p_{si} and p_{sf} are the initial and final shock ignition shock pressure, respectively. χ_{coll} is the shock amplification due to its collision with the main diverging shock as presented in the previous section. Its value can range from 2 to 6 depending of the strength of the shocks (mostly on the strength of the main diverging shock). χ_{imp} is the amplification due to the overall pressure amplification of the target due to its implosion. Finally χ_{shell} corresponds to the ignition shock amplification due to the pressure and density gradients in the shell. The evaluation of these two last amplification factors requires a more precise description of the shell during the implosion.

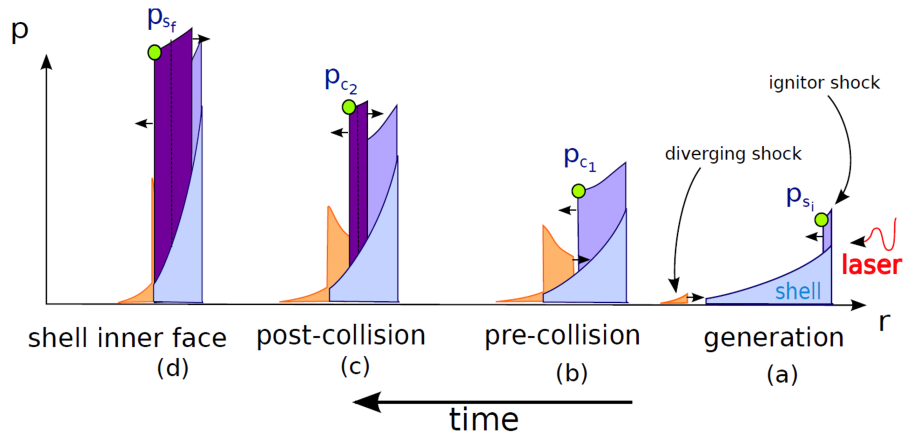


Fig. 4.19 Pressure profiles at four different steps of the ignition shock propagation: (a) the ignition shock is generated at the shell outer surface while the main diverging shock is propagating in the gas, (b) state before the shocks collision, (c) state after the shocks collision, (d) the ignition shocks reaches the shell inner surface [19].

Due to the mechanism of acceleration of the shell, its pressure and density profiles are not homogeneous as it has been assumed in the previous section. As presented in Figure 4.19 (a), the accelerated shell is characterized by a positive gradient of pressure and density. Indeed, the outer shell surface is maintained at the ablation pressure while the inner shell surface is at the pressure of the gas. Before the collision of the main diverging shock with the gas-shell interface, the gas pressure is negligible, so that the shell inner surface expands in the gas, leading to this profile. On the other hand, when the main diverging shock is propagating in the shell, the part of the shell behind it is decelerated. Due to accretion effect, it is characterized by a steep negative gradient of pressure and density as presented in 4.19 (b). Considering the ignition shock propagation, the shell can be separated in two main parts: the outer part is accelerated and has a positive gradient of pressure and density while the inner part is decelerated and has a steeper negative gradient. Figure 4.19 presents the profiles of pressure at four different steps of the ignition shock propagation. Between the generation (a) and the pre-collision (b) steps, the shock is propagating in the accelerated part of the shell. Then it collides with the diverging shock. Finally, it propagates in the decelerated part (from the post collision (c) to the shell inner surface (d)) until it breaks out in the gas.

The values of χ_{imp} and χ_{shell} are very different between these two parts. As the ignition shock propagates inward in the positive gradient of the accelerated part, its pressure decreases, leading to values of χ_{shell} smaller than one. The pressure amplification due to the shell convergence χ_{imp} in the accelerated part is positive but small. These two effects compensate each other leading to an overall shock amplification χ close to one. This is observed in

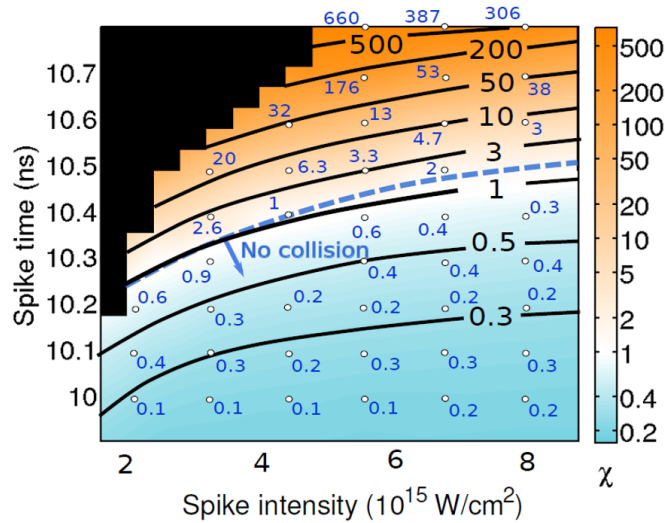


Fig. 4.20 Overall shock pressure amplification in the shell as function of the spike launching time and spike intensity for a HiPER target. The white dots represent results from CHIC simulations [19].

Figure 4.20 when the ignition shock launching time (spike time) is too early so that it breaks out in the gas before the main diverging shock as reached the gas-shell interface. Under the blue dashed line, only the mechanism of amplification in the accelerated shell contribute to the ignition shock pressure. Over this line, the ignition shock is also amplified by the shock collision and by the pressure amplification χ_{imp} and χ_{shell} in the decelerated part of the shell. In this part, the shell pressure quickly increases leading to amplification values of $\chi_{imp} \simeq 15$. Additionally, the shock propagates in a positive gradient of density and pressure which increases is pressure by a factor $\chi_{shell} \simeq 2$. The overall pressure amplification is presented in Figure 4.20. For late launching time of the ignition shock, the pressure amplification can reached very high values. In practice, the ignition shock cannot be launched too late due to the issues of robustness and rarefaction waves discussed in the previous section. Additionally, the hot spot pressure increases at later time, which leads to higher requirement on the ignition shock pressure when in enters the gas.

An overall shock pressure amplification of 80 is considered to be reasonable. In this case, the required 20 Gbar of shock pressure at the inner shell surface can be achieved with an ablation pressure ~ 300 Mbar. Such ablation pressures have been demonstrated experimentally [29].

4.3 Experimental study of implosion at relatively low spike intensity

An experiment has been realized on Omega aiming to measure the ablation front trajectories of implosions driven by shock ignition relevant pulses. The technique used for these measurements was the self emission shadowgraphy [71], a novel diagnostic on the Omega Laser facility [10].

4.3.1 Experimental setup

Figure 4.21 presents the target and laser pulses used in the experiment. The experiment used "warm" 40 μm thick CH shell with a outer radius of 330 μm and filled with D_2 at 12.6 bar. While cryogenic DT targets are more relevant for study of implosions, their cost and the possibility of contamination from Tritium is such that only a limited number of them are shot at the Omega Laser facility. The implosion of surrogate CH targets allow to extensively study implosions without these issues. This kind of target cannot ignite but the number of fusion reaction from the D_2 gas can be a good figure of merit for the evaluation of the performances of implosion. Also, due to the limited energy available on Omega, the targets have been scaled down in order to have a intensity on target and implosion velocity relevant to full scale implosion.

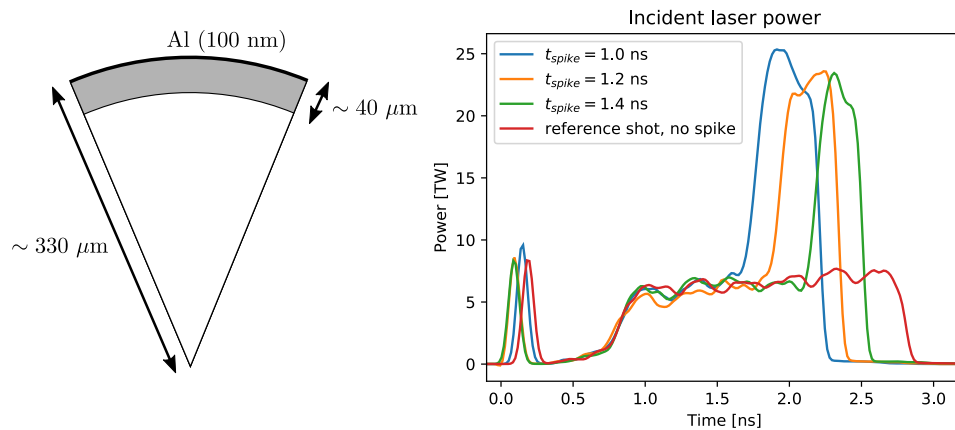


Fig. 4.21 Scheme of the spherical target (left) and measurement of the laser pulse shape (right) used in the experiment. The target is a CH shell filled with D_2 and coated with Al. Four different pulse shapes have been shot, with various delays between the main pulse and the spike. The spike launching time t_{spike} is defined as the delay between the half rise of the compression pulse and the half rise of the spike pulse.

The experiment used the 60 ultraviolet ($\lambda = 0.351 \mu\text{m}$) laser beams of the Omega Laser with polarization smoothing [72], smoothing by spectral dispersion [73] and distributed phases plates [74] SG2 (super Gaussian of order 2.2 with 95% of the energy contained within a $600 \mu\text{m}$ diameter focal spot), in order to have an uniform illumination of the target. The laser pulses had three distinctive parts: the adiabat shaping picket, the compression pulse and the spike pulse. The adiabat shaping picket [75] was a 100 ps long pulse carrying $\sim 1 \text{ kJ}$. It was used to send a decaying shock in the shell, which significantly heat the shell close to the outer surface, mitigating the hydrodynamic instabilities, while keeping the average adiabat of the shell relatively low (this picket has being designed for a shell adiabat of ~ 2.5). The compression and spike pulses had powers of $\sim 7 \text{ TW}$ and $\sim 22 \text{ TW}$, respectively.

To evaluate the intensity corresponding to these powers, the critical density surface has to be considered. Preliminary simulations have shown that, as the target implodes, the position of the critical density goes from the initial target outer radius $R_0 = 330 \mu\text{m}$ to $0.7 R_0$. Therefore, the intensity of the compression pulse on this surface goes from $4.4 \times 10^{14} \text{ W/cm}^2$ at the beginning of the pulse to $8.9 \times 10^{14} \text{ W/cm}^2$ at its end. During the spike, the position of the critical density stay rather constant at $0.65 R_0$ so that the intensity during the spike is $38 \times 10^{14} \text{ W/cm}^2$. To evaluate the hot electron production, it is more relevant to consider the intensity at the quarter-critical density surface. Simulations have shown that during the spike, the quarter critical density is around $1.2 R_0$, which results in an intensity during the spike of $11 \times 10^{14} \text{ W/cm}^2$. These estimations of the intensity have been realized by considering a radial illumination of the target so that the intensity is given by $I_{laser} = P_{laser}/(4\pi R^2)$, where P_{laser} is the foot or spike laser power (7 TW or 22 TW respectively) and R is the position of the critical density (or quarter-critical density) at the considered time. These estimations have been validated though Visrad simulations of the laser illumination on the critical and quarter-critical densities during the spike. These simulations took in account realistic intensity profiles for the 60 beams. The intensities calculated this way are $32 \times 14 \text{ W/cm}^2$ on the critical density and $10 \times 14 \text{ W/cm}^2$ on the quarter-critical density. This intensity is enough so that hot electrons can be produced through Stimulated Raman Scattering and Two-Plasmon Decay, while being significantly lower than the intensity considered in shock ignition implosions. In this study, the hot electron production and their effects on the implosion have been neglected.

The scanned parameter for this experiment was the spike launching time, the time that separates the power rising of the spike compared to the one of the compression pulse. Three launching times t_{spike} have been shot: 1.0, 1.2 and 1.4 ns. Also a shot has been realized without any spike, as a reference. The duration of the spike was constant from shot to shot, with $\sim 800 \text{ ps}$ full width half maximum. But the duration of the compression pulses

depended on the spike launching time, leading to non-energy equivalent shots. Shock ignition experiments and designs usually compare energy equivalent shots in order to put in evidence the gain obtained with this technique. This experiment proposed to compare shots with only one changing parameters (the spike launching time), making them easier to compare to each other for the understanding of the basic physics of shock ignition.

4.3.2 Self Emission Shadowgraphy

During the implosion, the plasma corona created by the laser irradiation emits a high flux of soft X-rays (with energies of few keV). The corona itself is mostly transparent to these radiations while the dense colder shell absorbs them. Especially, the ablation front is characterized by a steep gradient of X-ray absorption due to both density and temperature gradient. The imaging of the target X-ray emission with a pinhole array allows to see the "shadow" of the ablation front as presented in Figure 4.22. The measurement of the ablation front position along different lines of sight and for several times (using a framing camera, each line of sight can record 16 two-dimensional images) allows to reconstruct with the precision its trajectory. The uncertainty on the ablation front position is $10 \mu\text{m}$ due to the point spread function of the imaging system [76]. Also, an accuracy of 10 ps on the absolute timing of the images (compared to the laser pulse) has been demonstrated.

Additionally, during the deceleration phase of the implosion, the temperature of the gas inside the shell can become comparable to the temperature of the plasma corona during the acceleration phase. At this time, the laser irradiation is stopped and the X-ray emission from this hot spot can be seen on the self emission shadowgraphy diagnostic. Since the inner shell surface is also characterized by a sharp gradient X-ray absorption, its position can also be recorded as presented in Figure 4.23.

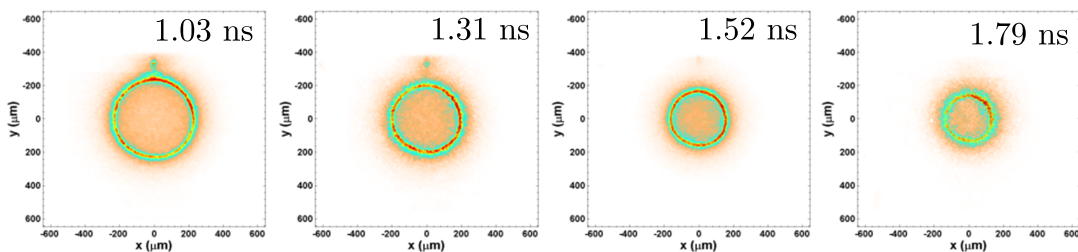


Fig. 4.22 Images of the plasma emission used for the measurement of the ablation front position at several times. This images correspond to the shot with a spike delay $t_{spike} = 1.4 \text{ ns}$.

Figure 4.24 presents the trajectories of the ablation front and inner shell surface for the different spike launching times. At early time, the ablation front trajectory is the same for all

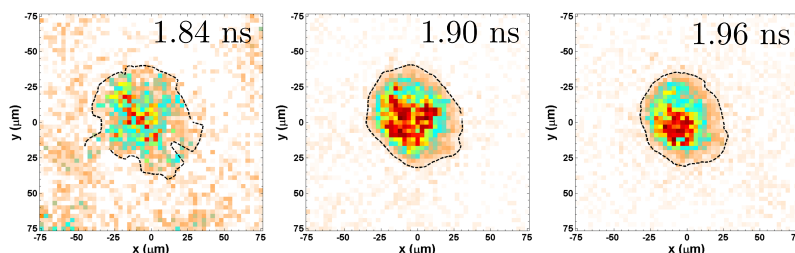


Fig. 4.23 Images of the hot spot emission used for the measurement of the inner shell position at several times. This images correspond to the shot with a spike delay $t_{spike} = 1.4$ ns.

the shot as expected. Then, for each shot, the ablation front is accelerated inward at the time of the spike launching time. The reference shot, without any spike pulse, has the slowest ablation front trajectory. From the trajectories of the inner shell surface, the time of the beginning of the deceleration phase can be infer. It is close to the time of the first measured point, when the gas start to be hot enough to emit X-rays. It appears that the deceleration phase starts earlier for the shot with the spike launched at 1.0 ns and 1.2 ns, compared to the reference shot. For the shot with a spike launched at 1.4 ns there is no visible difference with the reference shot. This suggests that launching the spike at 1.0 or 1.2 ns was too early, while launching it at 1.4 ns could be on time or too late. Indeed, a well time ignition shock should not modify the starting time of the deceleration phase. The deceleration phase starts when the main shock, sent at the beginning of the compression pulse, reaches the inner shell surface after having bounce on itself at the center of the gas. The ignition shock is supposed to collide with this main shock transmitted in the shell and therefore, after the beginning of the deceleration phase.

4.3.3 LILAC simulations

In order to analyze in details the effect of the spike launching time on the ignition shock propagation and on the implosion performance, radiation hydrodynamic simulations reproducing the trajectories of the ablation front and of the inner shell surface have to be realized. These simulations have been performed using the one-dimensional code LILAC [30] which include non-local electron transport [77] and cross beam energy transfer [78]. The measured laser pulse and target parameters have been considered. Figure 4.25 presents the electronic temperature as a function of time and radius from the simulation of the shot with $t_{spike} = 1.4$ ns. The solid blue line corresponds to the position of the ablation front in the simulation. The three parts of the laser pulse are clearly visible from the plasma temperature above the ablation front. First the picket creates a plasma which quickly cools down. At ~ 1 ns the

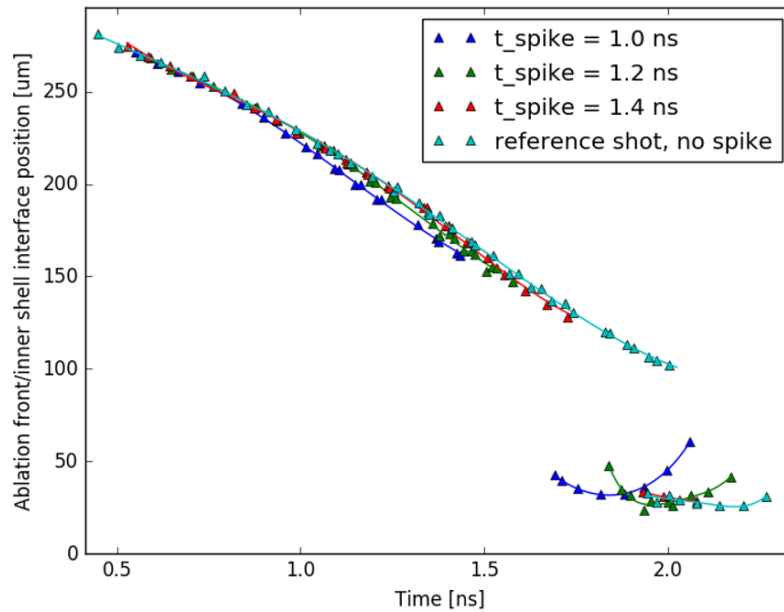


Fig. 4.24 Trajectories of the ablation front and inner shell surface recorded through self emission shadowgraphy for the different spike launching times. The uncertainties on the position of the ablation front and inner shell surface are $\pm 10 \mu\text{m}$, $\pm 10 \text{ps}$ [76].

compression pulse starts, creating a plasma of rather constant temperature and accelerating the target inward. Then at $\sim 2.4 \text{ ns}$, 1.4 ns after the launching of the compression pulse, the spike pulse starts, rising the corona temperature and accelerating moreover the implosion of the target. At the beginning of each of these parts of the laser pulse (at 0, 1.0 and 1.4 ns), a shock is sent through the shell. These shocks propagate in the shell, rising its temperature, until they breakout in the gas. Due to the lower density of the gas, the shocks propagate faster in it and lead to a larger increase of its temperature. Finally, during the deceleration phase, the gas temperature increases a lot while the shell stays relatively cold. This is the formation of the hot spot.

The white dots and white triangles are the measured positions of the ablation front and inner shell surface, respectively. They show good agreement with the simulation. Especially, the agreement between the measured and the simulated ablation front trajectories is better than $5 \mu\text{m}$. The simulations of the other spike launching times show similar agreement. This value is less than the precision achievable with self emission shadowgraphy and better agreements might be achieved by post processing the LILAC simulations with collisional-radiative code (such as *Spect3D* [79]) and convolution with the point spread function of the diagnostic [76].

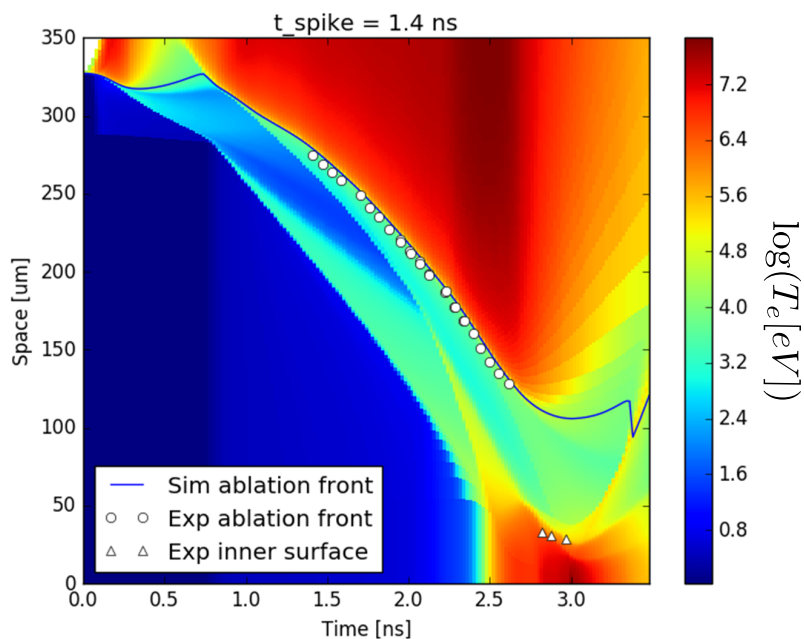


Fig. 4.25 Logarithm of the electron temperature as function of time and radius from a LILAC simulation of the shot with a spike launching time $t_{spike} = 1.4$ ns. The solid blue line corresponds to the ablation front position from the simulation. The white dots and white triangles are the measured ablation front and inner shell surface positions, respectively. The uncertainties on the position of the ablation front and inner shell surface are $\pm 10 \mu\text{m}$, ± 10 ps [76].

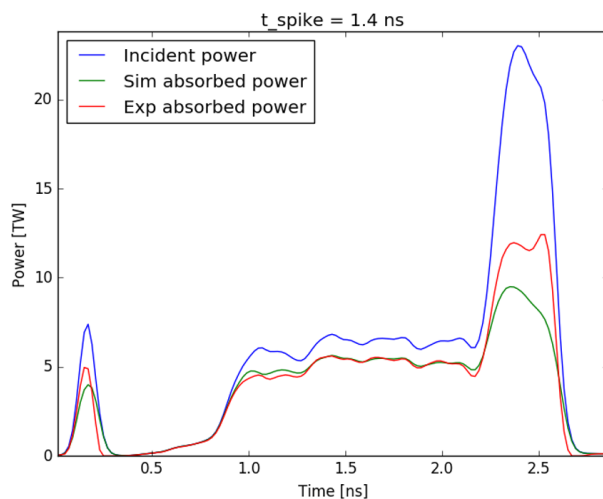


Fig. 4.26 Comparison between the measured and simulated laser absorption for the shot with a spike launching time $t_{spike} = 1.4$ ns.

In the experiment, the time-resolved absorbed laser power has also been measured using Full Aperture Back Scattering diagnostic [80]. Figure 4.26 presents the measured and simulated absorbed powers for the shot with $t_{spike} = 1.4$ ns. These are in reasonable agreement considering the diagnostic temporal resolution and the assumptions made in the simulation. The difference observed in the shape of the picket absorbed power is mostly due to the resolution of the diagnostic. In this case, it is more relevant to compare the absorbed picket energy (the integrated absorbed power). The measured and simulated absorbed picket energy are indeed in good agreement. The absorption measured during the compression pulse is very well reproduced by the simulation. Finally, the measured absorption during the spike is $\sim 10\%$ larger than in the simulation. This might be due to the assumption made in the simulation that the only absorption mechanism is collisional absorption. During the intense spike, collective effects might increase the absorption (as presented in section 2.3) and lead to the production of hot electron. Further simulations would have to take them in account in order to better reproduce the measured absorption.

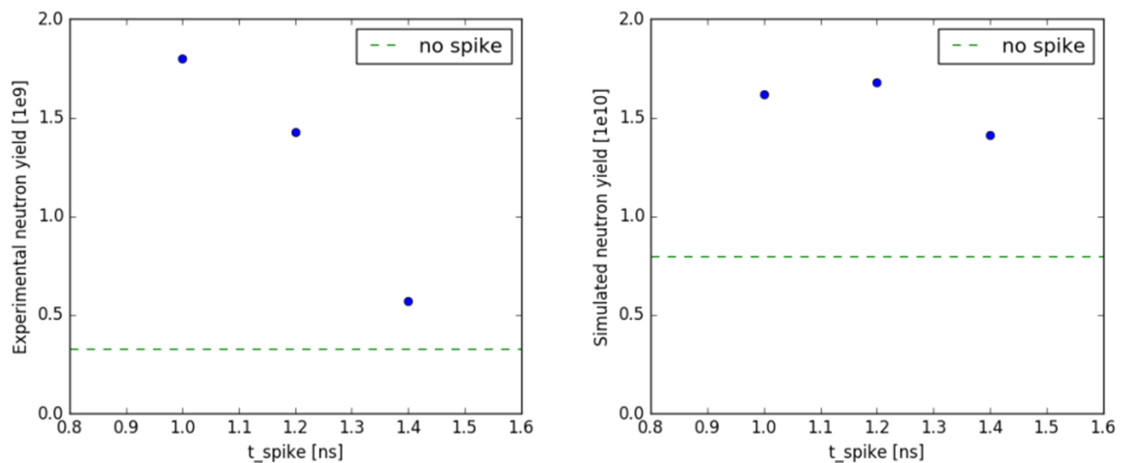


Fig. 4.27 Measured (left) and simulated (right) neutron yield as a function of the spike launching time (blue dots) and for the case without any spike pulse (green dashed line).

Finally the neutron yield have been measured using neutron time-of-flight diagnostic [81]. This diagnostic specifically measures the yield of the 2.45 MeV neutrons from the D-D fusion reactions. The neutron yield equals the number of primary fusion reactions in the gas and therefore, it is a measurement of the performance of the implosion. Figure 4.27 presents the measured and simulated neutron yields as a function of the spike launching time, and for the case without any spike pulse. The simulations predict a yield more than an order of magnitude large than it has been measured. This might indicates that the implosions are strongly perturbed by two-dimensional effects due to inhomogeneities of illumination.

Indeed, extensive work have been realized at the Omega Laser facility in order to optimize the homogeneity of illumination for the baseline down-scaled NIF targets [82]. As a results, implosion of such target are closer to ideal one-dimensional ones and their neutron yield is close to the predictions from simulations. However, shock ignition experiments require higher intensities, that can only be achieved on Omega by reducing the target radius and using phase plates with smaller focal spots. The optimization of the illumination for these shock ignition-like implosions is not as good as for the larger targets and such 2D effects are to be expected. Yet, the measured and simulated neutron yield from this experiment can be qualitatively compared. Both of them show an important degradation of the neutron yield for the latest spike launching time. Especially, the simulation with $t_{spike} = 1.4$ ns show a reduction of the neutron yield of $\sim 15\%$, compared to the simulation with $t_{spike} = 1.2$. This result suggests that early spike launching time are preferable. This is contradictory with the supposition made from the measurement of the inner shell surface trajectory, which seems to indicate that the spike launching time of 1.0 and 1.2 ns were too early. A more detailed analysis of the simulations is necessary in order to understand these results.

4.3.4 Effect of the spike launching time on the implosions performance

As seen in section 4.2.1, the goal of shock ignition is to realize the collision of the ignition shock with the main diverging shock, in the shell and close to the shell-gas interface. In the simulation with $t_{spike} = 1.0$ ns, the ignition shock catches up and coalesces with the main shock before it has reached the center of the gas. In the simulation with $t_{spike} = 1.2$ ns, the main shock had time to reach the center of the gas and the ignition shock collides with it in the gas. For both of these simulations, the ignition shock is clearly sent too early. In this case, the ignition shock ends up increasing the implosion velocity of the target which then decelerates and form a hot spot as in the classical scheme. On the other hand, for the simulation with $t_{spike} = 1.4$ ns, the ignition shock collides with the diverging shock exactly as expected for shock ignition. Figure 4.28 presents the evolution of the pressure around the shock collision from this simulation. The pressure is represented as a function of time and initial coordinates of the fluid element. Using the initial coordinates instead of the real coordinates allows to clearly see the dynamic of the shocks in the shell. In real coordinate, the collision is more difficult to visualize due to the implosion of the target, while in this representation, the ignition shock pressure amplification is clearly visible. At the ablation front, the ignition shock pressure is ~ 100 Mbar (1). Due to convergence effects, its pressure just before the collision with the main diverging shock is ~ 600 Mbar (2). The collision leads to an amplification of the ignition shock by a factor 3.75, so that the pressure just after the collision is ~ 2.25 Gbar (3). Then the ignition shock is amplified though the decelerating

shell. When it enters the gas, its pressure is ~ 7 Gbar (4). Overall, the pressure amplification of the ignition shock from the ablation front to the shell-gas interface is ~ 70 . These different stages of the shock amplification are very close to the ones expected from the theory of shock ignition implosion [19]. Finally, the maximum pressure achieved in the gas is ~ 22 Gbar (5).

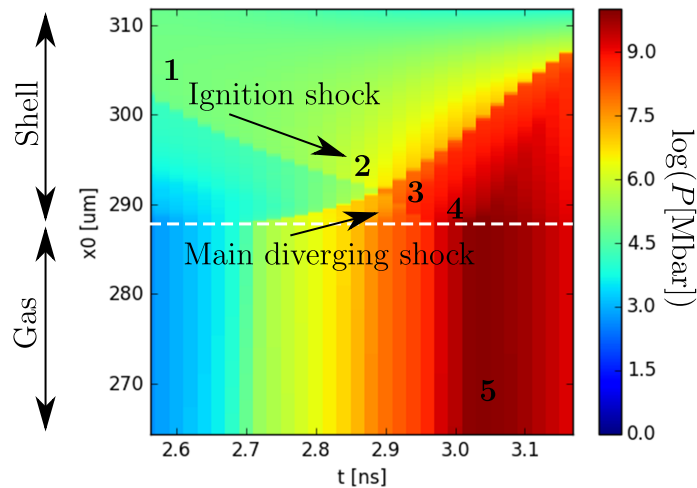


Fig. 4.28 Logarithm of the pressure as function of time and initial coordinate of the fluid element from a LILAC simulation with $t_{spike} = 1.4$ ns. The white dashed line corresponds to the shell-gas interface. The numbers denote the stages of pressure amplification of the ignition shock: 100 Mbar (1), 600 Mbar (2), 2.25 Gbar (3), 7 Gbar (4), 22 Gbar (5).

The simulation with $t_{spike} = 1.4$ ns is almost ideal for shock ignition, yet the corresponding neutron yield is the lowest of the experiment. In order to understand why this simulation seems to have the lowest performances, the thermodynamic conditions of the hot spot, during the deceleration, have to be considered. Indeed, in order to reach ignition, the hot spot has to reach conditions of high areal density and temperature as presented in Figure 1.6. In the case of a simulation where the hot spot is close to ignition, the flux of mass at the inner shell surface has to be considered, so that the hot spot mass increase in time. In these simulation, this flux of mass is negligible and the hot spot is only the heated mass of gas inside the target. Figure 4.29 presents the thermodynamic path of the gas as function of its areal density and electron temperature from the simulations with different spike launching times. The path followed by the simulation without ignition spike (in light blue) is representative of a classic implosion without ignition. In this regime of implosion, far from ignition, the heating from the α particles from the fusion reaction is negligible. The only source term for the gas power balance is the shell kinetic energy. First, this kinetic energy is converted in both temperature and areal density up to ~ 1.35 keV and $\simeq 13$ g/cm². At this time the remaining work from the shell kinetic energy equals the losses due to Bremsstrahlung radiation and electronic

conduction. The gas starts to cool down. The gas areal density continues to increase up to the time when the shell kinetic energy reaches zero. Finally, the target bounces on itself without igniting, leading to the further cooling down of the gas and the diminution of its areal density. The light blue triangle corresponds to the gas condition when the neutron rate (the number of fusion reaction per second) is the largest. It is the time when the gas is the closest to the ignition conditions, but still very far from it.

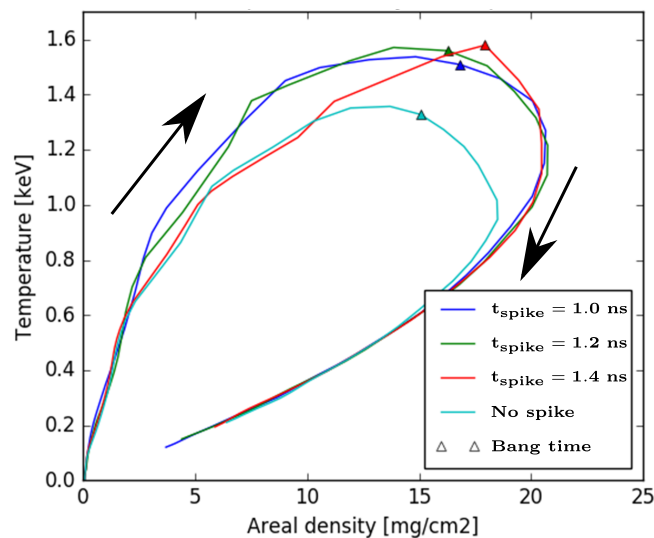


Fig. 4.29 Thermodynamic path of the gas in the plan $T_e, \rho r$ from LILAC simulation for the different spike launching time. The white triangle denotes the gas condition at time of of neutron rate (bang time).

The thermodynamic path of the gas for the simulations with $t_{spike} = 1.0$ ns (in dark blue) and 1.2 ns (in green) are very close to each other. Also, the shape of their path is very similar to the path from the simulation without spike. Actually, these two simulations correspond to classic implosions with an implosion velocity higher than for the simulation without spike. This higher implosion velocity leads to thermodynamic conditions of the gas closer to ignition, resulting in the higher neutron yield observed for these simulations. Yet, both of these implosions are not representative of shock ignition. On the other hand, the thermodynamic path of the gas for the simulation with $t_{spike} = 1.4$ ns (in red) is different. At first, it follows the same path as the simulation without spike. Then, when the ignition shock enters the gas, both the areal density and temperature quickly rise, up to values slightly higher than for the simulations with $t_{spike} = 1.0$ ns or 1.2 ns. At bang time, the gas from the simulation with $t_{spike} = 1.4$ ns has a % 10 increase in both areal density and temperature compared to the simulation with $t_{spike} = 1.2$ ns. Therefore, it is closer to ignition than the other simulations.

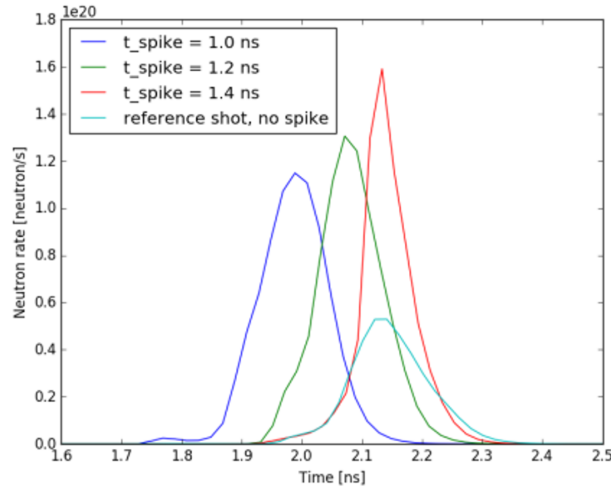


Fig. 4.30 Neutron rate from LILAC simulation for different spike launching time.

Figure 4.30 presents the neutron rate from the simulations with different spike launching times. The simulated neutron yield is the integral of these curves and the bang time (as presented in Figure 4.29) is their maximum. As expected from the gas thermodynamic conditions at bang time, the simulation with $t_{spike} = 1.4$ ns has the highest neutron rate (20 % increase compared to the simulation with $t_{spike} = 1.2$ ns). The low neutron yield observed for this simulation is actually due to the smaller duration of neutron emission, compared to the simulations with $t_{spike} = 1.0$ ns and 1.2 ns. For shock ignition implosion, the maximum of neutron rate is actually much more relevant in order to qualify the implosion performances than the neutron yield. In the case where the hot spot reaches the conditions of ignition, the burn of the target takes only few tens of picoseconds. Therefore, the dynamic of the neutron emission, especially after bang time, is not relevant in order to estimate if an implosion is close to ignition or not. Only the instantaneous neutron rate should be considered.

4.4 Conclusion

In this chapter, the effect of hot electron have been neglected in order to highlight key elements of shock ignition hydrodynamic.

Shock ignition like implosions in planar geometry have been simulated. The code used for these simulations combine the solving of shock interaction presented in the previous chapter with a propagation code. This code has successfully reproduced the results presented by Nora and Betti [70], which have been simulated with the one-dimensional hydrodynamic code LILAC. The mechanism of pressure amplification in the hot spot (in the classical

scheme) have been identified as the bouncing back and forth of the main shock in the gas. The main objectives of the shock ignition have also been identified: avoid the formation of rarefaction waves due to shocks coalescence in the shell and create a second strong shock bouncing back and forth in the gas. The evolution of the central pressure obtained by Nora and Betti have been well reproduced with this code. Yet, shock ignition timing and pressure proposed by Nora and Betti relies on three discontinuities collision which cannot be realized experimentally.

A more realistic shock timing have been proposed and investigated with the code developed in the first section. The ideal shock ignition implosion requires the quasi-symmetric collision of the ignition shock and the main diverging shock in the shell and close to the shell-gas interface (in order to avoid the formation of rarefaction waves from shocks coalescence). Additionally the mechanism of ignition shock pressure amplification in realistic implosions have been discussed. The overall amplification is due to three factors $\chi = \chi_{coll}\chi_{imp}\chi_{shell}$. The amplification due to shock collision χ_{coll} has been evaluated in the previous section. The amplification factors χ_{imp} and χ_{shell} correspond to the effects of the shell convergence in spherical geometry and the shell pressure and density profiles, respectively. An overall pressure amplification of 80 is found to be reasonable. Therefore an ablation pressure of 300 Mbar would be sufficient to reach the ignition shock pressure of 20 Gbar at the inner shell surface required for ignition.

Finally, a shock ignition relevant experiment realized on Omega Laser Facility have been presented. The experiment aimed at the measurement of the ablation front trajectories of implosions driven by pulses with different spike delay. These measurements have been realized with Self Emission Shadowgraphy and well reproduced with LILAC simulations. The simulation of the implosion with the latest spike launching time of 1.4 ns appeared to be close to ideal for the shock ignition scheme: the ignition shock and main diverging shock collide in the shell and close to the shell-gas interface resulting in a shock pressure amplification of 70. Compared to the other spike launching time, this simulation showed a variation of +10% in gas temperature and areal density, +20% in neutron rate and -15% in neutron yield. These results seems to indicate that the neutron yield is not a good figure of merit in order to evaluate the performance of shock ignition implosions. The measurement of the neutron rate is necessary in order to qualify such implosions.

Chapter 5

Effect of hot electron in planar geometry

Hot electrons are expected to have a significant impact on the hydrodynamic of implosions. In classical scheme, they might preheat the shell, leading to a deterioration of the implosion performance [83]. Indeed, the penetration power of electrons through matter increases rapidly as their energy increases. Compared to the thermal electrons of the plasma corona, the higher energy of the hot electrons allows them to penetrate in depth in the target, increasing its entropy and therefore making it more difficult to compress to the high densities required for ignition. However, the laser intensity used in the classical scheme is low enough so that the amount of hot electrons produced is very small and their effect can be neglected. On the other hand, in the shock ignition scheme, the intensity used during the spike is high enough so that a non-negligible amount of hot electrons can be produced. In that case, their effect on the implosion has to be considered. Since the hot electrons are produced at the end of the acceleration phase, when the shell areal density has risen significantly, they might be stopped in the outer part of the imploding shell. In this case they would not preheat the inner part of the shell. Instead they could increase the pressure of the ignition shock so that their effect on the implosion would be beneficial. An accurate description of the hot electron production and energy deposition in the hydrodynamic codes used for the design of implosions is therefore necessary in order to determine if their effect is beneficial or detrimental.

CHIC is a 2D Lagrangian radiation hydrodynamic code developed at CELIA in which a module allowing the description of hot electrons has been recently implemented. Experimentally, this module has been validated through few experiments only [32]. The comparison of the code predictions with data from experiments dedicated to the measurement of the effects of the hot electrons on hydrodynamic is necessary. While the realization of such experiments in spherical geometry is more relevant within the goal of characterizing the hot electron effects on shock ignition implosions, the spherical geometry lessens significantly the diagnostics that can be used. Additionally, the number of kilojoules laser facilities with spherical

geometry is very small (Omega, NIF ...) and accessing these facilities for the realization of experiments can be difficult. On the other hand, experiments in planar geometry have a much easier access for the diagnostics. This allows to have stronger constraints for the validation of the hot electron description in hydrodynamic codes. Also, planar geometry experiments can be realized on a larger number of laser facilities, which simplifies their access and diversifies the laser plasma interaction parameters.

In this chapter, the model implemented in CHIC for the description of the hot electrons is first described. Then three experiments realized in planar geometry and relevant to shock ignition are presented. The first one is an experiment that have been realized on the Prague Asterix Laser System [33]. Its interpretation has been realized with CHIC in order to reproduce the main observable of the experiment, the Streak Optical Pyrometry signal. Then an experiment realized on OmegaEP is presented. It has been designed using the code CHIC to find optimal parameters that allows to see the effects of hot electrons on hydrodynamic. The main diagnostic used in this experiment was the side radiography of the shock perturbed by the hot electrons. Finally, an experiment that will be realized on LMJ is presented. Its design, which is similar to the experiment on OmegaEP, has been realized using the code CHIC as well. The goal of this experiment is also the side radiography of a shock perturbed by hot electrons with plasma conditions relevant to shock ignition.

5.1 Description of hot electron in CHIC

In CHIC, the main model for the description of the laser propagation is based on Ray Tracing [84]. With this model, the laser beam is represented by a large number (few thousands) of infinitely thin rays which follow the laws of geometrical optics propagation. This model is computationally efficient and allows a good description of laser refraction and plasma heating through collisional absorption. But it is not sufficient for the modeling of laser plasma instabilities which requires knowledge of the laser intensity. Indeed, with the Ray Tracing model, the rays do not have a width and therefore they are characterized by their power only.

In order to have an accurate description of the intensity in the plasma, the Paraxial Complex Geometrical Optics (PCGO) [85] model has been developed. With this model, the laser beam is represented using a bunch of thick rays, each having a Gaussian intensity profile. The symmetry axis of each thick ray follows the laws of Geometrical Optics, while the Gaussian intensity profile and wave front curvature are described by a complex phase. This phase is calculated in the paraxial approximation, meaning that the radius of the thick rays is small compared to the plasma inhomogeneities. Figure 5.1 presents a comparison

in absorbed power between the Ray Tracing and PCGO models. The laser beam has an incidence angle of 50° and a initial radius of $21 \mu\text{m}$ with zero curvature at the plasma boundary. The plasma is characterized by a linear ramp $n_e/n_c = 1 - x/L$, with $L = 500 \mu\text{m}$. The modeling of the beam using Ray Tracing (left) used 10000 rays while the PCGO model (right) used a single ray. With the PCGO model, the position of the minimum width of the beam is shifted from its turning point. This is due to both refraction and diffraction of the Gaussian beam. This behavior is in agreement with the theory of Gaussian beam propagation[85]. The Ray Tracing model does not reproduce this shift.

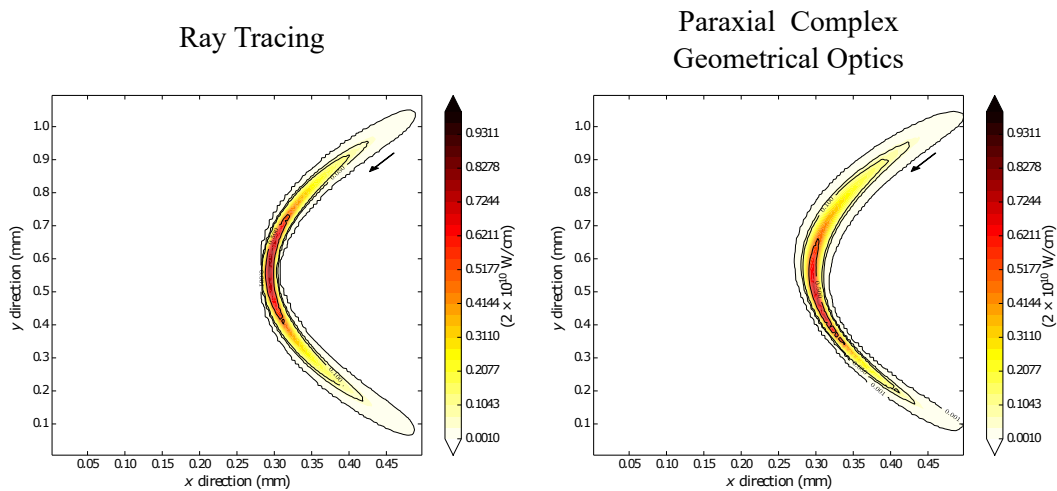


Fig. 5.1 Power absorbed by inverse bremsstrahlung in a linear density gradient using a single PCGO thick ray with an incidence angle of 50° [85]

However, the use of a single PCGO thick ray is not sufficient to reproduce the global characteristics and the overall intensity fluctuation statistic of a realistic beam. In this case, a bunch of overlapping thick rays has to be used. Figure 5.2 presents the intensity distribution obtained with 120 PCGO thick rays, mimicking the PALS beam near its focal spot. The intensity map (left) shows that the overlapping of the thick rays results in an inhomogeneous intensity distribution in both x and y directions which corresponds to a pseudo-speckle pattern mimicking the realistic speckle pattern of the beam. The intensity profile for $x = 0$ (right) shows this pseudo-speckle pattern along the direction transverse to the main axis of propagation of the beam. Along time, the position of the focal points of the rays are changed so that the time average intensity reproduces the global beam characteristic (a Gaussian with a full width half maximum of $150 \mu\text{m}$ in this example).

After that an accurate description of the laser intensity in the plasma has been obtained with the PCGO model, the hot electron source parameters resulting from laser-plasma interaction can be characterized. The mechanisms of generation of hot electrons are the stimulated Raman scattering, two-plasmon decay and resonant absorption. In CHIC, the

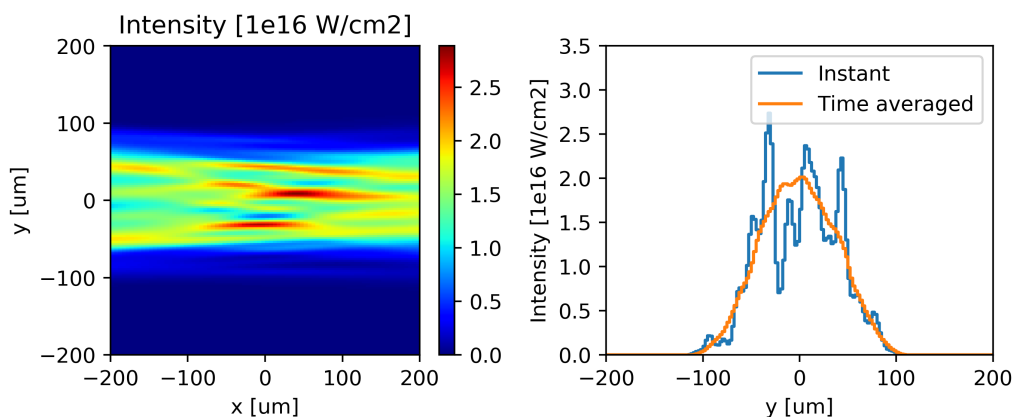


Fig. 5.2 Intensity distribution obtained with the 2D PCGO model, mimicking the PALS beam near its focal point. 120 thick rays are randomly focused in a box surrounding the focal spot.

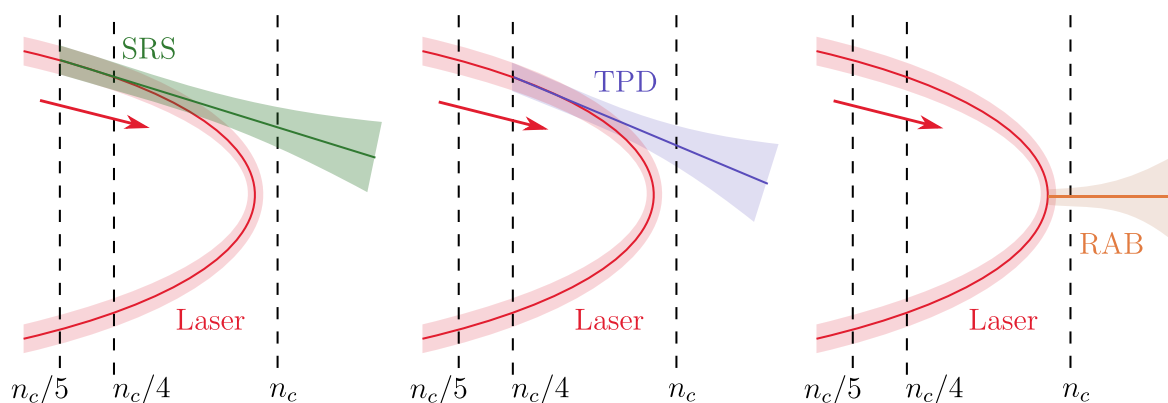


Fig. 5.3 Schematic of the hot electron beam generated by a PCGO thick ray propagating in a density gradient. First, the stimulated Raman scattering (SRS) is evaluated at the position $n_e = n_c/5$. Then the two-plasmon decay (TPD) is evaluated of the position $n_e = n_c/4$. Finally the resonant absorption (RAB) is evaluated at the thick ray turning power.

source parameters for each of these mechanisms are evaluated one after another in order to be consistent with respect to the laser beam propagation. Figure 5.3 presents a schematic of the hot electron beams generated by a PCGO thick ray propagating in a plasma gradient. The stimulated Raman scattering (SRS) and two-plasmon decay (TPD) sources are evaluated at the positions $n_e = n_c/5$ and $n_e = n_c/4$, respectively. This ensures that the SRS takes place before the TPD instability, in a spatial sense. The resonant absorption (RAB) source is then evaluated at the thick ray turning point.

The position and width of the source are the ones of the thick ray where the source is evaluated. For the SRS and TPD sources, the main direction of the hot electron beams is the one of the thick ray, while for RAB the direction is the normal to the thick ray direction. The hot electron temperatures and conversion efficiencies are computed from the plasma parameters at the position of the source using the scaling laws presented in Chapter 2. Especially, the laser intensity considered for the calculation of these parameters is the total intensity resulting from the overlapping of multiple thick rays (except for RAB where only the individual thick ray intensity is considered). The power of the hot electron sources is then given by $P_h = P_{PCGO}^- \times \eta_h$, where P_{PCGO}^- is the power of the PCGO thick ray just before the hot electron source and η_h the conversion efficiency of the considered mechanism. The power of the laser ray after the source, P_{PCGO}^+ , depends of the mechanism. For SRS, considering that the power of the backscattered light equals the power of the SRS hot electron source, $P_{PCGO}^+ = P_{PCGO}^- - 2P_{SRS}$. For TPD, hot electrons are emitted both forward and backward but the backward emission can be neglected as they do not heat the target. Considering that an equal amount of power for the hot electrons is emitted forward and backward, the power of the laser ray after the TPD source is $P_{PCGO}^+ = P_{PCGO}^- - 2P_{TPD}$. For RAB, all the energy lost by the thick ray is considered to be transferred to the hot electron source so that $P_{PCGO}^+ = P_{PCGO}^- - P_{RAB}$.

Once that the hot electron source parameters have been computed, the hot electron beam propagation and energy deposition have to be described. In CHIC, it is done using a model based on the angular scattering approximation [86]. In this model, an initially collimated (without any initial divergence) mono-energetics hot electron beam has its width increasing as it propagates through the target (mainly due to electron-ion collisions). Assuming that the beam propagates along the direction z , its width w increases at the rate

$$\frac{dw}{dz} = 2 \frac{\sqrt{1 - \langle \cos \theta \rangle^2(z)}}{\langle \cos \theta \rangle(z)}, \quad (5.1)$$

where $\langle \cos \theta \rangle(z)$ is the mean diffusion angle given by

$$\langle \cos \theta \rangle(z) = \exp \left[- \int_0^z 4\pi b_0^2 \ln \Lambda_{ei} dz' \right], \quad (5.2)$$

with b_0 is the impact parameter and $\ln \Lambda_{ei}$ the electron-ion collision Coulomb logarithm. Both of these quantities are computed from the hydrodynamic quantities T_e , T_i and ρ , which are interpolated continuously along the beam propagation path z' . As the beam propagates through the target, its energy ε decreases at the rate

$$\frac{d\varepsilon}{dz} = - \frac{1}{\langle \cos \theta \rangle(z)} S_e(\varepsilon), \quad (5.3)$$

where $S_e(\varepsilon)$ is the electron stopping power, which is mostly due to electron-electron collisions.

Since the hot electron beams come from Gaussian PCGO thick rays, they also have Gaussian intensity profiles, and therefore their propagation can be modeled using thick Gaussian rays, similarly to the PCGO laser rays. This allows to use the efficient projection algorithm developed for the PCGO rays. The Gaussian hot electron beams have no initial curvature (so that $\langle \cos \theta \rangle(0) = 1$), they propagate in straight line and the variation of their width is given by Eq. (5.1). The angular scattering approximation allows to describe the propagation of mono-energetic beams only and therefore, the hot electron sources which are characterized by a Maxwellian temperature, have to be approximated using a mutligroup description. With this description, the hot electron source of temperature T_h is split in a few tens a mono-energetic sources with energy ranging from $0.2T_h$ to $8T_h$. The source energy distribution is considered to be Maxwellian with two degrees of freedom (since this model is implemented in 2D hydrodynamic code), so that

$$f_h(\varepsilon_h) = \frac{1}{T} \exp \left[- \frac{\varepsilon_h}{T_h} \right]. \quad (5.4)$$

Therefore, the number of particles emitted by the source per unit time is $\dot{n}_h = P_h/T_h$, with P_h the power of the source. The number of particles emitted per unit time in the group k is then given by

$$\dot{n}_k = \int_{E_{k-1/2}}^{E_{k+1/2}} f_h(\varepsilon_h) d\varepsilon_h, \quad (5.5)$$

with $E_{k\pm 1/2}$ the intermediate energy between the group k and the group $k \pm 1$. The total energy deposited in the plasma by the hot electron beam is then the sum of the energy deposition resulting from the mono-energetic beams. Figure 5.4 presents a comparison of the energy deposition integrated along the transverse beam direction along the propagation axis of a hot electron beam with a temperature of 30 keV (left) and of 100 keV (right). Results with

increasing number of groups N_g are presented and compared to the energy deposition obtained using the M1 model [87–89] as a reference. M1 model is an angular moment approximation of the Vlasov-Fokker-Planck equation, based on entropy maximization principles, that is implemented in CHIC. For higher number of groups, the energy deposition converges toward the results from the M1 model. In the following simulations, 50 groups are being used as a trade off between precision of the energy deposition and computation time.

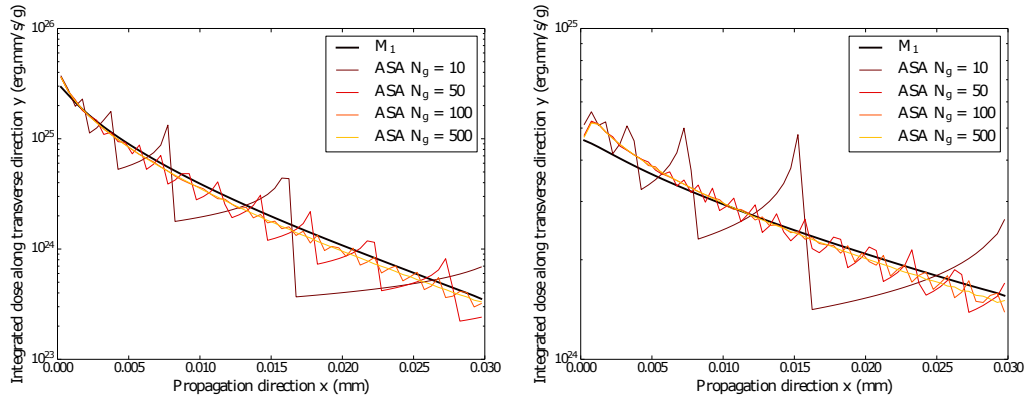


Fig. 5.4 Energy deposition integrated along the transverse beam direction as a function of the propagation direction for hot electron beam of temperature of 30 keV (left) and 100 keV (right). Results from the ASA model with different number of energy groups N_g are compared to the results from the M1 model.

Finally, a concern has to be addressed about the global divergence of the hot electron beam. Indeed, as seen in the chapter 2, the hot electrons resulting from TPD are expected to have a divergence significantly larger than the ones resulting from SRS. As seen with equation 5.1, the hot electron beams have a divergence due to the angular scattering approximation model. Additionally, the variation in direction of propagation of the PCGO thick rays, combined with their refraction in the under-dense plasma, results in a spread of the initial directions of the individual hot electron beams which broaden the electron beams divergence. However, both of these effects do not allow to reproduce the variation in beam divergence between SRS and TPD. To do so, an initial divergence of the electron beams has to be added. This has been realized by considering a user-defined beam aperture θ , which is specific to the mechanism producing the hot electrons. TPD accelerates hot electrons within a $\pm 45^\circ$ cone so that $\theta_{TPD} = \pm 45^\circ$. Hot electrons accelerated by SRS are more directional and they have been simulated by taking in consideration either $\theta_{SRS} = 20^\circ$ [32] or with no initial divergence [90] so that $\theta_{SRS} = 0^\circ$. For RAB, the hot electrons are accelerated only in the direction of the beam so that $\theta_{RAB} = 0^\circ$. The modeling of the initial beam divergence is realized by splitting the hot electron source in multiple sources with no initial divergence

($\langle \cos \theta \rangle(0) = 1$ as considered before) but with a main direction which ranges homogeneously between $-\theta$ and $+\theta$. Also, the hot electrons are assumed to have an isotropic distribution within the beam aperture so that the angular beams have the same power.

To summarize the description of the hot electrons in CHIC:

- The laser beam is modeled by the overlap of N_{PCGO} thick Gaussian rays which propagation follow the Paraxial Complex Geometrical Optics.
- Each PCGO thick ray creates three hot electron sources as it propagates in the plasma: at $n_c/5$ for the stimulated Raman scattering, at $n_c/4$ for the two-plasmon decay and at its turning point for resonant absorption.
- Each hot electron beam source is split in N_θ angular beams (except if the beam aperture is 0°). The beams are homogeneously distributed and they have the same power so that the emission is isotropic within the beam aperture.
- Each angular beam is split in N_g mono-energetic beams which have the same direction of propagation. The energy and particle flux of the beams are given by the Maxwellian energy distribution of the hot electron source.
- Each mono-energetic beam is modeled by a Gaussian beam which propagates in straight line. The increase in beam width as it propagates and its energy deposition are described in the Angular Scattering Approximation.

5.2 Experimental study of shock propagation at high intensity on PALS

The use of short wavelength during the compression phase of a shock ignition implosion is essential in order to guarantee a good hydrodynamic efficiency of the implosion and a low level of parametric instabilities. However, if the hot electrons happened to be beneficial to the shock formation during the spike, longer wavelength might be of interest. The combination of longer wavelength λ and higher intensity I during the spike would lead to a large increase of the interaction parameter $I\lambda^2$, so that a large amount of hot electrons is expected. Current laser facilities cannot realized such experiments, but the basic physics of shock formation and hydrodynamic using laser with longer wavelength can be study on intermediate laser facilities. The determination of the hot electron source parameters at these wavelength and their effect of hydrodynamic is necessary for the benchmarking of hydrodynamic codes prior

to their use for the design of implosions with different wavelengths between the compression and spike pulse.

In this context, an experiment has been realized on the Prague Asterix Laser System [33] (PALS) aiming to characterize hot electron populations and shock formation at intensities relevant to shock ignition.

5.2.1 Experimental set-up and diagnostics

PALS is a single beam laser capable of delivering 700 J at its fundamental wavelength ($\lambda = 1.315 \mu\text{m}$) and 300 J at its third harmonics ($\lambda = 0.438 \mu\text{m}$) in a 300 ps, full width half maximum (FWHM), Gaussian pulse. In this experiment, the laser was operating at the fundamental wavelength. In a previous experiment, calorimetric tools allowed to determine that only $\sim 50\%$ of the nominal energy is enclosed in the $100 \mu\text{m}$ (FWHM) Gaussian focal spot. Therefore, the effective laser energy during this experiment was 350 J. Figure 5.5 shows the laser power as function of time (left) and the intensity at peak power as function of radius (right). The peak power is 1.10 TW, which results in a peak intensity on axis of $0.97 \times 10^{16} \text{ W/cm}^2$. This results in an interaction parameter $I\lambda^2 = 1.68 \text{ W}\cdot\mu\text{m}^2/\text{cm}^2$ which is largely above the threshold for laser plasma instabilities, so that a significant amount of hot electrons is expected to have been produced.

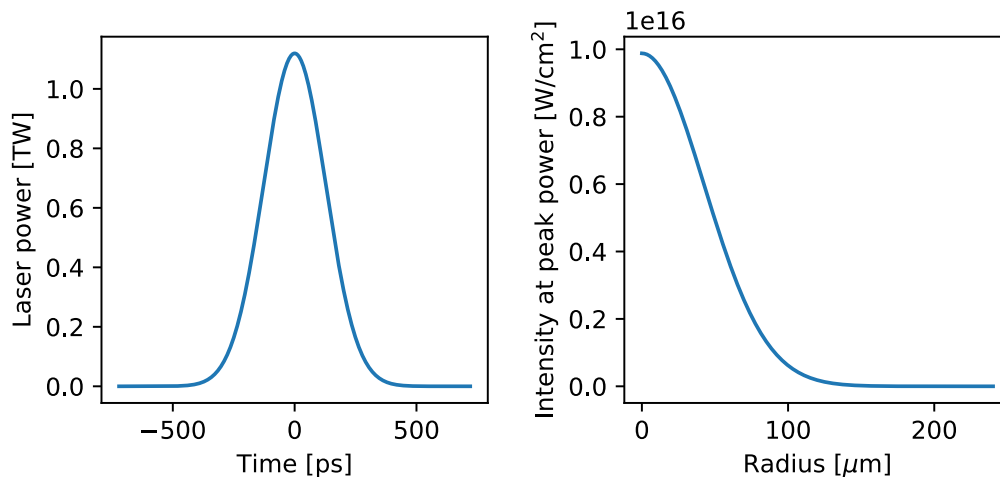


Fig. 5.5 PALS laser power as function of time (left) and intensity at peak power as function of radius (right) for a total energy of 350 J.

The PALS beam was used to irradiate two layers target with a first layer of polystyrene (CH) of variable thickness, ranging from $10 \mu\text{m}$ to $125 \mu\text{m}$, followed by $5 \mu\text{m}$ of titanium. The use of different plastic thicknesses allowed to obtain information on both shock waves

dynamic and hot electron energy spectrum. The information on hot electron energy distribution was obtained by spectroscopy of the K_α emission [91] of the titanium layer at the rear side of the target. When hot electrons reach the titanium layer, their collisions with the cold Ti atoms result in the creation of holes in the inner electronic shells. These holes are then filled by radiative transitions which energies are well defined. For titanium the transition $2p \rightarrow 1s$, which is referred as K_α emission line, corresponds to an energy of 4.51 keV. The measurement of the number of photons emitted by the titanium at this energy gives information on the flux of hot electrons reaching the layer. This flux of hot electrons depends on the thickness of the CH layer. Figure 5.6 presents the penetration depth of hot electrons in CH (at solid density) and for initial energies relevant to the shock ignition. Taking the example of targets with $50 \mu\text{m}$ of CH, only hot electrons with energies $> 50 \text{ keV}$ reach the titanium layer. For target with thicker CH layer, this cut-off energy increases, which results in a reduction of the flux of hot electrons reaching the Ti layer, and therefore a lower K_α signal. Figure 5.7 presents the analysis of the K_α signal as function of the thickness of the CH layer. The black scattered points represent the measured fluxes while the blue squares are the average values at each thickness. The analysis of these data has been realized using the Monte-Carlo code GEANT4 [92] in order to simulate the propagation of the hot electrons and the K-shell emission inside the studied target. The K-shell ionization cross sections were provided by the PENELOPE physics library [93, 94]. The green line in Figure 5.7 is the result of the Monte-Carlo simulation which best-fit the experimental data, using an exponential energy distribution for the HE, with temperature $T_h = 49 \pm 10 \text{ keV}$ and conversion efficiency $\eta_h = 2.69 \pm 0.58\%$.

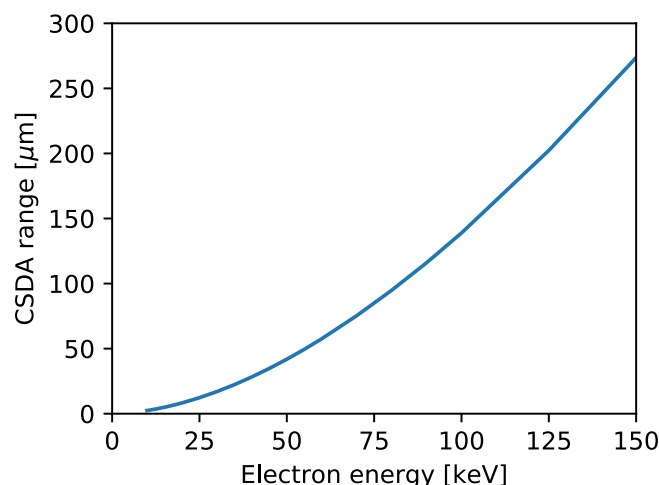


Fig. 5.6 Penetration depth of hot electrons in CH as a function of their initial energy.

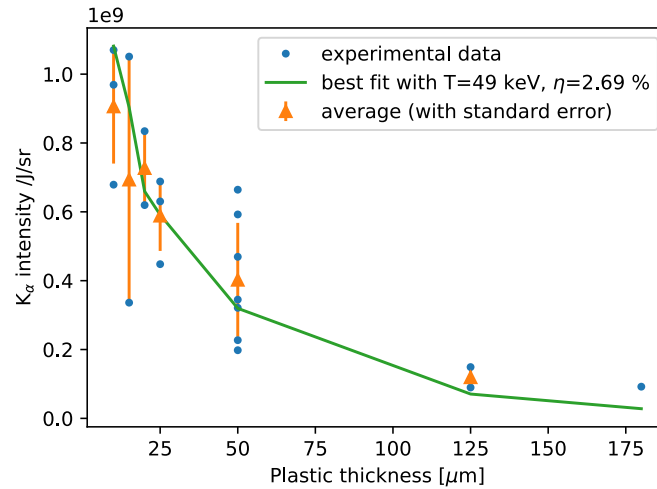


Fig. 5.7 Analysis of the K_α signal. The best fit curve have been obtained using the results from Monte-Carlo simulation assuming an exponential distribution for the hot electrons. The best fit parameters are a hot temperature of 49 ± 10 keV and a conversion efficiency of $2.69 \pm 0.58\%$.

The information on the shock wave dynamic was obtained by using Streak Optical Pyrometry (SOP). The target rear-side is imaged on the slit of a streak camera so that it records the self-emission of the Titanium layer in the visible range of the electromagnetic spectrum[95–97]. Figure 5.8 presents the SOP signal for three plastic thicknesses: $15 \mu\text{m}$, $50 \mu\text{m}$ and $125 \mu\text{m}$. In this Figure, line-outs of the SOP signal as function of time are also displayed. The peak of emission observed at early time is due to the preheating of the rear surface by the hot electrons. Once the laser is stopped, the emission decreases due to the rear surface cooling down. Then, at a later time which depends of the CH thickness, the shock breaks out of the target, increasing the rear side emission. For the target with $125 \mu\text{m}$ of CH, the delay between the peak emission due to the hot electrons and the signal rising due to the shock breakout is 4.1 ± 0.2 ns. For the target with $50 \mu\text{m}$, this delay is 1.0 ± 0.1 ns. For the target with $15 \mu\text{m}$ of CH, there isn't a signal rise due to the shock breakout so that such delay cannot be defined. Yet, after the peak emission due to the hot electrons, the signal decrease is slower for the target with $15 \mu\text{m}$ compared to the other thicknesses. This might be due to the shock breakout.

In order to understand the effect of the hot electrons on the hydrodynamic of the shock, CHIC simulations have been realized. The main objective of these simulations was to reproduce the delay observed on the SOP between the signal from the hot electron and from the shock breakout.

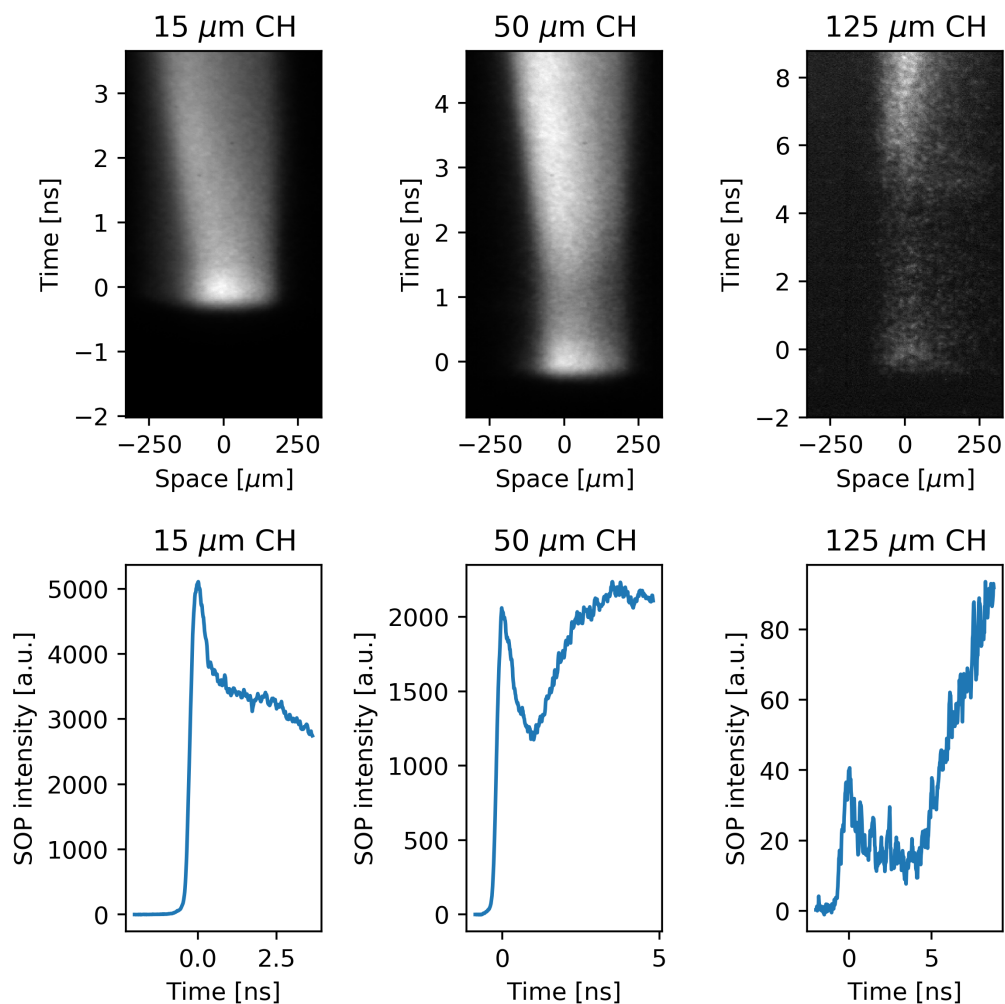


Fig. 5.8 Streak images of rear side emission (streak optical pyrometry) for different thicknesses of the CH layer (top row) and corresponding lineout as function of time (bottom row). The time $t = 0$ is define by the peak of the emission due to the hot electrons. For the target with a 125 μm thick CH layer, the signal rises at $t = 4.1 \pm 0.2$ ns due to shock breakout. For the target with 50 μm of CH, this rises is at $t = 1.0 \pm 0.1$ ns. For the target with 15 μm of CH, the shock breakout time cannot be well defined.

5.2.2 Characterization of shock breakout mistiming due to planar geometry simulations

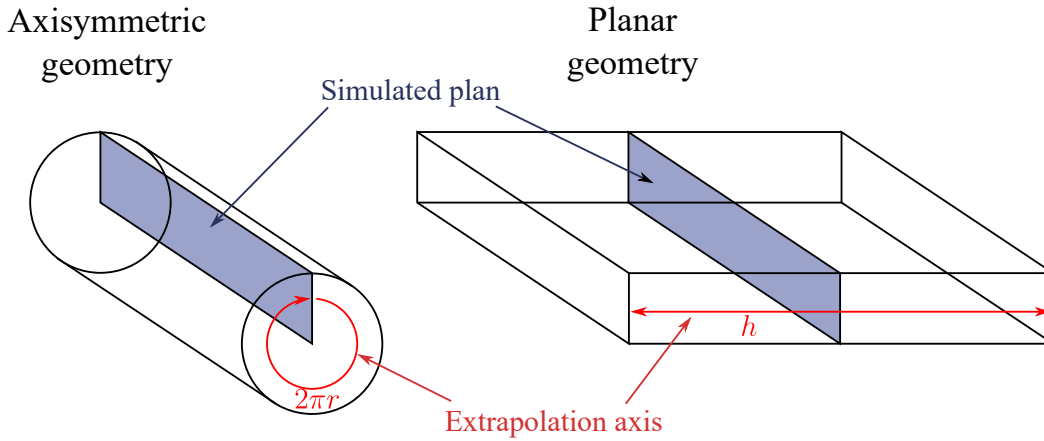


Fig. 5.9 Schematic of the two different extrapolation geometries in CHIC. In axisymmetric geometry, the length of the extrapolated axis increases with the radius r .

CHIC is a two dimensional code so that the hydrodynamic along the third dimension is invariant either by translation or by rotation. When the invariance is by translation, the simulation is in planar geometry and when the invariance is by rotation, it is in axisymmetric geometry. A good understanding of the differences between these two geometries is necessary in order to understand the uncertainty resulting from the simulation of experiments (which are 3D phenomena) using a 2D code. Especially, the PCGO model and hot electron transport package are currently implemented in planar geometry only.

Figure 5.9 shows a schematic of these geometries. In axisymmetric geometry, the simulated plan is (x, r) with x the direction of the normal to the target surface and r the transverse direction. The non-simulated axis is θ . This geometry allows to reproduce the irradiation of a target by a laser with a circular intensity profile and a normal incidence. For example, the laser spot can be Gaussian, as it is the case for PALS, so that the intensity profile is

$$I(r) = I_0 \exp \left[- \left| \frac{r}{r_0} \right|^o \right], \quad (5.6)$$

with I_0 the on axis intensity, r_0 the spot radius at $I = I_0/e^1$ and o the order of the super-Gaussian. The instantaneous laser power, which has to be injected in the axisymmetric simulation, is then

$$P_{axi} = \int_0^{2\pi} \int_0^\infty I(r) r \, dr \, d\theta = 2\pi I_0 \int_0^\infty \exp \left[- \left| \frac{r}{r_0} \right|^o \right] r \, dr. \quad (5.7)$$

However, in some situations the axisymmetric geometry cannot be used and the simulations have to be realized in planar geometry. This is the case when the PCGO and hot electron package are used. It is also the case when simulating a laser irradiating the target surface with an angle of incidence. In such cases, axisymmetric simulations cannot reproduce the asymmetry of the laser irradiation and planar simulations have to be realized.

In planar geometry, the simulated plan is (x, y) with x the direction normal to the target surface (as for the axisymmetric geometry) and y the transverse direction. The non simulated axis is z . Since the simulation is invariant along the z direction, it is not possible to modeled a circular laser spot in planar geometry. Instead the laser spot is a strip. In order to have the best agreement in terms of hydrodynamic between the simulation in planar geometry and the reality (or the axisymmetric simulation), the transverse intensity profile in the planar simulation $I(y)$ has to be identical to the axisymmetric intensity profile $I(r)$. With a super-Gaussian intensity profile, the instantaneous power that has to be injected in the planar simulation is

$$P_{plan} = \int_0^h \int_{-\infty}^{\infty} I(y) dy dz = h I_0 \int_{-\infty}^{\infty} \exp \left[- \left| \frac{y}{y_0} \right|^o \right] dy, \quad (5.8)$$

where $h = 1$ cm is the length of the non-simulated axis in the CHIC planar simulation and $y_0 = r_0$ is the spot width at $I = I_0/e^1$. I_0 and o have the same values as in the the axisymmetric case. This power, injected in the planar geometry, does not correspond to the real power of the laser.

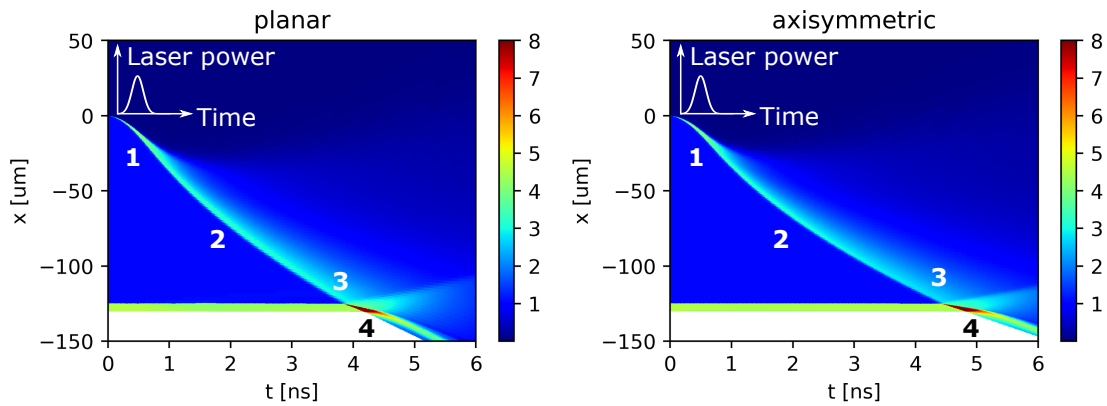


Fig. 5.10 Density as function of time and space from 2D CHIC simulation in planar and axisymmetric geometries. The space axis corresponds to the laser symmetry axis (the normal to the target surface). Both simulations have the same targets ($125 \mu\text{m}$ CH layer + $5 \mu\text{m}$ Ti layer) and laser intensity profiles. A 600 ps difference is observed in the rear side shock breakout time between the two simulations.

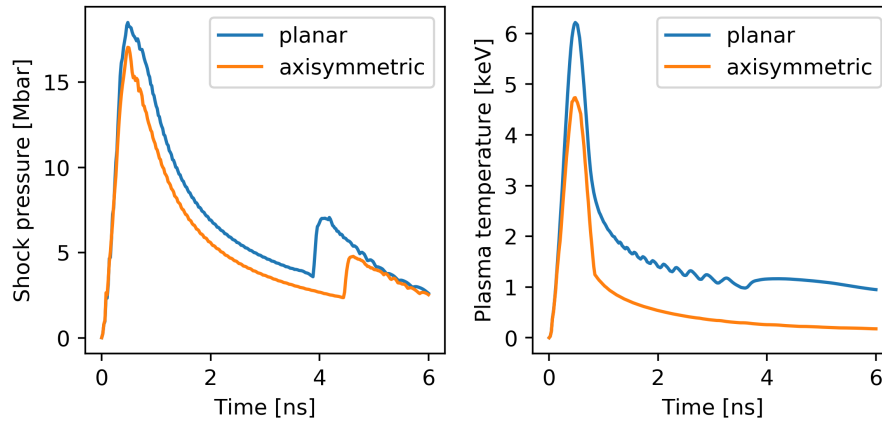


Fig. 5.11 Shock pressure (left) and plasma temperature (right) as function of time for the planar and axisymmetric simulations presented in Figure 5.10. The higher peak plasma temperature in the planar simulation leads to a higher initial shock pressure, and therefore a faster shock wave compared to the axisymmetric simulation

Even if the laser intensity profiles are identical between planar and axisymmetric simulations, differences in the plasma corona and shock hydrodynamic may exist between these. In order to evaluate these differences, two simulations have been realized with identical intensity profiles, corresponding to the PALS pulse of the experiment (Figure 5.5). In these simulations, the target was $125\ \mu\text{m}$ of plastic followed by $5\ \mu$ of Titanium, which corresponds to the thickest target shot during the experiment. Figure 5.11 presents the density as a function of time and space for these two simulations. The space axis x corresponds to the laser spot symmetry axis (the normal to the target surface). In both simulations, the hydrodynamic of the target is very similar:

1. The laser pulse irradiates the target surface initially at the position $x = 0$. It results in an ablation pressure that send a shock wave in the plastic.
2. When the laser power decreases the ablation pressure drops, which results in a rarefaction wave propagating in the compressed plastic. When it reaches the shock front, it results in a blast wave (similarly to presented in Figure 3.8).
3. The blast wave reaches the Titanium resulting a transmitted shock in the Titanium layer and a reflected shock in the CH.
4. The transmitted shock wave beaks out from the rear side of the target.

In the simulation in planar geometry, the shock breaks out at the rear side of the target ~ 600 ps earlier than in the simulation in axisymmetric geometry. This difference is due to an

initially higher shock pressure in the simulation in planar geometry (Figure 5.11, left). Once that the rarefaction wave has reached the shock front, the shock pressure decreases similarly in both simulations. The pressure increase observed around 4 ns in the planar simulation (4.5 ns in the axisymmetric simulation) is due to the collision of the shock with the Titanium layer. The initially small difference in shock pressure leads to a shock slightly faster in the planar simulation, which after ~ 4 ns of propagation, results in the observed difference in shock breakout time between the two simulations. The difference in initial shock pressure is itself due to a difference in peak temperature of the plasma corona (Figure 5.11, right). Indeed, due to higher transverse losses in the axisymmetric simulation, the corona has a lower temperature despite having a larger laser absorption (6.13% of the laser energy in the planar simulation, 6.52% in the axisymmetric simulation).

When comparing the experimental SOP data from the target with a 125 μm CH layer to planar CHIC simulations, this 600 ps difference in shock breakout time have to be taken in consideration. Additional simulations have been realized in order to evaluate this difference in shock breakout times between planar and axisymmetric simulations for the targets with a CH layer of 15 and 50 μm . For 50 μm , a 50 ps difference is observed, while for 15 μm there is no difference in shock breakout time.

5.2.3 CHIC simulations

Planar geometry CHIC simulations using the PCGO description for the laser propagation and a constant flux limiter of 7% for the thermal electron transport have been realized for the interpretation of this experiment. These simulations have included or not the hot electron package so that their effect on the hydrodynamic of the target could be put in evidence. A focus has been made on the interpretation of the shot on the target with the thickest CH layer (125 μm) since it is the most constraining for the simulations, due to the relative long propagation distance of the shock wave. Figure 5.12 presents the target (left) and laser pulse (right) used for this study. Four simulations with these target and laser parameters will be presented in this section. First, simulations without hot electron and with SRS and TPD hot electrons will be compared. Then two other simulations with modified hot electron sources parameters will be presented as they show better agreement with the experimental data.

Figure 5.13 presents the results from the simulation without hot electrons. In this simulation, 9.3% of the laser energy has been absorbed though inverse Bremsstrahlung. This low absorption is due to the short duration, long wavelength and high intensity of the laser pulse (section 2.1.2). The 2D maps of pressure and density 800 ps after the beginning of the simulation (Figure 5.13, top row) show a well defined shock front with a pressure of ~ 12 Mbar. The shock front is almost flat over 150 μm in the transverse direction. The pressure

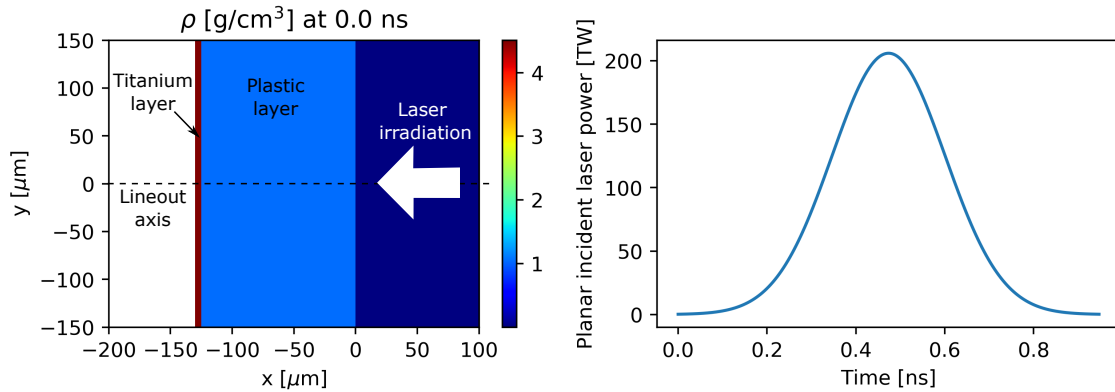


Fig. 5.12 Initial 2D density map of the target (left) and incident laser power in planar geometry (right). The laser power in planar geometry does not corresponds to the real laser power, it has been calculated using the equations 5.7 and 5.8.

and density as function of time and space (Figure 5.13, bottom row) show that the shock propagation is very similar as in the simulations presented in the previous section (which were using ray tracing). In this simulation, the shock breaks out at the rear side of the target 4.45 ns after the beginning of the simulation.

Figure 5.14 presents the results from the simulation with hot electrons. In this simulation SRS and TPD hot electrons have been considered. The temperatures and conversion efficiencies of the hot electron sources have been determined using the scaling laws presented in section 2.3 (equations 2.42, 2.43, 2.49 and 2.50). For the SRS hot electrons, the time average temperature and conversion efficiency are 38 keV and 9.2% respectively. For the TPD hot electrons, these parameters are 83 keV and 1.9%. The SRS hot electron sources had no initial divergence while the TPD hot electron sources had a $\pm 45^\circ$ divergence. Additionally, 8.2% of the laser energy was absorbed through inverse Bremsstrahlung. The 2D maps of pressure and density 800 ps after the beginning of the simulation (Figure 5.14, top row) show the effects these hot electrons have on the hydrodynamic of the target. The hot electrons have heated the target both upstream and downstream of the shock front. In the unshocked plastic, this heating has increased the pressure up to ~ 35 Mbar and in the shocked plastic it has increased up to ~ 80 Mbar. While the shock pressure has largely increased, its strength (the ratio of the downstream pressure to the upstream pressure) has decreased to ~ 2.3 . In the simulation without hot electrons, the upstream pressure being negligible, the shock strength is very large. Due to this low shock strength, the shock wave compresses the plastic only by a factor 1.14, against a factor 3.4 in the simulation without hot electrons. The pressure increase due to the hot electron energy deposition also leads to an expansion of the target from both sides. Since the pressure in the shocked plastic is larger than the ablation pressure, the front

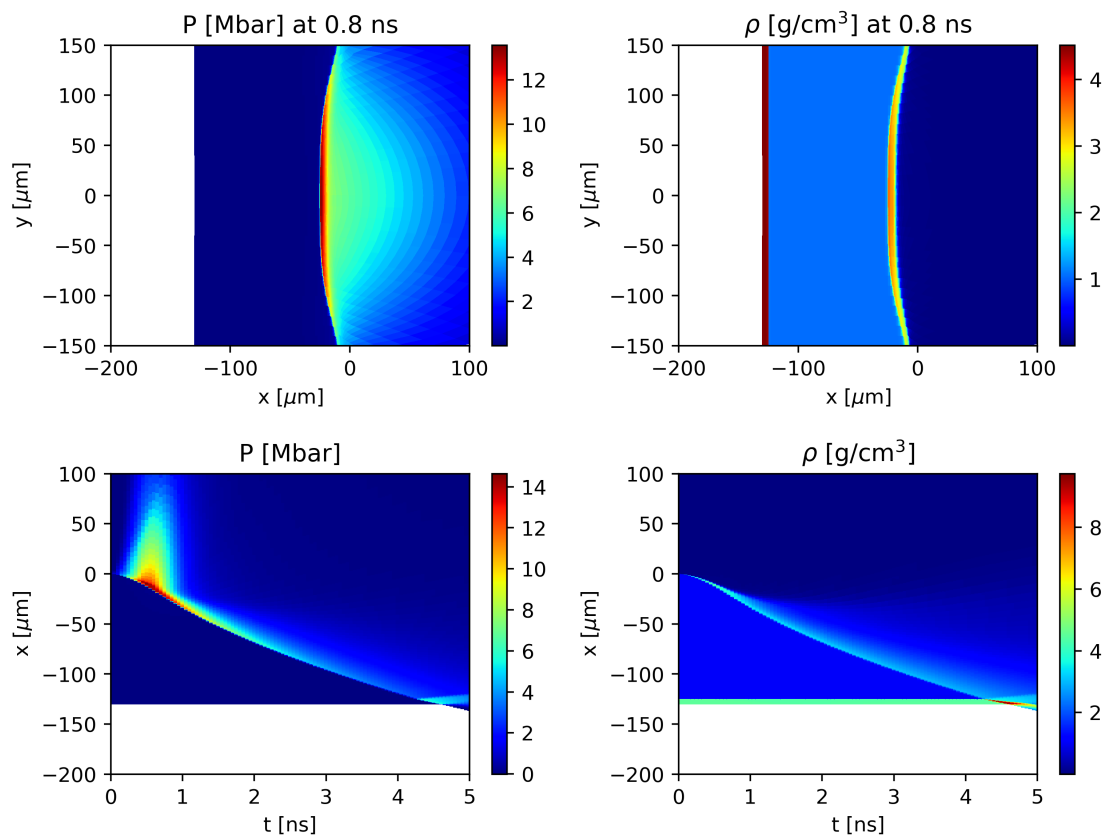


Fig. 5.13 Results of the simulation without hot electrons. (top right) 2D map of pressure at 800 ps. (top left) 2D map of density at 800 ps. (bottom left) pressure as function of time and space. (bottom right) density as function of time and space. The lineout axis for the bottom row figures is presented in Figure 5.12.

side of the target has expanded toward the laser, leading to a large density gradient. On the rear side, the heated Titanium layer has expanded in the vacuum, also creating a density gradient. Due to the directionality of the SRS hot electron sources, this heating is localized close to the laser symmetry axis in $y = 0$. As a consequence, the shock front curvature is larger in the simulation with hot electrons. The pressure and density as function of time and space (Figure 5.14, bottom row) show the increase of the heating of the target due to the electron along time. The shock is faster in the simulation with hot electrons and it reaches the Titanium layer around 1.7 ns, against 4.2 ns in the simulation without hot electrons. However, due to the large expansion of the Titanium layer, the breakout time at the rear side of the target is not well defined.

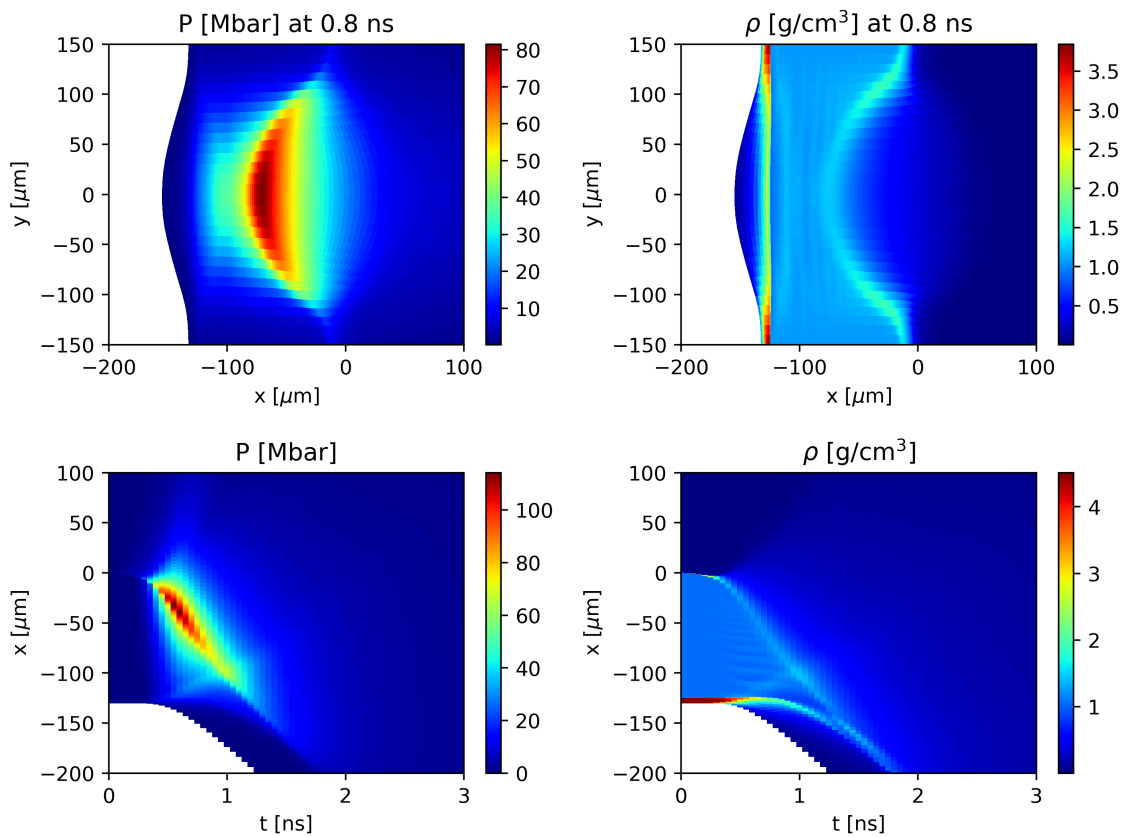


Fig. 5.14 Results of the simulation with hot electrons from SRS and TPD, using the scaling laws presented in chapter 2 and without initial divergence of the SRS hot electron sources. (top right) 2D map of pressure at 800 ps. (top left) 2D map of density at 800 ps. (bottom left) pressure as function of time and space. (bottom right) density as function of time and space. The line-out axis for the bottom row figures is presented in Figure 5.12.

Since the shock breakout time at the rear side of the target cannot be determined in the simulation with hot electrons, a x-ray post processor for CHIC has been used in order to evaluate the time at which the X-ray emission at the rear side of the target increases due to the shock. This post processor simulates a pinhole imaging the rear side of the target. Radiative transport calculation is then realized in order to evaluate the emissivity of the rear side in the visible range, between 1 and 4 eV, which corresponds to the cut-off transmission of the BK7 optics used to image the target in the experiment. Integration of the emissivity along the photon energy then allows to produce images that can be compared to the experimental SOP images. In order to be more relevant, these images are blurred by taking in account the experimental spatial and temporal resolutions, $80\ \mu\text{m}$ and $80\ \text{ps}$, respectively. Yet, since the spectral response of the streak camera used in the experiment is unknown, both absolute and relative comparison in the amplitude of the rear side emissivity cannot be made between the simulation and experiment and only time delays can be measured.

Figure 5.15 presents the results from the X-ray post-processing of the CHIC simulation presented in Figure 5.14. The emissivity of the rear side of the target in the simulation shows a behaviour similar as in the experiment. During the laser matter interaction (before $800\ \text{ps}$), there is a peak of emissivity due to the direct heating of the titanium layer by the hot electrons. This signal then decreases along time as the layer expands and cools down. Then the shock breaking out at the rear side of the target leads to an increase of the emissivity. In this simulation, the delay between the rising of the signal due to shock breakout and the peak of emission due to the hot electron is $1.5 \pm 0.1\ \text{ns}$. Even by considering the $600\ \text{ps}$ delay due to the simulation been realized in planar geometry, this delay is much shorter than the experimentally measured one, which was $4.1 \pm 0.2\ \text{ns}$. The shorter delay observed in the experiment compared to the simulation with the hot electrons might be due to an overestimation of the amount of hot electrons produced in the simulation. Indeed, in this simulation, 9.2% of the laser energy has been converted into SRS hot electrons with a temperature of $38\ \text{keV}$. While the temperature is close to what have been measured with the K_α diagnostic considering the error bars, the conversion efficiency is much larger in the simulation. This inaccuracy of the scaling laws used in order to determine the hot electron source parameters is not surprising since they have been determined from experiments and simulations at shorter wavelength ($0.351\ \mu\text{m}$). Therefore, additional simulations with reduced hot electron fluxes have been realized. The SRS conversion efficiency has been reduced by a factor four in order to approach the measured one. Also the TPD conversion efficiency has been reduced by a factor two so that there is still a significantly larger amount of SRS hot electrons in the simulation compared to TPD ones. For both SRS and TPD sources, the temperature and initial divergence have been kept the same.

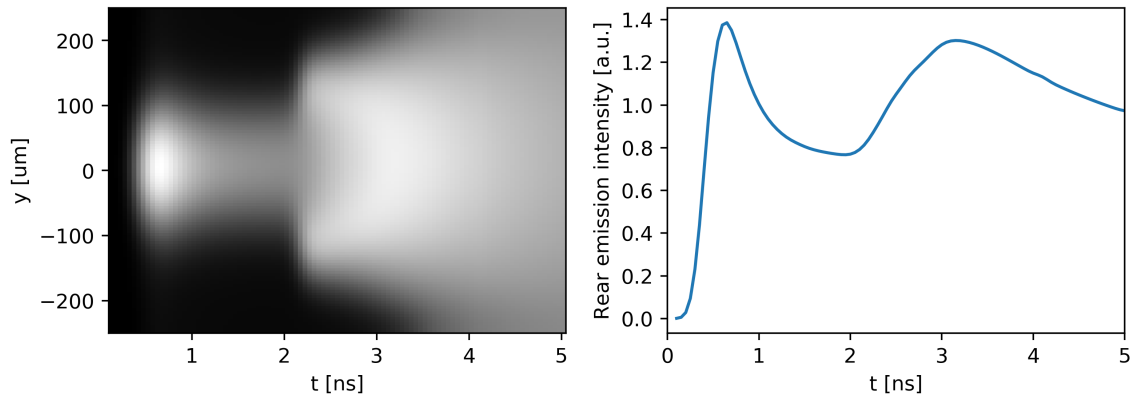


Fig. 5.15 Results from the X-ray post-processing of the CHIC simulation presented in Figure 5.14 (left) and line-out of this results along the axis $y = 0$ (right).

Figure 5.16 presents the results of this simulation with reduced hot electron fluxes. In the simulation, the conversion efficiency of SRS and TPD were 2.34% and 1.11 %, respectively. Additionally, 9.34% of the laser energy have been absorbed through inverse Bremsstrahlung. The 2D maps of pressure and density 800 ps after the beginning of the simulation (Figure 5.16, top row) show that despite the reduction of the fluxes, the hot electron still significantly heat the target. However, their effect is significantly reduced. The expansions of the titanium layer and of the shocked plastic are still visible but their velocities are reduced. The maximum pressure in the unshocked and shocked plastic have also been reduced to ~ 17 Mbar and ~ 32 Mbar, respectively. As a consequence, the shock front velocity is lower in this simulation. This can also be observed on the pressure and density as function of time and space (Figure 5.16, bottom row). The shock now reaches the titanium layer at ~ 2.2 ns. However, similarly to the precedent simulation, the expansion of the titanium layer prevents from determining the shock breakout time. Figure 5.17 presents the results from the X-ray post-processing of the reduced flux simulation presented in Figure 5.16. It shows that the rising of the signal due to the shock breakout is later, compared to the simulation with the initial hot electron fluxes. On the central line-out (Figure 5.17, right), the delay between the peak due to the hot electrons and the rising of the signal due to the shock breakout is 3.1 ± 0.14 ns. Adding the 600 ps due to the planar geometry of the simulation gives a delay of 3.7 ± 0.14 ns, which is closer to the measured delay, while still being shorter. The emissivity of the rear side as function of time and space (Figure 5.17, left) shows that the shock breaks out earlier away from the central axis (the earliest being for $y \simeq 150 \mu\text{m}$). Indeed, the expansion of the titanium layer is more important close to $y = 0$, so that at this position the shock has to propagate through on longer distance before breaking out. This effect is also visible in the

simulation with the initial hot electron fluxes, but it is amplified in this later one since the Titanium has more time to expand due to the lower shock velocity. This effect is not observed on the experimental image, which suggests that the directionality of the hot electrons in the simulation is overestimated. As it has been shown in section 5.1, there is an uncertainty on the initial divergence of the SRS hot electron sources in order to reproduce experiments. For both the initial and reduces fluxes simulations that have been presented, this divergence was taken to be 0° for numerical efficiency. Therefore an additional simulation with reduced fluxes and with a $\pm 20^\circ$ initial divergence for the SRS hot electron sources has been realized.

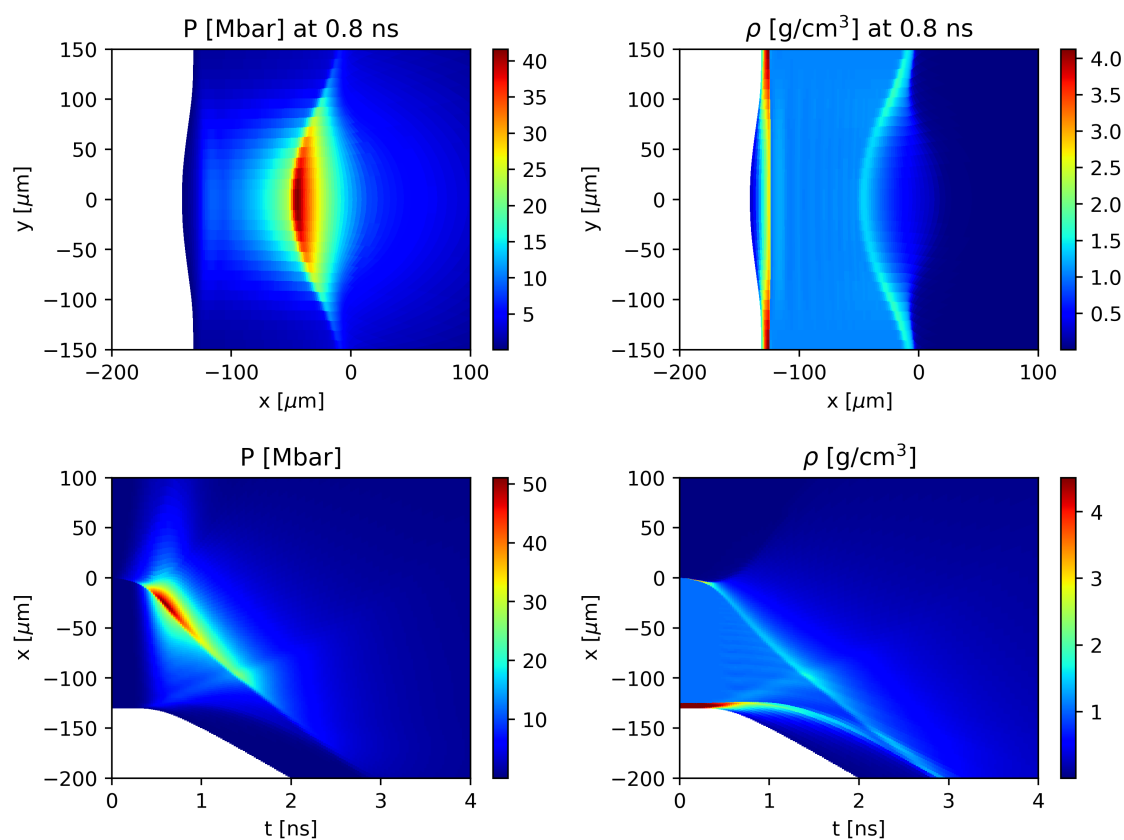


Fig. 5.16 Results of the simulation with hot electrons from SRS and TPD, with reduced hot electron conversion efficiency (by a factor 4 for SRS and by a factor 2 for TPD) and without initial divergence of the SRS hot electron sources. (top right) 2D map of pressure at 800 ps. (top left) 2D map of density at 800 ps. (bottom left) pressure as function of time and space. (bottom right) density as function of time and space. The line-out axis for the bottom row figures is presented in Figure 5.12.

Figure 5.18 presents the results of the simulation with reduced hot electron fluxes and increased SRS divergence. In this simulation, the temperature and conversion efficiency for SRS and TPD were the same as in the previous one. This is also the case for the collisional

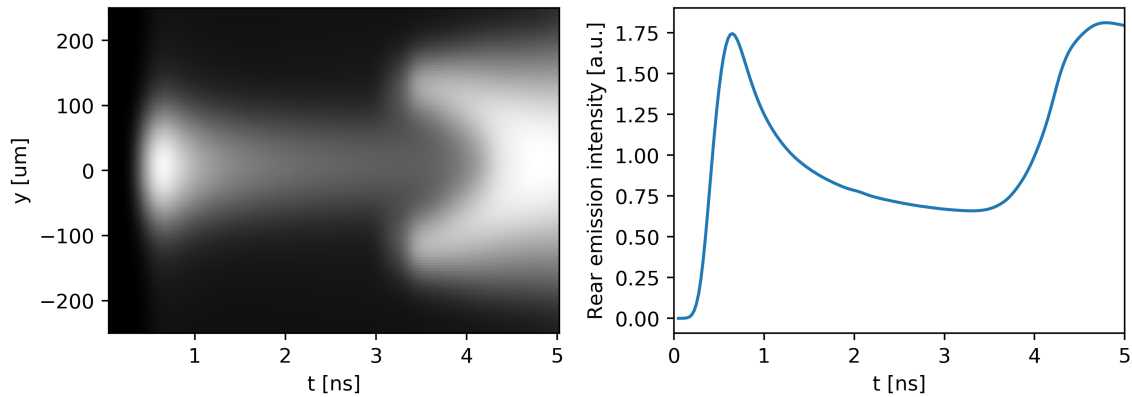


Fig. 5.17 Results from the X-ray post-processing of the CHIC simulation presented in Figure 5.16 (left) and line-out of this results along the axis $y = 0$ (right).

absorption rate. As expected, the hot electron heating that can be observed on the 2D maps of pressure and density 0.8 ns (Figure 5.18, top row) is significantly less directional. This results in a flatter shock front and a decrease of the pressure in both shocked and unshocked plastic. Yet, this decrease in shock pressure does not have a large impact on the shock velocity, as it can be seen in Figure 5.18, bottom row. Figure 5.19 presents the results from the post-processing of this simulation. As it can be seen on the emissivity as function of time and space (left), the curvature of the shock breakout signal is still visible but it is strongly reduced. Such curvature in the experimental image (Figure 5.8 might not be visible due to the low level of signal. The central line out of the rear side emission (Figure 5.19, right) shows a shock breakout slightly later than in the simulation without initial divergence for the SRS hot electron sources. In this simulation, the delay between the peak of emission due to the hot electrons and the increase in emission due to the shock breakout is 3.35 ± 0.1 ns. Taking in account the 600 ps due to the planar geometry of the simulation leads to a delay of 3.95 ± 0.1 ns which is in agreement with the measured delay considering the error bars. This last simulation therefore reproduce best the experimental SOP data. Yet, the increase of the signal due to the shock breakout is much steeper in the simulation and it also starts to decrease after ~ 4.2 ns. This behavior is very different than what is observed in the experiment where the SOP signal slowly increases along time. As it as been discussed before, the lack of information on the spectral response of the streak camera does not allow to compare the amplitudes of the simulated and experimental SOP images. Additionally, the equation of state and opacity of titanium might be inaccurate in the regime of low density and moderate temperature, in which the it is due to its expansion. These might also be sources of inaccuracy in the amplitude of the rear side emission. Table 5.1 presents the conversion efficiencies,

shock breakout time, SOP delay and some other key numbers from the simulations presented in this section (corresponding to the simulations presented in Figures 5.13, 5.14, 5.16 and 5.18).

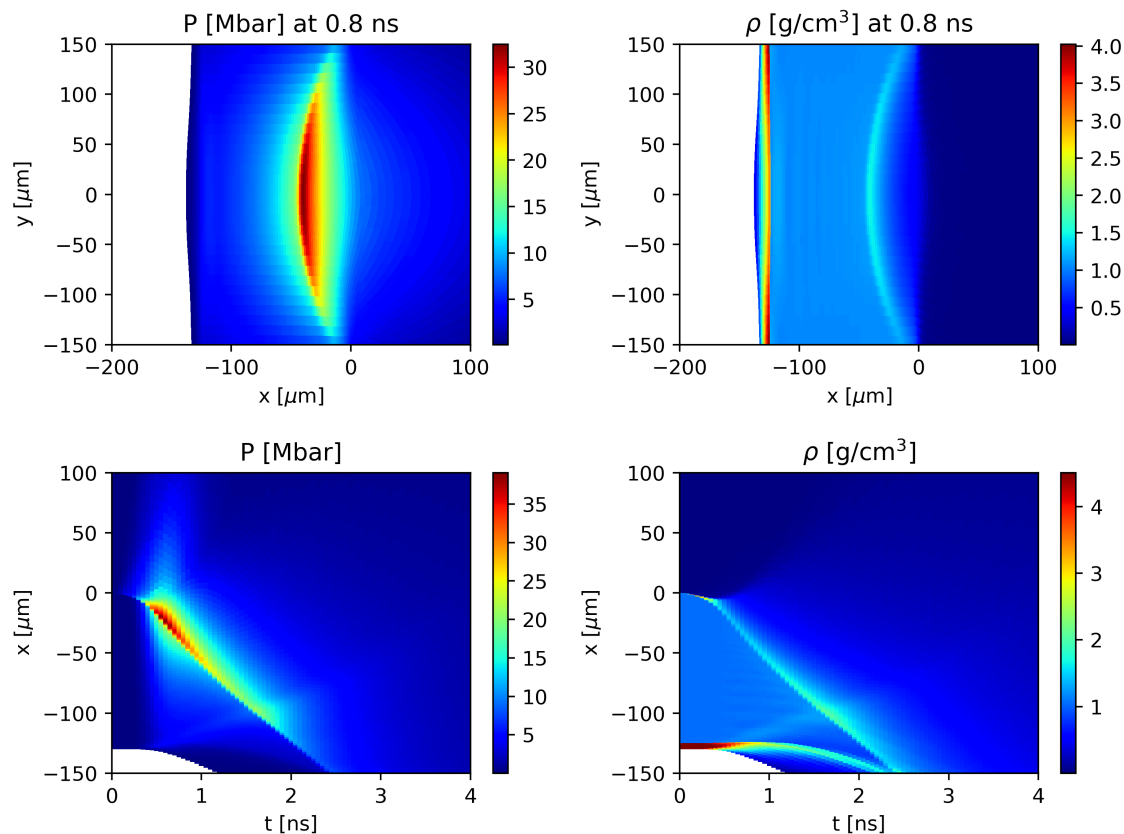


Fig. 5.18 Results of the simulation with hot electrons from SRS and TPD, with reduced hot electron conversion efficiency (by a factor 4 for SRS and by a factor 2 for TPD) and with a $\pm 20^\circ$ initial divergence of the SRS hot electron sources. (top right) 2D map of pressure at 800 ps. (top left) 2D map of density at 800 ps. (bottom left) pressure as function of time and space. (bottom right) density as function of time and space. The line-out axis for the bottom row figures is presented in Figure 5.12.

Simulations with these modifications for the hot electron sources (SRS conversion efficiency reduced by 4, TPD conversion efficiency reduced by 2 and SRS source divergence increased to $\pm 20^\circ$) have been realized for the target with plastic thickness of 15 and 50 μm . Figures 5.20 and 5.21 present the results of the post-processing of these simulations. For both, the simulated SOP signals are very similar to the measured ones. On the central line-out for the simulation with the 50 μm thick CH (Figure 5.20, right), the delay between the peak of emission due to hot electrons and the rising of the signal due to shock breakout is 1.15 ± 0.10 ns. This is in agreement with the measured delay (1.0 ± 0.1 ns) considering the error

	Without HE	With HE, $\theta_{SRS} = 0^\circ$	With HE, $\theta_{SRS} = 0^\circ$, reduced HE fluxes	With HE, $\theta_{SRS} = 20^\circ$, reduced HE fluxes
Collisional absorption fraction	9.26 %	8.20 %	9.34 %	9.33 %
SRS conversion efficiency	0 %	9.22 %	2.34 %	2.34 %
TPD conversion efficiency	0 %	1.87 %	1.11 %	1.11 %
Shock at plastic/titanium interface	4.25 ns	1.70 ns	2.20 ns	2.35 ns
Peak shock pressure in plastic	15.4 Mbar	106 Mbar	51.0 Mbar	39.1 Mbar
Shock front density jump at 0.8 ns	3.40	1.14	1.30	1.41
Rear surface peak expansion velocity	0 km/s	98.0 km/s	45.6 km/s	31.6 km/s
Synthetic SOP delay		1.5 ns	3.1 ns	3.35 ns
Synthetic SOP delay + 0.6 ns		2.1 ns	3.7 ns	3.95 ns

Table 5.1 Comparison between simulations realized for the interpretation of the experiment on PALS. All simulations have the same target and laser parameters. The shock front density jump is defined as the ratio of the upstream to the downstream densities, across the shock front. The synthetic SOP delay is defined as the delay between the peak of emission due to the hot electrons and the rising of the signal due to shock breakout observed with the X-ray post-processing of the simulations. The experimental SOP delay is 4.1 ± 0.2 ns.

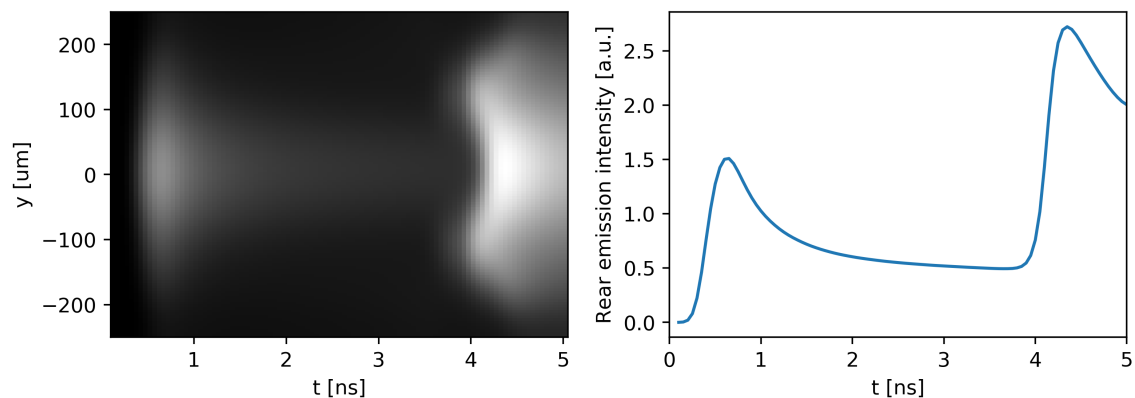


Fig. 5.19 Results from the X-ray post-processing of the CHIC simulation presented in Figure 5.18 (left) and line-out of this results along the axis $y = 0$ (right).

bars, even if considering the 50 ps additional delay due to the simulation being in planar geometry. On the central line-out for the simulation with the 15 μm thick CH (Figure 5.20, right) the shock breakout does not lead to a significant increase of rear side emissivity. It only changes the slope at which the rear side cools down after having being heated by the hot electrons. This is also what have been observed in the experimental image.

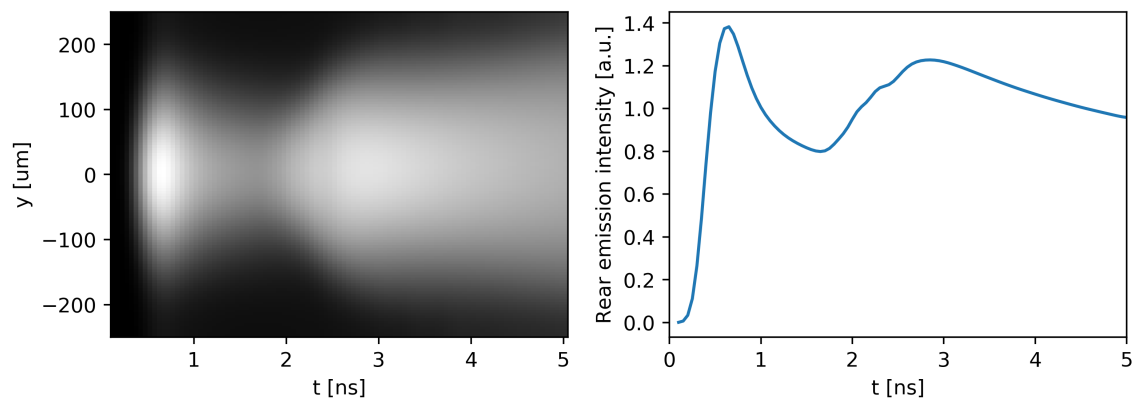


Fig. 5.20 Results from the X-ray post-processing of the CHIC simulation of the target with 50 μ of plastic (left) and line-out of this results along the axis $y = 0$ (right). This simulation have been realized using the same hot electron source parameters as the simulation presented in Figure 5.18.

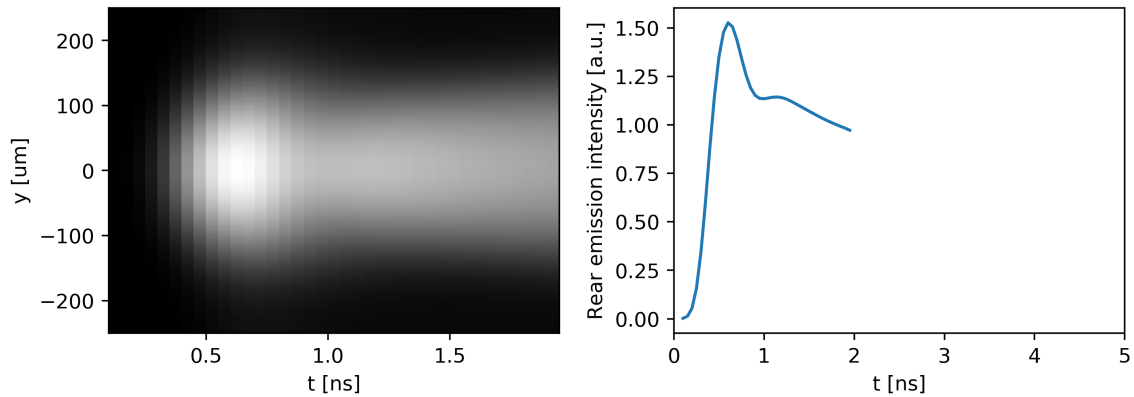


Fig. 5.21 Results from the X-ray post-processing of the CHIC simulation of the target with 15μ of plastic (left) and line-out of this results along the axis $y = 0$ (right). This simulation have been realized using the same hot electron source parameters as the simulation presented in Figure 5.18.

5.2.4 Conclusion

The last simulations presented, with reduced hot electron conversion efficiency and with SRS divergence of $\pm 20^\circ$, reproduces both the SRS hot electron source parameters measured by K_α and the delay observed on the SOP data between the peak of emission due to hot electrons and the increase in signal due to shock breakout (when taking in account the additional delay due to the simulation being realized in planar geometry instead of axisymmetric geometry).

The reduction of the hot electron conversion efficiencies indicates that the scaling laws currently used in CHIC cannot be used for the simulation of experiments using short pulse and long wavelength, as in this experiment. However, it has been shown that the measurement of the hot electron source parameters allows to modify the scaling law accordingly. An attention should be made about the measurement of these parameters in future experiments, specifically when these are in a regime where the CHIC scaling laws might be inaccurate. The increase in SRS source divergence indicates that despite being more numerically efficient and sufficient to reproduce experiments in spherical geometry, a divergence of 0° cannot be used for the interpretation of experiments in planar geometry. In this experiment, an initial divergence of $\pm 20^\circ$ was enough in order to flatten the shock breakout transverse profile observed on SOP. Also, this divergence is smaller than the TPD source divergence as expected from theory (section 2.3).

Finally, an issue about shock breakout measurements in such laser plasma conditions can be addressed. Indeed, the hot electrons produced during the pulse lead to a faster shock wave, but also to the expansion of the rear side of the target and therefore a longer distance

of propagation for the shock wave. Therefore the observed shock breakout time results from the competition between these two effects, which makes the interpretation of the streaked optical pyrometry data more difficult. In order to have a better measurement of the effect of hot electrons on the hydrodynamic of shocks, other diagnostics, such as side radiography, are therefore required.

5.3 Radiography of a shock perturbed by hot electrons on OmegaEP

The experiment presented in the previous section shows that two main issues come up about the effect of the hot electrons on the hydrodynamic of the shock. First, the laser pulse parameters of PALS might be out of the validity range of the scaling laws that are implemented in CHIC for the calculation of the hot electron source parameters. Using laser pulses with shorter wavelength ($\lambda = 0.351 \mu\text{m}$) and longer pulse ($> 1 \text{ ns}$) would be preferable. Then, the SOP diagnostic, which measure the shock breakout time, is an indirect way of measuring the effect of hot electrons on the shock propagation. A more direct diagnostic, such as the side radiography of the shock wave, would be much more constraining for the validation of hydrodynamic codes such as CHIC.

Considering these two issues, an experiment have been designed with the objective of realizing the side radiography of a shock wave perturbed by hot electrons. The laser facility considered for this experiment was OmegaEP, as it can provide laser pulses with duration ranging from 0.1 to 10 ns at the Nd:glass third harmonic ($\lambda = 0.351 \mu\text{m}$). Additionally, OmegaEP has four beamlines so that some of the laser beams can be used in order to drive the shock wave, while the others would irradiate a high-Z foil in order to generate X-rays that can be used for the realization of the side radiography.

This experiment has been realized recently and it is currently being analyzed. In this section, the CHIC simulations used for the design of this experiment are first presented. Then, a preliminary analysis of the experimental radiographies is done. Especially, thanks to the developmental of a post-processing tool, synthetic radiographies are compared to the experimental images.

5.3.1 CHIC simulations for the target and radiography design

The laser pulse configuration proposed for this experiment used one interaction beam in order to drive the shock wave and three radiography beams for the X-ray generation. The three radiography beams were 3 ns square pulses with SG8-750 distributed phase plates

(750 μm diameter at $1/e$, super Gaussian of order 8), resulting in an overlapped intensity of $\sim 5 \times 10^{14} \text{ W/cm}^2$. This configuration allowed to have a X-ray emission bright enough, over a large area and during a sufficiently long time. Thereby, radiography of the shock wave propagation could be realized by recording 2D images at several times using a framing camera. The interaction beam was a 1 ns square pulses without any Distributed Phase Plate (the estimated focal spot without phase plate is Gaussian with 180 μm diameter at $1/e$). These parameters result in a peak intensity of $\sim 5 \times 10^{15} \text{ W/cm}^2$ which should generate a large amount of hot electrons. Longer pulses (>1 ns) would have been preferable since it would result in larger structures (longer shock propagation distance) and therefore in clearer radiography. However, longer pulses have a decreasing peak power in order to avoid damage on the laser optics due to thermal effects [98]. The absence of distributed phase plate can be an issue since it might result in an inhomogeneous focal spot. Locally, the intensity can be significantly higher than the average intensity. Unfortunately, on Omega EP, the phase plate with the smallest focal spot is the SG10-400, which results in a focal spot of 400 μm (diameter at $1/e$, super Gaussian of order 10). Using this phase plate and with a 1 ns square pulse (1.25 TW peak power) the maximum intensity that can be achieved is only $\sim 1 \times 10^{15} \text{ W/cm}^2$. While this intensity is enough so that hot electrons would be produced, their amount would have been too small and their effect on the shock hydrodynamic might not have been measurable.

The target was a multi-layer cylinder with a front plastic layer (Polystyrene, CH), a copper layer and a rear plastic layer (Polystyrene, CH). The main objective of the experiment is to realize the radiography of the shock propagating in the front plastic layer. The copper layer is used in order to measure the hot electron population through K_α spectroscopy (similarly to the PALS experiment presented in section 5.2.1). A secondary objective is to measure the expansion of the copper layer due to its heating by the hot electrons. Indeed, in the PALS experiment the titanium K_α layer has expanded significantly due to this heating. The rear plastic layer is used as support for the other layers. CHIC simulations have been realized in order to determine the optimal thicknesses for the front plastic layer and the copper layer so that the effect of the hot electrons on the shock propagation (and potentially the copper layer expansion) would be the largest.

The simulation conditions were very similar to the one for the PALS experiment. They have been realized using PCGO for the laser description (and therefore the simulation are in planar geometry) and a constant flux limiter of 4% for the thermal electron transport. The laser parameters were the one presented before: 1 ns square pulse, Gaussian focal spot with 180 μm diameter at $1/e$, $\sim 5 \times 10^{15} \text{ W/cm}^2$ peak intensity. Additionally, the laser had an incidence angle of 23° with respect to the target normal, due to the geometry of OmegaEP

target chamber. The scaling laws used for the calculation of the hot electron temperatures and conversion efficiencies are the ones presented in section 2.3. At first, simulations including SRS hot electrons only have been compared to simulations including SRS and TPD hot electrons. In these simulations, 9.3% of the laser energy is converted into SRS hot electron with a temperature of 40 keV and 1.6% into TPD hot electrons with a temperature of 90 keV, when they were included in the simulations. These have shown that with these laser parameters, the TPD hot electrons have a negligible effect on the shock propagation. For numerical efficiency, further simulations have been realized with SRS hot electrons only, and without any initial divergence for the SRS hot electron sources.

For simplicity, only the simulations with the optimal thicknesses (which have been used in the experiment) are presented here. These are 175 μm for the front plastic layer and 20 μm for the copper layer. Figure 5.22, presents the target (left) and the laser power (right) used for these simulations. The thickness of the rear plastic layer in the simulation is 50 μm for numerical efficiency. In reality its thickness is few hundred micrometers.

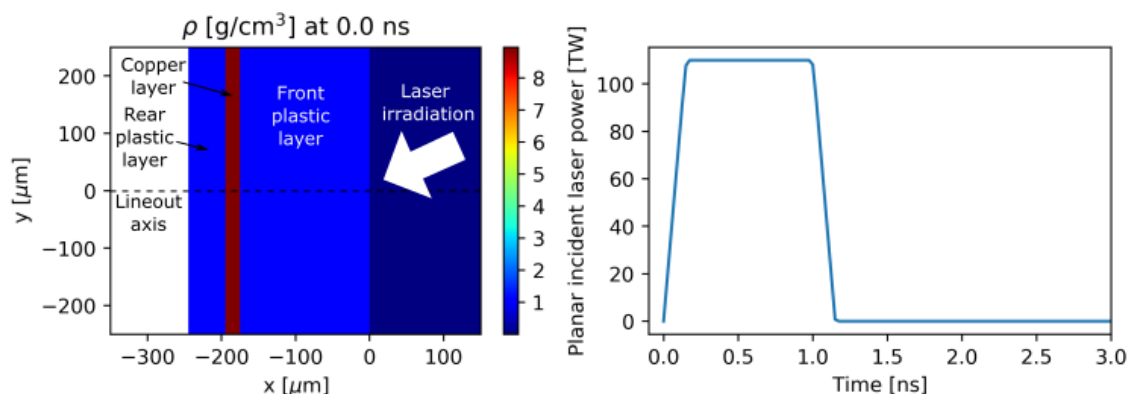


Fig. 5.22 Initial 2D density map of the target (left) and incident laser power in planar geometry (right). Unlike laser intensity, the laser power in planar geometry does not correspond to the real laser power, it has been calculated using the equations 5.7 and 5.8.

Figures 5.23 and 5.24 present the results from the simulations without hot electrons and with SRS hot electrons, respectively. For both figures, the top row images are the 2D map of pressure (left) and density (right) 1.2 ns after the beginning of the laser matter interaction. This time corresponds to the end of the laser pulse. Similarly to what have been observed for the PALS experiment, the hot electrons lead to an increase of the shock pressure, a faster shock front and a very inhomogeneous shocked plastic. For both figures, the bottom row corresponds to the pressure (left) and density (right) as function of time and space, along the line-out axis presented in Figure 5.22. For the simulation without hot electrons, the shocked plastic has a constant density until ~ 1.2 ns. After the end of the laser pulse, the ablation

pressure decreases which leads to a rarefaction wave propagating in the shocked plastic up to the shock front. Then, the shocked plastic has an inhomogeneous density, similarly to the simulation with the hot electrons. It is therefore interesting to realize the radiography of the shock front during the laser irradiation, before ~ 1.2 ns, as it corresponds to the times when the difference in density map between the simulations with and without hot electrons is the largest.

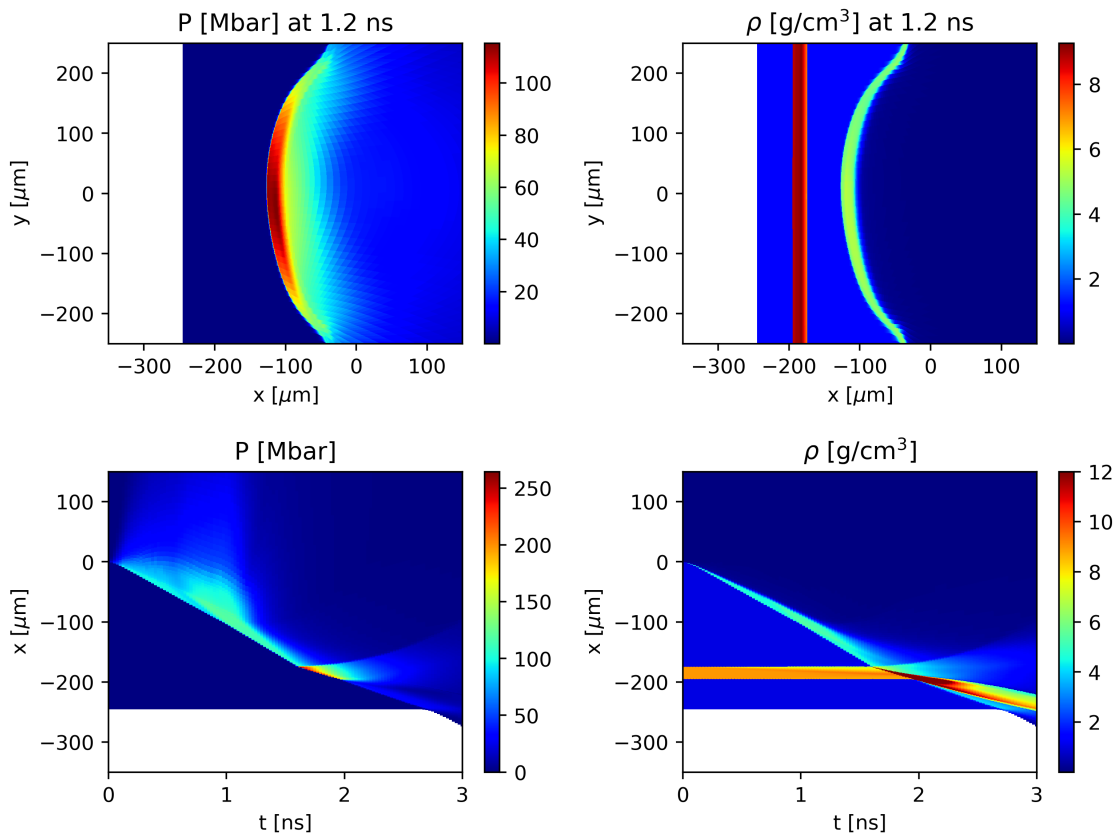


Fig. 5.23 Results of the simulation without hot electrons. (top right) 2D map of pressure at 1.2 ns. (top left) 2D map of density at 1.2 ns. (bottom left) pressure as function of time and space. (bottom right) density as function of time and space. The line-out axis for the bottom row figures is presented in Figure 5.22.

The front plastic thickness of $175 \mu\text{m}$ corresponds to the propagation distance of the shock front in the simulation with hot electrons, after 1.2 ns. This allows to realize the radiography of the shock before this time, while ensuring that a maximum amount of hot electrons reaches the copper layer. Having a large amount of hot electron reaching the copper layer allows to have a bright emission of K_{α} for the measurement of their temperature and number. It also allows to maximize the heating of the copper layer by the hot electrons,

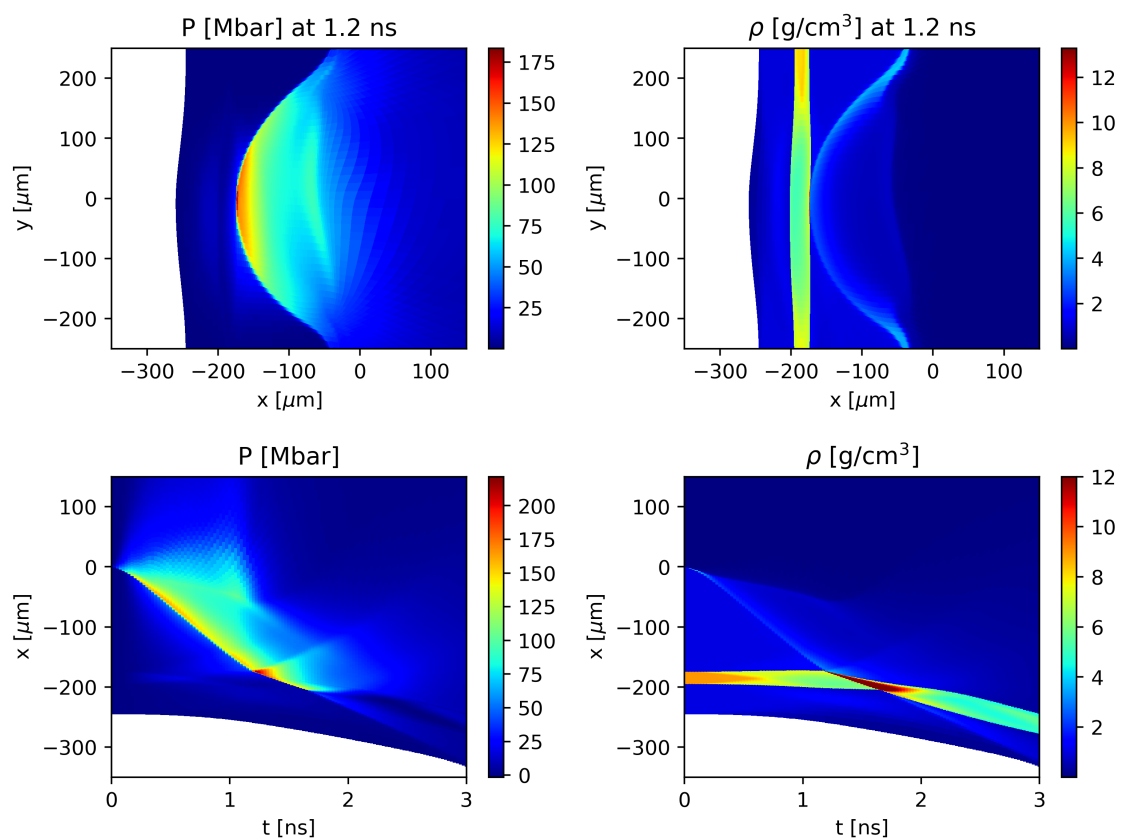


Fig. 5.24 Results of the simulation with SRS hot electrons ($\theta_{SRS} = 0^\circ$). (top right) 2D map of pressure at 1.2 ns. (top left) 2D map of density at 1.2 ns. (bottom left) pressure as function of time and space. (bottom right) density as function of time and space. The line-out axis for the bottom row figures is presented in Figure 5.22.

so that its expansion is fast enough to be seen on the radiography. The thickness of the copper layer has been determined in order to maximize the amplitude of its expansion. For thin copper layer, the expansion is fast but it stops quickly, as the pressure equilibrates with the surrounding plastic. For thick copper layer, the amount of hot electron that reach the rear side of the layer becomes very small so that it does not expand significantly. An optimal trade off for these laser parameters have been found with a thickness of 20 μm .

Several other simulations have been realized for the design of the experiment. Especially, considering the results from the study of the PALS experiment (section 5.2.3), simulations with an initial divergence for the SRS hot electron source of $\theta_{SRS} = \pm 20^\circ$ have been realized. Simulations with reduced energy have also been realized. Table 5.2 presents the conversion efficiency, shock breakout timing and some other key numbers from the simulations presented in Figure 5.23 and 5.24, along with the results from two other simulations:

- A simulation with SRS source divergence increased to $\theta_{SRS} = \pm 20^\circ$.
- A simulation with $\theta_{SRS} = \pm 20^\circ$ and a reduction of the incident laser energy to 70% of the nominal energy.

The results from these two last simulations are intermediates between the simulations without and with SRS hot electrons. Especially, the simulation with $\theta_{SRS} = \pm 20^\circ$ and the reduction in incident energy have a peak shock pressure and shock breakout times close to the simulation without hot electrons. Yet, in comparison, it has a significantly lower density jump at the shock front and it shows an expansion of the copper layer.

Finally the results from these simulations can be used in order to determine the optimal material for the X-ray source. Backlighters used for the generation of X-ray source are foil of high Z material (typically titanium, vanadium, iron, copper...) which, as they are irradiated by the laser, will produce a strong emission at a given photon energy. The energy of this line depends of the backlighter material and it typically ranges from 4 to 10 keV. An estimation of the transmission of these X-rays through the target can then be made by considering the X-ray absorption of a finite slab of plastic. The transmission is given by

$$T = \exp \left[- \left(\frac{\mu}{\rho} \right) \int \rho(z) dz \right] \quad (5.9)$$

where (μ/ρ) is the mass absorption coefficient of plastic, which depends of the X-ray energy, and $\rho(z)$ the plastic density along the radiography axis z . For this experiment, taking a 500 μm thick slab allows to have the information on the shock curvature while limiting the thickness of plastic that would not be perturbed by the shock. Two transmissions are particularly relevant:

	Without HE	With SRS, $\theta_{SRS} = 0^\circ$	With SRS, $\theta_{SRS} = \pm 20^\circ$	With SRS, $\theta_{SRS} = \pm 20^\circ$, 70% energy
Collisional absorption fraction	63.4 %	58.1 %	58.9 %	63.9 %
SRS conversion efficiency	0 %	9.34 %	9.27 %	8.33 %
Shock at front plastic/copper interface	1.62 ns	1.20 ns	1.27 ns	1.45 ns
Shock at copper/rear plastic interface	1.98 ns	1.65 ns	1.80 ns	2.02 ns
Peak shock pressure in front plastic	121 Mbar	161 Mbar	152 Mbar	122 Mbar
Average shock front density jump	4.23	1.86	2.06	2.28
Average copper layer expansion velocity	0 km/s	7.39 km/s	7.20 km/s	6.2 km/s

Table 5.2 Comparison between simulations realized for the design of the experiment on OmegaEP. All simulations have the same target parameters. The laser parameters only change for the fourth simulation, for which the total laser energy have been reduce to 70 %. The shock front density jump is defined as the ratio of the upstream to the downstream densities, across the shock front.

- The transmission of the uncompressed target. The integral for the calculation of the transmission then gives $\int \rho(z)dz = d_0 \times \rho_0$, with $d_0 = 500 \mu\text{m}$ the thickness of the slab and $\rho_0 = 1.05 \text{ g/cm}^3$ the initial density of the plastic.
- The transmission of the partially compressed target. X-ray passing through the shocked plastic also have to go through uncompressed plastic. As it can be seen on Figure 5.23, the thickness of the shock plastic along the transverse direction is $\sim 200 \mu\text{m}$. In this region, the plastic density is around four times its initial density. The integral for the calculation of the transmission then gives $\int \rho(z)dz = d_1 \times 4\rho_0 + (d_0 - d_1) \times \rho_0$, with $d_1 = 200 \mu\text{m}$ the thickness of the shock front along the transverse direction.

Figure 5.25, left, presents the values for these two transmissions as function of the X-ray energy. Each dot corresponds to the photon energy from different backlighter materials. Using titanium backlighter would lead to a low transmission and therefore, a dark radiography. Therefore, it seems better to use material with a higher photon energy such as iron or copper. However, it is also important to take in consideration the contrast between the two transmissions (the ratio of the uncompressed transmission to the partially compressed transmission). Figure 5.25, right, shows this ratio as function of the X-ray energy. For iron or copper, the contrast is very low (close to unity) so that the shock front would be barely visible on the radiography. A compromise between transmission and contrast has to be made. For the experiment, taking vanadium as the backlighter material allows to have a transmission in the uncompressed plastic of $>40\%$ while have a good contrast for the shock front.

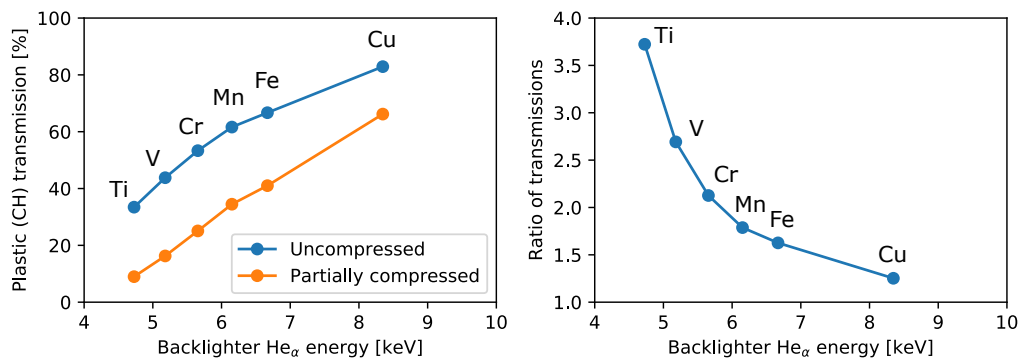


Fig. 5.25 Transmission of uncompressed and partially compressed plastic (left) and ratio of these transmissions (right) for the determination of the backlighter material for the OmegaEP experiment. The uncompressed curve corresponds to $500 \mu\text{m}$ of CH at solid density (1.05 g/cm^3). The partially compressed curve corresponds to $300 \mu\text{m}$ of CH at solid density + $200 \mu\text{m}$ of CH at four times the solid density (4.20 g/cm^3).

5.3.2 Experimental set-up and preliminary radiography results

This experiment has been realized on two separate shot days. Figure 5.26, left, presents a schematic of the set-up used on the first shot day. It corresponds exactly to the description given in the previous section. The multi-layer target was a 500 μm diameter cylinder with a 175 μm thick front plastic (CH) layer, 20 μm thick layer of copper and 250 μm thick rear layer of plastic (CH). The target was fixed on a 50 μm thick rectangular slab of plastic in order to facilitate its alignment. A fiber was also fixed on the target for this purpose. Indeed, the quality of the radiographies in such experiments strongly depends on the alignment of the target with respect to the radiography axis. As an example, since the copper layer is 500 μm long (in the direction of the radiography axis) for 20 μm thick, a misalignment of 1° would lead to an apparent thickness of the layer of 28 μm , therefore preventing its expansion from being visible. Three beams were used in order to irradiate the vanadium foil used for the generation of the X-rays and a heat shield was placed between the vanadium foil and the multi-layer target to block the low energy radiations from the foil. Figure 5.26, right, shows the corresponding overlapped laser intensity on the backlighter as seen from the radiography axis. On this view, the heat shield has been hidden and the multi-layer target is visible in transparency.

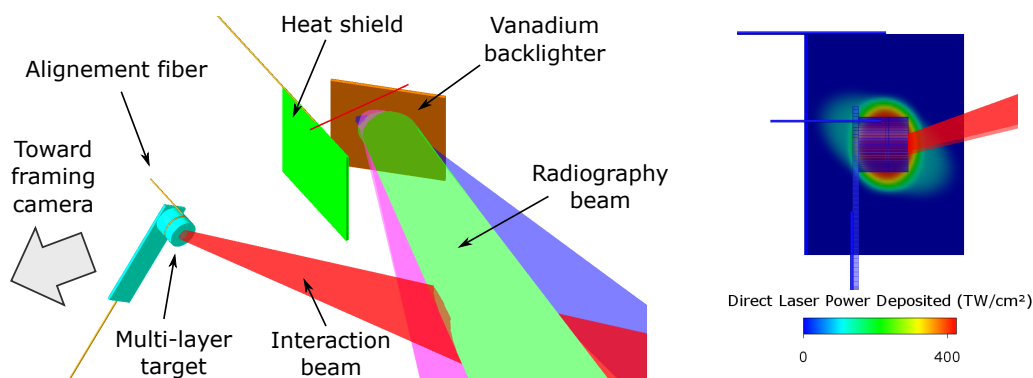


Fig. 5.26 Schematic of the radiography experiment on OMEGA EP used on the first shot day (left) and direct laser irradiation on the backlighter as seen from the radiography axis (right).

The radiographies are recorded on a framing camera which allows to obtain, from a single shot, 16 images at different times. Figures 5.27 and 5.28 present some of the radiographies obtained on two separate shots (shot 27785 and 27786, respectively) that have been realized with this configuration. The orientation of the radiographies is the same as presented in Figure 5.26, right. The vertical dark area corresponds to the copper layer and the horizontal one is the alignment fiber. For both shots, the shock wave can be seen propagating in the front plastic layer, from right to left. An asymmetry of the shock front is observed for both

shots. But its orientation is inverted compared to the simulation presented in Figure 5.24 (experimentally, the shock is faster for $y > 0$). This suggests that it is not due to an effect of the hot electrons. The observed asymmetry might be due to important inhomogeneities of irradiation in the focal spot of the interaction beam (since it did not use any phase plate). The apparent initial thickness of the copper layer is $\sim 75 \mu\text{m}$ for shot 27785 and $\sim 60 \mu\text{m}$ for shot 27786. These thicknesses are significantly larger than the expected $20 \mu\text{m}$. This can be due to a misalignment of the target by $\sim 4^\circ$. Another possibility is that the edges of the copper plate are thicker due to its machining. In both cases, due to this large initial apparent thickness, the expansion of the copper layer due to the heating by the hot electrons cannot be seen. Finally, the observed distance separating the middle of the copper layer from the target front surface does not match the expected $185 \mu\text{m}$ ($175 \mu\text{m}$ of plastic and $20/2 \mu\text{m}$ of copper). This distance is $\sim 205 \mu\text{m}$ for shot 27785 and $\sim 195 \mu\text{m}$ for shot 27786. This difference cannot be explained by the misalignment of the target and it might be due to a thick layer of glue between the front plastic layer and the copper layer. This uncertainty on the distance between the copper layer and the target front surface leads to larger error bars on the shock front position.

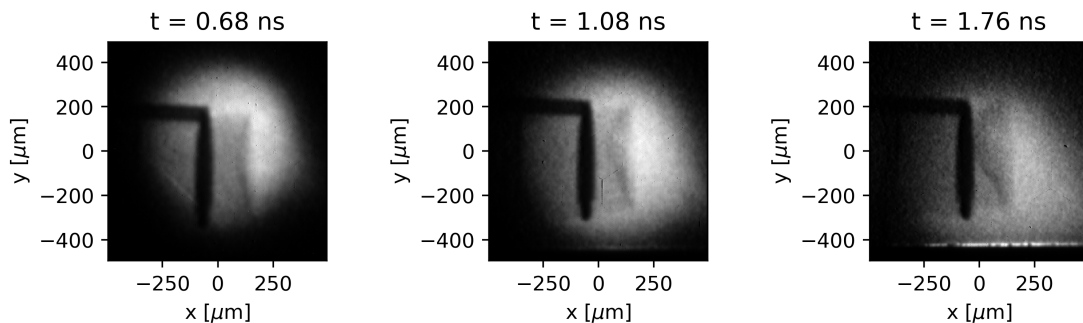


Fig. 5.27 Radiographies recorded on the framing camera from shot 27785. This shot used the configuration presented in Figure 5.26.

For the second shot day, few adjustments have been made compared to the configuration used on the first shot day. Figure 5.29, left, presents a schematic of the set-up used on the second shot day. The target has been simplified by removing the rear plastic layer. The copper layer was then directly glued on the $50 \mu\text{m}$ plastic slab. This allowed a better target assembly and an easier alignment. Also, only one beam was used in order to irradiate the vanadium foil. Indeed, the X-ray flux obtained using three radiography beams was high enough so that it suggested that using only one beam for the radiography would be sufficient. Figure 5.29, right, shows the corresponding laser irradiation on the backlighter as seen from the radiography axis. It is very similar to Figure 5.26, right, but with a lower maximum

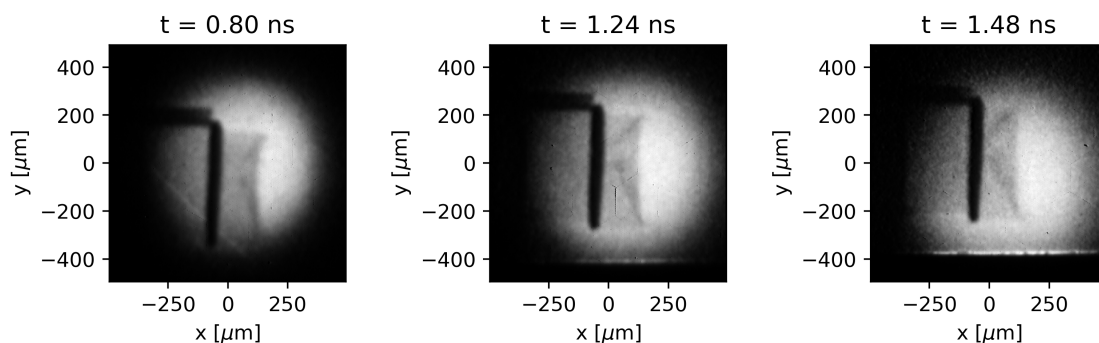


Fig. 5.28 Radiographies recorded on the framing camera from shot 27786. This shot used the configuration presented in Figure 5.26.

intensity. Figure 5.30 presents some of the radiographies obtained on shot 28507, which has been realized using this configuration. Similarly to the precedent radiographies, the dark vertical layer corresponds to the copper layer. The alignment fiber is not visible since it has been placed at a different position on the plastic slab. Similarly to the previous radiographies, the shock front can be seen propagating in the front plastic layer. Again, an asymmetry of the front shock can be seen, but this time it is orientated as in the simulation (the shock is faster for $y < 0$). As for the first shot day, this asymmetry cannot be interpreted as an effect of the hot electrons heating since the interaction beam did not use any phase plate. The interaction beam used on the second shot day was different from the one used on the first shot day. Therefore, the inhomogeneities of irradiation in the focal spot might be different between the two shot days, resulting in this difference of asymmetry in the shock front. Initially, the apparent thickness of the copper layer is $24 \pm 9 \mu\text{m}$, which is very close to the expected $20 \mu\text{m}$. This shows that on this shot, a very good alignment of the target has been realized. Then, the expansion of the copper layer can be observed. Its thickness is $30 \pm 9 \mu\text{m}$ at 0.93 ns and $37 \pm 9 \mu\text{m}$ at 1.43 ns . At 0.93 ns the shock has not reached the copper layer yet, so that this expansion can be attributed the heating by the hot electrons alone. At 1.43 ns , it is difficult to know if the shock has reached the copper layer. Yet, the expansion of the layer can still be attributed to the hot electrons since the shock wave has not reached the copper/rear plastic interface. The average velocity of expansion of the copper layer is then $12 \pm 6 \text{ km/s}$. This velocity is in agreement with the value presented in Table 5.2. However, it is not possible to discriminate between the different simulations that included the hot electrons due to the large error bar.

On both shot days, the shock front showed a stronger contrast on the sides compared to the center. Due to this low contrast at the center, the measurement of the shock front position is difficult, which results in large uncertainties. Figure 5.31 presents the shock front

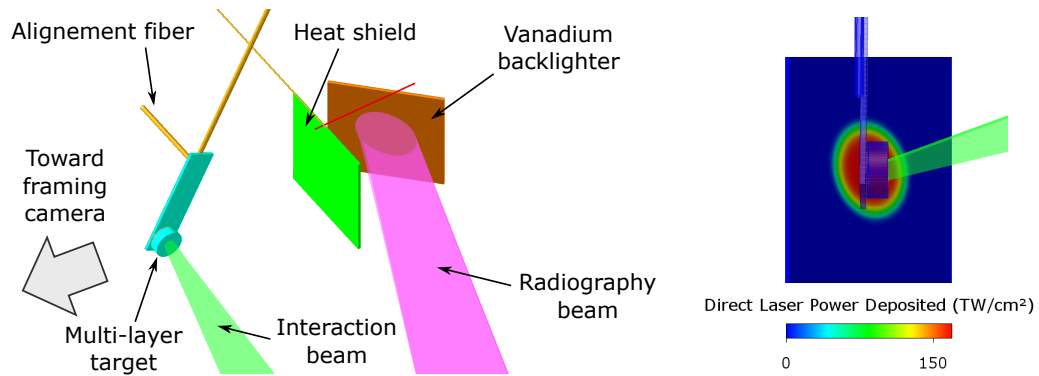


Fig. 5.29 Schematic of the radiography experiment on OMEGA EP used on the second shot day (left) and direct laser irradiation on the backlighter as seen from the radiography axis (right).

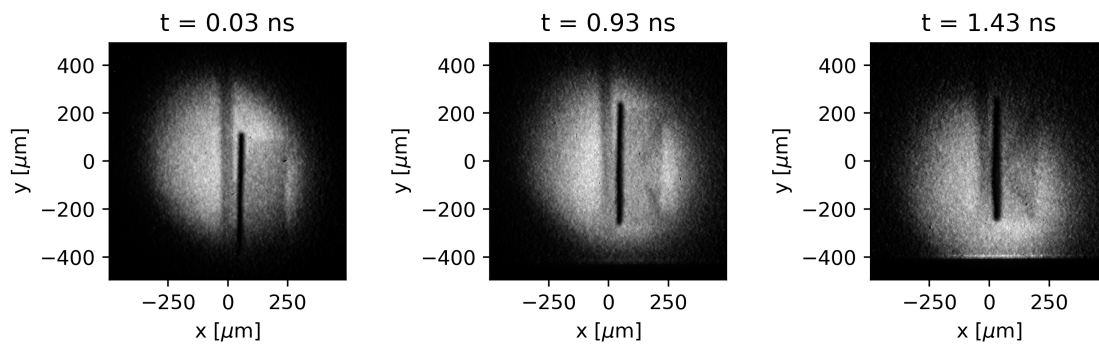


Fig. 5.30 Radiographies recorded on the framing camera from shot 28407. This shot used the configuration presented in Figure 5.29.

position as function of time measured on the radiographies of shots 27785, 27786 and 28507. The larger error bars for shots 27785 and 27786 are due to the additional uncertainty on the distance from the center of the copper layer to the target front surface. On this figure, the position of the shock front from the simulations presented in Table 5.2 are also shown. The change in slope observed for all simulations is due to the shock reaching the copper layer, where it has a lower velocity. The best agreement between simulation and the experimental data is obtained for the simulation with SRS hot electrons, $\theta_{SRS} = 20^\circ$, and 70% of the nominal incident energy. However, due to the large error bars, the other simulations also are in reasonable agreement with the experiment data. Looking only at the shock front position along time do not allow to conclude on the presence, or absence, of hot electrons during the experiment. In such case, the full 2D radiographies have be considered and compared to the simulations.

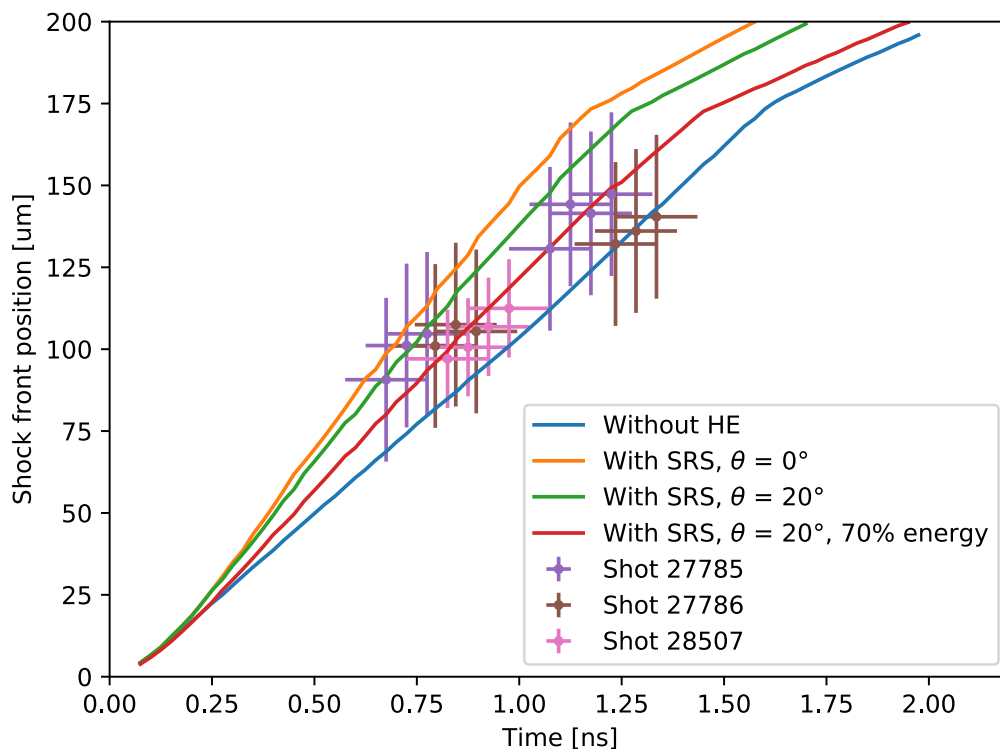


Fig. 5.31 Experimental and simulated shock front position as function of time. The solid lines are the shock front position from the simulations presented in Table 5.2. The experimental shock front position have been measured from the images presented in Figure 5.27 for shot 27785, in Figure 5.28 for shot 27786 and for in Figure 5.30 for shot 28507. The error bars for the shock front position for shots 27785 and 27786 are significantly larger than for shot 28507 due to the additional uncertainty on the front layer thickness.

5.3.3 Post-processor radiographic for planar CHIC simulation

In order to compare the 2D experimental radiographies to the simulations, synthetic radiographies have to be produced. Since the plan simulated with CHIC is orthogonal to the radiography axis, an extrapolation of simulation along the radiography axis have to be made. Figure 5.32, left, presents a schematic of the way it is usually realized. The target is separated in two parts. The perturbed target is the result of the hydrodynamic simulation at the time of the radiography $t = t_{radio}$. The unperturbed target is the target in its initial condition which is equivalent to the simulation at $t = 0$. This is this method of extrapolation that have been used for the estimation of the target transmission presented in Figure 5.25. The main issues with this method is that the hydrodynamic profile along the radiography axis is discontinuous. As a consequence the contrast of the shock front can be badly estimated and some regions can have non-physical transmissions. Since the low contrast at the shock front seems to be characteristic of the effect of the hot electrons on the shock hydrodynamic, a better method of extrapolation is required. In this section, a new method of extrapolation of 2D CHIC simulations into 3D geometry for the calculation of synthetic radiography is presented. This method is applied to the simulations presented in Table 5.2 and the resulting radiographies are compared to the experimental ones.

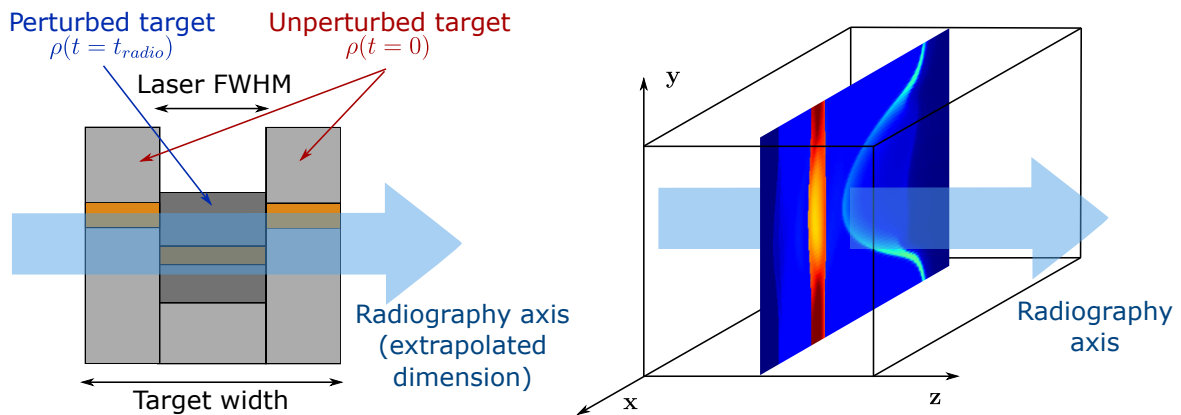


Fig. 5.32 Schematic of the usual way to extrapolate 2D simulation data for the realization of synthetic radiography (left) and orientation of the axis used for the new method of extrapolation (right).

The objective of the extrapolation method is to calculate the value of the hydrodynamic variables in the 3D space (x, y, z) at the time of the radiography $t = t_{radio}$. Here, (x, y, z) are defined so that x is direction normal to the target surface (the main direction of propagation of the shock), y the simulated transverse direction and z the non-simulated radiography axis (as shown in Figure 5.32, right). Considering only the density ρ for simplicity, this means determining $\rho(t = t_{radio}, x, y, z)$ from the simulation data $\rho(t, x, y, z = 0)$. A way of

extrapolation is to consider that ρ has a symmetry axis in $x = 0$. However, this assumption cannot be made for this experiment since it would prevent from reproducing the asymmetry observed in the simulations, along the traversal simulated direction y . In a more general way, the density at given position y_1 , $\rho(t, x, y = y_1, z)$, cannot be function of the density at a different position along the y axis, $\rho(t, x, y \neq y_1, z)$. Under this constrain, the proposed solution is to consider that the density at $t = t_{radio}$, away from the simulated plan, is similar the density in the simulated plan ($z = 0$) at an earlier time $t < t_{radio}$. There is therefore a pairing function f so that $\rho(t = t_{radio}, x, y = y_1, z) = f[\rho(t < t_{radio}, x, y = y_1, z = 0)]$. In order to determine this pairing function, an assumption has to be made on the hydrodynamic along the z direction. A possibility is to consider that the shock front position $x_{shock}(t, y, z)$ is axisymmetric so that $x_{shock}(t = t_{radio}, y, z = 0) = x_{shock}(t = t_{radio}, y = 0, z)$ and that the pairing function f is invariant along the y direction. The assumption on the shock front position is significantly less strong than assuming that the whole hydrodynamic is axisymmetric. In this case the pairing function f is given by solving the equality $x_{shock}(t = t_{radio}, y, z = 0) = f[x_{shock}(t < t_{radio}, y = 0, z = 0)]$. Once the pairing function have been determined, it can be applied for every coordinate along the y axis independently in order to give $\rho(t = t_{radio}, x, y, z)$.

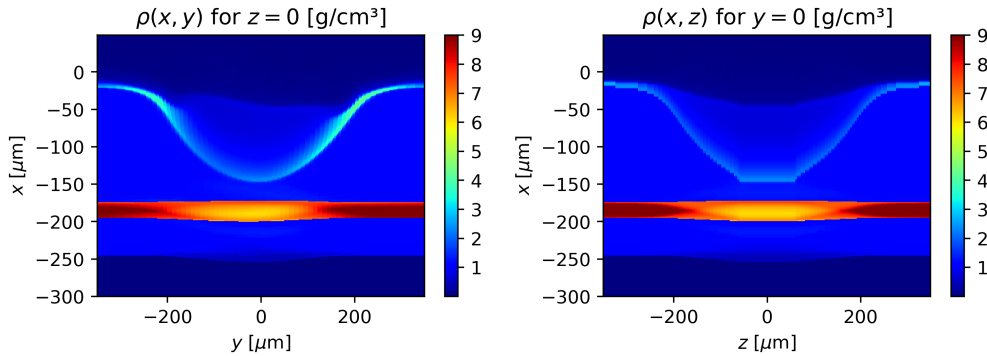


Fig. 5.33 2D map from the extrapolated 3D density at 1.0 ns for the simulation with SRS hot electron and $\theta_{SRS} = 0^\circ$. (left) Plan defined by $z = 0$, which corresponds to the simulated plan. (right) Plan defined by $y = 0$ which is extrapolated.

Figure 5.33 presents the results of the extrapolation of the simulation with SRS hot electrons and $\theta_{SRS} = 0^\circ$ at 1.0 ns (presented in Table 5.2). The density map on the left corresponds to the plan $\rho(t = t_{radio}, x, y, z = 0)$, which is the plan simulated with CHIC. The density map on the right corresponds to the plan $\rho(t = t_{radio}, x, y = 0, z)$, which have been extrapolated. Along the radiography axis z , the density does not have non-physical discontinuities. Also, for large value of z , far from the simulated plan, the density profile tends toward the hydrodynamic profile of non-perturbed target, as expected. Once that the hydrodynamic variables have been extrapolated, the transmission can be calculated using the

equation 5.9. Since the target is actually a cylinder with radius $r = 250 \mu\text{m}$, the density is fixed to zero for $r^2 > y^2 + z^2$. Finally, to take in account the spatial resolution of the pinhole array used for the imaging of the target, the synthetic radiography is blurred using a $15 \mu\text{m}$ full width half maximum 2D Gaussian convolution.

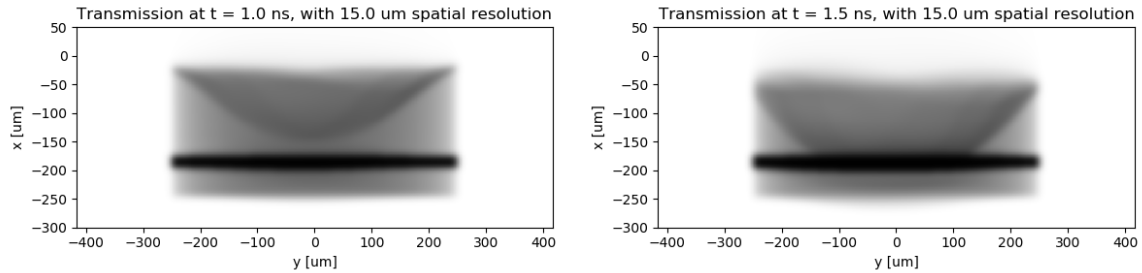


Fig. 5.34 Synthetic radiographies obtained from the simulation including the SRS hot electrons and with $\theta_{SRS} = 0^\circ$, at 1.0 ns (left) and 1.5 ns(right). The radiographies took in account the $15 \mu\text{m}$ spatial resolution of the diagnostic.

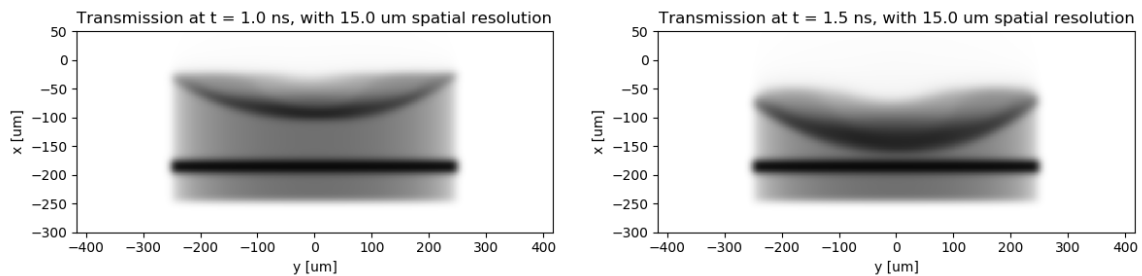


Fig. 5.35 Synthetic radiographies obtained from the simulation that did not include any hot electrons, at 1.0 ns (left) and 1.5 ns(right). The radiographies took in account the $15 \mu\text{m}$ spatial resolution of the diagnostic.

Figure 5.34 presents the synthetic radiographies obtained at 1.0 ns and 1.5 ns from the simulation with SRS hot electron and $\theta_{SRS} = 0^\circ$. On the synthetic radiography at 1.0 ns, the contrast of the shock front in the center is very low, similarly to what have been observed experimentally (on Figures 5.27, 5.28 and 5.30). Also, both on the synthetic and experimental radiographies, the contrast at the shock front is better on the sides of the shock than in its center. Yet, the shock front position and curvature do not match the experimental radiographies. Experimentally, the shock seems to be slower and flatter. Figure 5.35 presents the synthetic radiographies obtained at 1.0 ns and 1.5 ns from the simulation without any hot electrons. The shock front position and curvature on these radiographies is close to the one observed experimentally. Yet, these radiographies do not reproduce the low contrast of the shock front that has been observed. On these synthetic radiographies, the contrast is

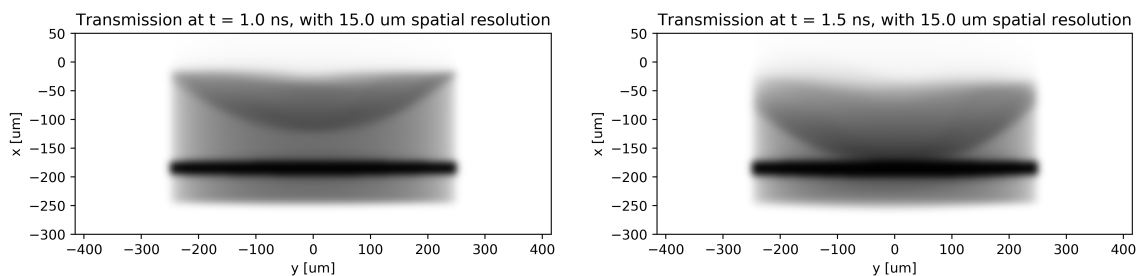


Fig. 5.36 Synthetic radiographies obtained from the simulation including the SRS hot electrons, with $\theta_{SRS} = \pm 20^\circ$ and a incident energy reduce to 70% of the nominal energy, at 1.0 ns (left) and 1.5 ns(right). The radiographies took in account the 15 μm spatial resolution of the diagnostic.

maximum at the center of the shock front, where the transmission drop close to zero. Finally, the best match between the synthetic and experimental radiographies is obtained with the simulation with SRS hot electrons, $\theta_{SRS} = \pm 20^\circ$ and 70% of the nominal incident energy. Figure 5.36 presents the synthetic radiographies obtained at 1.0 ns and 1.5 ns from this simulation. These radiographies reproduce qualitatively the shock front position, curvature and contrast.

5.3.4 Conclusion

From the two shot days of this experiment, improvement have been made in the set-up. The target have been simplified and the alignment procedure improved, which allowed to achieve a very good alignment on the second shot day (better than 1° with respect to the radiography axis). This allowed to the see the expansion of the copper plate due to the heating by the hot electrons. The comparison of the experimental radiographies with the results of CHIC simulations realized with and without hot electrons has been realized. For this purpose a post-processor for the realization of synthetic radiographies from CHIC simulations has been developed. The comparison of these synthetic radiographies with the experimental images has shown that hot electrons have to be taken in account in order to reproduce the shock front position, curvature and contrast. Especially, a best match between simulation and experiment have been found for the simulation that included SRS hot electrons with an initial divergence $\theta_{SRS} = \pm 20^\circ$ and a reduction of the incident energy to 70% of the nominal one.

Experimental measurements of the hot electron temperature and total energy are currently being realized though the analysis of data from K_α emission of the copper layer and Bremsstrahlung emission. Measurements of the laser absorption are also being analyzed. The results presented in this section are only preliminary and they did not take in account

these. Additional simulations with the experimental hot electron source parameters and laser absorption will be realized in the future.

This experiment have allowed to point out some major limitations for the realization of the radiography of a shock wave perturbed by hot electrons. Due to the heating of the hot electron, the contrast at the shock front was very low, which results in large error bars on its position. In future experiments, this contrast should be improved. A possibility is to use larger laser focal spot in order to maximize the width of the shock front along the radiography axis. Finally, the main issue in this experiment in the absence of phase plate for the interaction beam. Since the intensity distribution in the focal spot is unknown and might be very inhomogeneous, any conclusion made in this section has to be taken with care. Future experiments aiming at the radiography of the shock front should imperatively use phase plates in order to remove this source of uncertainty.

5.4 Design of shock ignition relevant experiment in planar geometry on LMJ

In the experiment presented in the previous section, the laser intensity was around 5×10^{15} W/cm² in order to reproduce the intensity of a shock ignition spike. Yet, the energy available on OmegaEP was not enough so that both the intensity and the plasma conditions present during a shock ignition spike could be reproduced. Indeed, in realistic shock ignition implosions, the irradiation of the target during the compression phase results in a large plasma corona surrounding the target. This plasma corona might significantly modify the conditions for the development of laser plasma instability during the ignition spike, as well as the transport of the hot electrons that might be produced. In order to be more relevant for the study of shock dynamic in the context of shock ignition, such large plasma corona has to be produced though the irradiation of the target by a low intensity foot pulse. Then the target can be irradiated using a high intensity spike pulse to study the effect of the hot electrons on the shock dynamic. The Laser MegaJoule (LMJ) allows to have such pulses with a low intensity foot and a high intensity spike. In this section is presented the design of an experiment on LMJ aiming at the measurement of the propagation of a strong shock produced in shock ignition relevant conditions.

Figure 5.37 shows a schematic of the set-up proposed for this experiment. In this set-up, four quads (a bundle of four beams) of the LMJ facility are used. Indeed, the LMJ is an under construction laser facility designed for the study of indirect drive implosion. Figure 5.38 presents a schematic of the geometry of irradiation of the LMJ quads. The quads are

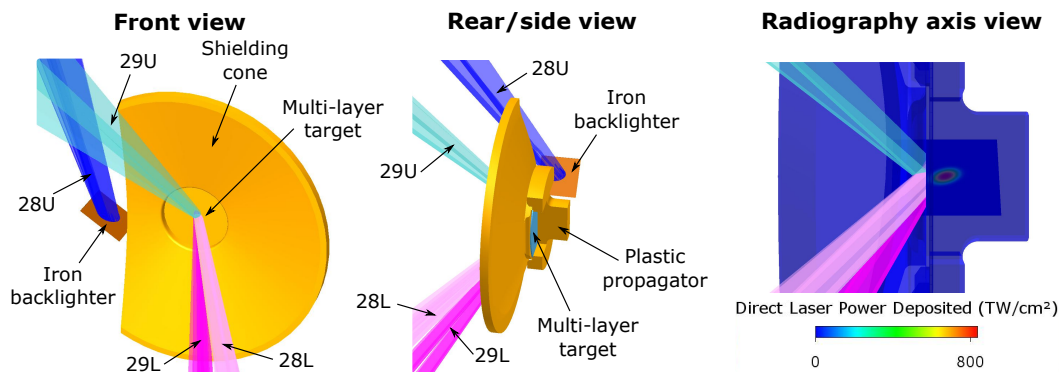


Fig. 5.37 Schematic of the experiment proposed on LMJ. Each quad (28U, 28L, 29U and 29L) is a bundle of four beams. For the radiography axis view, the calculation of the intensity on the backlighter have been realising considering an elliptical type A phase plate [99] and a power of 4 TW for the quad 28U.

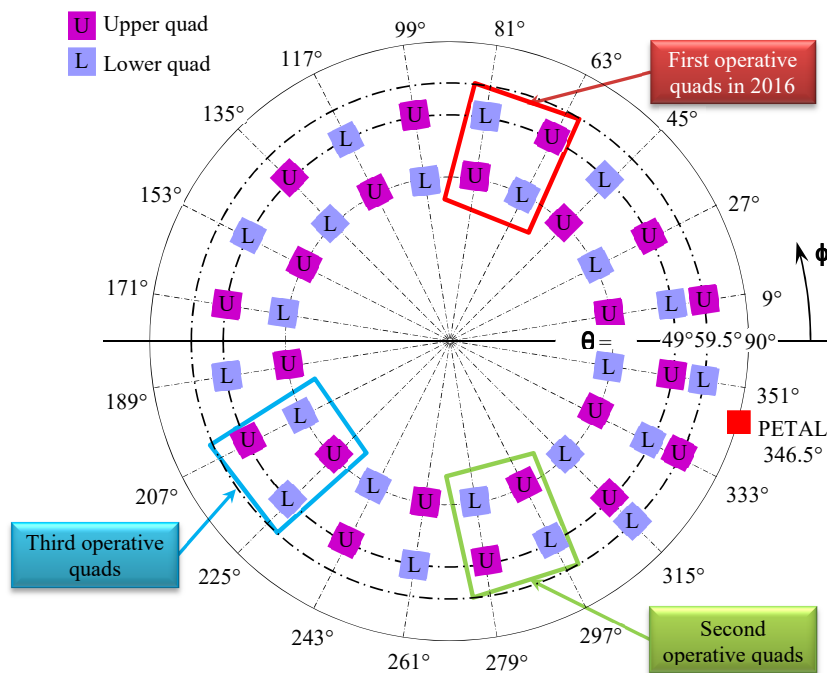


Fig. 5.38 Irradiation geometry of LMJ quads and PETAL beam [99]. The quads considered for this experiment are the first operative quads indicated by the red box.

organized in four cones at 33° and 49° for the upper quads and -33° (or 147°) and -49° (or 131°) for the lower quads. This geometry of irradiation in cones is optimized for the irradiation of the inner surface of hohlraums. Currently, only the four quads indicated by the red box are operational. While this prevents from realizing spherical geometry experiments, it allows to do planar geometry experiments such as the one proposed here. These quads are labelled 28U, 28L, 29U and 28L. For this experiment, three quads (28L, 29U and 28L) are used for the irradiation of the target and one quad (28U) is used for the irradiation of the backlighter that produces the X-rays for the side radiography of the shock wave. The normal to the surface of the multi-layer target is orientated in $(\theta = 90^\circ, \Phi = 58.8^\circ)$, so that the quads have relatively small angles in the azimuthal direction (22.5° for 29U and 4.5° for 28U and 28L). In these conditions, 2D planar geometry can be used for the simulations for the target design. The only angle that is taken in account in these simulations is then the polar angle θ . The angle of the quads with respect to the normal to the target surface are 41° for 29U, -41° for 28L and -57° for 29L.

The three quads used to irradiate the multi-layer target have the same pulse shape. It is composed of a foot and a spike. During the spike, the laser power is 4.4 TW per quads, which is the maximum available on the facility for pulses with duration between 0.7 and 3 ns [99]. Also, in order to maximize the overlapped intensity during the spike, these quads are equipped with the phase plates allowing to have the smallest focal spot available on the facility. These are the Type F continuous phase plates, which results in a circular Gaussian spot with a radius at $1/e$ of $168 \mu\text{m}$ [99]. With these parameters, the overlapped intensity on the target surface during the spike is $\sim 7.7 \times 10^{15} \text{ W/cm}^2$, which is relevant for shock ignition. On the other hand, the intensity during the foot has to be relatively small in order to avoid laser plasma instabilities that would lead to the production of a large amount of hot electrons. Indeed, the diagnostics used for the measurement of the hot electron populations, such as K_α spectroscopy (section 5.2.1) and Bremsstrahlung spectroscopy (section 6.3), are time integrated. Therefore, they cannot discriminate between hot electrons produced during the spike or during the foot. Minimizing the amount of hot electrons produced during the foot allows to have a better measurement of the hot electrons produced during the spike. During the foot, the power is 0.4 TW per quads, which results in an overlapped intensity on the target surface of $\sim 7 \times 10^{14} \text{ W/cm}^2$.

To determine the duration of the foot pulse, the gradient length of electronic density at $n_c/4$, $L_{n_e} = n_e \nabla n_e$, is considered. It is a particularly relevant parameter for characterizing the plasma conditions since it appears in the scaling laws used in CHIC for the calculation of the SRS and TPD hot electron conversion efficiencies (equations 2.43 and 2.50). 1D radiation hydrodynamic simulations have shown that at the end on the compression phase of shock

ignition like implosion, this length is around $350 \mu\text{m}$ [100]. CHIC simulations in 2D planar geometry have been realized in order to find an optimal foot pulse duration which reproduces this gradient length. In these simulations, the LMJ quads have been modeled using three PCGO beams, with angles of incidence described before. For numerical efficiency, this simulations did not include hot electrons. An optimal foot pulse duration of 3 ns has been found. Figure 5.39 presents the target at $t = 0$ (left) and the laser pulse per quads used in this simulation (right). The results of this simulation are presented in Figure 5.40. The gradient length has been evaluated along two different lines, at 0° (corresponding to the normal to the target surface) and 45° (close to the angle of incidence of the laser beams). Along both line-out axis, the gradient length increases with time. At the end of the foot pulse, at 3 ns, the gradient length is $\sim 300 \mu\text{m}$ for the 0° line-out and $\sim 400 \mu\text{m}$ for the 45° line-out. The pulse shape considered in this experiment is then composed of a foot with a power of 0.4 TW per quad during 3 ns followed by a spike with a power of 4.4 TW per quad during 1.3 ns .

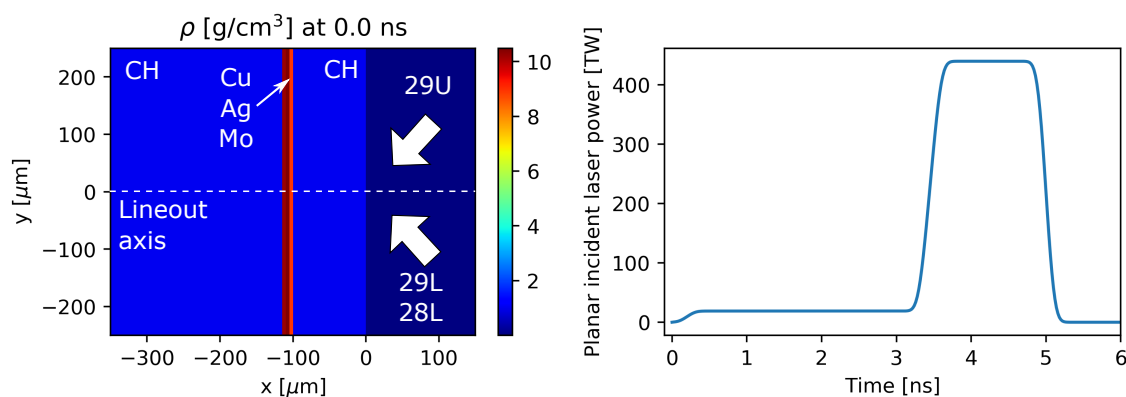


Fig. 5.39 Initial 2D density map of the target (left) and incident laser power in planar geometry for one quad (right). The quads incidence angles are -57° (28L), -41° (29L) and 41° (29U). Unlike laser intensity, the laser power in planar geometry does not correspond to the real laser power, it has been calculated using the equations 5.7 and 5.8.

The target irradiated by this pulse has two parts: a cylindrical multi-layer target and a rectangular plastic propagator. The multi-layer target has a radius of $\sim 5 \text{ mm}$ and is composed, from front to rear, by a $100 \mu\text{m}$ thick plastic (CH) ablator followed by three $5 \mu\text{m}$ thick layers of Copper, Silver and Molybdenum used as K_α layer for the measurement of the hot electron population. Compared to the mono material K_α layer used in the PALS and OmegaEP experiments, the use of multi-material allows to have a better measurement of the hot electron temperature by considering the ratio of K_α emissivity of the different layers. At the back of the Molybdenum layer is fixed the rectangular plastic (CH) propagator. In order to evaluate the thickness of this slab along the radiography axis, the backlighter material, and

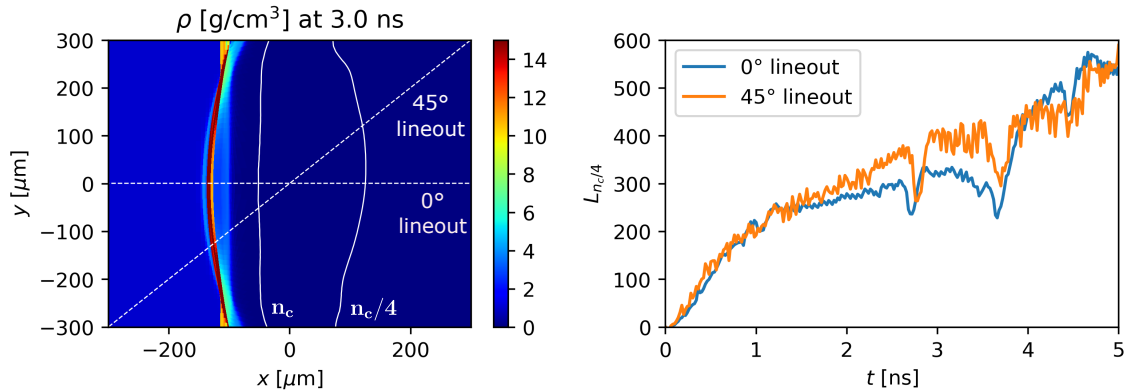


Fig. 5.40 Density map from the simulation without hot electrons at 3 ns (left) and electron density gradient length at $n_c/4$ (right). The 0° and 45° lineout axis are indicated in dashed lines on the density map. The critical density n_c and quarter critical density $n_c/4$ are indicated in solid lines.

the optimal time for radiography, CHIC 2D simulations including the hot, or not, electrons have been realized. The comparison between these simulations also allows to understand the effects of the hot electrons on the shocks hydrodynamic.

Figures 5.41 and 5.42 present the results from CHIC simulations of this experiment without and with hot electron, respectively. The simulations are in 2D planar geometry with PCGO description for the laser propagation and a constant flux limiter of 4% for the thermal electron transport. The simulation with hot electrons included SRS hot electrons with nominal scaling laws and $\pm 20^\circ$ divergence for the sources. For both simulations, the target initial condition and the laser pulse are identical as the ones presented in Figure 5.39. Before the spike (which starts at 3.3 ns), both simulations have very similar hydrodynamic as it can be seen on the density and pressure as function of time and space (Figures 5.41 and 5.42, bottom row). The shock created by the foot pulse has a pressure of ~ 50 Mbar in the CH ablator. Its pressure is raised to around 100 Mbar as it collides with the K_α layers. Then this foot shock breaks out in the CH propagator where its pressure is ~ 30 Mbar. Then around 3.3 ns, the spike launches another shock. Similarly to the foot shock, its initial pressure is amplified as it collides with the K alpha layer before being reduce when it it breaks out in the CH propagator. It then coalescences with the foot pulse in the CH propagator, resulting in a single decaying shock (see section sec:coal). Table 5.3 presents the spike shock pressures in CH ablator, K_α layer and CH propagator from the simulations with and without hot electrons presented in Figure 5.42 and 5.41, respectively. Results from a simulation realized with SRS hot electrons but with a initial divergence for the hot electron sources of $\theta_{SRS} = 0^\circ$ are also

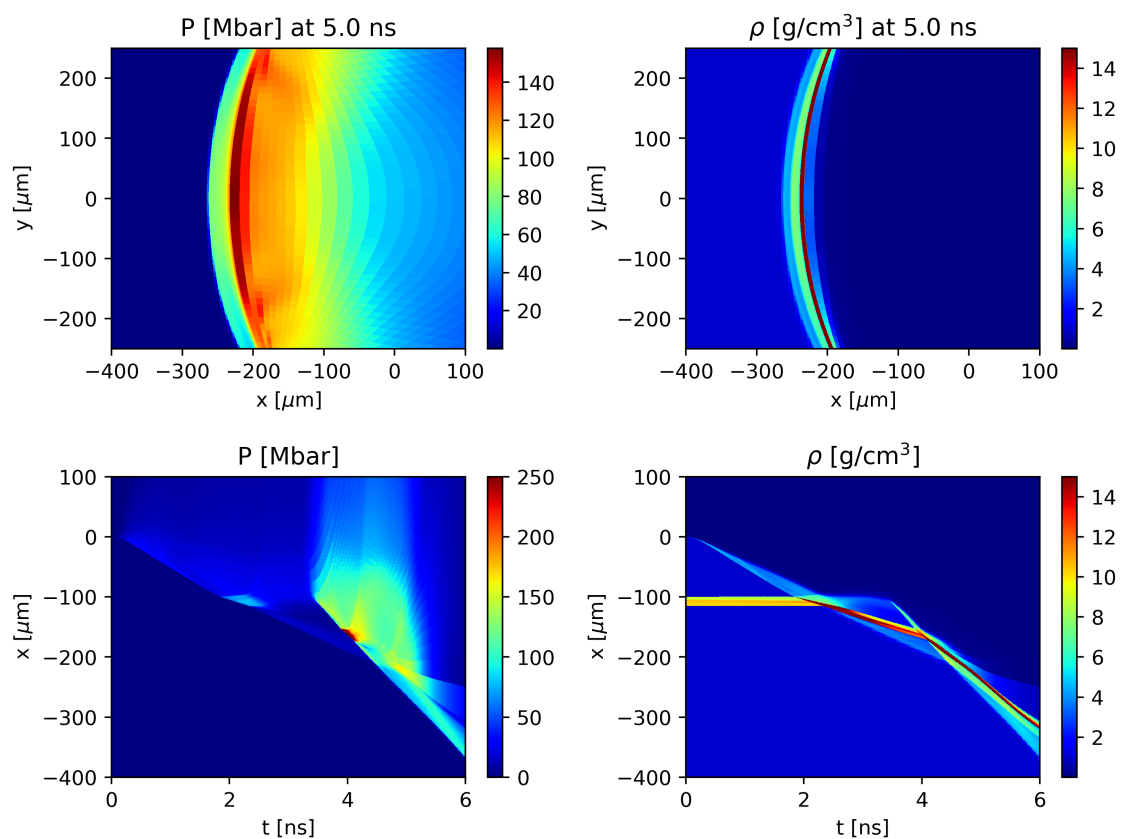


Fig. 5.41 Results of the simulation without hot electrons. (top right) 2D map of pressure at 5.0 ns. (top left) 2D map of density at 5.0 ns. (bottom left) pressure as function of time and space. (bottom right) density as function of time and space. The line-out axis for the bottom row figures is presented in Figure 5.39.

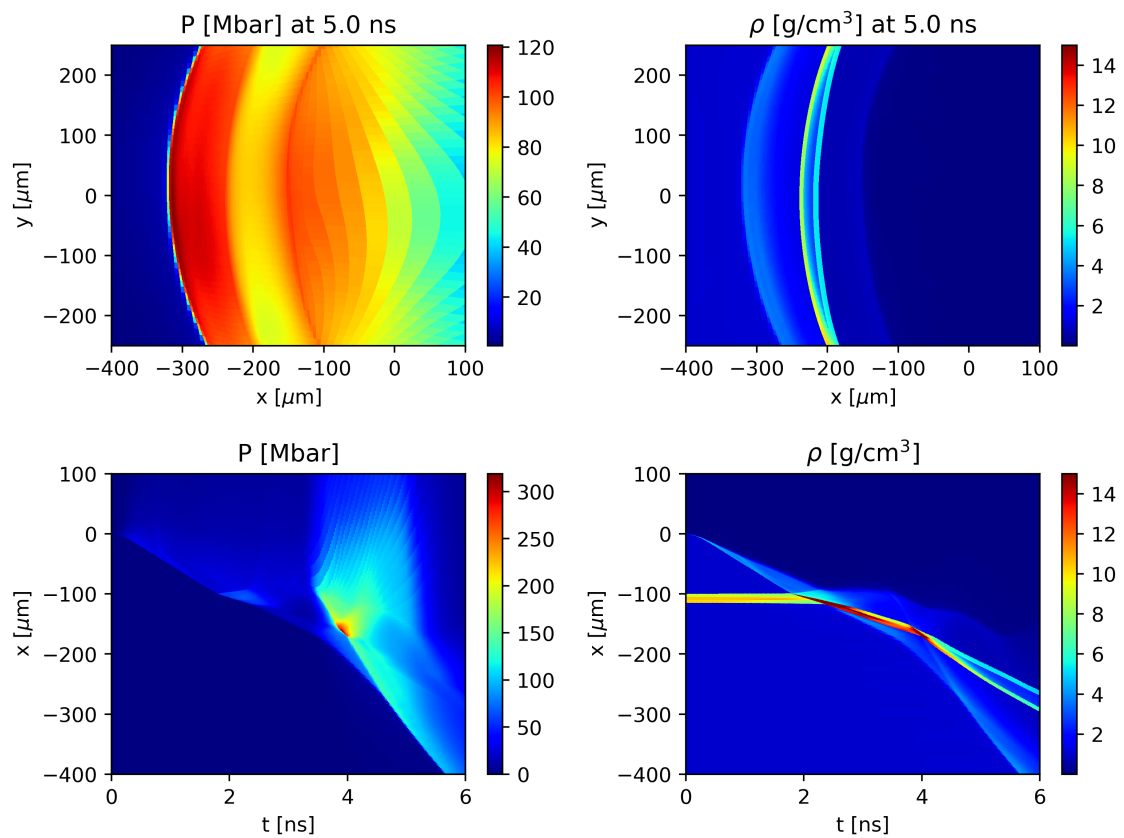


Fig. 5.42 Results of the simulation with SRS hot electrons ($\theta_{SRS} = \pm 20^\circ$). (top right) 2D map of pressure at 5.0 ns. (top left) 2D map of density at 5.0 ns. (bottom left) pressure as function of time and space. (bottom right) density as function of time and space. The line-out axis for the bottom row figures is presented in Figure 5.39.

	Without HE	With SRS, $\theta_{SRS} = 0^\circ$	With SRS, $\theta_{SRS} = \pm 20^\circ$
Collisional absorption fraction during foot pulse	58.2 %	55.2 %	55.4 %
Collisional absorption fraction during spike pulse	45.4 %	35.3 %	36.1 %
SRS conversion efficiency during foot pulse	0 %	1.3 %	1.4 %
SRS conversion efficiency during spike pulse	0 %	10.6 %	10.6 %
Spike shock pressure in plastic ablator	200 Mbar	204 Mbar	188 Mbar
Spike shock pressure in K_α layers	350 Mbar	344 Mbar	311 Mbar
Spike shock pressure in plastic propagator before coalescence	125 Mbar	173 Mbar	153 Mbar
Spike shock pressure in plastic propagator after coalescence	80 Mbar	160 Mbar	122 Mbar
Spike shock average velocity between 5.5 and 6.5 ns	107 km/s	116 km/s	109 km/s
K_α layer average velocity between 5.5 and 6.5 ns	67 km/s	45.3 km/s	53.3 km/s

Table 5.3 Comparison between simulations realized for the design of the experiment on LMJ. All simulations have the same target and laser parameters.

presented. Collisional absorption rate and SRS conversion efficiency are also presented in this table.

The comparison between the simulations with and without hot electrons shows that their effect on the shock hydrodynamic is similar to what has been observed in the experiment on OmegaEP. They results in a higher shock pressure and velocity. Yet this difference is smaller compared to what have been observed in the simulations of the experiment on OmegaEP. Despite this smaller difference, due to the longer propagation time of the shock front the difference in position of the shock front is clearly visible (Figures 5.41 and 5.42, top row). Similarly to the simulations for the OmegaEP experiment, the density jump at the shock front is smaller when hot electrons are being taken in account. Yet this difference is smaller due to the blast wave behavior of the shock after its coalescence. Also the target downstream of the spike shock has an inhomogeneous density due to the expansion of the ablation front

toward the laser. It can be seen in the simulation including the hot electrons that they also perturbed the shock created by foot pulse. They increase its pressure and velocity before the coalescence, which results in a delayed coalescence time. Since the goal of the experiment is to realize the radiography of the shock front after the coalescence, the considered times for radiography are after 5 ns. This constraint on the time of the radiography explains the position of the K_α layers. Indeed, since the K_α layers significantly perturbed the propagation of both shocks, it might have been preferable to place them at the rear of the target, so that the radiography of the shock would be realized in the front CH layer similarly to the OmegaEP experiment. However, in this case the plastic layer would have been more than $500\ \mu\text{m}$ thick so that the amount of hot electrons reaching the K_α layer would be too small, resulting in large uncertainty on the measurement of their temperature and number. In the case where the K_α layers are close to the front surface, their velocity can be measured, giving information on the fluid velocity in the shocked target. This velocity of the K_α layers from the simulations with and without hot electrons is presented in Table 5.3. It appears that this velocity is lower in the simulation with the hot electrons due to the expansion of the shocked target that has been heated by the hot electrons.

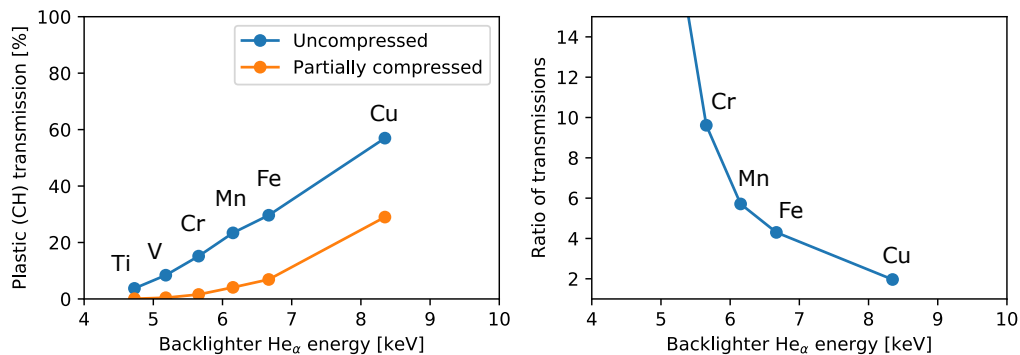


Fig. 5.43 Transmission of uncompressed and partially compressed plastic (left) and ratio of these transmissions (right) for the determination of the backlighter material for the LMJ experiment. The uncompressed curve corresponds to $1500\ \mu\text{m}$ of CH at solid density ($1.05\ \text{g}/\text{cm}^3$). The partially compressed curve corresponds to $1000\ \mu\text{m}$ of CH at solid density + $500\ \mu\text{m}$ of CH at four times the solid density ($4.20\ \text{g}/\text{cm}^3$).

Due to the larger laser focal spots and the later radiography times, the thickness of the plastic propagator along the radiography axis has to be significantly larger than what have been considered in the OmegaEP experiment. A thickness of $1500\ \mu\text{m}$ has been taken. The choice of the backlighter material has been realized using the same method as for the OmegaEP experiment (section 5.3.1). Figure 5.43 presents the estimation of the transmission for this experiment assuming a $1500\ \mu\text{m}$ thick CH target with $500\ \mu\text{m}$ of the

target compressed at four times the initial density. It appears that the transmissions for titanium, vanadium and chromium backlighters are lower than 20° (Figure 5.43, left). Using one of those material would results in too dark radiographies. On the other hand, using copper backlighter allows to have a good transmission but a low contrast of the shock front (Figure 5.43, right). For this experiment, iron backlighter is a good compromise between transmission and contrast. In order to validate this choice of material, synthetic radiographies using the post-processor presented in section 5.3.3 have been realized.

Figures 5.44 presents the synthetic radiographies obtained from the simulation that did not take in account the hot electrons (Figure 5.41). In this simulation, the difference in velocity between the shock front and the K_α layers is relatively small. Therefore, at 5.5 ns, the shock did not traveled a distance long enough so that it can be seen on the synthetic radiography when the $35 \mu\text{m}$ spatial resolution of the diagnostic is taken in consideration. It is visible a 6.5 ns but it still close to the K_α layers and its measurement might not be possible. Figures 5.45 presents the synthetic radiographies obtained from the simulation with SRS hot electrons and without an initial divergence for the SRS sources ($\theta_{SRS} = 0^\circ$). Due to the larger difference in velocity between the shock front and the K_α layers, the shock is clearly visible at 5.5 and 6.5 ns. The higher transmission area between the shock front and the K_α layers is due to the the hot electron heating the shock target which expands, accelerating the shock wave and slowing down the K_α layers. The images show a clear asymmetry which is due to a higher hot electron heating of the right side of the target (for $y > 0$). Indeed, for a given laser beam, the main direction of propagation of the hot electrons is close to the incidence angle of the laser beam. Since the beams are pointed toward the initial target surface ($x = 0, y = 0$), the hot electron produced by the quads 29U in the region ($x > 0, y > 0$) heat the target in the region ($x < 0, y < 0$). And respectively, the quads 28L and 29L produce hot electrons in the region ($x > 0, y < 0$) which heat the target in the region ($x < 0, y > 0$). There is therefore more hot electrons heating the ($x < 0, y > 0$) region which results in the observed shock asymmetry. Figures 5.46 presents the synthetic radiographies obtained from the simulation with SRS hot electrons and with an initial divergence for the SRS sources $\theta_{SRS} = \pm 20^\circ$. In this images, the positions of the shock front and K_α layers are similar as in the radiographies from the simulation with $\theta_{SRS} = 0^\circ$. Yet, the asymmetry is not visible anymore and the shock front has a smaller curvature. This is directly an effect of the initial divergence of the SRS hot electron sources.

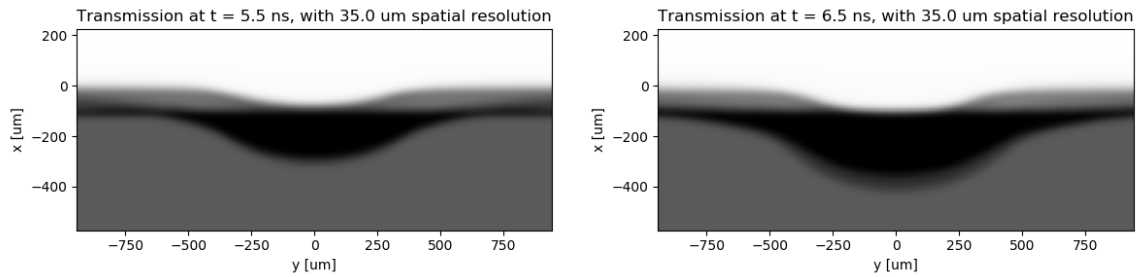


Fig. 5.44 Synthetic radiographies obtained from the simulation without hot electrons, at 5.5 ns (left) and 6.5 ns(right). The radiographies took in account the estimated 35 μm spatial resolution of the diagnostic.

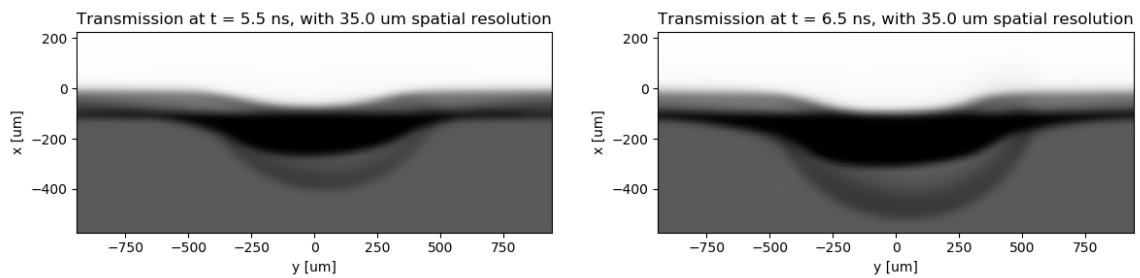


Fig. 5.45 Synthetic radiographies obtained from the simulation including SRS hot electrons with $\theta_{SRS} = 0^\circ$, at 5.5 ns (left) and 6.5 ns(right). The radiographies took in account the estimated 35 μm spatial resolution of the diagnostic.

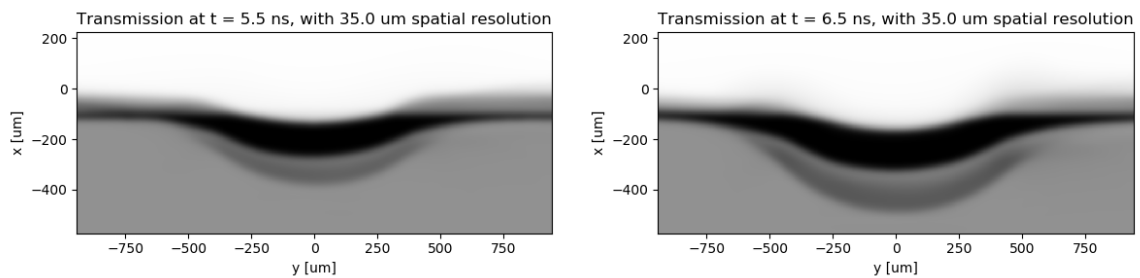


Fig. 5.46 Synthetic radiographies obtained from the simulation including SRS hot electrons with $\theta_{SRS} = \pm 20^\circ$, at 5.5 ns (left) and 6.5 ns(right). The radiographies took in account the estimated 35 μm spatial resolution of the diagnostic.

5.5 Conclusion

In this chapter, the effect of hot electrons produced in shock ignition relevant conditions have been studied in planar geometry. These studies used the radiation hydrodynamic code CHIC in order to interpret or design experiments.

The models recently implement in CHIC for the description of the laser and hot electrons propagation have been presented. They use a Complex Paraxial Geometrical Optics model for the description of the laser propagation and an Angular Scattering Approximation model for the description of the hot electrons propagation and energy deposition. The hot electron source parameters (temperatures and conversion efficiencies) are determined from the local intensity and plasma conditions using the scaling laws presented in section 2.3. These models have been validated through comparisons with simulations and few experiments. Yet, further comparison with experiments realized in conditions relevant to shock ignition are necessary.

First, an experiment realized on the Prague Asterix Laser System (PALS) have been presented. In this experiment, the main diagnostic was the time-resolved emission of the rear side of the target (Streak Optical Pyrometry, SOP). CHIC simulations including SRS and TPD hot electrons have been realized and synthetic SOP images have been produced from these simulations using a radiative transport post-processor. On these images a peak of emission due to the heating of the rear side of the target by the hot electron, during the laser plasma interaction, is visible. At later time, the signal rises due to the shock breakout. This behaviour is observed on the experimental images. In order to reproduce the delay measured between the peak of emission due to the hot electrons and the rising of the signal due to the shock breakout, the hot electron conversion efficiencies in the simulations had to be reduced and an initial divergence of $\pm 20^\circ$ for the SRS hot electron sources had to be introduced. This shows that the scaling laws presented in section 2.3 are not valid for these laser parameters (at a wavelength of $1.3 \mu\text{m}$). Also, it shows that the increase in hot electron beam width due to the Angular Scattering Approximation is not enough to reproduce the divergence of the SRS hot electrons.

Then, CHIC simulations realized for the design of an experiment on OmegaEP have been presented. The objective of this experiment was to realize the side-radiography of a shock perturbed by hot electrons. The laser pulse for this experiment have been design so that it is relevant to shock ignition, with a peak intensity of $5 \times 10^{15} \text{ W/cm}^2$. Yet, the energy available on this facility did not allowed to create an extended plasma corona. This experiment have been realized and a preliminary analysis of the 2D radiographies have been proposed. The measured shock front trajectory is well reproduce with CHIC simulations including SRS hot electrons, with an initial divergence for the SRS sources of $\pm 20^\circ$ and an incident energy reduce to 70%. This results confirms that an initial divergence for the

SRS hot electron sources is necessary in CHIC. Also, the reduction in incident energy might be due to Stimulated Brillouin Scattering which is not taken in account in the simulations. This agreement, observed between simulation and experiment for the shock front trajectory, is confirmed by the comparison of the 2D experimental radiographies with synthetic ones. These synthetic radiographies have been calculated using a new post-processor that have been presented.

Finally, the design of an experiment on LMJ is presented. Similarly to the experiment on OmegaEP, this experiment aims at the measurement of a shock perturbed by hot electrons. At the difference of the previous experiment, the energy available on LMJ allows to have an intensity and plasma conditions that a relevant for shock ignition. Especially concerning the gradient length of the electron density at the quarter critical density. CHIC simulations with and without an initial divergence for the SRS hot electrons sources have been realized and post-processed in order to produce synthetic radiographies. These showed that, without an initial divergence for the SRS hot electrons, the shock front presents an asymmetry. This asymmetry disappear in the synthetic radiography for the simulation that included an initial divergence of $\pm 20^\circ$. The presence or not of an asymmetry in the experimental radiographies should then give information on the initial divergence of the SRS sources needed in CHIC.

The effects of hot electrons on the shock hydrodynamic for these three experiments are similar. By heating the shocked target, they increase the shock pressure and velocity. Yet, since they also preheat the target ahead of the shock front, the shock strength and Mach number are reduced compared to simulations that did not include hot electrons. Due to the low compressibility of the preheated target, the density jump at the shock front is very low in the simulations that included the hot electrons. Finally, since the pressure in the shocked target is higher than the ablation pressure, the ablation front expand toward the laser beam. This results in a very inhomogeneous density of the shocked target.

Chapter 6

Effect of hot electron in spherical geometry

In the shock ignition scheme, the spike is launched around the end of the acceleration phase. At this time, the shell areal density increases greatly due to convergence effects, as presented schematically in Figure 6.1. The hot electrons produced in the corona by parametric instabilities, such as SRS or TPD, have a penetration depth that depends on the shell areal density. During the spike, if the shell areal density is significantly larger than their penetration depth, the hot electrons are expected to be stopped in the shell outer part. In this case, they would not preheat significantly the inner part of the shell and they could even contribute to the ignition shock pressure. On the other hand, if their penetration depth is similar or larger than the shell areal density, the whole shell would be heated by the hot electrons. This would lead to a less efficient compression of the shell during the deceleration phase and therefore a reduction of the implosion performance. Depending of the time of launching of the spike, the hot electrons could have a beneficial or detrimental effect.

So far, the dependence of hot electron preheating with the time when the hot electrons are generated during the implosion has been studied only through simulations [28]. Experimentally, a correlation between the deterioration of the implosion performance and the spike launching time has been observed [101]. Yet this deterioration could be due to hydrodynamic alone, as it has been observed in the simulations in section 4.3.3. Further experiments with a precise characterization of the hot electrons are required in order to confirm this correlation. In this context, an experiment has been realized on the Omega Laser Facility aiming to evaluate the effects of hot electron preheat on the performance of shock ignition implosions.

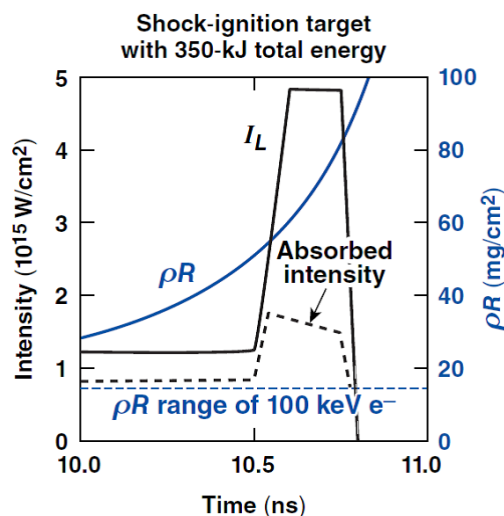


Fig. 6.1 Schematic of the intensity evolution of a shock-ignition laser pulse (solid black curve), the calculated collisional absorbed intensity (dashed black curve), and the DT shell areal density (solid blue curve) during the power spike. The horizontal dashed line indicates the range of a 100-keV electrons in the DT shell [28].

6.1 Experimental set-up

Omega is a 60-beam laser that is operating at the third harmonic of the Nd:glass laser wavelength ($\lambda = 0.351 \mu\text{m}$). The 60 beams are actually separated in three legs, each feeding into two clusters of 10 beams. A particularly interesting characteristic of the facility is the possibility to have totally different pulse shapes for each of the three legs. For shock ignition studies, this provides the opportunity to use two separate pulse shapes with independent control over the two beam groups. In this experiment, two legs (40 beams) were used to implode the shell and the third leg (20 beams) was used to drive a late shock and generate hot electrons. This is the so called 40+20 configuration. The beams were repointed to reduce the illumination non-uniformity in the 40 compression beams to 2.8% rms. Previous experiments have demonstrated that repointing significantly improved the implosion performance in this configuration [101]. The 40 compression beams were equipped with distributed phase plates [74] with super-Gaussian intensity distribution of fourth order and used polarization smoothing [72] and smoothing by spectral dispersion [73]. The 20 spike beams were not equipped with phase plate and used neither polarization smoothing or smoothing by spectral dispersion in order to maximize the intensity on target and therefore the hot electron production.

The Figure 6.2 presents the target and pulse shape used in this experiment. The targets were $34.8 \pm 0.2 \mu\text{m}$ thick deuterated plastic shell (CD) with an outer radius of $435 \mu\text{m}$

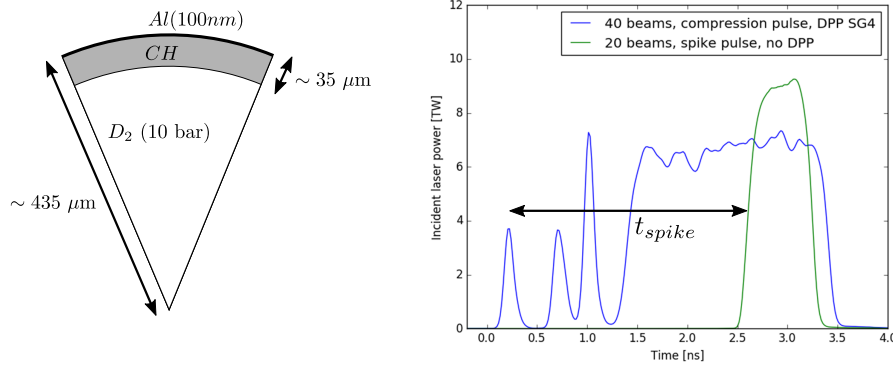


Fig. 6.2 Target (left) and pulse shape (right) used in the experiment. The compression pulse (in blue) used 40 beam and the spike pulse (in green) used 20 beams. The spike launching time t_{spike} is define as the time between the maximum of the first picket of the compression pulse and the half-maximum rise of the spike pulse.

and coated with $0.1 \mu\text{m}$ of aluminum. The shells were filled with ~ 10 bar of D_2 gas. The 40-beams compression pulse (in blue) delivered 15.3 ± 0.2 kJ on target using a triple picket pulse to implode the shell on a low adiabat ($\alpha \simeq 3$). The implosion of room temperature plastic target with such triple picket have been extensively studied in the standard 60-beams configuration [102]. The use of triple picket and smoothing by spectral dispersion significantly improved the implosion performance of 40-beam only implosion compared to previous 40+20 experiments that used no smoothing and a single adiabat shaping picket [101]. The 20-beams spike pulse (in green) delivered $5.7 \pm$ kJ on target using a ~ 600 ps square pulse. The spike beams were defocus by moving the lens position by 1.5 mm, providing a $\sim 200 \mu\text{m}$ spot on the initial target surface.

The scanned parameter was the spike launching time, defined as the time between the maximum of the first picket from the compression pulse and the half-maximum rising of the spike pulse. Several shots using the compression pulse only (shots 59749 to 59751) have been realized in order to optimize the implosion. Shot 59751 obtained the highest experimental neutron yield and is considered to be optimal. Then shots 59752, 59753 and 59755 have been performed with delays for the spike launching time of 2.4, 2.8 and 3.2 ns, respectively.

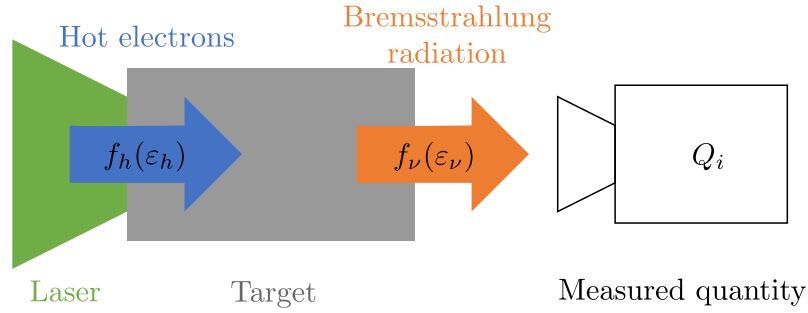


Fig. 6.3 Principle of hot electron measurement by high-energy differential-filtering photon spectroscopy.

6.2 Hot electron measurement by high-energy differential-filtering photon spectroscopy

In this experiment, the hot electron source parameters have been indirectly measured using the Hard X-Ray Diagnostic (HXRD). The principle of this diagnostic is presented schematically in Figure 6.3. In the plasma corona, the parametric instabilities lead to the production of hot electrons with a energy distribution $f_h(\epsilon_h)$, where ϵ_h is the hot electron energy. As these hot electrons propagate in the solid target, they are slowed down though electron-ion collisions. During this process, hard x-rays are emitted with a distribution $f_\nu(\epsilon_\nu)$, where ϵ_ν is the photon energy. The target is mostly transparent to these X-rays, so that they escape it and can be measured. The spectroscopy of this photon distribution is challenging due to its high energy (which is typically in the range 10 to 1000 keV). However, the use of multi-channel detector allows to measure the photon distribution parameters, given that its shape is known. Even if the detector itself is not spectrally resolved, the variation of filtering between its different channels i leads too different measured quantities Q_i . In order to determine the photon distribution parameters, this measured quantities have to be compared to an expected quantity $S_i(T_\nu, N_\nu)$, where T_ν and N_ν are the temperature and number of photons, respectively. The hot electron distribution parameters can also be determined by comparing the measured quantities Q_i with expected quantities $S_i(T_h, N_h)$, where T_h and N_h are the temperature and number of hot electrons, respectively.

Several diagnostics use this principle of differential filtering for the measurement high energy photon distribution or hot electron distribution (HXRD, BMXS, LTSE, CRAAC ...). From a diagnostic to another, the measured physical quantity, the number of channels or diagnostic geometry can fully change, yet the method of analysis presented in this section can be applied to any of them.

For any of these diagnostics, the expected signal on the channel i can be expressed as

$$S_i = \alpha_i \int f_v(\epsilon_v) \times F_i(\epsilon_v) d\epsilon_v, \quad (6.1)$$

where α_i is the factor of proportionality between the quantity measured by the detector and the energy deposited by the photons in it. In most cases, α_i is determined experimentally by an absolute calibration of the detector. $f_v(\epsilon_v)$ is the photon energy distribution in photon by unit energy, so that the number of photons is $N_v = \int f_v(\epsilon_v) d\epsilon_v$. $F_i(\epsilon_v)$ is the energy deposited in the channel i by a photon of energy ϵ_v . F_i correspond to both the absorption probability of a photon by the detector and the filters transmission in front the channel i . While F_i can be determined by taking in consideration the mass absorption coefficient of the filters material (from database like CRXO or NIST), in most cases particle transport simulations have to be realized. In first approximation, the photons can be assumed to have a Maxwellian distribution in energy, which writes

$$f_v(\epsilon_v, T_v, N_v) = N_v \times \frac{\epsilon_v^2}{2T_v^3} \exp\left[-\frac{\epsilon_v}{T_v}\right], \quad (6.2)$$

where T_v is the temperature of the photon distribution in unit of energy. Yet, making an assumption on the photon distribution is not necessary. This distribution can be expressed as a function of the hot electron distribution

$$f_v(\epsilon_v) = \int I_{br}(\epsilon_h, \epsilon_v) \times f_h(\epsilon_h) d\epsilon_h, \quad (6.3)$$

where $I_{br}(\epsilon_h, \epsilon_v)$ is the distribution of photons emitted by a hot electron of energy ϵ_h that has propagate in the target. I_{br} is target dependent and has to be calculated using particle transport simulations. $f_h(\epsilon_h)$ is the hot electron energy distribution in hot electron per unit energy, so that the number of electrons is $N_h = \int f_h(\epsilon_h) d\epsilon_h$. Similarly to the photon distribution, an assumption has to be made on the hot electron distribution. Assuming a three dimensional Maxwellian, it writes

$$f_h(\epsilon_h, T_h, N_h) = N_h \times f_h^M(\epsilon_h, T_h) = N_h \times 2 \sqrt{\frac{\epsilon_h}{\pi T_h^3}} \exp\left[-\frac{\epsilon_h}{T_h}\right], \quad (6.4)$$

where $f_h^M(\epsilon_h, T_h)$ is the normalized Maxwellian distribution and T_h the hot electron temperature in unit of energy. The total energy carried by the hot electrons is a parameter more relevant than the number of particle since it can be easily linked to conversion efficiency of the laser energy into hot electrons. For this Maxwellian distribution, the total energy is given by

$$E_h = \int \varepsilon_h f_h(\varepsilon_h) d\varepsilon_h = \frac{3}{2} N_h T_h. \quad (6.5)$$

The expected signal then can be express as a function of hot electron temperature T_h and total energy E_h

$$S_i(T_h, E_h) = \alpha_i \frac{E_h}{1.5 T_h} \int F_i(\varepsilon_v) \left[\int I_{br}(\varepsilon_h, \varepsilon_v) \times f_h^M(\varepsilon_h, T_h) d\varepsilon_h \right] d\varepsilon_v. \quad (6.6)$$

This expression can be used for the measurement of hot electrons using any diagnostic based on differential filtering photon spectroscopy. It requires a particle transport simulation of the diagnostic to determine $F_i(\varepsilon_v)$, a particle transport simulation of the target to determine $I_{br}(\varepsilon_h, \varepsilon_v)$ and the absolute calibration of the detector α_i .

Once the expected signal $S_i(T_h, E_h)$ has been calculated, the hot electron temperature and total energy can be determined from the measured signal Q_i using a χ^2 analysis. In order to determined the uncertainty on the measured parameters, it is more relevant to calculate the reduced $\tilde{\chi}^2 = \chi^2/l$, where l is the number of degrees of freedom of the analysis. It is given by $l = n - m$ with n the number of data set in the analysis and m the number of fitted parameters. For this analysis, n is the number of channels of the detector and $m = 2$ since two parameters are fitted, T_h and E_h . $\tilde{\chi}^2$ then writes

$$\tilde{\chi}^2(T_h, E_h) = \frac{1}{n-2} \sum_{i=1}^n \frac{[S_i(T_h, E_h) - Q_i]^2}{\delta S_i(T_h, E_h)^2 + \delta Q_i^2} \quad (6.7)$$

where n is the number of channels of the detector, $\delta S_i(T_h, E_h)$ the uncertainty on the expected signal and δQ_i the uncertainty on the measured signal. The uncertainty on the expected signal is mostly due to the uncertainty on the absolute calibration of the detector $\delta \alpha_i$. In this case it writes $\delta S_i/S_i = \delta \alpha_i/\alpha_i$. The measured value of T_h and E_h are given by $\tilde{\chi}^2(T_h, E_h) = \tilde{\chi}_{min}^2$ and the 68% confidence uncertainty by $\tilde{\chi}^2(T_h, E_h) = \tilde{\chi}_{min}^2 + 2.3$, where $\tilde{\chi}_{min}^2$ is the minimum value of the $\tilde{\chi}^2$. The value of 2.3 for the determination of the uncertainty is due to the number of fitted parameters which, in this case, is two (for a single parameter fit, the uncertainty would be given by $\tilde{\chi}^2(T_h, E_h) = \tilde{\chi}_{min}^2 + 1$). Finally, considering an ideal normal distribution of measured signals, the expected value for $\tilde{\chi}_{min}^2$ is 1.

6.3 Hot electron measurement with HXRD

The generic method of analysis presented in the previous section can be applied to the HXRD measurements. This diagnostic has four channels with different high-pass filters of cut-off energies of 20, 40, 60 and 80 keV. Each channel uses a fast scintillator coupled to a fast

t_{spike}	Channel 1	Channel 2	Channel 3	Channel 4
2.4 ns	68.7 ± 1.4	185.4 ± 1.7	30.8 ± 0.8	20.4 ± 0.4
2.8 ns	71.6 ± 1.6	183.1 ± 1.8	30.2 ± 0.4	20.3 ± 0.4
3.2 ns	55.0 ± 1.3	145.7 ± 0.9	22.9 ± 0.6	15.3 ± 0.6

Table 6.1 HXRD charge measurements for each channel (in pC)

microchannel-plate and a photomultiplier tube, such that the measured quantity is a collected charge. The HXRD is actually time resolved. The collected charge is measured by integrating the output voltage (converted in current using a 50Ω resistance). The charges, measured on the HXRD channels for the 3 different spike launching times, are presented in Table 6.1.

For this study, the target response, I_{br} , has been calculated for given hot electron temperatures (assuming a 3D Maxwellian), instead of mono energetic energy groups as presented in the previous section. In this case, the expression of $S_i(T_h, E_h)$ used for this analysis is slightly different,

$$S_i(T_h, E_h) = \alpha_i \frac{E_h}{1.5T_h} \int F_i(\epsilon_v) I_{br}(T_h, \epsilon_v) d\epsilon_v. \quad (6.8)$$

The spectra $I_{br}(T_h, \epsilon_v)$ in this equation corresponds to the expression between bracket in 6.6. Generally, calculating the target response to mono energetic electron groups is more efficient. Taking in consideration an energy distribution in the simulations for I_{br} leads to longer computation time and therefore, it limits the number of simulations than can be reasonably done. For this analysis $I_{br}(T_h, \epsilon_v)$ have been calculated with the Monte Carlo code EGSnrc [103] for $T_h = 31, 50$ and 70 keV and then interpolated in order to have I_{br} over the range of interest for T_h (as presented in Figure 6.4). In this case, modeling the exact spherical shape of the shell is not essential. The simulations have been performed using a planar target with an areal density of twice the shell areal density ($112 \mu\text{m}$ of polystyrene at solid density). The angle of injection of the electrons do not change significantly the results of the simulation due to scattering that causes the electrons to lose their directionality in the target. For these simulations, the electrons have been injected normal to the target surface. The sum of the hard X-ray emission from the front and the back of the target represents the total emission from a spherical target.

The α_i values have been determined by cross-calibration of the different channels and an absolute calibration of the channel 2. The absolute calibration of the channel 2 have been realized recently using single-photon detection from radioactive sources and a charge sensitive amplifier [104]. In this experiment, the data from the channel 1 of the detector were discard due to the larger uncertainty of the absolute calibration of this channel compared to the others. This is primarily due to the fact that this channel is using a different scintillator

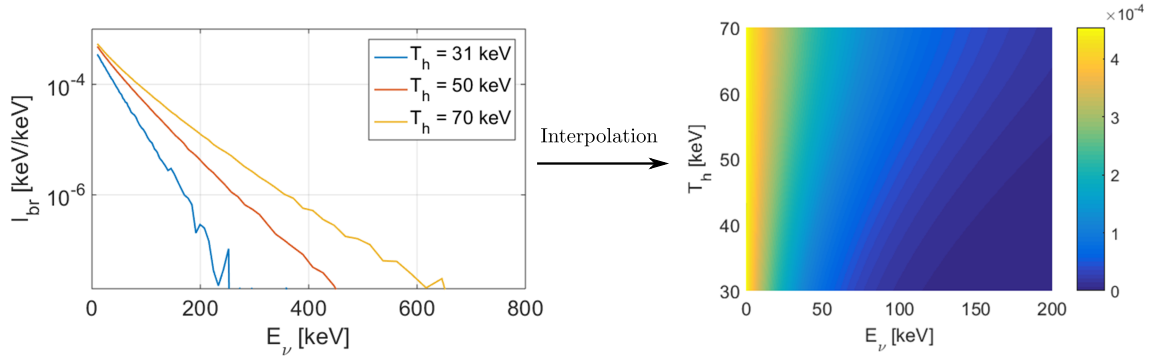


Fig. 6.4 Bremsstrahlung spectra from hot electrons with a 3D Maxwellian distribution of temperature T_h that are stopped in a plastic target (left) and interpolation of these spectra over the range of interest for T_h (right). The calculations were performed with the Monte Carlo code EGNrc [103].

material and photocathode, as well as being sensitive to lower photon energy (thermal plasma emission might affect this channel). The values of α_i are 1.32×10^{-11} pC/keV, 1.33×10^{-11} pC/keV and 1.81×10^{-11} pC/keV for the channel 2, 3 and 4, respectively. The Figure 6.5 presents the F_i spectra for the channel 2, 3 and 4. They have been determined from Monte Carlo simulations of particle transport using the code Geant4 [92]. The Geant4 simulations took in consideration the actual detector geometry, including the port cover, the lead collimator, the filter foils and the aluminum housing.

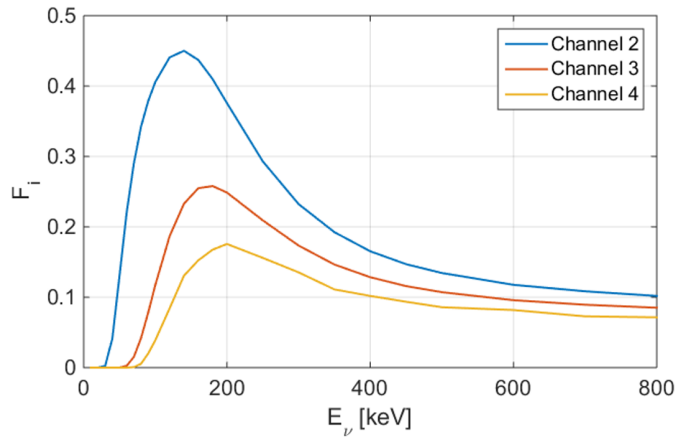


Fig. 6.5 Product of the filter transmission and the scintillator absorption probability for channel 2, 3 and 4 of the hard x-ray diagnostic. The calculations were performed using the Monte Carlo code Geant4 [92].

Once α_i , F_i and I_{br} have been determined, S_i and $\tilde{\chi}^2$ can be calculated. The uncertainty δS_i is mostly due to the error on the absolute calibration of the channel 2, which is known

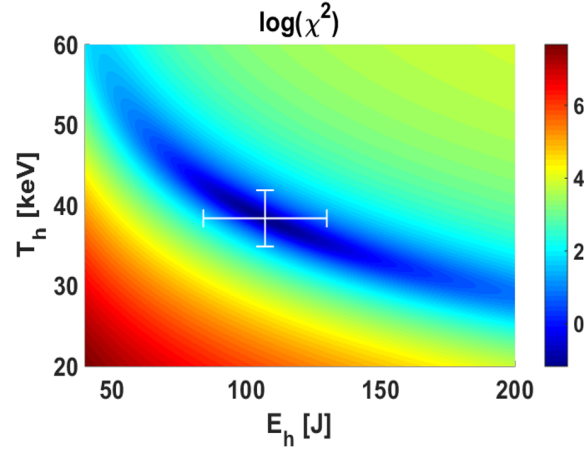


Fig. 6.6 χ^2 analysis of the shot with $t_{spike} = 2.4$ ns in the (T_h, E_h) plane. χ^2 is in logarithmic scale. The white error bar correspond to the 68% confidence uncertainty presented in Figure 6.7.

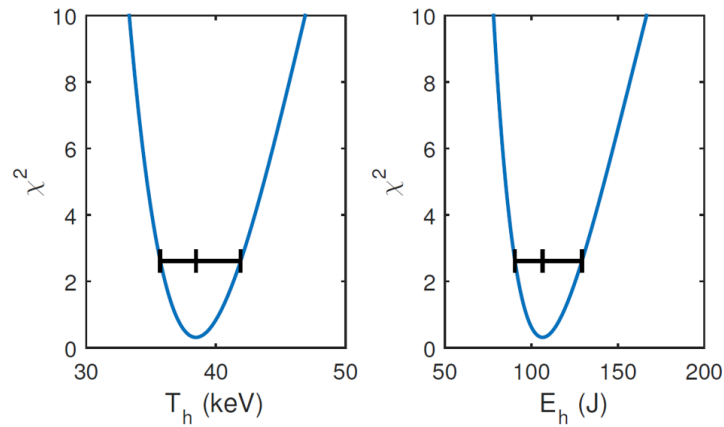


Fig. 6.7 χ^2 profiles as function of T_h for $E_h = 107$ J (left) and as function of E_h for $T_h = 38.4$ keV (right) for the shot with $t_{spike} = 2.4$ ns. The condition $\tilde{\chi}^2 = \tilde{\chi}_{min}^2 + 2.3$ determines the error bar.

with a relative error of 20% [104]. Therefore, $\delta S_i = 0.2 S_i$. For the experiment, the number of channels is 3, so that the number of degrees of freedom is 1 which leads to $\tilde{\chi}^2 = \chi^2$. The Figure 6.6 presents the χ^2 analysis of the shot with the spike launching time of 2.4 ns. It shows a clear minimum for $T_h = 38.4$ keV and $E_h = 107$ J. The uncertainty on T_h can be evaluated by considering the profile $\tilde{\chi}^2(T_h, E_h = 107 \text{ J})$ (Figure 6.7, left). The error bar displayed in this figure corresponds to the 68% confidence interval defined by the condition $\tilde{\chi}^2 = \tilde{\chi}_{min}^2 + 2.3$. Similarly, the profile $\tilde{\chi}^2(T_h = 34.8 \text{ keV}, E_h)$ provides the uncertainty of E_h (Figure 6.7, right). In Figure 6.7, $\tilde{\chi}^2$ shows a minimum that is significantly smaller than the expected value of 1. This might be due to an overestimation of the uncertainty δS_i and therefore of $\delta \alpha_i$. However, only a $\tilde{\chi}_{min}^2$ significantly larger than 1 would lead to discard the results of this analysis.

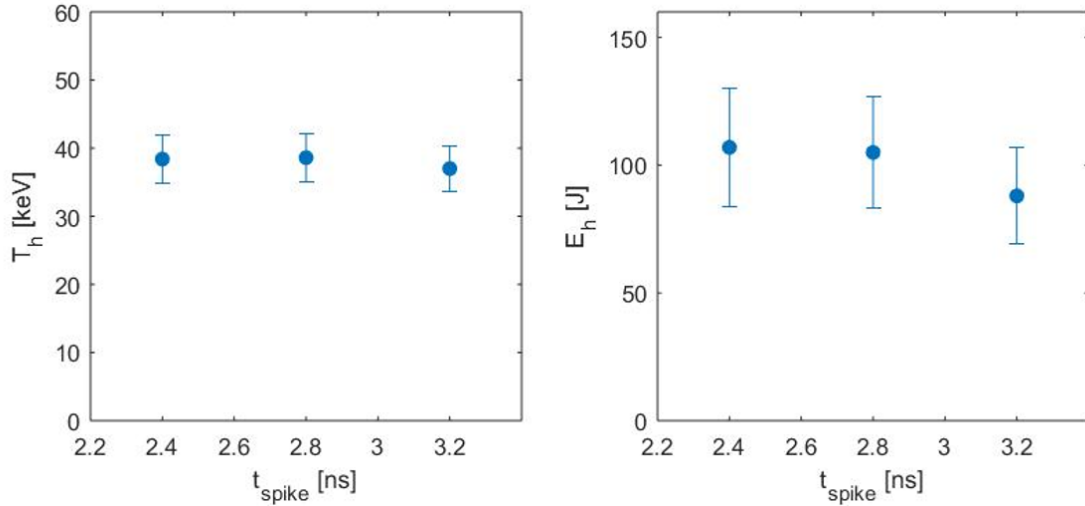


Fig. 6.8 Measured hot electron temperature and total energy as function of the spike launching time.

Figure 6.8 presents the measured hot electron temperature and total energy for the different spike launching times. A temperature of ~ 38 keV and a total of energy of ~ 100 J are found, relatively independently from spike launching time. The moderate temperature found for the hot electrons seems to indicate that they are mostly due to Stimulated Raman Scattering. Between 1.5% and 2% of the spike laser energy is converted into hot electrons.

6.4 LILAC simulations

The measured hot electron temperature and total energy have been used as source terms in 1D radiation hydrodynamic simulations using the code LILAC [30]. The simulations

took in account the measured target parameters and laser pulse shapes. They were performed using multigroup radiation diffusion model, standard SESAME equation of state tables and a constant flux limiter of 6% for the thermal electron transport. Crossbeam energy transfer was included. The hot electrons were generated at the quarter critical density, during the spike pulse only, with a single temperature Maxwellian distribution and with a 90° full-divergence angle in the forward direction (which is relevant for stimulated Raman scattering [48]). The power of the hot electron source was taken to match the measured total energy. The hot electrons were transported in straight line into the target.

The main experimental observable to be reproduced with the simulations is the average areal density $\langle \rho r \rangle$ probed by the secondary protons [105]. Close to the stagnation of the imploded shell, the D-D fusion reactions in the central hot spot region produce secondary D- ^3He fusion reactions. These fusion reactions produce energetic protons which propagate through the dense cold shell where they lose energy. The measurement of the down-shifted kinetic energy spectrum of these protons gives information on the shell's areal density. Using the proton wedge-range-filter diagnostic [105], an accurate reconstruction of the proton spectrum is possible, from which the areal density is inferred. This inferred areal density is averaged over the proton production rate, which is strongly correlated to the neutron production rate $n_{rate}(t)$. Therefore, the probed $\langle \rho r \rangle$ can be expressed as

$$\langle \rho r \rangle = \frac{1}{n_y} \int n_{rate}(t) \times \rho r(t) dt, \quad (6.9)$$

where $n_y = \int n_{rate}(t) dt$ is the neutron yield.

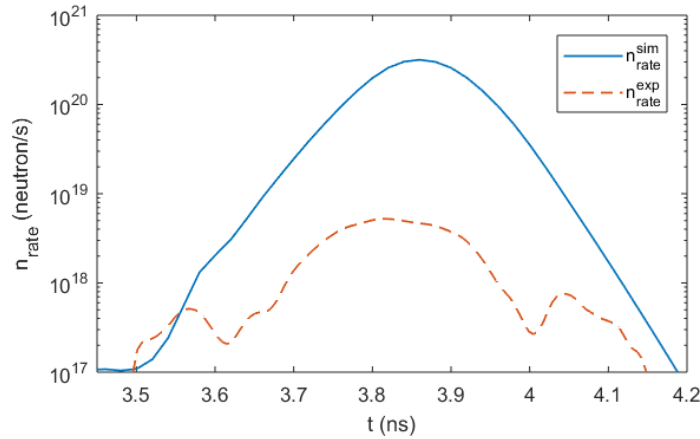


Fig. 6.9 Experimental (dashed red) and simulated (solid blue) neutron rate for the shot with $t_{spike} = 2.4$ ns.

In the experiment, the neutron rate $n_{rate}^{exp}(t)$ have also been measured using the neutron temporal diagnostic [106] and the neutron time-of-flight diagnostic [81]. As presented in Figure 6.9, the experimental neutron rate is several order of magnitude lower compared to the simulation and it is also shorter in duration. In order to be more relevant, the experimental neutron rate n_{rate}^{exp} is used to evaluate $\langle \rho r \rangle$ from the experiment,

$$\langle \rho r \rangle^{sim} = \frac{1}{n_y^{exp}} \int n_{rate}^{exp}(t) \times \rho r_{sim}(t) dt, \quad (6.10)$$

where $n_y^{exp} = \int n_{rate}^{exp}(t) dt$ is the experimental neutron yield. The absolute timing for n_{rate}^{exp} is known only with a ± 100 ps error for these shots due to the relatively low neutron yield and a poor neutron statistics in the neutron temporal diagnostic data. To compare the simulation results with the experiment, the timing of n_{rate}^{exp} has to be adjusted with respect to the timing of the simulated neutron rate n_{rate}^{sim} by adding a delay Δt . In this case, the simulated average areal density writes

$$\langle \rho r \rangle^{sim}(\Delta t) = \frac{1}{n_y^{exp}} \int n_{rate}^{exp}(t) \times \rho r_{sim}(t + \Delta t) dt. \quad (6.11)$$

The delay Δt can be considered constant from shot to shot since it is mostly dependent on the experimental set-up. Therefore, it can be determined though a χ^2 analysis between the simulated $\langle \rho r \rangle^{sim}(\Delta t)$ and experimental $\langle \rho r \rangle^{exp}$ average areal densities

$$\tilde{\chi}^2(\Delta t) = \frac{1}{l} \sum_{i=1}^n \frac{[\langle \rho r \rangle_i^{sim}(\Delta t) - \langle \rho r \rangle_i^{exp}]^2}{\delta \langle \rho r \rangle_i^{exp}}, \quad (6.12)$$

where i denotes the different shots of the experiment and l is the number of degrees of freedom. In this case $l = 5 - 1 = 4$ since five shots have been realized in the experiment and one parameter is fitted. $\delta \langle \rho r \rangle_i^{exp}$ is the uncertainty on the experimental measurement of the areal density. The Figure 6.10 presents the curve $\tilde{\chi}^2(\Delta t)$. It shows a clear minimum of 0.25 for a delay of $\Delta t = -48$ ps. The fact that the minimum of the curve is smaller than 1 indicates that the assumption that Δt was constant from shot to shot is reasonable, while there might be an overestimation of the experimental uncertainty. For this 1D χ^2 analysis, the 68% confidence uncertainty is given by the condition $\chi^2(\Delta t) = \chi_{min}^2 + 1$, which then results in $\Delta t = -48 \pm 8$ ps. The corresponding simulated average areal density $\langle \rho r \rangle^{exp}$ are presented in Figure 6.11, along with the experimental measurements. The experimental areal densities are well reproduced by the simulations, for all spike launching times and for the shot without spike pulse.

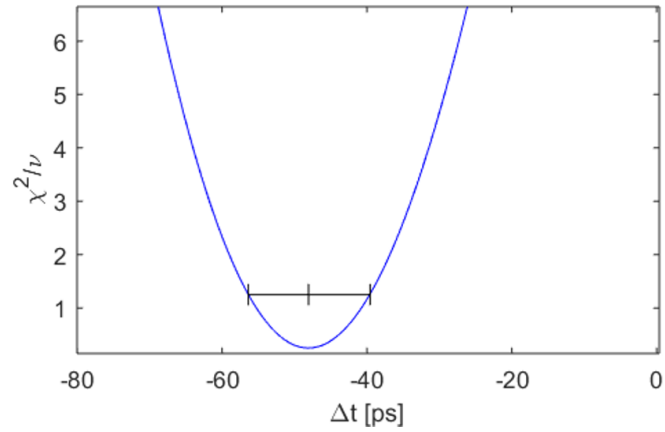


Fig. 6.10 χ^2 analysis of the different shots of the experiment for the determination of the delay Δt . The error bar corresponds to the 68% confidence uncertainty given by the condition $\chi^2(\Delta t) = \chi_{min}^2 + 1$.

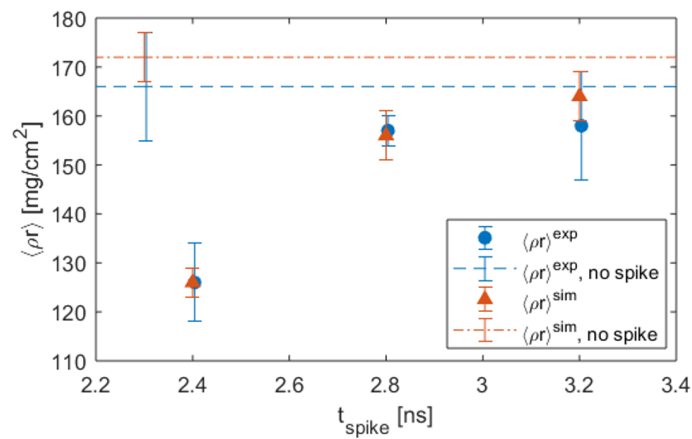


Fig. 6.11 Experimental (blue) and simulated (red) proton-probed average areal density for the different spike launching times. The dashed lines corresponds to the reference shot without spike pulse.

6.5 Effect of the hot electron preheat on the performance of implosions

In Figure 6.11, a deterioration of the areal density is observed at early spike launching time. Also, all shots with spike showed an areal density lower than the reference shot, without spike pulse. This deterioration cannot be directly attributed to the hot electron preheat alone. The hydrodynamic of the implosion is different depending on the spike launching time and it might results in variation of the implosion performance. In order to put in evidence the effects of hot electrons on the implosion performance, a second set of simulations which did not included them have been realized. In these simulations, the parameters were identical to the previous set of simulations, except for the power of the hot electron source that has been set to zero. The proton-probed areal density corresponds roughly to the areal density at the bang time, the maximum of the neutron production rate. At this time, the areal is still increasing, such that its maximum is at later time. In order to evaluate the performance of implosion, the maximum areal density is a more relevant parameter than the areal density at bang time.

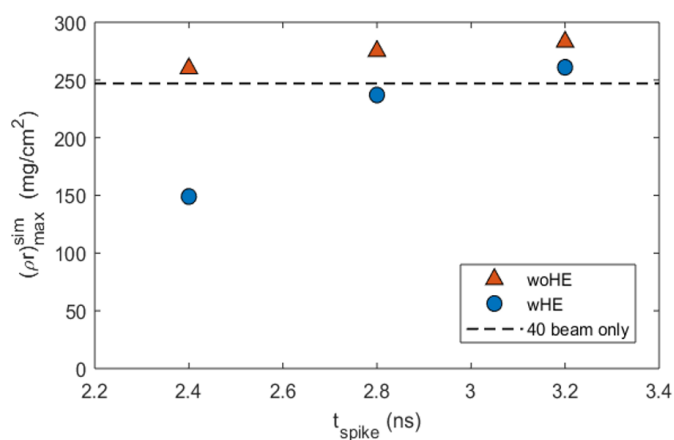


Fig. 6.12 Simulated maximum areal density from LILAC simulation as a function of the spike launching time. The triangle represents the values from simulations without hot electron and the circles are from simulations including them. The dashed line corresponds to the simulation without spike pulse.

Figure 6.12 presents the maximum areal density $(\rho r)_{\text{max}}$ achieved in the simulation with and without hot electrons. As expected, the maximum areal densities for the simulations with the hot electron are significantly higher than the proton-probed ones (in Figure 6.11). For the simulations without hot electrons, the spike launching time has a very small effect on $(\rho r)_{\text{max}}$. Including hot electrons in the simulations leads to a reduction of $(\rho r)_{\text{max}}$. This reduction is

larger when the spike was launched earlier. For $t_{spike} = 2.4$ ns the reduction is 43% while for $t_{spike} = 3.2$ ns it is only 8%. This shows that the degradation of areal density observed for early spike launching time can be attributed the effect of hot electrons. This effect can be understood by evaluating the average penetration depth of the hot electrons in the shell. In the context of dense plasma heating, the average penetration depth of a Maxwellian distribution of hot electrons of temperature T_h is similar to the range of a mono-energetic beam with energy $\varepsilon_0 \simeq T_h/0.516$ [107]. For a temperature of 38 keV, this corresponds to an energy of ~ 75 keV and a range of ~ 8 mg/cm² in polyethylene [108]. This range is represented in Figure 6.13 (dashed line) along with the areal density of the shell at the time of the spike launch, for the different spike launching times. For $t_{spike} = 2.4$ ns, the shell areal density is smaller than the range of the hot electrons, resulting in a preheating of the entire target. This preheat increases the shell adiabat, which limits its compression. On the other hand, for $t_{spike} = 3.2$ ns, the areal density is more than twice the average range of the hot electrons and only the outer part of the shell is preheated. The inner part stays at a low adiabat, which is essential in order to reach a high compression.

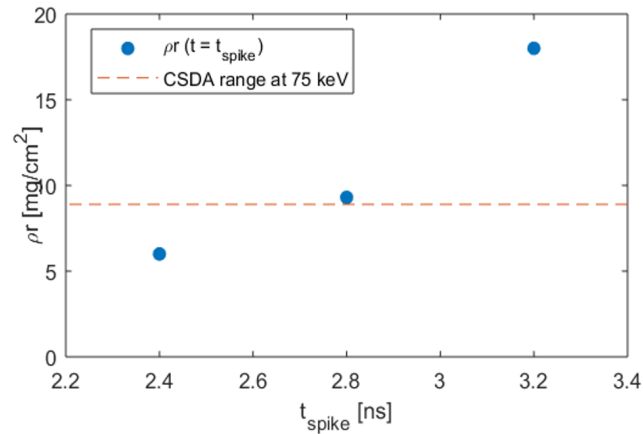


Fig. 6.13 Shell areal density at the time of the spike launching time for the different spike launching times. The dashed line corresponds to the range of hot electrons with a Maxwellian distribution of temperature 38 keV (or a mono energetic distribution of energy 75 keV).

The difference in target preheat also impact the neutron yield. Figure 6.14 presents the predicted neutron yield n_y^{sim} divided by the total laser energy as function of the spike launching time, for the simulation with (circle) and without (triangle) hot electrons. This normalization is motivate by the main objective of the shock ignition scheme, which is the redistribution of laser energy into a compression pulse and a spike pulse, in order to improve the performance of implosions. Therefore, it is more relevant to compare energy equivalent implosions, or at default, to normalized the neutron yield by the total incident laser energy.

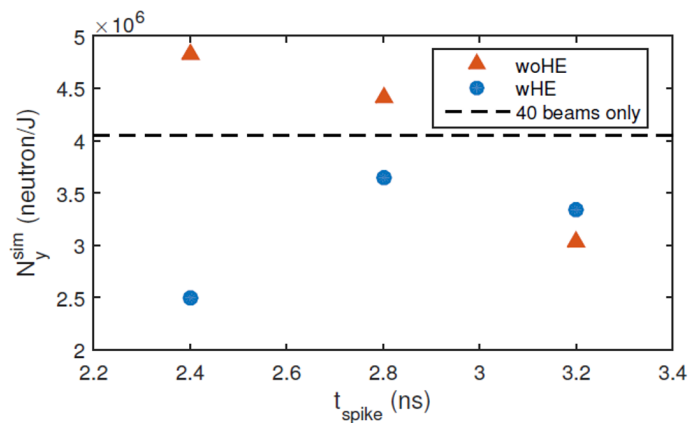


Fig. 6.14 Simulated neutron yield from LILAC simulations as a function of the spike launching time, with and without hot electrons. The neutron yield was normalized to the total laser energy. The dashed line corresponds to the reference case, without spike.

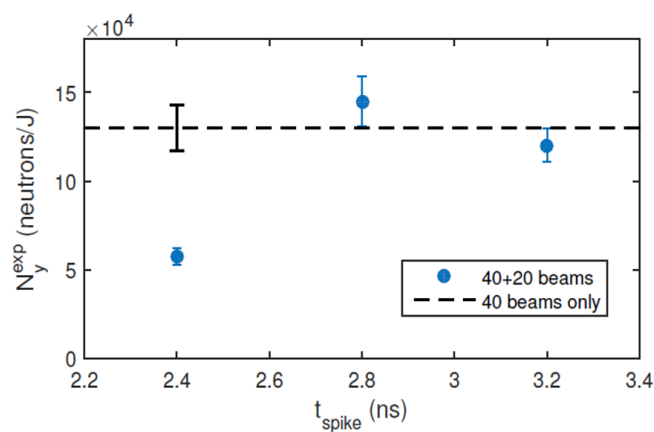


Fig. 6.15 Experimental neutron yield as a function of the spike launching time. The neutron yield was normalized to the total laser energy. The dashed line corresponds to the reference case, without spike.

In the experiment, the total laser energy for the shots with spike was ~ 21 kJ while the shot without spike it was only ~ 15 kJ. The simulations without hot electrons show that n_y^{sim} decreases for a later spike launching time because of shock mistiming. This seems to indicate that an earlier spike is preferable. However, taking in account the hot electrons in the simulations leads to a large decrease of the neutron yield for the earliest spike launching time (2.4 ns). For $t_{spike} = 2.8$ ns and 3.2 ns, the neutron yield is almost the same as in the simulations without hot electrons. This results from a counter balancing effect between the shock mistiming and an enhanced hot-electron energy deposition in the outer part of the shell.

The experimental neutron yield is presented in Figure 6.15. It shows a similar behavior as the neutron yield from the simulations that included the hot electrons. Compared to the reference shot without spike, a degradation of the yield is observed for $t_{spike} = 2.4$ ns. For the later spike launching time (2.8 and 3.2 ns), it is very close to the yield with the 40 beams only. The large difference in neutron yield between the experimental data and LILAC simulations can be attributed to effects from the non-uniformity of laser irradiation. This non-uniformity leads to instability growth at the inner shell surface (and therefore to fuel mixing [109]) and low-mode deformation of the hot spot [110]. Both of these 2D effects limit the neutron yield and are not accounted for in the 1D simulations. Compared to standard 60 beams implosion on Omega, the 40+20 configuration has a significantly lower homogeneity of irradiation [101], which might enhance these limiting effects. Yet, these detrimental effects are mostly independent from the spike launching time since the shell has acquired most of its kinetic energy during the compression pulse. In this case, the hot electron energy deposition in the shell is the main mechanism that can vary the neutron yield with the spike launching time.

6.6 Conclusion

In this chapter, an experiment relevant to shock ignition has been presented. This experiment consists in the implosion of CH shell using the 40+20 configuration of Omega Laser. The 40-beams were used for the compression of the target, while the 20-beams were used to generate an intense laser spike at the end of the compression phase. The hot electron source parameters (temperature and total energy) and the performance of implosion (proton-probed average areal density and neutron yield) have been measured.

The measurement of the hot electron temperature and total energy have been realized using HXRD. This diagnostics is based on high-energy differential-filtering photon spectroscopy of the Bremsstrahlung radiation emitted by the hot electrons as they are slowed down

in the shell. A generic method of analysis for the measurement of hot electron temperature and total energy using this kind of diagnostic have been proposed. This method have been applied to the HXRD data, resulting in a measured temperature of ~ 38 keV and total energy of ~ 100 J, relatively independently to the spike launching time.

These measurements of the hot electron source parameters, along with the measurements of the target parameters and laser pulse shapes, have been used in order to realized 1D LILAC simulations of the implosions. Two set of simulations have been realized, with or without hot electrons. The simulations with hot electrons reproduced well the measured proton-probed average areal density. A deterioration of the areal density have been observed for early spike launching time and the comparison between the simulations with and without hot electron allowed to attribute this degradation to hot electron preheat. This preheat is strongly reduced for the later spike launching times, leading to higher areal areal densities. Despite a large difference in absolute values, the variation of neutron yield in simulations and experiment showed the same trend of degradation for early spike launching time and a recovery for later times.

Chapter 7

Conclusions

The objective of this thesis is to give a description of the effects of hot electrons on the hydrodynamic of shocks and implosions in the context of the shock ignition scheme. To do so, results from experiments realized in conditions relevant to shock ignition are compared to simulations that included, or not, a description of the hot electrons.

Before considering the effects of the hot electrons on the hydrodynamic of shocks and implosions, a good understanding of the mechanisms that produce them is necessary. This has been realized in chapter 2, where the anomalous absorption mechanisms of light have been presented. This study focused on the mechanisms that might produce hot electrons at intensities and plasma conditions relevant to shock ignition. These are the resonant absorption, the Stimulated Raman Scattering (SRS) and the Two-Plasmon Decay (TPD). These three mechanisms result in different populations of hot electrons in terms of energy and angular emission. Due to the complexity of the collective effects in realistic plasma, results of simulations and experiments are used in order to characterize these populations. Resonant absorption produces hot electrons that have a temperature close to the temperature of the plasma corona (~ 8 keV) so that they deposit their energy mostly in the plasma corona or the conduction zone. SRS produces hot electrons with temperature of ~ 40 keV and with a conversion energy efficiency of $\sim 10\%$. These hot electrons are mostly produced in the direction of the laser beam, meaning a small initial divergence. TPD produces hot electrons with a higher temperature of ~ 90 keV and a lower conversion efficiency of $\sim 2.5\%$. The divergence of TPD hot electrons is also significantly larger than the SRS ones, typically in a 45° cone. Both of these populations of hot electrons can propagate up to the cold part of the target, ahead of the shock front, and therefore heat it. Due to the higher temperature of the TPD hot electrons, they can go deeper in the target, yet since their conversion efficiency is lower and beam divergence larger, their heating might be negligible in comparison to the SRS hot electrons.

A good understanding of the hydrodynamic of the shocks and implosions in the context of shock ignition is also necessary before considering the effects the hot electrons have on them. In chapter 3, the hydrodynamic of shock wave is presented. For this purpose, a semi-analytical tool for the calculation of the shock polar curves (Hugoniot curves) has been developed. This tool also allows to calculate the characteristics of the waves emerging from the interaction of a shock with another shock (shock collision or shock coalescence), a rarefaction wave or a contact discontinuity. It has been used in order to characterize the set of all possible shock collisions, shock at contact discontinuities and shock coalescences in the case of an ideal gas. In chapter 4, the hydrodynamic of shocks in shock ignition implosion is presented. The tool developed in chapter 3 has been coupled to a code of propagation of discontinuities, in planar geometry, developed for this purpose, in order to give a semi-analytical code of discontinuities propagation. This code reproduces accurately the results from planar 1D simulations of shock ignition like implosions (realized with LILAC by Nora *et al.* [70]). The results from this semi-analytical code allowed to put in evidence the dynamic of the ignition shock, especially its amplification in the gas during the deceleration phase. It also showed how the coalescence of the diverging shocks in the shell leads to rarefaction waves that limit the pressure that can be achieved in the gas. Finally, this code has been used to propose a shock ignition technique more robust than the one presented in the article of Nora *et al.*, which relies on the symmetric collision of the ignition shock in the shell with the first diverging shock.

In the chapter 4, the results from a shock ignition experiment that have been realized on OMEGA are also presented. In this experiment, the intensity during the spike was moderate ($1.1 \times 10^{15} \text{ W/cm}^2$) allowing to neglect hot electrons in first approximation. This experiment has been interpreted using 1D LILAC simulations that did not include hot electrons. The simulations reproduced the main observables of the experiment, which were the trajectories of the ablation front and the inner shell surface during the deceleration phase. In the experiment, the scanned parameter was the spike launching time. Simulations show that for early spike launching time (1.0 and 1.2 ns) the ignition shock breaks out in the gas too early, before the beginning of the deceleration phase. For the 1.4 ns spike launching time, the ignition shock collides with the diverging shock in the shell, which is ideal for shock ignition. Yet, the neutron yield, which is usually used to characterize the performance of implosions, was lower for this later spike launching time, both in the experiment and in the simulation. However, the simulations show that the peak of instantaneous neutron production is significantly higher for the 1.4 ns launching time. This higher production peak is due to conditions in the gas at stagnation that are closer to ignition than for the other launching times. The lower total neutron yield is due to a shorter confinement time. This put

in evidence the fact that the observable usually used in order to characterize the performance of implosions in the classical scheme cannot be directly used for shock ignition implosions.

In order to study the effects of hot electrons on the hydrodynamic of shocks and implosions, it is necessary to implement in radiation hydrodynamic codes packages that allow to described the hot electron production and transport. This is the case for the CHIC code in which a model for the description of the laser propagation has been recently implemented. This model allows to calculate the local intensity in the plasma and therefore, the hot electron source parameters (temperature and conversion efficiency). The hot electron propagation and energy deposition are then determined in the angular scattering approximation. This model of laser and hot electron propagation in CHIC has been validated though comparison with simulations and few experiments. Furthermore comparison of CHIC simulations with experiments relevant to shock ignition are necessary in order to confirm the validity of this model. Especially, in the angular scattering approximation, the width of the hot electron beams increases as they propagate though the target, even though the sources are originally collimated. It is not determined yet if this increase in width is sufficient to reproduce the divergence of the SRS hot electrons. Considering an initial divergence of the sources as it is the case for the TPD hot electron might be necessary.

In the chapter 5, CHIC is used for the interpretation and design of experiments in planar geometry. First is presented an experiment that have been realized at Prague Asterix Laser Facility. In this experiment, plastic targets of different thicknesses (ranging from 10 to 180 μm) have been irradiated with a short duration (300 ps), long wavelength (1.3 μm) pulse. The peak intensity in this experiment was $\sim 10^{16}$ W/cm^2 . On the rear surface of the plastic layer, a 5 μm titanium layer was set and the main observable for this experiment was the time resolved emissivity of the rear side of the target (Streak Optical Pyrometry, SOP). CHIC simulations including SRS and TPD hot electrons have reproduced the delay observed on the SOP images between the peak of emission due to the heating by the hot electrons and the rising of the signal due to the shock breakout. These simulations used reduced conversion efficiencies for the hot electron sources (compared to the scaling laws presented in chapter 2) and an initial divergence for the SRS hot electron sources of $\pm 20^\circ$. These results indicate that the scaling law presented in chapter 2 are not valid for these laser parameters (especially concerning the long wavelength of 1.3 μm) and that an initial divergence in the hot electron sources has to be included in the simulations in order to reproduce the divergence of the SRS hot electrons. Then, CHIC simulations have been realized for the design of an experiment on OmegaEP. The goal of this experiment was to realize the side-radiography of a shock wave perturbed by hot electrons. The laser pulse has been design to reproduce the intensity of an ignition spike ($\sim 5 \times 10^{15}$ W/cm^2) but the energy available in this facility was not high

enough to realized plasma conditions relevant to shock ignition. This experiment has been performed recently and a preliminary analysis of the 2D radiographies is proposed. A good agreement between simulation and experiment has been found in the measurement of the shock front trajectory for a simulation with a divergence of $\pm 20^\circ$ for the SRS sources and a reduce incident energy to 70% of the nominal one. The reduction of the incident energy might be due to Stimulated Brillouin Scattering that is not taken in account in the simulations. In order to compare the 2D radiographies to the simulations, a post processor for the realization of synthetic radiographies has been developed. The results from this comparison confirm the results observed with the measurement of the shock front trajectory. Finally, CHIC simulations have been realized for the design of an experiment on the Laser MegaJoule. The goal of this experiment is similar to the one on OmegaEP, the side-radiography of a shock perturbed by hot electrons. The energy available on LMJ allows the pulse to have a foot part in order to produce an extended plasma corona relevant to shock ignition, as well as a spike with an intensity of $\sim 10^{16}$ W/cm². This experiment will be realized in 2019.

The comparison between simulations with and without hot electrons allows to see their effects on the shock hydrodynamic. For the three experiments presented in chapter 5, these effects are similar (while not having the same magnitude). The heating of the target by the hot electrons results in an increase of the pressure both upstream and downstream of the shock front. Therefore, even if the shock has a higher pressure, its strength (the ratio of the downstream pressure to the upstream one) is lower when taking in account the hot electrons. Similarly, the shock velocity increases, even though its Mach number decreases due to the higher sound velocity ahead of the shock front. The density jump at the shock front is also smaller when taking in account the hot electrons since the preheated target is less compressible. This last point is visible on the experimental and synthetic radiographies of the OmegaEP experiment. Another effect of the heating by the hot electrons is that the pressure in the shocked target is higher than the ablation pressure so that the ablation front expands toward the laser. This creates a rarefaction wave that propagates in the shocked target, up to the shock front. In this case, the material behind the shock can be very inhomogeneous, even if it has been irradiated at a constant intensity.

Finally, in chapter 6 is presented a shock ignition experiment realized on Omega in spherical geometry. This experiment used the 40+20 beams configuration where 40 beams were used to compressed the target at low intensity and 20 beams were then used to simulate a shock ignition spike. This experiment have been interpreted with the 1D radiation hydrodynamic code LILAC. While this code has a package that allows to describe the propagation and energy deposition of the hot electrons, it does not allow to calculate the local intensity. Therefore the hot electron source parameters cannot be determined self-consistently in the

simulations. In this case, these parameters have to be determined through measurement of the hot electron population. In this experiment, this measurement have been realized using the Hard X-Ray Detector (HXRD). A method based on χ^2 analysis have been developed in order to realize the measurement of the hot electron temperature and total energy from this diagnostic. This method have also been extended for the analysis of data from other high-energy differential-filtering photon spectrometer (such as Bremsstrahlung canons). In this experiment, a hot electron temperature of ~ 38 keV and conversion efficiency of $\sim 1.5\%$ have been measured. Simulations taking in account these hot electrons reproduced the measured areal densities. Comparison between simulations with and without hot electrons have shown that the degradation of the areal density observed at early spike launching time is due to the preheating of the inner surface of the shell by the hot electrons. For the latest spike launching time, the areal density of the simulation with and without hot electron are very close. This shows that, with well timed spike, the preheating of the hot electrons can be controlled so that they are not detrimental to the implosion.

The work realized in this thesis have shown the capability, in radiation hydrodynamic codes, to describe the production and energy deposition of hot electrons. It also has shown that these hot electrons have a significant effects on the shocks and implosions hydrodynamic. The perspectives to this work are numerous and they can be organized in three main objectives.

- First, there is a need for further improvements of the description of the hot electrons in the hydrodynamic codes. One of the main uncertainty of the work presented in the thesis concerns the parameters of the hot electron sources. To improve the accuracy and range of validity of the scaling laws that are used in order to calculate them, simulations and dedicated experiments should be realized. The realization of extensive Particle In Cell (PIC) simulations, with realistic hydrodynamic profiles (from hydrodynamic simulations for example) could allow to determine the SRS and TPD temperatures, conversion efficiencies and divergences over a large range of intensities and density gradients. In parallel, experiments aiming to the measurement of these hot electrons could be realized on intermediate laser facility (OmegaEP, PALS, Gekko, LULI . . .) in order to validate the results from PIC simulations.
- Then, the description of the propagation and energy deposition of the hot electrons could be improved, or further validated. Indeed, in CHIC the propagation of the hot electrons uses an angular and energy multi-groups description. A better accuracy could be achieved by coupling the hydrodynamic code with a Monte-Carlo description for the hot electron propagation. Yet a trade off would have to be found between accuracy and numerical efficiency of the simulations. In order to validate such new model, or to

further validate the current one, the comparison of simulation results with experiments will have to be done. The OmegaEP and LMJ experiments presented in this work are examples of such experiments. The side radiography of shock waves seems to be a promising diagnostic in order to characterize the effects of hot electrons on hydrodynamic. Yet, more experiment are necessary in order to improve this diagnostic (backlighter material, laser power on the backlighter, target dimension along the radiography axis ...).

- Finally, new designs of shock ignition implosions taking in account the hot electrons could be realized. The initial designs for shock ignition used targets that were close to the one used in the classical scheme for inertial confinement fusion. In these design, the effect of hot electron have been either neglected or considered as a small perturbation. Recently, it has been shown that taking in account realistic fluxes of hot electrons prevent such design to reach ignition [90]. The current state of radiation hydrodynamic codes should allow to design shock ignition implosions that take in account these realistic fluxes of hot electrons. These designs would probably use targets with thicker shells or layers of denser materiel in order to improve the shell stopping power. In such case, a larger fraction of the hot electrons would be stopped in the outer part of the shell, thus preventing preheat of the gas and increasing the ignition shock pressure.

References

- [1] E.E. Bloom, R.W. Conn, J.W. Davis, R.E. Gold, R. Little, K.R. Schultz, D.L. Smith, and F.W. Wiffen. Low activation materials for fusion applications. *Journal of Nuclear Materials*, 122(1):17 – 26, 1984.
- [2] S. Atzeni and J. Meyer-Ter-Vehn. *The Physics of Inertial Fusion: Beam Plasma Interaction, Hydrodynamics, Hot Dense Matter*. Oxford University Press, 2004.
- [3] J D Lawson. Some criteria for a power producing thermonuclear reactor. *Proceedings of the Physical Society. Section B*, 70(1):6–10, jan 1957.
- [4] Hiroki Hondo. Life cycle ghg emission analysis of power generation systems: Japanese case. *Energy*, 30(11):2042 – 2056, 2005. International Symposium on CO2 Fixation and Efficient Utilization of Energy (CandE 2002) and the International World Energy System Conference (WESC-2002).
- [5] GL Kulcinski, WJ Hogan, RW Moir, K Mima, and VV Kharitonov. *Energy from inertial fusion*. International Atomic Energy Agency, Vienna, 1995.
- [6] V.A. Shcherbakov. Ignition of a laser-fusion target by a focusing shock wave. *Soviet Journal of Plasma Physics*, 9(2):240–241, 1983.
- [7] R. Betti, C. D. Zhou, K. S. Anderson, L. J. Perkins, W. Theobald, and A. A. Solodov. Shock ignition of thermonuclear fuel with high areal density. *Phys. Rev. Lett.*, 98:155001, Apr 2007.
- [8] Mark C. Herrmann, Max Tabak, and John D. Lindl. Ignition scaling laws and their application to capsule design. *Physics of Plasmas*, 8(5):2296–2304, 2001.
- [9] Lawrence Livermore National Laboratory. Nif user guide, 2016.
- [10] T.R Boehly, D.L Brown, R.S Craxton, R.L Keck, J.P Knauer, J.H Kelly, T.J Kessler, S.A Kumpan, S.J Loucks, S.A Letzring, F.J Marshall, R.L McCrory, S.F.B Morse, W Seka, J.M Soures, and C.P Verdon. Initial performance results of the omega laser system. *Optics Communications*, 133(1):495 – 506, 1997.
- [11] W. Theobald, R. Betti, C. Stoeckl, K. S. Anderson, J. A. Delettrez, V. Yu. Glebov, V. N. Goncharov, F. J. Marshall, D. N. Maywar, R. L. McCrory, D. D. Meyerhofer, P. B. Radha, T. C. Sangster, W. Seka, D. Shvarts, V. A. Smalyuk, A. A. Solodov, B. Yaakobi, C. D. Zhou, J. A. Frenje, C. K. Li, F. H. Séguin, R. D. Petrasso, and L. J. Perkins. Initial experiments on the shock-ignition inertial confinement fusion concept. *Physics of Plasmas*, 15(5):056306, 2008.

- [12] X Ribeyre, G Schurtz, M Lafon, S Galera, and S Weber. Shock ignition: an alternative scheme for hiper. *Plasma Physics and Controlled Fusion*, 51(1):015013, 2009.
- [13] S. Atzeni, A. Schiavi, J. J. Honrubia, X. Ribeyre, G. Schurtz, Ph. Nicolai, M. Olazabal-Loumé, C. Bellei, R. G. Evans, and J. R. Davies. Fast ignitor target studies for the hiper project. *Physics of Plasmas*, 15(5):056311, 2008.
- [14] X Ribeyre, M Lafon, G Schurtz, M Olazabal-Loumé, J Breil, S Galera, and S Weber. Shock ignition: modelling and target design robustness. *Plasma Physics and Controlled Fusion*, 51(12):124030, 2009.
- [15] X. Ribeyre, V. T. Tikhonchuk, J. Breil, M. Lafon, and E. Le Bel. Analytic criteria for shock ignition of fusion reactions in a central hot spot. *Physics of Plasmas*, 18(10):102702, 2011.
- [16] K. G. Guderley. Starke kugelige und zylindrische verdichtungsstosse in der nahe des kugelmittelpunktes bzw. der zylinderachse. *Luftfahrtforschung*, 19:302, 1942.
- [17] M. Lafon, X. Ribeyre, and G. Schurtz. Gain curves and hydrodynamic modeling for shock ignition. *Physics of Plasmas*, 17(5):052704, 2010.
- [18] A. Vallet, X. Ribeyre, and V. Tikhonchuk. Finite mach number spherical shock wave, application to shock ignition. *Physics of Plasmas*, 20(8):082702, 2013.
- [19] A. Vallet. *Hydrodynamic modeling of the shock ignition scheme for inertial confinement fusion (in French)*. PhD thesis, Université de Bordeaux, 2014.
- [20] S Atzeni, A Schiavi, and A Marocchino. Studies on the robustness of shock-ignited laser fusion targets. *Plasma Physics and Controlled Fusion*, 53(3):035010, 2011.
- [21] M. Lafon, X. Ribeyre, and G. Schurtz. Optimal conditions for shock ignition of scaled cryogenic deuterium–tritium targets. *Physics of Plasmas*, 20(2):022708, 2013.
- [22] L. J. Perkins, R. Betti, K. N. LaFortune, and W. H. Williams. Shock ignition: A new approach to high gain inertial confinement fusion on the national ignition facility. *Phys. Rev. Lett.*, 103:045004, Jul 2009.
- [23] K. S. Anderson, R. Betti, P. W. McKenty, T. J. B. Collins, M. Hohenberger, W. Theobald, R. S. Craxton, J. A. Delettrez, M. Lafon, J. A. Marozas, R. Nora, S. Skupsky, and A. Shvydky. A polar-drive shock-ignition design for the national ignition facility. *Physics of Plasmas*, 20(5):056312, 2013.
- [24] S. Skupsky, J. A. Marozas, R. S. Craxton, R. Betti, T. J. B. Collins, J. A. Delettrez, V. N. Goncharov, P. W. McKenty, P. B. Radha, T. R. Boehly, J. P. Knauer, F. J. Marshall, D. R. Harding, J. D. Kilkenny, D. D. Meyerhofer, T. C. Sangster, and R. L. McCrory. Polar direct drive on the national ignition facility. *Physics of Plasmas*, 11(5):2763–2770, 2004.
- [25] W. Kruer. *The Physics of Laser Plasma Interactions*. Frontiers in Physics, 2003.
- [26] G H McCall. Laser-driven implosion experiments. *Plasma Physics*, 25(3):237, 1983.

- [27] D. W. Forslund, J. M. Kindel, and K. Lee. Theory of hot-electron spectra at high laser intensity. *Phys. Rev. Lett.*, 39:284–288, Aug 1977.
- [28] R Betti, W Theobald, C D Zhou, K S Anderson, P W McKenty, S Skupsky, D Shvarts, V N Goncharov, J A Delettrez, P B Radha, T C Sangster, C Stoeckl, and D D Meyerhofer. Shock ignition of thermonuclear fuel with high areal densities. *Journal of Physics: Conference Series*, 112(2):022024, 2008.
- [29] R. Nora, W. Theobald, R. Betti, F. J. Marshall, D. T. Michel, W. Seka, B. Yaakobi, M. Lafon, C. Stoeckl, J. Delettrez, A. A. Solodov, A. Casner, C. Reverdin, X. Ribeyre, A. Vallet, J. Peebles, F. N. Beg, and M. S. Wei. Gigabar spherical shock generation on the omega laser. *Phys. Rev. Lett.*, 114:045001, Jan 2015.
- [30] J. Delettrez, R. Epstein, M. C. Richardson, P. A. Jaanimagi, and B. L. Henke. Effect of laser illumination nonuniformity on the analysis of time-resolved x-ray measurements in uv spherical transport experiments. *Phys. Rev. A*, 36:3926–3934, Oct 1987.
- [31] G. Cristoforetti, A. Colaïtis, L. Antonelli, S. Atzeni, F. Baffigi, D. Batani, F. Barbato, G. Boutoux, R. Dudzak, P. Koester, E. Krousky, L. Labate, Ph. Nicolai, O. Renner, M. Skoric, V. Tikhonchuk, and L. A. Gizzi. Experimental observation of parametric instabilities at laser intensities relevant for shock ignition. *EPL (Europhysics Letters)*, 117(3):35001, 2017.
- [32] A. Colaïtis, G. Duchateau, X. Ribeyre, Y. Maheut, G. Boutoux, L. Antonelli, Ph. Nicolai, D. Batani, and V. Tikhonchuk. Coupled hydrodynamic model for laser-plasma interaction and hot electron generation. *Phys. Rev. E*, 92:041101, Oct 2015.
- [33] K. Jungwirth, A. Cejnarova, L. Juha, B. Kralikova, J. Krasa, E. Krousky, P. Krupickova, L. Laska, K. Masek, T. Mocek, M. Pfeifer, A. Präg, O. Renner, K. Rohlena, B. Rus, J. Skala, P. Straka, and J. Ullschmied. The prague asterix laser system. *Physics of Plasmas*, 8(5):2495–2501, 2001.
- [34] C. Garban-Labaune, E. Fabre, C. E. Max, R. Fabbro, F. Amiranoff, J. Virmont, M. Weinfeld, and A. Michard. Effect of laser wavelength and pulse duration on laser-light absorption and back reflection. *Phys. Rev. Lett.*, 48:1018–1021, Apr 1982.
- [35] V. E. Zakharov. Collapse of langmuir waves. *Sov. Phys. JETP*, 35(5), 1972.
- [36] N. G. Denisov. On a singularity of the field of an electromagnetic wave propagated in an inhomogeneous plasma. *Sov. Phys. JETP*, 4(544), 1957.
- [37] V. L. Ginzburg. *The Properties of Electromagnetic Waves in Plasma*. Physics. Pergamon, New York, 1964.
- [38] K. R. Manes, V. C. Rupert, J. M. Auerbach, P. Lee, and J. E. Swain. Polarization and angular dependence of 1.06- μm laser-light absorption by planar plasmas. *Phys. Rev. Lett.*, 39:281–284, Aug 1977.
- [39] Kent Estabrook and W. L. Kruer. Properties of resonantly heated electron distributions. *Phys. Rev. Lett.*, 40:42–45, Jan 1978.

- [40] D. C. Slater, Gar. E. Busch, G. Charatis, R. R. Johnson, F. J. Mayer, R. J. Schroeder, J. D. Simpson, D. Sullivan, J. A. Tarvin, and C. E. Thomas. Absorption and hot-electron production for 1.05 and 0.53 μm light on spherical targets. *Phys. Rev. Lett.*, 46:1199–1202, May 1981.
- [41] J. P. Freidberg, R. W. Mitchell, R. L. Morse, and L. I. Rudsinski. Resonant absorption of laser light by plasma targets. *Phys. Rev. Lett.*, 28:795–799, Mar 1972.
- [42] K. G. Estabrook, E. J. Valeo, and W. L. Kruer. Two-dimensional relativistic simulations of resonance absorption. *The Physics of Fluids*, 18(9):1151–1159, 1975.
- [43] D. W. Forslund, J. M. Kindel, Kenneth Lee, E. L. Lindman, and R. L. Morse. Theory and simulation of resonant absorption in a hot plasma. *Phys. Rev. A*, 11:679–683, Feb 1975.
- [44] Arnaud Colaitis. *Multiscale description of the laser-plasma interaction : application to the physics of shock ignition in inertial confinement fusion*. PhD thesis, 2015. Thèse de doctorat dirigée par Tikhonchuk, VladimirNicolai, Philippe et Duchateau, Guillaume Astrophysique, plasmas, nucléaire Bordeaux 2015.
- [45] F. W. Perkins and J. Flick. Parametric instabilities in inhomogeneous plasmas. *The Physics of Fluids*, 14(9):2012–2018, 1971.
- [46] J. C. Adam and A. Heron. Parametric instabilities in resonant absorption. *The Physics of Fluids*, 31(9):2602–2614, 1988.
- [47] J. F. Drake, P. K. Kaw, Y. C. Lee, G. Schmid, C. S. Liu, and Marshall N. Rosenbluth. Parametric instabilities of electromagnetic waves in plasmas. *The Physics of Fluids*, 17(4):778–785, 1974.
- [48] C. S. Liu, Marshall N. Rosenbluth, and Roscoe B. White. Raman and brillouin scattering of electromagnetic waves in inhomogeneous plasmas. *The Physics of Fluids*, 17(6):1211–1219, 1974.
- [49] K. Tanaka, B. Boswell, R. S. Craxton, L. M. Goldman, F. Guglielmi, W. Seka, R. W. Short, and J. M. Soures. Brillouin scattering, two-plasmon decay, and self-focusing in underdense ultraviolet laser-produced plasmas. *The Physics of Fluids*, 28(9):2910–2914, 1985.
- [50] P. Kaw, G. Schmidt, and T. Wilcox. Filamentation and trapping of electromagnetic radiation in plasmas. *The Physics of Fluids*, 16(9):1522–1525, 1973.
- [51] A. G. Litvak. Finite-amplitude wave beams in a magnetoactive plasma. *Sov. Phys. JETP*, 30, 1970.
- [52] A. J. Palmer. Stimulated scattering and self-focusing in laser-produced plasmas. *The Physics of Fluids*, 14(12):2714–2718, 1971.
- [53] Bruce I. Cohen and Claire Ellen Max. Stimulated scattering of light by ion modes in a homogeneous plasma: Space-time evolution. *The Physics of Fluids*, 22(6):1115–1132, 1979.

- [54] P. E. Young, H. A. Baldis, R. P. Drake, E. M. Campbell, and K. G. Estabrook. Direct evidence of ponderomotive filamentation in a laser-produced plasma. *Phys. Rev. Lett.*, 61:2336–2339, Nov 1988.
- [55] J. J. Thomson. Stimulated raman scatter in laser fusion target chambers. *The Physics of Fluids*, 21(11):2082–2085, 1978.
- [56] O Klimo, S Weber, V T Tikhonchuk, and J Limpouch. Particle-in-cell simulations of laser–plasma interaction for the shock ignition scenario. *Plasma Physics and Controlled Fusion*, 52(5):055013, 2010.
- [57] D. Batani, L. Antonelli, S. Atzeni, J. Badziak, F. Baffigi, T. Chodukowski, F. Consoli, G. Cristoforetti, R. De Angelis, R. Dudzak, G. Folpini, L. Giuffrida, L. A. Gizzi, Z. Kalinowska, P. Koester, E. Krousky, M. Krus, L. Labate, T. Levato, Y. Maheut, G. Malka, D. Margarone, A. Marocchino, J. Nejd, Ph. Nicolai, T. O’Dell, T. Pisarczyk, O. Renner, Y. J. Rhee, X. Ribeyre, M. Richetta, M. Rosinski, M. Sawicka, A. Schiavi, J. Skala, M. Smid, Ch. Spindloe, J. Ullschmied, A. Velyhan, and T. Vinci. Generation of high pressure shocks relevant to the shock-ignition intensity regime. *Physics of Plasmas*, 21(3):032710, 2014.
- [58] K. Tanaka, L. M. Goldman, W. Seka, M. C. Richardson, J. M. Soures, and E. A. Williams. Stimulated raman scattering from uv-laser-produced plasmas. *Phys. Rev. Lett.*, 48:1179–1182, Apr 1982.
- [59] R. K. Kirkwood, R. L. Berger, C. G. R. Geddes, J. D. Moody, B. J. MacGowan, S. H. Glenzer, K. G. Estabrook, C. Decker, and O. L. Landen. Scaling of saturated stimulated raman scattering with temperature and intensity in ignition scale plasmas. *Physics of Plasmas*, 10(7):2948–2955, 2003.
- [60] J. F. Drake and Y. C. Lee. Temporally growing raman backscattering instabilities in an inhomogeneous plasma. *Phys. Rev. Lett.*, 31:1197–1200, Nov 1973.
- [61] Y. C. Lee and P. K. Kaw. Temporal electrostatic instabilities in inhomogeneous plasmas. *Phys. Rev. Lett.*, 32:135–138, Jan 1974.
- [62] C. S. Liu and Marshall N. Rosenbluth. Parametric decay of electromagnetic waves into two plasmons and its consequences. *The Physics of Fluids*, 19(7):967–971, 1976.
- [63] Martin V Goldman. Parametric plasmon-photon interactions: Part ii. analysis of plasmon propagator and correlation functions. *Annals of Physics*, 38(1):117 – 169, 1966.
- [64] E. Atlee Jackson. Parametric effects of radiation on a plasma. *Phys. Rev.*, 153:235–244, Jan 1967.
- [65] A. Simon, R. W. Short, E. A. Williams, and T. Dewandre. On the inhomogeneous two-plasmon instability. *The Physics of Fluids*, 26(10):3107–3118, 1983.
- [66] D. T. Michel, A. V. Maximov, R. W. Short, J. A. Delettrez, D. Edgell, S. X. Hu, I. V. Igumenshchev, J. F. Myatt, A. A. Solodov, C. Stoeckl, B. Yaakobi, and D. H.

- Froula. Measured hot-electron intensity thresholds quantified by a two-plasmon-decay resonant common-wave gain in various experimental configurations. *Physics of Plasmas*, 20(5):055703, 2013.
- [67] H. X. Vu, D. F. DuBois, J. F. Myatt, and D. A. Russell. Hot-electron production and suprathermal heat flux scaling with laser intensity from the two-plasmon-decay instability. *Physics of Plasmas*, 19(10):102703, 2012.
- [68] R. Yan, C. Ren, J. Li, A. V. Maximov, W. B. Mori, Z.-M. Sheng, and F. S. Tsung. Generating energetic electrons through staged acceleration in the two-plasmon-decay instability in inertial confinement fusion. *Phys. Rev. Lett.*, 108:175002, Apr 2012.
- [69] I.A.B. Zel'dovich and Y.P. Raizer. *Physics of Shock Waves and High-Temperature Hydrodynamic Phenomena*. Dover Books on Physics. Dover Publications, 2002.
- [70] R. Nora and R. Betti. One-dimensional planar hydrodynamic theory of shock ignition. *Physics of Plasmas*, 18(8):082710, 2011.
- [71] D. T. Michel, C. Sorce, R. Epstein, N. Whiting, I. V. Igumenshchev, R. Jungquist, and D. H. Froula. Shell trajectory measurements from direct-drive implosion experiments. *Review of Scientific Instruments*, 83(10):10E530, 2012.
- [72] T. R. Boehly, V. A. Smalyuk, D. D. Meyerhofer, J. P. Knauer, D. K. Bradley, R. S. Craxton, M. J. Guardalben, S. Skupsky, and T. J. Kessler. Reduction of laser imprinting using polarization smoothing on a solid-state fusion laser. *Journal of Applied Physics*, 85(7):3444–3447, 1999.
- [73] S. Skupsky, R. W. Short, T. Kessler, R. S. Craxton, S. Letzring, and J. M. Soures. Improved laser-beam uniformity using the angular dispersion of frequency-modulated light. *Journal of Applied Physics*, 66(8):3456–3462, 1989.
- [74] Y. Lin, T. J. Kessler, and G. N. Lawrence. Design of continuous surface-relief phase plates by surface-based simulated annealing to achieve control of focal-plane irradiance. *Opt. Lett.*, 21(20):1703–1705, Oct 1996.
- [75] V. N. Goncharov, T. C. Sangster, T. R. Boehly, S. X. Hu, I. V. Igumenshchev, F. J. Marshall, R. L. McCrory, D. D. Meyerhofer, P. B. Radha, W. Seka, S. Skupsky, C. Stoeckl, D. T Casey, J. A. Frenje, and R. D. Petrasso. Demonstration of the highest deuterium-tritium areal density using multiple-picket cryogenic designs on omega. *Phys. Rev. Lett.*, 104:165001, Apr 2010.
- [76] D.T. Michel, A.K. Davis, W. Armstrong, R. Bahr, R. Epstein, V.N. Goncharov, M. Hohenberger, I.V. Igumenshchev, R. Jungquist, D.D. Meyerhofer, and et al. Measurements of the ablation-front trajectory and low-mode nonuniformity in direct-drive implosions using x-ray self-emission shadowgraphy. *High Power Laser Science and Engineering*, 3:e19, 2015.
- [77] V. N. Goncharov, T. C. Sangster, P. B. Radha, R. Betti, T. R. Boehly, T. J. B. Collins, R. S. Craxton, J. A. Delettrez, R. Epstein, V. Yu. Glebov, S. X. Hu, I. V. Igumenshchev, J. P. Knauer, S. J. Loucks, J. A. Marozas, F. J. Marshall, R. L. McCrory, P. W. McKenty, D. D. Meyerhofer, S. P. Regan, W. Seka, S. Skupsky, V. A. Smalyuk, J. M. Soures,

- C. Stoeckl, D. Shvarts, J. A. Frenje, R. D. Petrasso, C. K. Li, F. Seguin, W. Manheimer, and D. G. Colombant. Performance of direct-drive cryogenic targets on omega. *Physics of Plasmas*, 15(5):056310, 2008.
- [78] I. V. Igumenshchev, W. Seka, D. H. Edgell, D. T. Michel, D. H. Froula, V. N. Goncharov, R. S. Craxton, L. Divol, R. Epstein, R. Follett, J. H. Kelly, T. Z. Kosc, A. V. Maximov, R. L. McCrory, D. D. Meyerhofer, P. Michel, J. F. Myatt, T. C. Sangster, A. Shvydky, S. Skupsky, and C. Stoeckl. Crossed-beam energy transfer in direct-drive implosions. *Physics of Plasmas*, 19(5):056314, 2012.
- [79] J.J. MacFarlane, I.E. Golovkin, P. Wang, P.R. Woodruff, and N.A. Pereyra. Spect3d – a multi-dimensional collisional-radiative code for generating diagnostic signatures based on hydrodynamics and pic simulation output. *High Energy Density Physics*, 3(1):181 – 190, 2007. Radiative Properties of Hot Dense Matter.
- [80] W. Seka, D. H. Edgell, J. P. Knauer, J. F. Myatt, A. V. Maximov, R. W. Short, T. C. Sangster, C. Stoeckl, R. E. Bahr, R. S. Craxton, J. A. Delettrez, V. N. Goncharov, I. V. Igumenshchev, and D. Shvarts. Time-resolved absorption in cryogenic and room-temperature direct-drive implosions. *Physics of Plasmas*, 15(5):056312, 2008.
- [81] V. Yu. Glebov, D. D. Meyerhofer, C. Stoeckl, and J. D. Zuegel. Secondary-neutron-yield measurements by current-mode detectors. *Review of Scientific Instruments*, 72(1):824–827, 2001.
- [82] R.L. McCrory, R.E. Bahr, R. Betti, T.R. Boehly, T.J.B. Collins, R.S. Craxton, J.A. Delettrez, W.R. Donaldson, R. Epstein, J. Frenje, V.Yu. Glebov, V.N. Goncharov, O.V. Gotchev, R.Q. Gram, D.R. Harding, D.G. Hicks, P.A. Jaanimagi, R.L. Keck, J.H. Kelly, J.P. Knauer, C.K. Li, S.J. Loucks, L.D. Lund, F.J. Marshall, P.W. McKenty, D.D. Meyerhofer, S.F.B. Morse, R.D. Petrasso, P.B. Radha, S.P. Regan, S. Roberts, F. Séguin, W. Seka, S. Skupsky, V.A. Smalyuk, C. Sorce, J.M. Soures, C. Stoeckl, R.P.J. Town, M.D. Wittman, B. Yaakobi, and J.D. Zuegel. Omega icf experiments and preparation for direct drive ignition on nif. *Nuclear Fusion*, 41(10):1413, 2001.
- [83] R.E. Kidder. Hot-electron preheat of laser-driven targets. *Nuclear Fusion*, 21(2):145, 1981.
- [84] Thomas B. Kaiser. Laser ray tracing and power deposition on an unstructured three-dimensional grid. *Phys. Rev. E*, 61:895–905, Jan 2000.
- [85] A. Colaïtis, G. Duchateau, P. Nicolai, and V. Tikhonchuk. Towards modeling of nonlinear laser-plasma interactions with hydrocodes: The thick-ray approach. *Phys. Rev. E*, 89:033101, Mar 2014.
- [86] C. K. Li and R. D. Petrasso. Stopping of directed energetic electrons in high-temperature hydrogenic plasmas. *Phys. Rev. E*, 70:067401, Dec 2004.
- [87] M Touati, J-L Feugeas, Ph Nicolai, J J Santos, L Gremillet, and V T Tikhonchuk. A reduced model for relativistic electron beam transport in solids and dense plasmas. *New Journal of Physics*, 16(7):073014, 2014.
- [88] B. Dubroca, J.-L. Feugeas, and M. Frank. Angular moment model for the fokker-planck equation. *The European Physical Journal D*, 60(2):301–307, Nov 2010.

- [89] D. Del Sorbo, J.-L. Feugeas, Ph. Nicolaï, M. Olazabal-Loumé, B. Dubroca, S. Guisset, M. Touati, and V. Tikhonchuk. Reduced entropic model for studies of multidimensional nonlocal transport in high-energy-density plasmas. *Physics of Plasmas*, 22(8):082706, 2015.
- [90] A. Colaïtis, X. Ribeyre, E. Le Bel, G. Duchateau, Ph. Nicolaï, and V. Tikhonchuk. Influence of laser induced hot electrons on the threshold for shock ignition of fusion reactions. *Physics of Plasmas*, 23(7):072703, 2016.
- [91] E. Martinolli, M. Koenig, J. M. Boudenne, E. Perelli, D. Batani, and T. A. Hall. Conical crystal spectrograph for high brightness x-ray k-alpha spectroscopy in subpicosecond laser–solid interaction. *Review of Scientific Instruments*, 75(6):2024–2028, 2004.
- [92] S. Agostinelli, J. Allison, K. Amako, J. Apostolakis, H. Araujo, P. Arce, M. Asai, D. Axen, S. Banerjee, G. Barrand, F. Behner, L. Bellagamba, J. Boudreau, L. Broglia, A. Brunengo, H. Burkhardt, S. Chauvie, J. Chuma, R. Chytrcek, G. Cooperman, G. Cosmo, P. Degtyarenko, A. Dell’Acqua, G. Depaola, D. Dietrich, R. Enami, A. Feliciello, C. Ferguson, H. Fesefeldt, G. Folger, F. Foppiano, A. Forti, S. Garelli, S. Giani, R. Giannitrapani, D. Gibin, J.J. Gómez Cadenas, I. González, G. Gracia Abril, G. Greeniaus, W. Greiner, V. Grichine, A. Grossheim, S. Guatelli, P. Gumplinger, R. Hamatsu, K. Hashimoto, H. Hasui, A. Heikkinen, A. Howard, V. Ivanchenko, A. Johnson, F.W. Jones, J. Kallenbach, N. Kanaya, M. Kawabata, Y. Kawabata, M. Kawaguti, S. Kelner, P. Kent, A. Kimura, T. Kodama, R. Kokoulin, M. Kossov, H. Kurashige, E. Lamanna, T. Lampén, V. Lara, V. Lefebure, F. Lei, M. Liendl, W. Lockman, F. Longo, S. Magni, M. Maire, E. Medernach, K. Minamimoto, P. Mora de Freitas, Y. Morita, K. Murakami, M. Nagamatu, R. Nartallo, P. Nieminen, T. Nishimura, K. Ohtsubo, M. Okamura, S. O’Neale, Y. Oohata, K. Paech, J. Perl, A. Pfeiffer, M.G. Pia, F. Ranjard, A. Rybin, S. Sadilov, E. Di Salvo, G. Santin, T. Sasaki, N. Savvas, Y. Sawada, S. Scherer, S. Sei, V. Sirotenko, D. Smith, N. Starkov, H. Stoecker, J. Sulkimo, M. Takahata, S. Tanaka, E. Tcherniaev, E. Safai Tehrani, M. Tropeano, P. Truscott, H. Uno, L. Urban, P. Urban, M. Verderi, A. Walkden, W. Wander, H. Weber, J.P. Wellisch, T. Wenaus, D.C. Williams, D. Wright, T. Yamada, H. Yoshida, and D. Zschesche. Geant4—a simulation toolkit. *Nuclear Instruments and Methods in Physics Research Section A: Accelerators, Spectrometers, Detectors and Associated Equipment*, 506(3):250 – 303, 2003.
- [93] Francesc Salvat, José M Fernández-Varea, and Josep Sempau. Penelope-2006: A code system for monte carlo simulation of electron and photon transport. In *Workshop proceedings*, volume 4. Nuclear Energy Agency, Organization for Economic Cooperation and . . . , 2006.
- [94] O Renner, M Šmíd, D Batani, and L Antonelli. Suprathermal electron production in laser-irradiated cu targets characterized by combined methods of x-ray imaging and spectroscopy. *Plasma Physics and Controlled Fusion*, 58(7):075007, 2016.
- [95] Michel Koenig, Bernard Faral, Jean Michel Boudenne, Dimitri Batani, Alessandra Benuzzi, and Simone Bossi. Optical smoothing techniques for shock wave generation in laser-produced plasmas. *Phys. Rev. E*, 50:R3314–R3317, Nov 1994.

- [96] Michel Koenig, Bernard Faral, Jean Michel Boudenne, Dimitri Batani, Alessandra Benuzzi, and Simone Bossi. Optical smoothing techniques for shock wave generation in laser-produced plasmas. *Phys. Rev. E*, 50:R3314–R3317, Nov 1994.
- [97] D. Batani, F. Strati, B. Telaro, Th. Löwer, T. Hall, A. Benuzzi-Mounaix, and M. Koenig. Production of high quality shocks for equation of state experiments. *The European Physical Journal D - Atomic, Molecular, Optical and Plasma Physics*, 23(1):99–107, Apr 2003.
- [98] B. C. Stuart, M. D. Feit, A. M. Rubenchik, B. W. Shore, and M. D. Perry. Laser-induced damage in dielectrics with nanosecond to subpicosecond pulses. *Phys. Rev. Lett.*, 74:2248–2251, Mar 1995.
- [99] Direction des Applications Militaire Commissariat aux Energies Atomique et Alternatives. Laser MegaJoule, PETawatt Aquitaine Laser, User Guide, 2017.
- [100] V. Brandon, B. Canaud, M. Temporal, and R. Ramis. Low initial aspect-ratio direct-drive target designs for shock- or self-ignition in the context of the laser megajoule. *Nuclear Fusion*, 54(8):083016, jun 2014.
- [101] W. Theobald, R. Nora, M. Lafon, A. Casner, X. Ribeyre, K. S. Anderson, R. Betti, J. A. Delettrez, J. A. Frenje, V. Yu. Glebov, O. V. Gotchev, M. Hohenberger, S. X. Hu, F. J. Marshall, D. D. Meyerhofer, T. C. Sangster, G. Schurtz, W. Seka, V. A. Smalyuk, C. Stoeckl, and B. Yaakobi. Spherical shock-ignition experiments with the 40 + 20-beam configuration on omega. *Physics of Plasmas*, 19(10):102706, 2012.
- [102] P. B. Radha, C. Stoeckl, V. N. Goncharov, J. A. Delettrez, D. H. Edgell, J. A. Frenje, I. V. Igumenshchev, J. P. Knauer, J. A. Marozas, R. L. McCrory, D. D. Meyerhofer, R. D. Petrasso, S. P. Regan, T. C. Sangster, W. Seka, and S. Skupsky. Triple-picket warm plastic-shell implosions on omega. *Physics of Plasmas*, 18(1):012705, 2011.
- [103] I Kawrakow and D W.O. Rogers. The egsrc code system: Monte carlo simulation of electron and photon transport. 01 2000.
- [104] C. Stoeckl, W. Theobald, S. P. Regan, and M. H. Romanofsky. Calibration of a time-resolved hard-x-ray detector using radioactive sources. *Review of Scientific Instruments*, 87(11):11E323, 2016.
- [105] F. H. Séguin, J. A. Frenje, C. K. Li, D. G. Hicks, S. Kurebayashi, J. R. Rygg, B.-E. Schwartz, R. D. Petrasso, S. Roberts, J. M. Soures, D. D. Meyerhofer, T. C. Sangster, J. P. Knauer, C. Sorce, V. Yu. Glebov, C. Stoeckl, T. W. Phillips, R. J. Leeper, K. Fletcher, and S. Padalino. Spectrometry of charged particles from inertial-confinement-fusion plasmas. *Review of Scientific Instruments*, 74(2):975–995, 2003.
- [106] R. A. Lerche, D. W. Phillion, and G. L. Tietbohl. 25 ps neutron detector for measuring icf-target burn history. *Review of Scientific Instruments*, 66(1):933–935, 1995.
- [107] E. Llor Aisa, X. Ribeyre, S. Gus’kov, Ph. Nicolai, and V. T. Tikhonchuk. Dense plasma heating and shock wave generation by a beam of fast electrons. *Physics of Plasmas*, 22(10):102704, 2015.

-
- [108] Martin J Berger. Estar, pstar, and astar: Computer programs for calculating stopping-power and range tables for electrons, protons, and helium ions. *Unknown*, 1992.
- [109] P D Roberts, S J Rose, P C Thompson, and R J Wright. The stability of multiple-shell icf targets. *Journal of Physics D: Applied Physics*, 13(11):1957, 1980.
- [110] R. C. Shah, B. M. Haines, F. J. Wysocki, J. F. Benage, J. A. Fooks, V. Glebov, P. Hakel, M. Hoppe, I. V. Igumenshchev, G. Kagan, R. C. Mancini, F. J. Marshall, D. T. Michel, T. J. Murphy, M. E. Schoff, K. Silverstein, C. Stoeckl, and B. Yaakobi. Systematic fuel cavity asymmetries in directly driven inertial confinement fusion implosions. *Phys. Rev. Lett.*, 118:135001, Mar 2017.